Bimodal microstructure and fatigue properties of nanocrystalline and ultrafine grained nickel

Dissertation

Zur Erlangung des Grades des
Doktors der Ingenieurwissenschaften (Dr.-Ing.)
der Naturwissenschaftlich-Technischen Fakultät III
Chemie, Pharmazie, Bio- und Werkstoffwissenschaften
der Universität des Saarlandes

Von
M.Sc. Tao Qian
Saarbrücken, 2013

Eingereicht am:	07.02.2013
Tag des Kolloquiums:	24.07.2013
Dekan:	Prof. Dr. Volkhard Helms
Berichterstatter:	Prof. Dr. H. Vehoff
	Prof. Dr. R. Busch
Vorsitzender:	Prof. Dr. C. Boller
Akad. Mitarbeiter:	Dr. C. Gachot

To my wife Ying and my son Haoting

Acknowledgments

Looking back on my time in the Institute of Materials Science and Methods in Saarland University, I would like to express my sincere thanks to all of those who have supported me and have thereby contributed to the accomplishments in this thesis. It is my distinct pleasure to acknowledge here my coworkers, friends and family, without whom I would not have chance to finish this work.

In the first place I would like to express my gratitude to Prof. Dr. rer. nat. Horst Vehoff for providing me the opportunity and the guidance of my Ph.D study. He has an exceptional insight in the material science and his helpful discussions and scientific comments inspired me to continue my research.

Equally important, I am sincerely grateful to Dr. Michael Marx for his supervision and support to my work and research. He was always very patient to take discussions with me and to propose many meaningful suggestions. From a beginner to a person who acquires good skills on the electron microscope I learned much from him. Besides, he spent lots of time to read this thesis and gave his critical comments.

I gratefully acknowledge Prof. Dr. rer. nat. Ralf Busch for being part of the Reading Committee and his comments about this thesis.

I am grateful to the financial support from the German Research foundation (DFG) with the researching project MA 3322/3-1.

I would like to thank Philipp Kerger, my assistant, for preparing my specimens, conducting the heat treatment experiments and processing the experimental data, Chen Chen for preparing my specimens, and Halima Bayad for supporting in the in-situ annealing.

My thanks go particular to Kerstin Schüler for being a such nice colleague and friend and helping me in different areas, to Dr. Nousha Kheradmand for sharing the office and many interesting talks, to Dr. Afrooz Barnoush for sharing of his knowledge, to Dr. Wolfgang Schäf for introducing the FIB-crack method and performing the hydraulic testing machine, and to Mohammad Zamanzadeh, Dr. Camille Perrin, Dr. Markus Welsch and Alain Knorr for their help in the institute. I would also like to thank my friend Dirk Hillerbrecht for his patience improving my German speaking and our

long-standing badminton playing.

I am very grateful to our technicians Peter Limbach and Stephan Schmitz who were always ready for preparing my specimens and had good ideas and workmanship for my specimen holders, to Andreas Kirsch from whom I could get my support and help anytime and anywhere, and to Rita Maron for her availability and support in the laboratories. I would like to thank Mrs. Elisabeth Ohm and Miss Diana Born for their support in the institute life and making the administrative work.

I would like to than Dr. I. Karaman in Texas A&M University for processing of the ECAP nickel billets, to thank Dr. Flavio Soldera and Dipl.Ing. Christoph Pauly from the Institute of the functional Materials for their support in the FIB operation and the preparation of my first microcracks, to thank Dipl.Ing. Benjamin Bax from the Institute of the functional Materials for conducting the surface laser heat treatment, and to thank Dipl. Ing. Jörg Schmauch from the Institute of Technical Physics for his support in performing the EBSD measurements and the other REM and TEM measurements.

I would like to thank my parents who give me everything but never expect anything in return. Their support, encouragement and love make me go further in my life. I would like to thank my parents in-law for their understanding and supporting to take care of my wife and my son when I was so long absent.

Finally, I am so grateful to my wife Ying for her love, without her understanding and encouragement it is impossible for me to finish this work, and to my lovely son Haoting for bringing me so much happiness and giving me courage and power to keep on going.

Contents

List of Figures

List of Tables

Abstract

The nanocrystalline (NC) and ultrafine grained (UFG) materials show very high strength but low ductility. In this work bimodal microstructures are developed by introducing larger grains into the finer grained matrix, to combine high strength and considerably high ductility at the same time.

Different bimodal microstructures are developed by heat treatment of the PED NC nickel and the ECAP UFG nickel. The grain growth kinetics is quantitatively analyzed using the JMAK model and the Burke and Turnbull model for the PED nickel. However, the annealing phenomena for the ECAP UFG nickel are difficult to be described quantitatively due to the initial severe plastic deformed state and are only qualitatively analyzed.

Microhardness measurement and tensile tests show that the finer grains provide the strength and the coarser grains ensure the ductility in the bimodal microstructures. The fatigue behavior and crack growth resistance is systematically investigated for the different microstructures. The microcracks introduced by focus ion beam propagate during the fatigue experiments and induce the ultimate fracture for the PED NC, NC/UFG and UFG nickel. Among them the bimodal NC/UFG nickel shows the best fatigue performance. However, the ECAP nickel is not sensitive to the microcracks, and therefore the macro-notches are introduced to investigate the crack growth behavior. Dynamic recrystallization is found to be the main mechanism for the plastic deformation in the ECAP nickel.

Zusammenfassung

Nanokristalline (NK) und ultrafeinkörnige (UFG) Materialien besitzen sehr hohe Festigkeit aber niedrige Duktilität. In dieser Arbeit werden bimodale Mikrostrukturen, die gleichzeitig hohe Festigkeit und gute Duktilität haben, durch das Einbringen größerer Körner in die feinkörnige Matrix entwickelt.

Verschiedene bimodale Mikrostrukturen werden durch Wärmebehandlungen von NK PED Nickel und UFG ECAP Nickel entwickelt. Die Kornwachstumskinetik des PED Nickels wird quantitativ erfolgreich nach dem JMAK Modell und Burke und Turnbull Modell analysiert. Die Kornwachstumsphänomene von ECAP Nickel können hingegen wegen ihrer komplizierten Anfangsmikrostruktur nur qualitativ beschrieben werden.

Mikrohärtemessung und Zugversuche zeigen, dass in den bimodalen Gefügen die feineren Körner die Festigkeit und die gröberen Körner die Duktilität gewährleisteten. Ermüdungsverhalten und Risswachstumswiderstand der verschiedenen Gefüge werden erforscht. Die durch Focused Ion Beam geschnittenen Mikrorisse breiten sich während der Ermüdungszyklen aus und führen zum endgültigen Bruch fr das PED NK, NK/UFG und UFG Nickel. Das bimodale NK/UFG Nickel zeigt das beste Ermüdungsverhalten. Im Gegensatz zum PED Nickel wird festgestellt, dass das ECAP Nickel nicht mikrorissempfindlich ist. Daher werden Makrokerben initiiert, um die Rissausbreitung zu untersuchen. Für das ECAP Nickel ist dynamische Recrystallization der Hauptmechanismus für die plastische Verformung in den Ermüdungsexperimenten.

Acronyms

8C	eight passes with route C
8E	eight passes with route E
AFM	atomic force microscope
ARB	accumulative roll bonding
bcc	body centered cubic
CG	corse grained
EBSD	electron backscattered diffraction
ECAP	equal channel angular pressing
EDS/EDX	Energy-dispersive X-ray spectroscopy
fcc	face centered cubic
FE	finite element
FIB	focused ion beam
GB	grain boundary
HAGB	high angle grain boundaries
HCF	high cycle fatigue
HPT	high pressure torsion
IGC	inert gas condensation
LAGB	low angle grain boundary
LCF	low cycle fatigue
MC	microcrystalline
NC	nanocrystalline
NC/UFG	mixture of nanocrystalline and ultrafine grains
OIM	orientation imaging microscopy
PED	pulsed electrodeposition
PSB	persistent slip band
SB	shear band
SEM	scanning electron microscope
SMAT	surface mechanical attrition treatment
SPD	severe plastic deformation

SRS	strain rate sensitivity
TEM	transmission electron microscope
UFG	ultrafine grained
UFG/CG	mixture of ultrafine grains and coarse grains
XRD	X-ray diffraction

1. Introduction

Nanocrystalline (NC) materials, defined as polycrystalline materials with grain sizes typically below 100 nm, and ultrafine grained (UFG) materials, with grain sizes between $100 - 1000$ nm, are receiving increasing interest of materials scientists and researchers since they have emerged as materials with unusual physical and mechanical properties in the 1980s [*Gleiter*, 1989; *Valiev et al.*, 1990, 1991]. The unique microstructure with grain refinement into the NC or UFG range ensures a high strength of such materials which is 5-10 times of conventional materials of similar composition. However, the decrease in grain size also results in a drop of work hardening or uniform elongation, leading to low tensile ductility and plastic instability of the NC and UFG materials.

Strength and ductility are two of the most important mechanical properties for the structural materials. However, they are usually opposing characteristics: *"the higher the strength, the lower the ductility; and vice versa. This correlation is associated with the nature of plasticity: the more difficult it is for dislocations to appear and to move, the stronger but the more brittle and less ductile is any crystalline material [Valiev, 2002]."* It has been confirmed by lots of experimental results that most bulk NC or UFG materials have relatively low ductility [*Park et al.*, 2000; *Jia et al.*, 2001; *Tsuji et al.*, 2002; *Koch*, 2003; *Wang and Ma*, 2003, 2004b; *Zhu and Liao*, 2004; *Ovid'ko*, 2005; *Meyers et al.*, 2006; *Ovid'ko*, 2007; *Wang et al.*, 2008b], which limits the application of these materials. Therefore, it has been and will still be a long-standing goal for materials scientists to process structural materials with balanced combination of high strength and high ductility [*Wang and Ma*, 2004a; *Lu et al.*, 2009; *Zhao et al.*, 2010b; *Zhu et al.*, 2012; *Ovid'ko and Langdon*, 2012].

There have been some methods developed in recent years efficiently to achieve high strength and good ductility at the same time. The first method is to embed coarse grains into the fine grained matrix constructing a bimodal grain size distribution [*Tellkamp et al.*, 2001; *Wang et al.*, 2002b; *Joshi et al.*, 2006; *Hoeppel et al.*, 2010; *Patra et al.*, 2012]. In these materials, the high strength comes from the fine grained matrix phase, and the coarser grains ensure the ductility. The second method is to engineer coherent internal boundaries such as the twin boundaries at the nanometer scale [*Lu et al.*, 2004;

Zhang et al., 2004; *Shen et al.*, 2006; *Singh et al.*, 2011; *Yu et al.*, 2012]. By decreasing the twin spacing to the nanometer scale, the yield strength and ductility are both improved in these kinds of metals. Some other strategies have also been reported, such as by Zhao et al. who observed a simultaneous increase in ductility and strength of the UFG Cu by tailoring the stacking fault energy via alloying with Zn [*Zhao et al.*, 2006a], and by Zhao et al. who demonstrated the occurrence of simultaneous improvements in the ductility and strength of UFG materials by introducing a high density of pre-existing deformation twins and increasing the fraction of high angle grain boundaries [*Zhao et al.*, 2006b].

Among the above mentioned methodologies to improve the ductility of the NC or UFG material, the bimodal grain size distribution is the most popular. There have already been lots of studies on the bimodal microstructures, mainly concentrating on the monotonic loading conditions, to investigate the mechanical properties and the deformation mechanisms [*Tellkamp et al.*, 2001; *Wang et al.*, 2002b; *Lee et al.*, 2005; *Fan et al.*, 2006; *Prasad et al.*, 2009; *Ramtani et al.*, 2010; *Patra et al.*, 2012]. However, there are only few results that concern the fatigue behaviour of the bimodal microstructures until the recent works by Nelson et al. [*Nelson et al.*, 2011] and Korn et al. [*Korn et al.*, 2011]. Nelson et al. investigated the bimodal Al 5083 alloy and simulated the fatigue tests in finite element (FE) model. In their cyclic FE model the crack initiated in a coarse grain and propagated along the coarse grain and the surrounding UFG matrix until it was large enough to cause failure. Korn et al. concentrated on the evolution of the bimodal grain size distribution and found that the bimodal microstructure could enhance the monotonic and fatigue strength properties of the UFG materials considerably or only marginally, depending on the annealing conditions and the materials.

In this work the concept of the bimodal microstructure is empolyed, with the aim to develop the different bimodal microstructures and to investigate their corresponding mechanical properties, especially the fatigue behaviour. Two groups of fine grained materials were used as the researching objectives: the NC nickel synthesized by pulsed electrodepositon (PED) and the UFG nickel processed by equal channel angular pressing (ECAP) where the PED and ECAP techniques are currently the most commonly used processes to produce full-dense and intrinsically flaw-free bulk NC and UFG metals or alloys. The low ductility in these materials is mainly due to the inability of the grains to accumulate dislocations, i.e. due to the smallness of the grain size of the PED processed NC materials or the initially high dislocation density of the ECAP processed UFG materials.

The motivation of this study is to achieve the bimodal microstructures in the different ranges, to improve the ductility and the fatigue response of the fine grained nickel.

The first aim is to obtain a series of bimodal microstructures with different grain size distributions such as the NC/UFG, UFG/CG and micron/CG distributions, starting from the PED NC nickel and the ECAP UFG nickel. Among the different microstructures, the bimodal NC/UFG distribution, mixing of nanograins and ultrafine grains, is a novel class of the bimodal microstructures developed from the NC nickel. Based on the observation of the annealing phenomena, the grain growth kinetics of the NC and UFG nickel will be investigated. The second aim is to investigate the influence of the different microstructures to the fatigue properties and to examine whether the bimodal microstructures show the improved performances over their monomodal counterparts in the fatigue experiments. Experiments were developed to probe the fatigue crack resistance of the different microstructures, based on the methodology of initiating microcracks with focus ion beam (FIB) on the specimen surface. The underlying deformation mechanisms of the different microstructures are to be investigated.

2. Literature Review

2.1. Nanocrystalline and ultrafine grained materials

Over the past decades, nanocrystalline (NC) and ultrafine grained (UFG) materials have achieved great interests of the materials scientists and researchers. It has been found that grain refinement into the UFG and NC range is accompanied by the beneficial improvements in the materials mechanical properties, such as strength, hardness, fatigue resistance et al. [*Gleiter*, 1989; *Valiev et al.*, 2000; *Valiev and Langdon*, 2006; *Kumar et al.*, 2003; *Hanlon*, 2004]. However, there is often some loss in the ductility which limits the applications of these materials. Nevertheless, due to the unique mechanical properties, different techniques have been developed to synthesize or to process the NC or UFG materials, resulting in different microstructures with the same 'nominal' grain size.

In this section, there is firstly a short introduction about the pulsed electrodeposiston and equal channel angular pressing. The second part is a general survey on the mechanical properties for the NC and UFG materials. Thirdly, the actual development and achievements about the bimodal microstructures are introduced.

2.1.1. Electrodepositon and equal channel angular pressing

Generally, there are two basic concepts of the applied techniques to prepare the NC or UFG materials. The first concept is the 'bottom-up' method, such as inert gas condensation (IGC) [*Gleiter*, 1989; *Fougere et al.*, 1995], pulsed electrodeposition (PED) [*Rofagha et al.*, 1991; *Erb*, 1995; *Lu et al.*, 2004] and mechanical milling [*Witkin and Lavernia*, 2006; *Youssef et al.*, 2005]. This is the conventional route to produce the materials with the grain size in the nanoscale range. The second concept is the 'top-down' method, i.e the so-called severe plastic deformation (SPD), which has emerged as a promising method to produce ultrafine grained materials with bulk volume since last three decades. SPD refers to a class of mechanical deformation processes that impart large plastic deformations such as high pressure torsion (HPT) [*Witkin and Lavernia*, 2006; *Youssef*

et al., 2005; *Lowe and Valiev*, 2004], accumulative roll bonding (ARB) [*Tsuji et al.*, 2002, 2003] and equal channel angular pressing (ECAP) [*Valiev et al.*, 2000; *Valiev and Langdon*, 2006].

In this study two groups of fined grained nickel, which are full-dense and intrinsically flaw-free, have been used as the researching objectives, i.e. the PED synthesized NC nickel and the ECAP processed UFG nickel, where PED and ECAP are the most used processes among the 'bottom-up' and 'top-down' methods, respectively.

Pulsed electrodeposition

Electrodeposition is known as a coating technique for a long time, but the synthesis of nanocrystalline metals or alloys by electrodeposition has been studied from only the last twenty years [*Aust et al.*, 1993; *El-Sherik and Erb*, 1995; *Natter and Hempelmann*, 1996]. Electrodeposition is an electrode reaction which involves oxidation/reduction of a solid metal and its dissolved ions. The process can be considered as a special form of grain boundary engineering in which the grain boundary content (types and quantities) of a material are controlled during material processing to achieve certain physical, chemical and mechanical properties [*Aust et al.*, 1993].

The principle of this method is that an applied electric field draws precursor ions towards the substrates surface. When an ion reaches the surface, it bonds chemically with certain bounding sites and stays there. Figure 2.1 shows the pulsed electrodeposiston sequence schematically [*Meyers et al.*, 2006]. The realization of the nanostructured metals with this technique is possible if a large number of grain nuclei on the electrode surface is created and if the growth of nuclei and crystallites is strongly impeded. The relevant experimental parameters are subdivided into physical parameters (pulse characteristics t_{on}, t_{off}, I_{pulse} and I_a) and chemical parameters (addition of complex formers or inhibitors). The $t_{on}-$time is the length of a current pulse, the $t_{off}-$time is the time between two pulses, I_{pulse} is the pulse height, and I_a is the averaged current density. In addition pH value, bath temperature and hydrodynamic conditions also have some effect [*Natter et al.*, 1998; *Natter and Hempelmann*, 2008]. This technique is suitable to create not only thin film metals and alloys, but also fully dense bulk nanocrystalline plates with thickness of several millimeters.

Electrodepositon has many advantages over other 'botton-up' techniques such as IGC and mechanical milling including: (1) the potential to synthesize large variety of pure metals, alloys and composite materials with grain size less than 100 nm, (2) few shape and size limitations, (3) high production rates, (4) low initial capital investment re-

quirements and (5) easy technology transfer from the research laboratory to existing infrastructure in electroplating and electroforming industries [*Erb*, 1995; *Meyers et al.*, 2006].

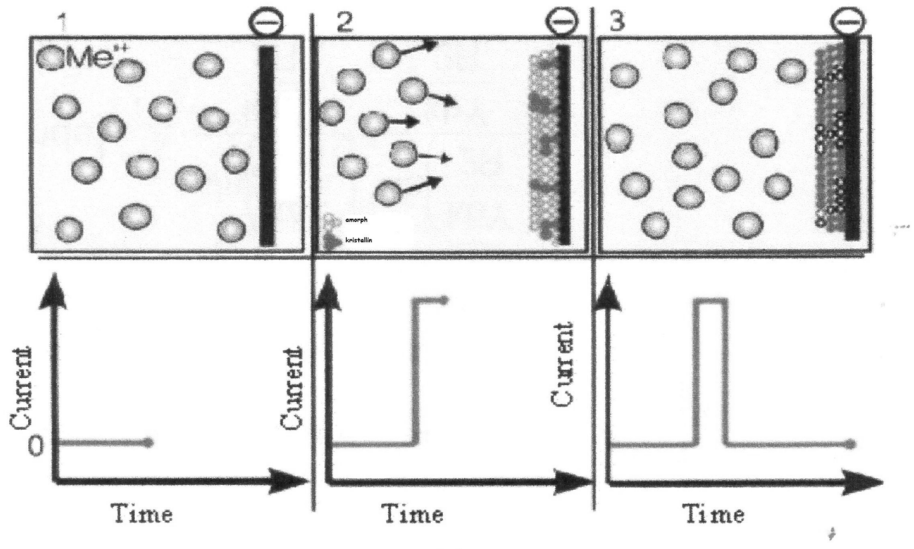

Figure 2.1.: Schematic drawing of the pulsed electrodepositon set-up for synthesizing NC materials [*Meyers et al.*, 2006].

Equal channel angular pressing

Equal channel angular pressing (ECAP) has emerged as a widely known procedure for grain refinement of metals and alloys typically to the sub-micrometer level in the last two decades. It is a processing method in which a metal billet is subjected to an intense plastic straining through simple shear without significantly altering in its cross-section. Numerous well-established methods, including the standard industrial metal-working processes of rolling or extrusion, have been developed for subjecting metallic samples to an imposed strain but there is always a change in the physical dimensions of the samples. By contrast, ECAP differs from these conventional procedures because the cross sectional dimensions of the sample remain unchanged during straining [*Furukawa et al.*, 2001].

The principle of ECAP is depicted schematically in figure 2.2 in three-dimensional illustration. The ECAP die contains two channels, equal in cross section, intersecting at an angle near the center of the die. The metallic billets are pressed through the die using a plunger. Simple shearing strain is imposed at the shearing plane which is shown in figure 2.2. Three planes may be defined for the metallic billet at the point of exiting

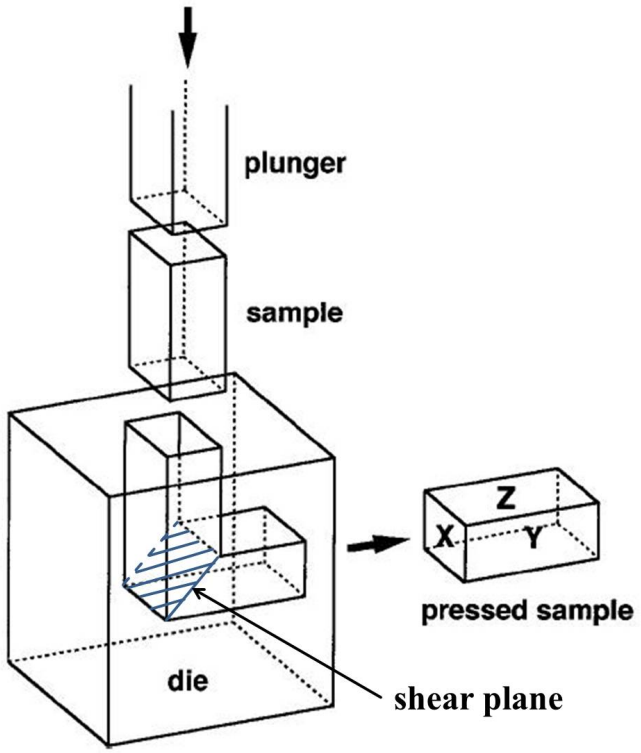

Figure 2.2.: Schematic illustration of the ECAP die showing the three orthogonal planes x, y and z.

from the die, where x-plane is perpendicular to the longitudinal axis of the sample and y-plane and z-plane are parallel to the side and top faces respectively.

An important parameter for the ECAP is the processing route. In practice, the metallic billets for the ECAP process are with square or round cross-sections. It is convenient to develop processing routes by rotating the billets with different grades (with increments of 90°) between two passes. The often used ECAP routes are four fundamental routes (A, B_A, B_C and C), as well as two additional hybrid routes (E and F). A brief description of the different ECAP routes is given in table 2.1. In this study, the UFG nickel processed with route C and route E have been used.

The UFG materials processed by ECAP have some unique microstructural characteristics. As the metals are imposed to a very high strain during the ECAP process, the resultant UFG microstructures are usually in a metastable state. Therefore, the equilibrium grain size and the homogeneity of the microstructures are significantly influenced by the stacking fault energy of the metals. It is found that the equilibrium grain size in pure aluminum, which is of high stacking fault energy, is $\sim 1.2-1.3$ μm and the microstructure is extremely homogeneous after pressing at room temperature (RT).

route	Rotations
A	0°, all passes
B_A	90°, N even; 270°, N odd
B_C	90°, all passes
C	180°, all passes
E	180°, 90°, 180°, 270°, four passes as a circle
F	90°, 180°, 270°, 180°, four passes as a circle

Table 2.1.: A brief description of the different ECAP routes

By contrast, the equilibrium grain size for pure copper, which is of low stacking fault energy, pressed at RT is much smaller (typically ~ 0.27 μm), but the microstructure is not fully homogeneous. In this manner, the equilibrium grain size is very small and the microstructure is essentially homogeneous for pure nickel, with a stacking fault energy between pure aluminum and pure copper [*Komura et al.*, 1999; *Neishi et al.*, 2002; *Valiev and Langdon*, 2006]. Another microstructural characteristic is the high density of dislocations, which are inside the grains and trapped at the grain boundaries which induce the grain boundaries in a non-equilibrium state [*Zhao et al.*, 2004; *Reihanian et al.*, 2008]. Besides, there are strong textures of the microstructure introduced during the ECAP pressing [*Zhilyaev et al.*, 2004, 2005; *Skrotzki et al.*, 2008].

2.1.2. Mechanical properties

Generally, NC and UFG materials are structurally characterized by a large volume fraction of grain boundaries (figure 2.3), which play an important role in the physical, mechanical and chemical properties of the NC and UFG materials. Compared with their conventional coarse grained (CG) counterparts, the NC and UFG materials usually have ultrahigh hardness and yield strength, fracture strength and superior wear resistance [*Dao et al.*, 2007]. Investigation on strengthening of the materials with grain size refinement can be traced back to the early work by Hall and Petch [*Hall*, 1951; *Petch*, 1953]. The empirical Hall-Petch (H-P) relationship describes the grain size dependence of the yield strength (σ_y) as

$$\sigma_y = \sigma_0 + kd^{-0.5}, \tag{2.1}$$

where σ_0 and k are material dependent constants and d is the mean grain size. The validity of H-P relationship has been confirmed for many metals and alloys with an av-

erage grain size of 100 nm or larger, where dislocations pile-up against grain boundaries along with other transgranular dislocation mechanisms are the dominant strengthening mechanisms [*Yang and Vehoff*, 2005; *Dao et al.*, 2007; *Godon et al.*, 2010].

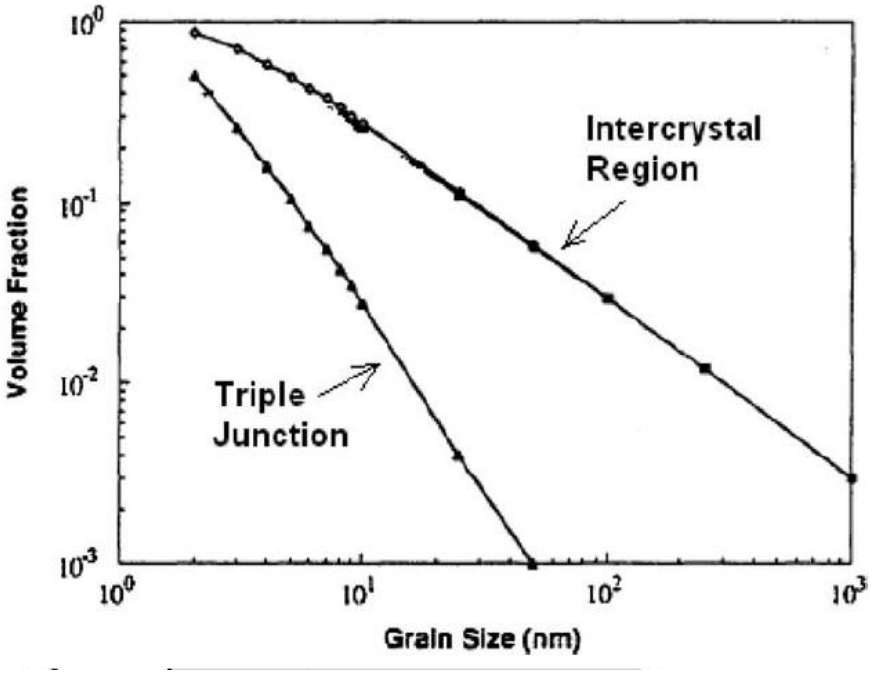

Figure 2.3.: The effect of grain size on calculated volume fraction of intercrystal regions and triple junctions [*Meyers et al.*, 2006].

Extremely high strength and hardness have been observed in NC and UFG metals, which have been found to increase with decreasing grain size. A summary of the hardness and the yield strength of nanocrystalline Cu vs. $d^{-1/2}$ has been reported by Chen el al., as shown in figure 2.4 [*Chen et al.*, 2006]. Similar results have been summarized by Krasilnikov et al. for the UFG nickel [*Krasilnikov et al.*, 2005]. It is remarkable to note that a relatively soft metal as Cu can be made to exhibit a strength as high as $\sim$ 1 GPa through nanostructuring. It has been found that, when the grain size is extremely small, grain boundary mediated mechanisms could be enhanced to control the plastic deformation [*Kumar et al.*, 2003; *Cao et al.*, 2008].

Initially it was only possible to produce the nanostructured materials with thin films or specimens of small scale, and the high strength of the NC and UFG materials is satisfactory for the applications. However, the low ductility of the NC and UFG materials seemed to be a main problem when the bulk NC and UFG materials had been provided. Strength and ductility usually exhibit an inverse relationship: increasing the strength sacrifices the ductility; and vice versa. It has been confirmed by lots of experimental

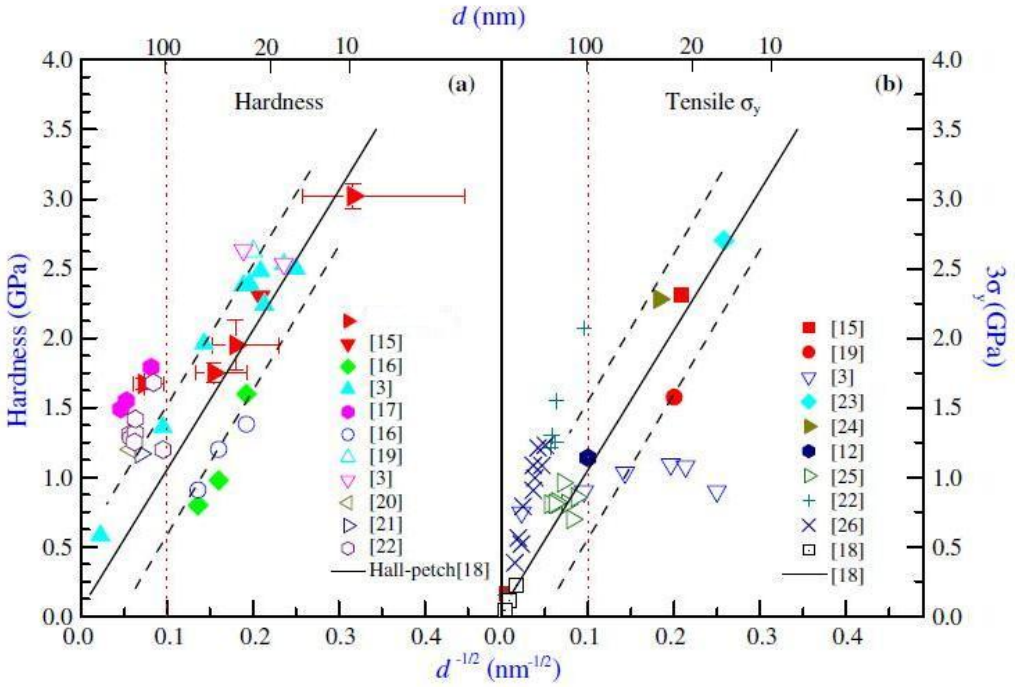

Figure 2.4.: Variation of hardness and tensile yield strength with the grain size for various Cu samples, in which the straight lines represent the H-P relationship extrapolated from the CG-Cu [*Chen et al.*, 2006].

results that most bulk NC materials have relatively low ductility [*Park et al.*, 2000; *Jia et al.*, 2001; *Tsuji et al.*, 2002; *Zhu and Liao*, 2004; *Meyers et al.*, 2006; *Wang et al.*, 2008b], which limits the application of these materials. The reason for the low ductility of the NC and UFG materials can be classified into two groups: extrinsic processing artifacts and intrinsic microstructure/deformation mechanisms. The extrinsic processing artifacts are mainly due to the material synthesizing processes. When these flaws exist, they seem to be the controlling factor that causes the failure of the materials before any significant plastic deformation occurs [*Sanders et al.*, 1997a,b; *Zhao et al.*, 2010a]. To minimize or eliminate the processing flaws of the NC or UFG materials was an important task in the earlier years [*Zhang et al.*, 2002; *Youssef et al.*, 2005].

Bulk NC materials synthesized by electrodeposition and UFG materials processed by severe plastic deformation are generally free from extrinsic flaws. Nevertheless, their ductility is still comparatively low due to the intrinsic microstructures/deformation mechanisms. The ductility of these materials is controlled by two parameters: strain hardening and strain rate sensitivity (SRS). However, the effect of SRS is marginal compared to that of strain hardening. Increasing the value of SRS by an order of magnitude, the effect is still very low and does not affect the onset of yielding. Therefore,

increasing strain hardening effect is critical for improving the ductility of NC/UFG materials.

Strain hardening is generated by the accumulation of crystalline defects, such as dislocations, and makes further deformation harder. The low strain hardening rate of NC and UFG materials is caused by their low efficiency for the dislocation storage because of the small grains and/or high dislocation density inside the grains. There may be enough space for the large grains ensuring the dislocation motion inside the grains. However, if the grain size is down to the NC range, such as the PED NC nickel, dislocations may generally no longer accumulate within the grains, and grain interiors are often dislocation free, which induces a minimal hardening effect [*Budrovic et al.*, 2004; *Zhu et al.*, 2003]. The results from molecular dynamic (MD) simulation supporte this viewpoint that dislocations can be emitted from one side of a grain boundary, travel through the grain interior and then be absorbed by other side of the grain boundary, resulting in no dislocation accumulation inside the grains [*Yamakov et al.*, 2004; *Swygenhoven et al.*, 2004]. Materials processed by SPD technique, such as the ECAP UFG nickel, usually have grain size much larger than 100 nm and contain a high density of dislocations [*Valiev and Langdon*, 2006; *Zhao et al.*, 2006b]. Since the dislocation density is so high, sometimes to a saturated value, the further accumulation of dislocations is difficult or impossible, leading to a low strain hardening capability. Therefore, the NC and UFG materials are usually of low ductility, which limits their practical applications (figure 2.5).

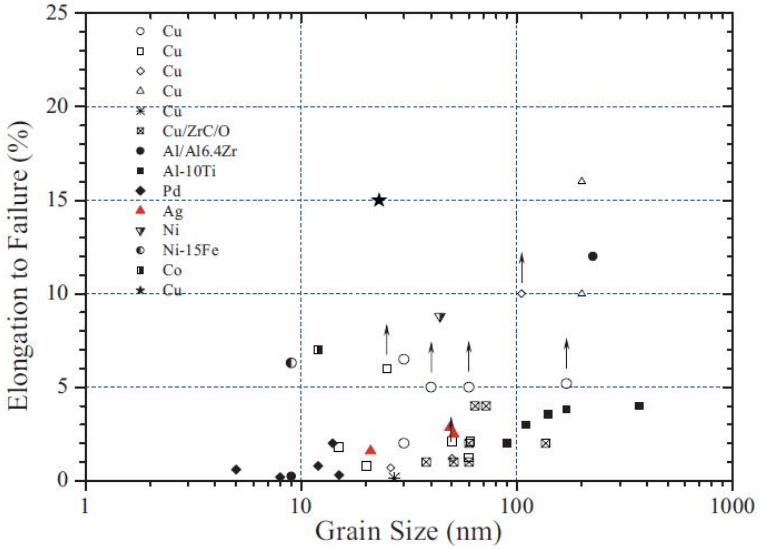

Figure 2.5.: Elongation to failure in tension versus grain size for a variety metals and alloys [*Koch et al.*, 2005].

2.1.3. Bimodal grain size distribution

The low ductility and toughness seriously restrict the use of nanocrystalline metals in many practical applications. As an effective approach to obtain both high strength and good ductility, rendering the bimodal grain size distributions in nanostructured metals or alloys, has attracted much interest in the last decade. The bimodal nanostructured alloys and metals were firstly reported by Tellkamp et al. [*Tellkamp et al.*, 2001] and Wang et al. [*Wang et al.*, 2002b], respectively. In their work, high strength and good ductility were achieved simultaneously in aluminium alloys and copper.

Tellkamp et al. generated a nanostructured aluminium 5083 alloy with an intrinsic bimodal microstructure via consolidation of cryomilled nanostructured aluminium powders using hot isostatic pressing and hot extrusion. This Al 5083 alloy has yield strength of 334 MPa, ultimate strength of 462 MPa and elongation of 8.4% (Table 2.2). They suggested that the presence of the coarse grains in the nanocrystalline matrix was responsible for the good ductility. In this particular case, the coarse grains arose as a result of thermomechanical processing of the nanostructured powders, i.e. consolidation and extrusion.

Wang et al. annealed the cryo-rolled nanostructured Cu to produce a bimodal grain size distribution, with micrometer-sized grains ($1 - 3$ μm) with about 25% volume fraction embedded inside the matrix of nanocrystalline and ultrafine (< 300 nm)

	bimodal Al 5083	Al 5083-0	Al 5083-H	UFG Al 5083
yield strength	334 MPa	124 MPa	269 MPa	370 MPa
ultimate strength	462 MPa	276 MPa	345 MPa	420 MPa
elongation	8.4%	16%	8%	11%

Table 2.2.: Mechanical properties of Al 5083 with different microstructures. (*) Al 5083-0 is the commercial 5083 in the untreated state. Al 5083-H is the strongest form of the commercial 5083. [*Tellkamp et al.*, 2001]

grains [*Wang et al.*, 2002b]. The resultant bimodal microstructural Cu showed a significantly improved ductility than the cryo-milled NC Cu, as shown in figure 2.6. However, the increase in ductility is usually accompanied by a loss of the strength. This is because the larger grains have lower strength and yield first during the tensile tests.

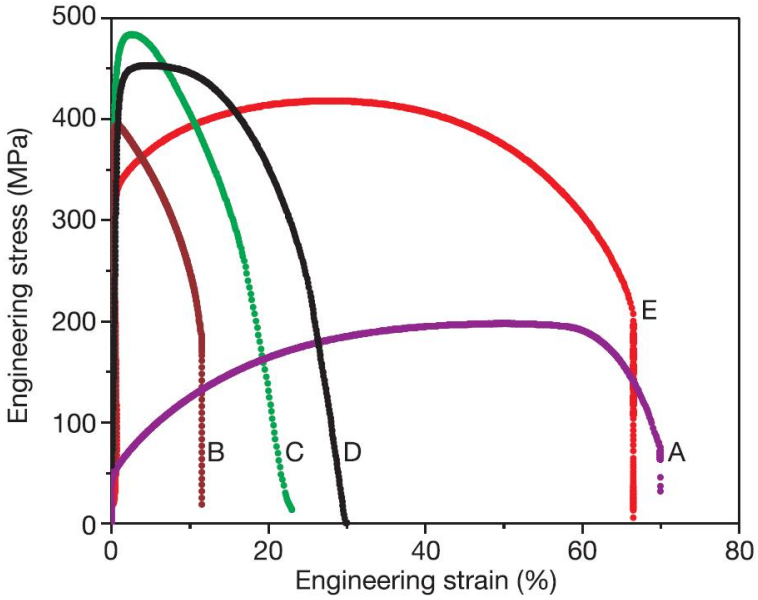

Figure 2.6.: Engineering stress-strain curves for pure Cu with different working processes. Curve A: annealed, coarse grained Cu; Curve B: room temperature rolling to 95% cold work (CW); Curve C: liquid-nitrogen-temperature rolling to 93% CW; Curve D: 93% CW + 180℃, 3 min; and Curve E: 93% CW + 200℃, 3 min. Note the coexisting high strength and large uniform plastic strain as well as large overall percentage elongation to failure for curve E for bimodal Cu [*Wang et al.*, 2002b].

There are usually two ways to prepare the bimodal materials, either via cryomilling and consolidation of metal powders with different grain sizes, followed by extrusion or via annealing of the monotonic NC or UFG metals under controlled conditions. Actually, the works by Tellkamp et al. and Wang et al. represented these two methods,

respectively. The advantage of the first method is that the volume fraction of the coarse and fine grains is easier to be controlled and a relatively homogeneous bimodal microstructure can be obtained. But usually impurities or porosity may be introduced during the milling or consolidating process. The method of low temperature annealing to the UFG or NC metals induces an abnormal grain growth, i.e. large grains in the UFG or NC matrix. The disadvantage of the cryomilling and consolidation is avoided with this method. However, the annealing process is usually difficult to control because of different influencing factors such as the starting microstructures, sample geometries, annealing temperature and annealing time.

After the pioneering work in this field, various studies have been carried out to explore the mechanical performance of the bimodal nanostructured metals and alloys, such as Wang and Zhao et al. for Cu and Ni [*Wang et al.*, 2004; *Zhao et al.*, 2008, 2011], Lavernia et al. for Al alloys [*Tellkamp et al.*, 2001; *Lee et al.*, 2005; *Joshi et al.*, 2006; *Zhang et al.*, 2009] and Wang et al. for iron and steels [*Zhao et al.*, 2007; *Azizi-Alizamini et al.*, 2007; *Wang et al.*, 2008b; *Srinivasarao et al.*, 2008]. To name a few, Zhao et al. synthesized bulk dense nanostructured Ni using cryomilling and quasi-isostatic forging with both high ductility and high strength, which benefited from the large fraction of equilibrium HAGBs and bimodal/multimodal grain size distributions [*Zhao et al.*, 2008]. Li et al. prepared nanostructured copper with bimodal grain size distribution by means of dynamic plastic deformation which induced static recrystallization, leading to decreased yield strength and enhanced ductility compared with monomodal NC copper [*Li et al.*, 2008b]. Ahn et al. investigated the tensile properties and deformation response of an UFG Al-Mg alloy with bimodal grain structure using a micro-straining unit and a strain mapping technique and they detected the inhomogeneous strain between the UFG and CG regions after yielding [*Ahn et al.*, 2008].

Han et al. investigated the crack growth mechanism in tension experiment for the Al-5083 alloy with the bimodal lamellar structure, in which coarse grains of grain size ~ 1 μm with different volume fractions were mixed with the fine grain matrix of grain size $\sim$ 200 nm [*Han et al.*, 2005]. On the basis of microstructural characteristics, a model of crack blunting combined with the concept of delamination was developed as shown in figure 2.7. In the bimodal Al alloys, microcracks were expected to nucleate first in the harder nanostructured regions, and propagated along grain boundaries. When a microcrack meeted a CG band, the band would retard propagation by blunting the crack or by delamination of interfaces between coarse and fine grained regions (figure 2.7a). When more dislocations were emitted into the coarse grain, a new slip surface might be formed, eventually leading to necking and cavitation within the CG bands (figure 2.7b).

Finally, dimples on the CG regions and delamination at interfaces would be generated on fracture surface (figure 2.7c). If delamination occurred near one end of a CG band, the final failure of the band would not produce dimples. The delamination at interfaces and the necking deformation of ductile CG regions would cause significant energy loss, resulting in an enhanced tensile ductility.

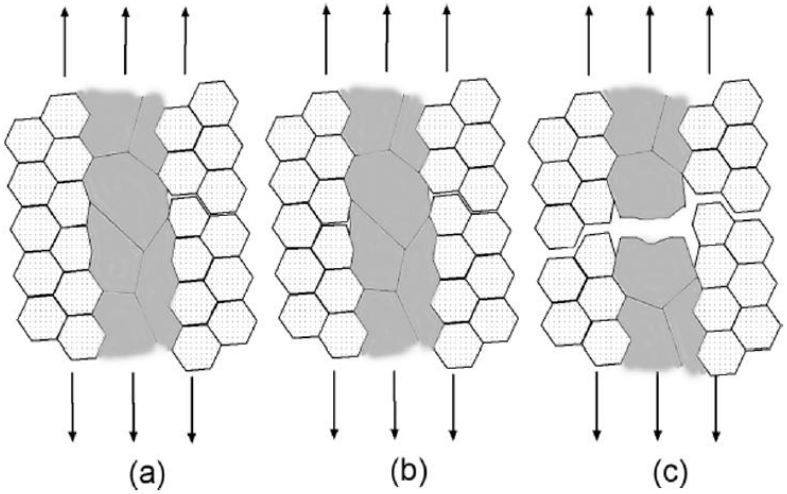

Figure 2.7.: Model for the crack propagation in the bimodal microstructure proposed by Han et al. [*Han et al.*, 2005].

Similar crack growth plus fracture mechanism were proposed by Lee et al. who investigated the tensile fractures of the UFG Al-Mg alloy with a bimodal lamellar structure in which the mean grain sizes of the UFG and CG regions were estimated to be $\sim$ 100 nm to 300 nm and 1 μm, respectively [*Lee et al.*, 2010]. The bimodal grain structures exhibited the deformation and fracture mechanisms similar to ductile-phase toughening of brittle materials. The ductile coarse grains in the UFG matrix effectively impeded propagation of microcracks, resulting in an enhanced ductility and toughness while remaining high strength. In view of their experimental observations, they proposed a descriptive model for tensile deformation and fracture of bimodal UFG metals, as shown in figure 2.8. The tensile deformation and fracture stage were described by the four steps in the schematic. First, the CG regions were elongated along the extrusion direction in the as-extruded specimen, and uniaxial tension was applied to the specimen along the extrusion direction (figure 2.8(a)). When the stress reached the yield point of CG material, plastic deformation occurred within these regions. Second, as the stress increased and reached the yield point of UFG material, voids initiated within the UFG regions and at the UFG-CG interfaces, and the CG bands underwent elongation (figure 2.8(b)). Third, as the tensile strain increased, cracks grew from the voids and extend transverse to

the load axis. However, the cracks tended to be localized in the UFG regions between CG regions (figure 2.8(c)). Cracks were effectively impeded by the CG stringers, which blunted and bridged the cracks, causing deflection and branching in CG regions and at the UFG-CG interfaces. Finally, fracture ensued when cracks linked and the CG regions could no longer sustain the load, as shown in figure 2.8(d).

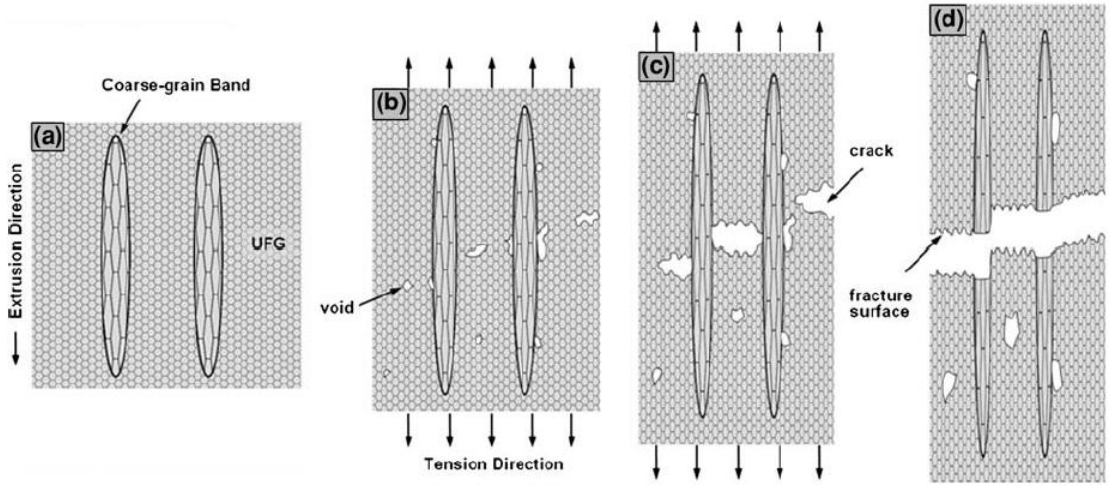

Figure 2.8.: Schematic of tensile deformation and fracture mechanism of bimodal UFG Al-Mg alloys under tension along the extrusion direction: (a) as extruded, (b) void nucleation and growth, (c) crack growth, and (d) fracture [*Lee et al.*, 2010].

The prediction of mechanical behaviors in bimodal metals or alloys has become a key issue in optimizing the grain size distribution and volume fraction of constituents for achieving both high strength and good ductility. A micro-mechanics-based model was proposed by Zhu and Lu to explain the mechanical behavior of the polycrystalline metals with bimodal grain size distributions, which focused on the behavior of nano/microcracks. The nano/microcracks nucleated in the nano/ultrafine grained phase and stoped at the boundary of large grains during the plastic deformation [*Zhu and Lu*, 2012]. They found that the nano/microcracks did not lead to catastrophic failure; instead, they induced the back stress for the strain hardening and also the variation of the mechanical behaviour in the nano/ultrafine grained phase. Their numerical results showed that the proposed micro-mechanics-based model could successfully describe the enhanced strength and ductility of the bimodal metals. The predictions of the bimodal nickels were in good agreement with the experimental results.

2.2. Fatigue properties and crack behaviour of the nanocrystalline and ultrafine grained materials

2.2.1. Fatigue properties

The fatigue behavior of metals is strongly governed by the grain size variation. Up to now the vast majority of researches upon fatigue have dealt with microcrystalline (MC) metals or alloys with an average grain size larger than 1 μm. Like the tensile strength, the fatigue limit increases with decreasing grain size in the MC regime. Although there are already many investigations about the deformation behavior of the NC and UFG materials under tension which is shown in the last section, there is relatively little information about the fatigue properties of such materials.

An early systematic investigation of the fatigue behaviour of the NC and UFG metal was carried out by Hanlon et al., who concentrated on the NC and UFG nickel which were processed by pulsed electrodeposition [*Hanlon et al.*, 2003; *Hanlon*, 2004; *Hanlon et al.*, 2005; *Moser et al.*, 2006]. Because of the limitation to achieve really bulk nanostructured materials, their fatigue specimens were typically on the order of 100 μm thick and with loading only in tension. They conducted the fatigue tests on nominally smooth specimens and found that there was an improvement in fatigue resistance with decreasing grain size. The stress-life curves, which provided an indication of the dependence of total fatigue life on cyclic stress, were shown for the nickel specimens in different grain size ranges (figure 2.9). It was found that grain refinement to the NC and UFG regimes affected the total fatigue life substantially under stress-controlled fatigue. Electrodeposited NC and UFG nickel exhibited a significantly higher resistance to S-N fatigue, relative to their MC nickel counterpart.

Although the experimental results by Hanlon et al. showed a grain size dependence of the fatigue behaviour in the NC regime, the underlying mechanisms about the fatigue deformation operating in these materials should be investigated more carefully. As a general behavior, it was observed that the fatigue limit of NC metals increased with decreasing grain size, and the crack initiation susceptibility decreased and the crack growth rate increased coupled with the grain refinement [*Agnew et al.*, 1999; *Mughrabi and Hoeppel*, 2000; *Cavaliere and Cabibbo*, 2008; *Cavaliere*, 2009].

Actually, it is important to distinguish low cycle fatigue (LCF) and high cycle fatigue (HCF) carefully. In LCF of deformable metals cyclic plasticity is precursor to fatigue crack initiation. Even in high cyclic fatigue where the macroscopic loading conditions are nominally elastic, local micro-plasticity drives crack initiation. Therefore, inves-

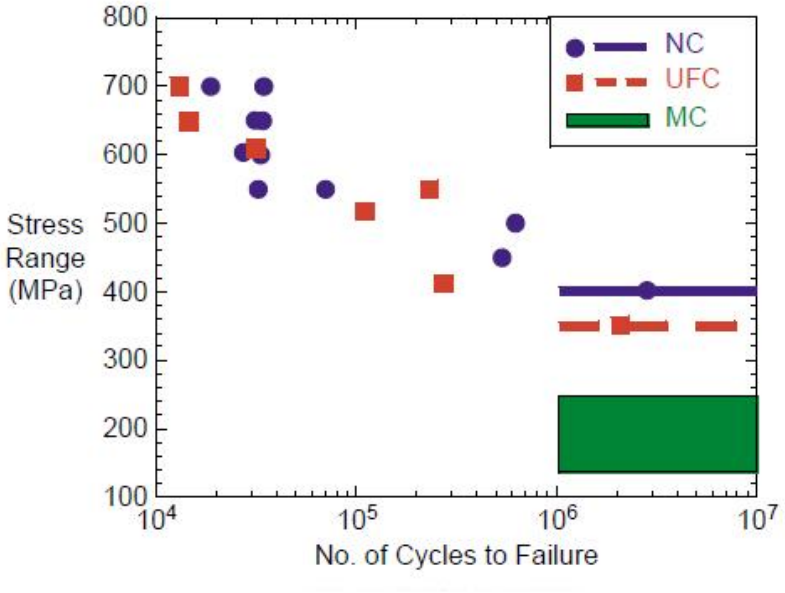

Figure 2.9.: The effects of grain size from the micro to the nano-regime on the stress vs. fatigue life plot in pure Ni [*Hanlon et al.*, 2005].

tigation of the cyclic plasticity in NC and UFG materials gives great significance to understand the subsequent fatigue mechanisms. The influences of the microstructure are totally different when considering to research the LCF and HCF behavior and sometimes the results are even contradictory. The conflicting results can also be induced by different experimental conditions. In stress-controlled HCF tests the NC and UFG materials showed an improved fatigue resistance to their MC (CG) counterparts [*Agnew et al.*, 1999; *Vinogradov et al.*, 2001; *Vinogradov and Hashimoto*, 2001; *Hoeppel et al.*, 2002, 2006]. However, the NC and UFG materials showed an obviously lower fatigue life in strain-controlled LCF tests [*Agnew and Weertman*, 1998; *Agnew et al.*, 1999; *Vinogradov and Hashimoto*, 2001; *Hoeppel and Valiev*, 2002; *Mughrabi et al.*, 2004]. Besides, Vinogradov et al. found that addition of scandium in Al-Mg alloys stabilized significantly the fine grained structure formed during ECAP. The observed combination of high strength and ductility gave a hope for obtaining the Al-Mg-Sc particles with enhanced fatigue properties in both HCF and LCF regimes [*Vinogradov et al.*, 2003b].

Goto et al. conducted a series of fatigue experiments on UFG copper processed by ECAP [*Goto et al.*, 2006, 2007, 2008, 2009]. They found that the material showed a better fatigue resistance under stress-controlled mode and a shorter fatigue life under strain-controlled mode. The results observed by Wong et al. on UFG aluminum processed by ECAP also confirmed the shorter fatigue life under strain-controlled fatigue

tests in LCF range. They even concluded that the smaller the grain size was, the shorter the fatigue life was [*Wong et al.*, 2007]. However, the research on an ECAP processed UFG magnesium alloy AM60 by Kulyasova et al. showed a different result [*Kulyasova et al.*, 2009]. The Mg-alloy AM60 behaved a superplasticity, unlike the typical UFG materials showing low ductility, which ensured the Mg-alloy deformable. They found that all the specimens showed higher fatigue lives than their coarse grained counterparts under strain-controlled fatigue tests, even in the LCF range, and the improved fatigue behavior correlated well with the refinement of the grain size and followed the Hall-Petch relationship. The results by different researching groups seemed to be controversy because they concentrated on different experimental conditions which relied more on the materials strength or ductility. Therefore it is of significant importance to investigate the fatigue properties according to the practical applications.

Hardening and softening phenomena

Cyclic hardening and softening are the usual phenomena during the fatigue experiments, especially in the initial stage [*Li et al.*, 2008a]. Cyclic hardening or softening occurs under the cyclic loading, stabilizing the microstructure of the materials. Li et al. investigated the ECAP processed UFG copper under the stress-controlled loading condition with different stress amplitudes from LCF to HCF range. Softening behaviour was observed for all the specimens, and it appeared earlier and more strongly with higher stress amplitudes. Xu et al. investigated the fatigue behaviour on ECAP processed UFG low-purity copper [*Xu et al.*, 2008]. The found that cyclic stress-strain response of UFG Cu under stress-controlled loading changed from cyclic softening to cyclic hardening with stress amplitude decreasing. However, the UFG samples under strain-controlled loading showed rapid cyclic softening, which occurred under all applied plastic strain amplitudes in the early stage of testing. Besides, the softening was faster under higher plastic strain amplitudes. Wong et at. found three types of cyclic hardening curves when observing the fatigue properties of ECAP processed UFG aluminum under strain-controlled loading [*Wong et al.*, 2007]. For large plastic strain, only cyclic softening occurred; for small plastic strain amplitudes, cyclic hardening was followed by a saturation stage; and for intermediate plastic strain amplitudes, cyclic hardening was followed by cyclic softening (figure 2.10).

Cyclic hardening and softening were observed by Cheng et al. who investigated the fatigue phenomena of PED processed UFG nickel under load-controlled mode [*Cheng et al.*, 2009]. Cyclic hardening or softening was observed under different loading con-

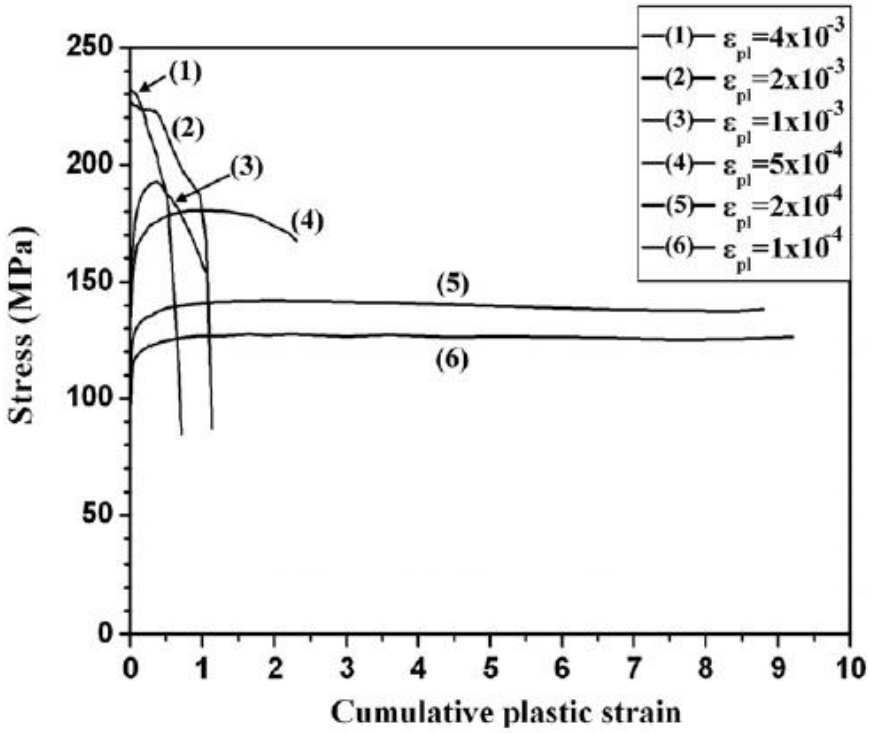

Figure 2.10.: Cyclic hardeing curves of ufg aluminum with grain size of 0.36 μm under different plastic strain amplitudes [*Wong et al.*, 2007].

ditions. Whether hardening or softening occurred depended more on the grain size of the investigated specimens and was less dependent on the stress amplitudes. They concluded that the dislocation emission and accumulation from grain boundaries were responsible for the cyclic hardening, while dislocation disentangling led to a decrease of dislocation density which was accounted for the cyclic softening. However, fatigue experiments on PED processed NC and UFG nickel under stress-controlled loading by Hanlon and Moser et al. showed a different result where all the specimens demonstrated only hardening behaviour [*Hanlon*, 2004; *Moser et al.*, 2006]. The stress-strain hysteresis exhibited a decreasing opening width according to the decreasing strain amplitude with increasing cycles (figure 2.11).

Generally, cyclic softening was observed under large stress/strain amplitudes, while a low stress/strain amplitude led to the cyclic hardening behaviour. In the mediate stress/strain amplitude range there seemed to be a transition from cyclic hardening to softening with increasing cycles. However, there is no general statement to the fatigue behaviour of the NC and UFG materials because of the different processing methods of the materials and experimental conditions. Therefore, a closer investigation of the

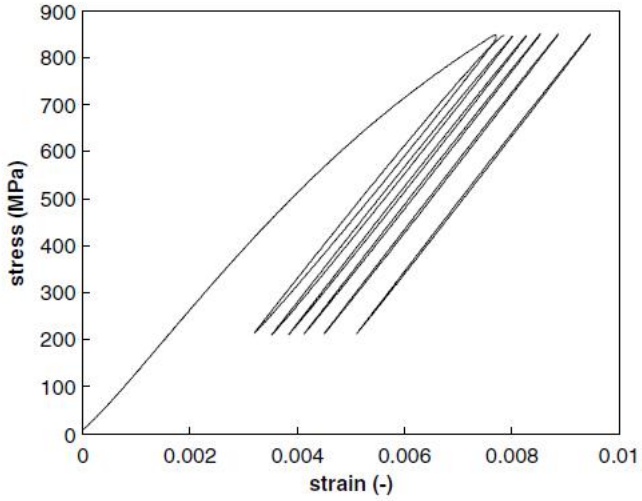

Figure 2.11.: Stress-strain response of cyclically loaded electrodeposited nc nickel with increasing fatigue cycles [*Moser et al.*, 2006].

mechanism based on the microstructures of the materials should be conducted.

Fatigue mechanisms to UFG and NC materials

Usually the initiation of the fatigue cracks emerges on the surface of the specimen, therefore, an observation of the damage process on the NC or UFG specimen surface under cyclic loading brings a better understanding to the fatigue mechanism. Agnew and Weertman [*Agnew and Weertman*, 1998] and Hashimoto [*Hashimoto et al.*, 1999] investigated this surface damage phenomenon of UFG copper and found the formation of shear bands (SBs) with a large area. The morphology of the shear bands were similar to the extrusions of the persistent slip bands (PSBs) in the CG materials (figure 2.12) [*Agnew and Weertman*, 1998; *Vinogradov et al.*, 2002; *Wu et al.*, 2003]. Actually, two kinds of shear bands, i.e. PSB-like SB and step-like SB, were found in cyclically deformed UFG Cu processed by ECAP. The formation of PSB-like SBs and the step-like SBs might be attributed to the local reversible and irreversible deformation, respectively [*Wu et al.*, 2004]. There were many efforts to relate shear bands to grain coarsening/recrystallization, but without providing convincing evidence.

Upon observing the microstructural evolution and dislocation movement through TEM, Cheng el al. investigated the fatigue mechanisms of the PED processed UFG nickel [*Cheng et al.*, 2009]. Similar to the other authors, they did not find the microstructural evolution like grain coarsening. However, different deformation mechanisms were observed: twinning, dislocation emission, stack faults and dislocation disentanglement.

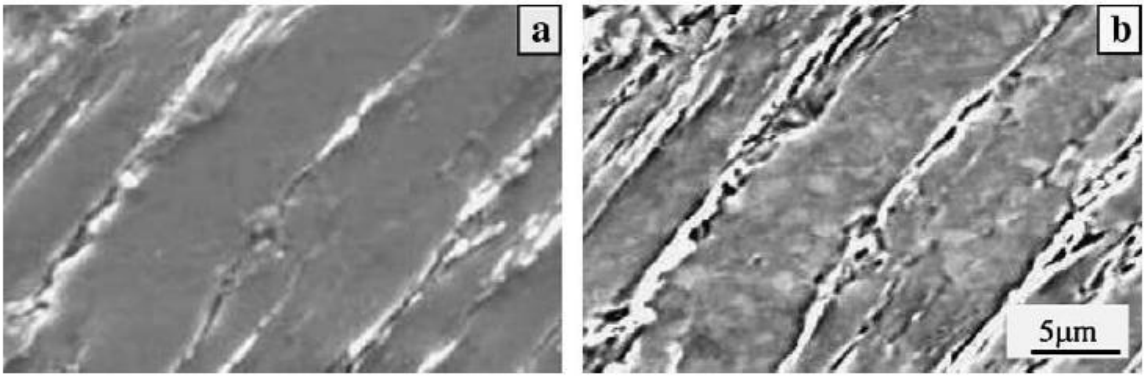

Figure 2.12.: SEM (a) and SEM-ECC (b) images of PSB-like SBs [*Wu et al.*, 2003].

The deformation process began in the larger grains. Formation of the twinning was observed in the first fatigue cycle and dislocation emission dominated in the following cycles. The hardening effect was induced through dislocation emission and accumulation from grain boundaries. Dislocation annihilation, which caused the decreasing dislocation density, was the reason for the following softening with further cycles. Similar mechanism for the cyclic hardening was suggested by Hanlon who studied the fatigue behaviour of PED NC and UFG nickel [*Hanlon*, 2004]. He proposed the enhanced dislocation interaction with increasing numbers of stacking faults produced during cyclic loading. Besides, exhaustion of the dislocation sources could be a reason to the cyclic hardening as an additional effect.

However, the work by Li et al. on ECAP UFG copper showed a different result like above stated by Cheng et al., where they proposed the grain coarsening as the main fatigue mechanism [*Li et al.*, 2008a]. Upon fatigue experiments with the stress amplitudes in different regimes, i.e. HCF regime, LCF regime and in-between regime they suggested different stress-amplitude-dependent microstructures (figure 2.13). In the HCF regime, the surface deformation feature was manifested by the macroscopic SBs consisting of many short single shear bands, and cracks formed separately along the single shear bands. The corresponding microstructural changes were embodied by grain coarsening, and no typical dislocation arrangement was visible in the coarsened grains. In the in-between regime, the surface deformation morphology was featured by locally-formed dense SB clusters, and many micro-cracks formed together within the SB clusters. Remarkable grain coarsening took place as well, and some developing dislocation arrangements formed in a few of coarsened grains. In the LCF regime, the surface deformation morphology was mainly characterized by the large-scale SBs extending over the whole specimen surface, and cracks or voids formed along these large-scale SBs. Dif-

ferent dislocation structures could be found to form in many coarsened grains, depending upon the orientation of those coarsened grains. Actually, this viewpoint had already been proposed by the same author in an earlier work that the temperature dependent grain coarsening and microstructural changes in the coarsened grains were believed to be the governing reasons for the decrease of fatigue life [*Li et al.*, 2004].

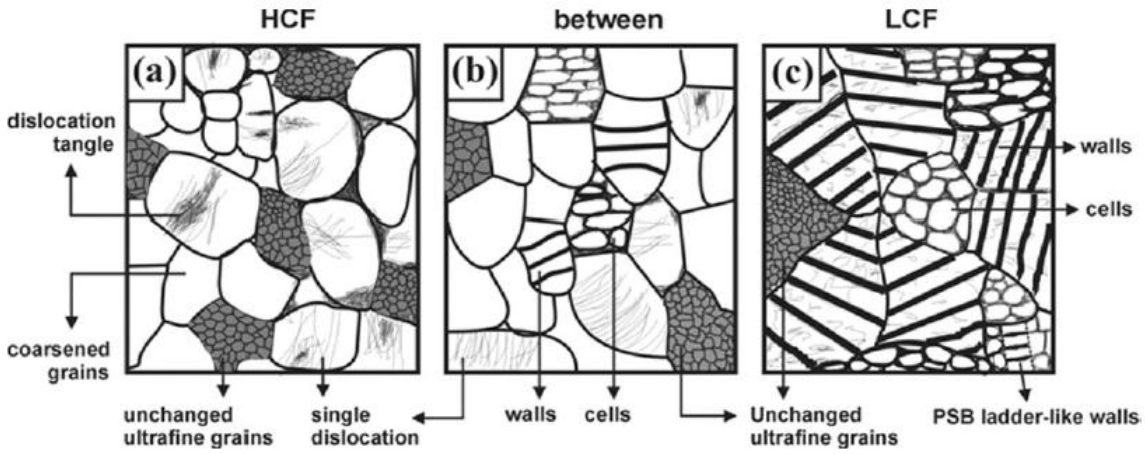

Figure 2.13.: Schematics of stress-amplitude-dependent microstructures in fatigued ufg copper. (a) HCF regime, (b) regime between HCF and LCF, (c) LCF regime [*Li et al.*, 2008a].

2.2.2. Crack initiation and growth

Crack initiation

When metals or alloys are fabricated without pre-existing critical defects, the first step in the fatigue failure process is the formation of a fatigue crack. Under HCF conditions the crack initiation process dominates a vast majority of the fatigue life time. Even under LCF conditions, the crack initiation phase is a necessary precursor to fatigue failure when there are no pre-existing defects. A key factor to enhance the fatigue performance in NC and UFG metals or alloys lies in the potential for these materials to suppress the crack initiation.

Investigation of the fatigue crack initiation in NC or UFG metals has relied mainly on the microscale observations after fracture to draw conclusions about the relevant mechanism. In many CG metals, fatigue crack initiation occurs due to the formation of surface extrusions and intrusions caused by PSBs. In NC and UFG metals, both internal and surface defects have been noted as nucleation sites for the fatigue cracks.

In contrast to the CG materials in which subsurface crack initiation was much less common only with very high cycles ($> 10^7$ cycles) [*Wang et al.*, 2002a; *Chai*, 2007], observation of the fatigue fracture surface in NC and UFG nickel revealed subsurface crack initiation sites under LCF conditions ($\sim 10^3$ cycles) [*Cheng et al.*, 2007]. One possible explanation for this shift is that the critical crack length is quite small in the low ductile NC and UFG metals, which enables internal defects and inclusion to become initial sites. For this reason, internal processing defect is an important concern in NC and UFG materials.

Like their CG counterparts, when critical internal defects are avoided, crack initiation in NC and UFG metals occurs almost invariably on the surface. An early work by Witney et al. who studied the fatigue behaviour of the NC Cu demonstrated the formation of surface extrusions in fatigue loaded samples with the grain size of approximately 20 nm [*Witney et al.*, 1995]. In this case the protrusion length was spanned several grains and extended roughly 1 μm out of the surface. Despite grain growth of 30%, coarsened grains were still several orders of magnitude smaller than the dimensions of the extrusions. Despite the similarity between these fracture features and extrusions found in CG copper, it was not clear whether these features were caused by PSBs in the traditional sense, particularly since the grain size was far smaller the length at which dislocation activity leaded to PSBs [*Suresh*, 1998].

A possible explanation for the extrusions observed in NC copper was suggested by Xie et al. who studied the nucleation mechanisms in fatigue of NC nickel (figure 2.14) [*Xie et al.*, 2008]. They examined the areas surrounding fatigue cracks using an AFM, and found increased surface roughness arranged in large cell structures. The cell diameters were average 108 nm in size, compared with the grain size of 26 nm. The results suggested that collective grain motion allowed the formation of the surface features at larger scale than the grain size. One feature of the fatigued NC nickel samples in their study was that there was typically just a single fatigue crack that formed at the surface. This was in contrast to the formation of one dominant fatigue crack among several smaller cracks in CG nickel samples which were tested for comparison. Therefore, Xie et al. suggested that in the CG nickel, grain boundaries served as obstacles to the many fatigue cracks nucleated by PSB formation, until one crack grew to dominance. Whereas in the NC nickel, grain boundaries did not act as obstacles to collective grain motion.

For the ECAP processed UFG materials, strain localization was often observed during both monotonic and cyclic deformation [*Youngdahl et al.*, 2001; *Vinogradov and Hashimoto*, 2003]. Figure 2.15 shows the shear band oriented at 45° to the loading

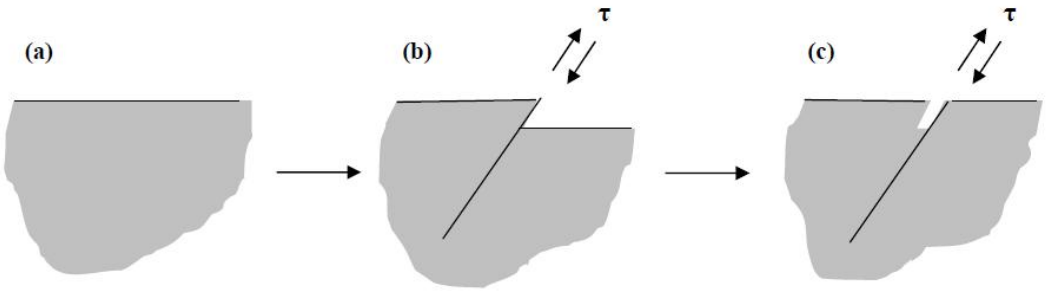

Figure 2.14.: Schematic illustration of fatigue crack initiation mechanism for NC nickel. (a) as-received sample, (b) After a cycle of loading, parts of samples slip along the shear plane and a step forms at surface, and (c) After another cycle of loading, parts of samples slip along adjacent shear plane and a valley forms at surface [*Xie et al.*, 2008].

axis. They often appeared shortly after yielding in tensile deformation or at the end of saturation in cyclic testing. The cracks initiated and propagated along the shear bands. The shear banding was the major form of fatigue damage of wavy slip UFG materials. The strain localization occurred primarily along the grain boundaries, indicating the grain boundaries as the preferring sites for the crack initiation and propagation.

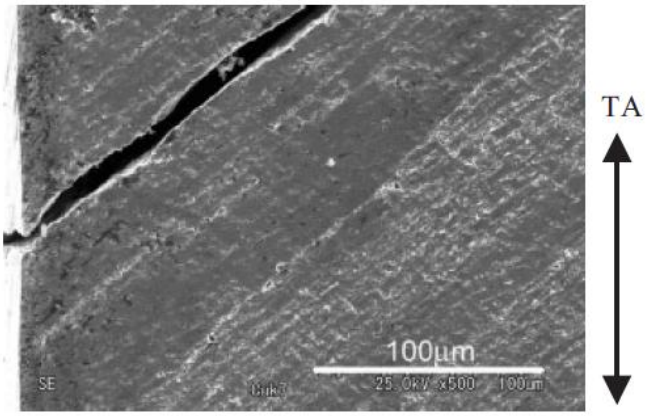

Figure 2.15.: Shear bands on the surface of ECAP Cu deformed cyclically at $\Delta\epsilon_{\mathrm{pl}}/2 = 10^{-3}$ [*Vinogradov and Hashimoto*, 2003].

Crack growth

After the cracks initiate in the specimen, they propagate until rendering the ultimate fracture. Experimental results on different NC and UFG materials show that the fatigue crack thresholds are lowered and the fatigue crack growth rates are enhanced, with decreasing grain size [*Pao et al.*, 2005; *Huebner et al.*, 2006; *Mughrabi and Hoeppel*, 2010].

In general, as grain size is reduced the resistance to crack propagation is diminished. This relationship between grain size and crack propagation resistance is commonly observed even in conventional metals, and is often attributed to the increased crack path tortuosity and more extensive crack tip plasticity associated with larger grain size. Crack growth data for NC ($20 - 40$ nm), UFG (300 nm) and MC (10 μm) nickel shown in figure 2.16 demonstrate a clear relationship between grain size and resistance to crack propagation. The accelerated crack growth with diminishing grain size is expected due to the decrease in crack-path tortuosity and the diminishing contribution of roughness and plasticity induced crack closure.

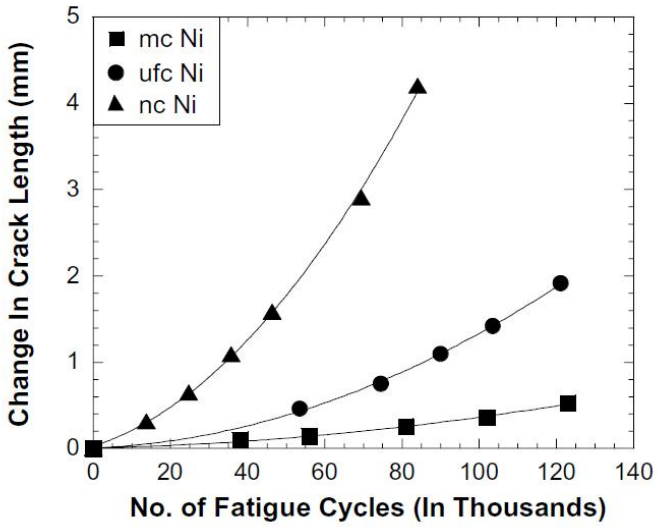

Figure 2.16.: A comparison of the variation of fatigue crack length as a function of the number of fatigue cycles for NC, UFG and MC pure nickel subjected to an initial stress intensity factor range of 11.5 MPa$\sqrt{\text{m}}$ at R = 0.3 at a fatigue frequency of 10 Hz at room temperature [*Hanlon et al.*, 2003].

Actually, the crack deflection model stated above is not sufficient to rationalize the crack growth rate in coarser grained samples. Because the deformation at the crack tip of NC nickel is of shear band mode, the real volume of the plastic zone of NC nickel is much less than that of CG nickel. Therefore, the difference in the values of plasticity at

the crack tip between NC and CG Ni can be very large. A higher degree of plasticity will lead to higher crack growth resistance [*Xie et al.*, 2007].

In CG metals, the cyclic plastic zone size is related to the process zone for cyclic crack advance and striation formation. An MD model simulating fatigue crack growth at the nanoscale for a polycrystal with 6 nm grain size showed that the cyclic plastic zone size was on the order of the grain size, and the fatigue crack growth mechanism involved dislocations emitted from the crack tip and nanovoids formed ahead of the main crack [*Farkas et al.*, 2005]. This value was two orders of magnitude smaller than that predicted by either the Irwin or Dugdale model which should be on the order of 500 nm or larger [*Padilla-II and Boyce*, 2010]. Therefore, further work should be conducted in examination of the large discrepancy between simulation and traditional continuum approaches.

2.3. Annealing phenomena and nanoscale grain growth kinetics

2.3.1. Recovery, recrystallization and grain growth

The free energy of a crystalline material is raised during deformation by generation of dislocations and interfaces. If a deformed material is annealed at an elevated temperature, the microstructure and also the properties may be partially restored into their original values before deformation by recovery, in which annihilation and rearrangement of the dislocations occur. The microstructural changes during recovery are relatively homogeneous and usually do not affect the boundaries between the deformed grains. Recovery generally causes only partial restoration of properties because the dislocation structure is not completely removed, but reaches a metastable state. Actually, recovery is not only confined to plastically deformed materials, and may also occur in crystal into which a non-equilibrium, high concentration of point or line defects has been introduced. A further restoration process - recrystallization, may occur in which new dislocation-free grains are formed within the deformed or recovered structure. These dislocation-free grains then grow consuming the old grains, resulting in a new grain structure with low dislocation density [*Humphreys and Hatherly*, 2004]. Figure 2.17 describes the annealing process of a deformed material.

Recovery, recrystallization and grain growth may occur heterogeneously throughout the material, such that they may be described in terms of nucleation and growth stages

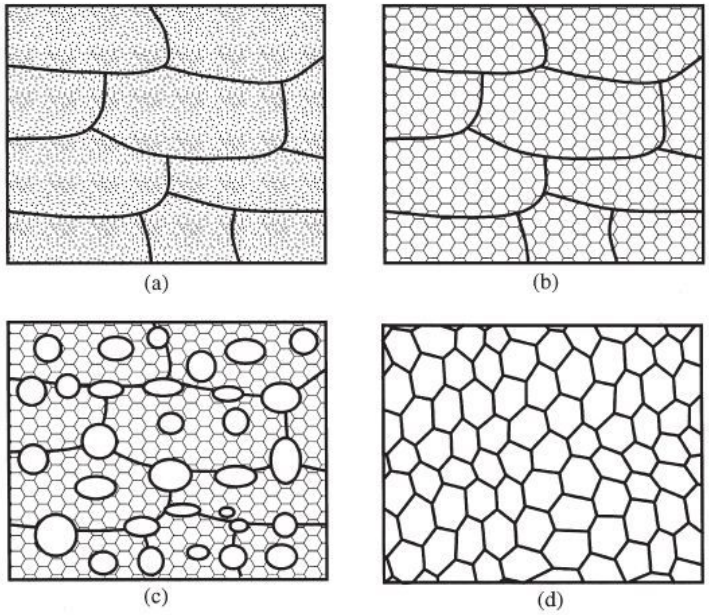

Figure 2.17.: Schematic illustration of the annealing process of a deformed material: (a) deformed state, (b) recovered, (c) partially recrystallized and (d) fully recrystallized [*Humphreys and Hatherly*, 2004].

- discontinuous processes. Alternatively, they may occur uniformly, such that the microstructures evolve gradually with no identifiable nucleation and growth stages - continuous processes. The continuous phenomena include recovery by subgrain growth, continuous recrystallization and normal grain growth, while the discontinuous phenomena include discontinuous subgrain growth, primary recrystallization and abnormal grain growth [*Humphreys*, 1997]. If the microstructure can be considered to be one of subgrains and grains, then all above mentioned six annealing phenomena can be considered to occur by the migration of high or low angle grain boundaries, where the differences between them are characterized by the spatial distribution and the properties (e.g. energy and mobility) of the grain boundaries. Uniform coarsening of the microstructures leads to continuous process, and growth with instabilities causes discontinuous process (figure 2.18).

Kinetics of recrystallization - the JMAK model

Recovery is a relatively homogeneous process in terms of both space and time. When viewed on a scale which is larger than the cell or subgrain size, most areas of a sample are changing in a similar way. Recovery processes gradually with time and there is no readily identifiable beginning or end of the process. In contrast, recrystallization

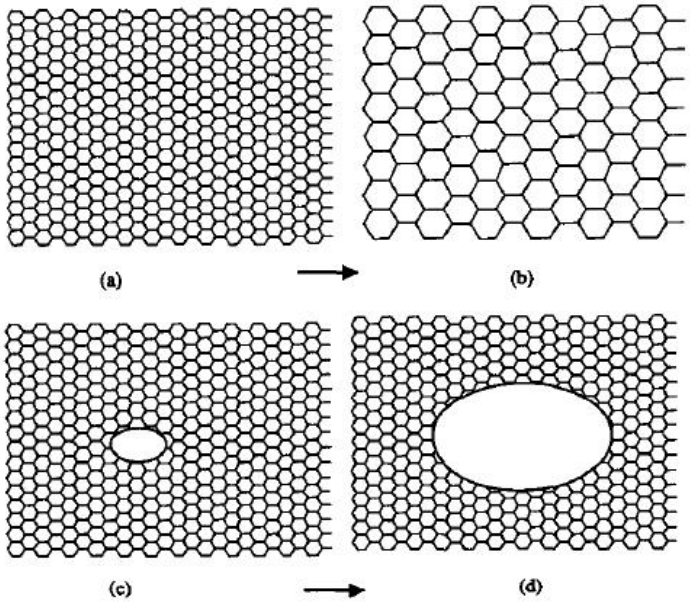

Figure 2.18.: Schematic illustration of (a-b) continuous, and (c-d) discontinuous annealing phenomena [*Humphreys*, 1997].

involves the formation of new strain-free grains in certain parts of the specimen and the subsequent growth of these to consume the deformed or recovered microstructure. The microstructure at any time is divided into recrystallized or non-recrystallized regions as shown in figure 2.19. The fraction recrystallized increases from **0** to **1** as the transformation proceeds. This is typical of a discontinuous annealing phenomenon. Recrystallization of the deformed microstructure is often called primary recrystallization in order to distinguish it from the process of abnormal grain growth which may occur in fully recrystallized material and which is sometimes called secondary recrystallization.

It is convenient to divide primary recrystallization into two regimes, **nucleation** which corresponds to the first appearance of new grains in the microstructure and **growth** during which the new grains replace deformed material. Although these two events occur consecutively for any particular grain, both nucleation and growth may be occurring at any time throughout the specimen. The kinetics of recrystallization are therefore superficially similar to those of a phase transformation which occurs by nucleation and growth [*Humphreys and Hatherly*, 2004].

The process of recrystallization with time during isothermal annealing is commonly represented by a plot of the volume fraction of material recrystallized (X_V) as a function of log(time). This plot usually has the characteristic sigmoidal form and typically shows an apparent incubation time before recrystallization is detected. This is followed by

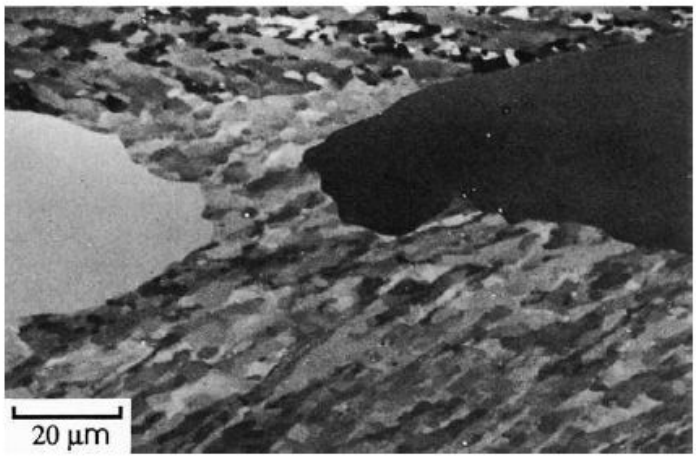

Figure 2.19.: An SEM channelling contrast microsgraph of aluminium showing recrystallized grains growing into the recovered subgrain structure [*Humphreys and Hatherly*, 2004].

an increasing rate of recrystallization, a linear region, and finally a decreasing rate of recrystallization (figure 2.20).

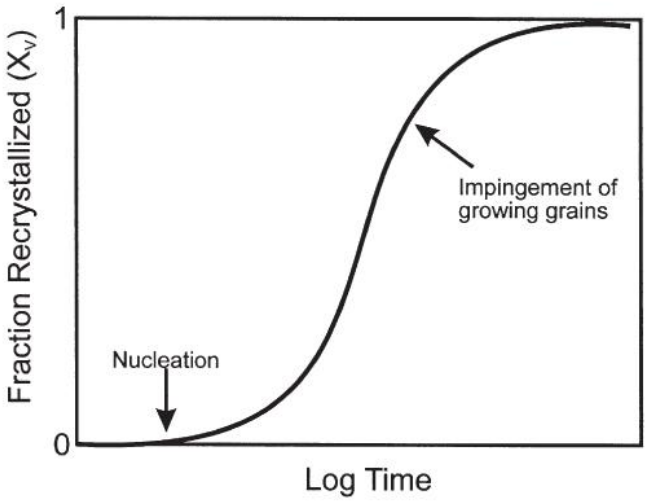

Figure 2.20.: Typical recrystallization kinetics during isothermal annealing [*Humphreys and Hatherly*, 2004].

The type of curve shown in figure 2.20 is typical of many transformation reactions, and may be described phenomenologically in terms of the constituent nucleation and growth process. The early work is due to Kolmogorov (1937), Johnson and Mehl (1939) and Avrami (1939) and is commonly known as the JMAK model. The equation to describe the volume fraction of the recrystallized areas with the annealing time is given

with the following form:

$$X_V = 1 - exp(-Bt^n) \tag{2.2}$$

where B is a constant depending on the nucleating rate ($\dot{N}$) and grain growth rate ($\dot{G}$). This equation is often called Avrami, Johnson-Mehl or JMAK equation. When assuming that the rates of nucleation and growth remain constant during recrystallization, the exponent **n** is 4.

The annealing temperature has a profound effect on the recrystallization kinetics. If we consider the transformation as a whole and take the time for 50% recrystallization ($t_{0.5}$) to be a measure of the rate of recrystallization, we might expect a relationship of the type:

$$Rate = \frac{1}{t_{0.5}} = C\, exp\left(-\frac{Q}{kT}\right) \tag{2.3}$$

where C is a constant, Q is the activation energy, k is the Boltzmann constant and T is the annealing temperature.

The rate of heating of the specimen to the annealing temperature can also affect the rate of recrystallization, but in this work a fixed heating rate was chosen and the influence of the heating rate is not considered.

Kinetics of grain growth - the Burke and Turnbull model

When primary recrystallization, which is driven by the stored energy of cold work, is complete, the structure is not yet stable, and further growth of the recrystallized grains may occur. The driving force for this is a reduction in the energy which is stored in the material in the form of grain boundaries. The driving pressure for grain growth is often some two orders of magnitude less than that for primary recrystallization, and is typically $\sim 10^{-2}$ MPa [*Humphreys and Hatherly*, 2004]. Consequently, at a particular temperature, grain boundary velocities will be slower than during primary recrystallization, and boundary migration will be much more affected by the pinning effect of solutes and second-phase particles.

Although primary recrystallization often proceeds grain growth, it is of course not a necessary precursor. Therefore, the theory of grain growth for the recrystallized materials is equally relevant to grain growth in materials produced by casting or vapour deposition. Grain growth is a process in which grain size increases with time. The growth of the grains is considered just under the driving force due to boundaries which

can be induced to migrate by externally applied forces such as those due to stress or by magnetic fields.

Most analytic theories of normal grain growth in highly pure, single-phase materials predict an asymptotic power-law depended, $\overline{R} \propto t^m$, for the isothermal evolution of the mean grains $\overline{R}$ with annealing time t. For example, Burke (1949) and Burke and Turnbull (1952) deduced the kinetics of grain growth on the assumption that the driving force (P) on a boundary arises only from the curvature of the boundary:

$$\overline{R}^2 - \overline{R_0}^2 = c_2 t \tag{2.4}$$

where $\overline{R}$ is the mean grain size at time t, $\overline{R_0}$ is the initial mean grain size and c_2 is a constant.

This parabolic growth law is expected to be valid for both 2-D and 3-D microstructures, although the constant c_2 will be different for the two situations. In the limit where $\overline{R}^2 >> \overline{R_0}^2$

$$\overline{R}^2 = c_2 t \tag{2.5}$$

Equation 2.4 and 2.5 may be written in the more general form

$$\overline{R}^n - \overline{R_0}^n = c_2 t \tag{2.6}$$

$$\overline{R} = c_2 t^{1/n} \tag{2.7}$$

The constant **n**, often termed the grain growth exponent is, in this analysis equal to **2**.

The use of equations 2.4 and 2.5 to describe grain growth kinetics was first suggested by Beck et al. (1949). These authors found that **n** was generally well above 2 and that it varied with composition and temperature. It is significant that very few measurements of grain growth kinetics have produced the grain growth exponent of 2 predicted by equations 2.4 and 2.5, and values of 1/n for a variety of metals and alloys as a function of homologous temperature are shown in figure 2.21. The trend towards lower values of **n** at higher temperatures has been reported in many experiments [*Higgins*, 1974].

Abnormal grain growth

Grain growth may be divided into two types, normal grain growth and abnormal grain growth. Normal grain growth is classified as a continuous process in which the

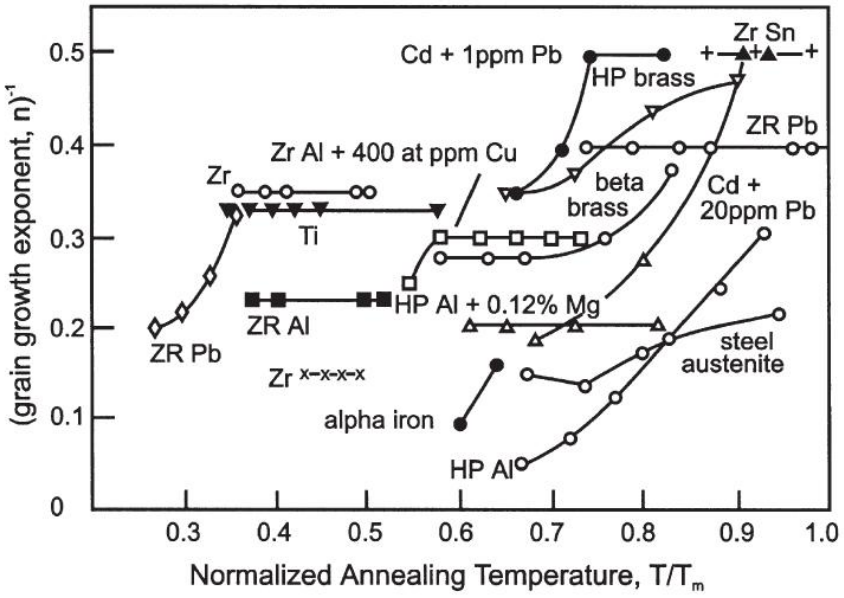

Figure 2.21.: The temperature dependence of the grain growth exponent **n** for isothermal grain growth in a variety of materials [*Higgins*, 1974; *Humphreys and Hatherly*, 2004].

microstructure coarsens uniformly. There is a relatively narrow range of grain sizes and shapes, and the form of the grain size distribution is usually independent of time and hence of scale as shown in figure 2.22a. Abnormal grain growth is a discontinuous process in which a few grains grow much faster than the rest of the grains in the microstructure. Therefore, a bimodal grain size distribution develops during the abnormal grain growth process. Figure 2.22b schematically illustrated grain size distribution describing the formation of the bimodal microstructures when annealing continues.

Because this discontinuous growth of selected grains has similar kinetics to primary recrystallization and has some microstructural similarities, it is also known as secondary recrystallization. Abnormal grain growth is an important method of producing large grained materials. The avoidance of abnormal grain growth at high temperatures is an important aspect of grain size control in steels and other alloys. The driving force for abnormal grain growth is also the reduction in grain boundary energy as for normal grain growth. However, in thin materials an additional driving force may arise from the orientation dependence of the surface energy. Abnormal grain growth originates by the preferential growth of a few grains which have some special growth advantage over their neighbors, and the progress of abnormal grain growth may be described in some cases by the JMAK kinetics.

An important question to consider is whether or not abnormal grain growth can occur

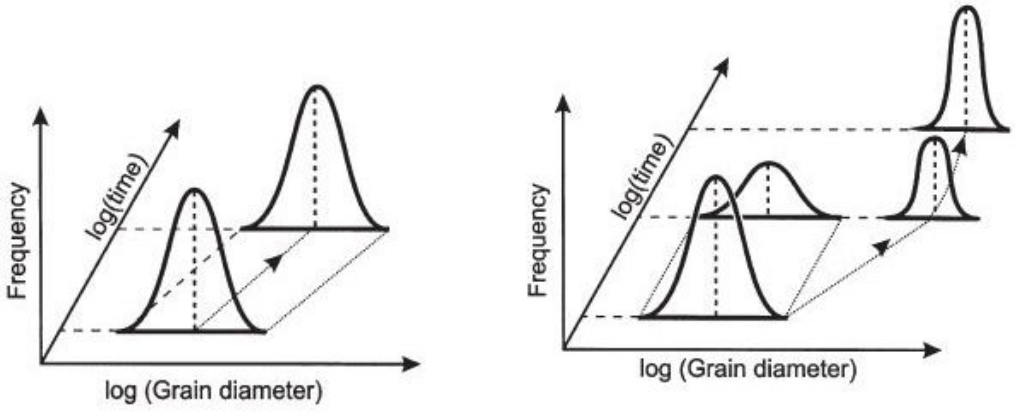

Figure 2.22.: Schematic representation of the change in grain size distribution during (a) normal grain growth and (b) abnormal grain growth [*Humphreys and Hatherly*, 2004].

in an 'ideal grain assembly' i.e. one in which there are no impurities and the boundary energy is constant. Consider the growth of a particular grain of radius R and grain boundary energy γ in an assembly of grains of mean radius $\overline{\mathrm{R}}$ and mean grain boundary energy $\overline{\gamma}$ (figure 2.23).

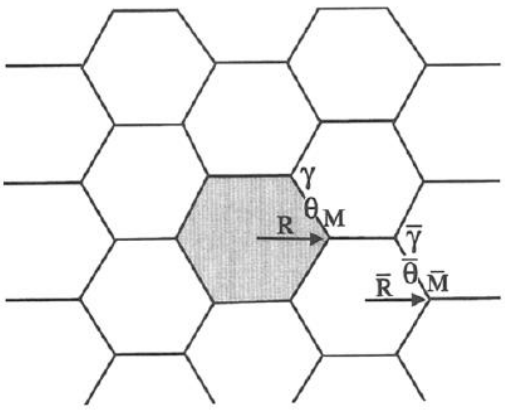

Figure 2.23.: Idealized cellular microstructure assumed in the analysis [*Humphreys*, 1997].

The growth rates of the grain and the assembly are given by equation [*Humphreys*, 1997]

$$\frac{dR}{dt} = MP = M(\frac{\overline{\gamma}}{\overline{R}} - \frac{\gamma}{R}) \tag{2.8}$$

which is modified for a more general case from the expression derived by Hillert in his

classic paper in which the energies of all grain boundaries are equal $\gamma = \overline{\gamma}$ [*Hillert*, 1965]. As shown first by Thompson et al., a large grain will grow faster than the normally growing grains and leads to instability of the microstructure by discontinuous growth if [*Thompson et al.*, 1987]

$$\overline{R}\frac{dR}{dt} - R\frac{d\overline{R}}{dt} > 0. \tag{2.9}$$

Taking dR/dt from the equation 2.8, the instability condition for the abnormal grain growth of the particular grain is given by equation

$$M\overline{\gamma} - \frac{\overline{R}M\gamma}{R} - \frac{R\overline{M}\overline{\gamma}}{4\overline{R}} > 0. \tag{2.10}$$

For the 'ideal' material, all boundary energies and mobilities are equal and the condition for abnormal growth then becomes

$$\frac{4R}{R} - \frac{R^2}{R^2} - 4 > 0. \tag{2.11}$$

This conditions is never achieved, although the left hand side equals zero when R = $2\overline{\mathrm{R}}$. Thus, a very large grain will always grow more slowly than the average grain relative to the grain assembly, and will eventually rejoin the normal size distribution. Therefore abnormal grain growth cannot occur in an 'ideal grain assembly' [*Humphreys and Hatherly*, 2004]. Abnormal grain growth can only occur when normal grain growth is inhibited, unless the abnormal growing grain enjoys some advantage other than size over its neighbours. The main factors which lead to abnormal grain growth are second-phase, texture and surface effects.

2.3.2. Nanoscale grain growth kinetics

Grain growth in NC materials is primarily driven by the excess energy stored in the grain or interphase boundaries. Analogous to the growth of cells in soap froths, the boundaries move toward their centers of curvature and the rate of movement varies with the amount of curvature [*Malow and Koch*, 1997; *Gleiter*, 2000]. The model by Burke and Turnbull, i.e. equations 2.4 and 2.6 was adopted to rationalize the grain growth process.

It has been noted by Lu that grain growth started at a lower temperature in the NC sample with smaller grains and that grain growth was rapid above a certain temperature and became negligible for longer annealing time [*Lu*, 1991]. Ganapathi et al. studied

the grain growth kinetics of the NC Cu and tried to fit their grain growth data and observed an excellent fit for values of **n** of 1/2, 1/3 or 1/4. Thus, they concluded that it was difficult to identify the grain growth mechanism on the basis of the exponent **n** alone, and that the grain growth in NC materials probably occurred in a manner similar to that in conventional CG materials [*Ganapathi et al.*, 1991].

Actually, for NC metals or alloys, the large change of the total grain boundary areas accompanying grain growth would greatly affect the grain growth kinetics. As GB area diminishes, the concentration of solute or impurity atoms segregated to the GBs is expected to increase, and introduces a grain-size dependent retarding force on GB migration. Therefore, Michels et al. found that the kinetics of grain growth in NC materials could rarely be described by a simple power law of the type applicable to the grain growth in highly pure, CG polycrystalline materials. The practically unavoidable presence of impurities or solute atoms, pores or precipitates in NC samples gives rise to significant retarding forces on grain boundary movement that manifest themselves during an isothermal annealing as an eventual stagnation of grain growth at a limiting grain size. In conventional materials, the influence of such pinning forces is usually modeled under the assumption that their strength is independent of the average grain size $\overline{\mathrm{R}}$. For the case of solute drag, however, the retarding force is proportional to the concentration of solute atoms segregated to the grain boundaries. In NC materials, this concentration is expected to depend strongly on the average grain size, because the grain boundary area available for segregation changes rapidly with $\overline{\mathrm{R}}$ whenever the magnitude of $\overline{\mathrm{R}}$ is small. For this reason, solute drag was expected to have a qualitatively different influence on grain growth in NC materials than in conventional CG materials [*Michels et al.*, 1999]. On this basis, Michels et al. obtained the modified grain growth equation:

$$\overline{R}(t) = \overline{R}_{max}^2 - (\overline{R}_{max}^2 - \overline{R(0)}^2)exp[-2At/\overline{R}_{max}^2]^{1/2}, \tag{2.12}$$

where A is a temperature- and material-dependent constant describing the GB mobility which is corresponding to c_2 in equation 2.4, and $\overline{\mathrm{R}_{\mathrm{max}}}$ is the limiting grain size.

The viewpoint by Michels et al. that the solute drag by the alloying or impurity atoms reduced the GB mobility was supported by some other authors earlier or later [*Moelle and Fecht*, 1995; *Liu and Muecklich*, 2001]. However, there were also some authors with the viewpoint that the reducing GB mobility was due to a vanishing driving force, i.e. the GB energy [*Weissmueller et al.*, 1992; *Kirchheim*, 2002; *Liu and Kirchheim*, 2004]. The GB energy, σ_{b}, reduced with solute segregation. If it was possible to reduce σ_{b} to zero or negligible values, then there would be no driving force for grain growth or

coarsening in such a solid:

$$\sigma_b = \sigma_0 - \Gamma_{b0} RTlnX_0 + \Delta H_{seg}, \tag{2.13}$$

where σ_0 is the GB energy for pure solvent, X_0 is the bulk content, Γ_{b0} ($= X_b d\rho$ with X_b, d and ρ as the concentration, the width and the density of GB at saturation [*Liu and Kirchheim*, 2004]) is the solute excess of GB monolayer available for segregation at saturation, and ΔH_{seg} is the energy change of segregation per mole of solute. Whenever σ_b is positive, grain growth will decrease the free energy of the system. Since systems with $\sigma_b < 0$ are not thermodynamically stable, the only case where grain growth can be suppressed is where $\sigma_b = 0$ [*Liu et al.*, 2006].

By incorporating the decrease in GB energy with GB segregation into the grain growth parabolic kinetics, Chen et al. developed a thermokinetic description for grain growth in NC materials [*Chen et al.*, 2009]. Based on Borisov's equation, a qualitatively physical description between self-diffusion in the lattice and along the GBs and the GB energy was provided. It was shown that the incorporation of GB energy into the grain growth kinetics was physically practicable. A model of grain size dependent GB energy was proposed, and by introducing the above model into the grain growth kinetics, a thermokinetic model for grain growth considering the mixed effect of kinetics and thermodynamics was derived. Different from the result by Michels et al., they argued that the main cause of a stabilized NC structure was not solute drag but a reduction in GB energy.

3. Experimental

3.1. Materials investigated

In this work, two different kinds of model materials are investigated. The first is the NC nickel, which has been processed by the 'bottom-up' method - pulsed electrodeposition (PED). The PED plates were synthesized by Schüler et al. at the institute of materials science and methods in Saarland University. The size of the as-received electrodeposited NC nickel plates is about 60 mm in length and 30 mm in width, with thickness larger than 1.5 mm. Figure 3.1 shows the original scale of the as-electrodeposited NC nickel plate and the specimens cut by wire spark erosion for later fatigue experiments. The NC plates processed with this method are with a high purity and hardly any porosity. The parameters for the PED plates are listed in Appendix A. More detailed information about the synthesis of the PED plates can be found in the diplom thesis of Philippi [*Philippi*, 2011].

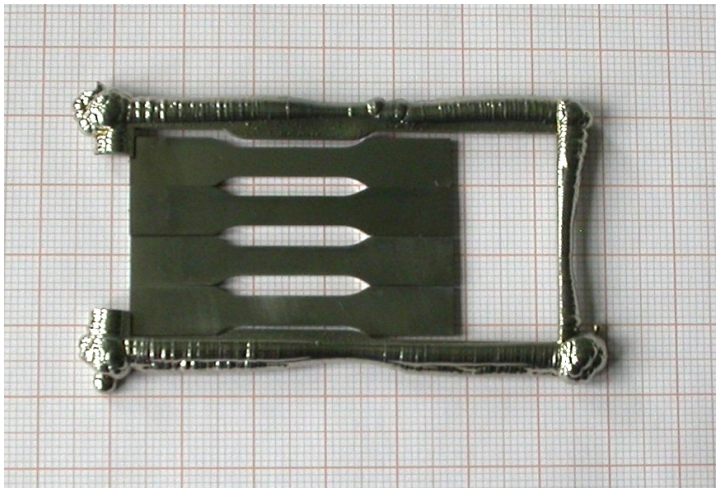

Figure 3.1.: The as-received PED NC nickel plate and prepared specimens.

The second model material is the UFG nickel, which is processed by the 'top-down' method - equal channel angular pressing (ECAP). The ECAP UFG nickel was prepared by Karaman in Texas A&M University. Two different ECAP routes, i.e. route C and

route E, were used for preparation of the ECAP billets. The as-received ECAP billet is with a scale of 25.5 mm × 25.5 mm × 132 mm (figure 3.2). The specimens are with a high purity (99.99 + %) and free of porosity.

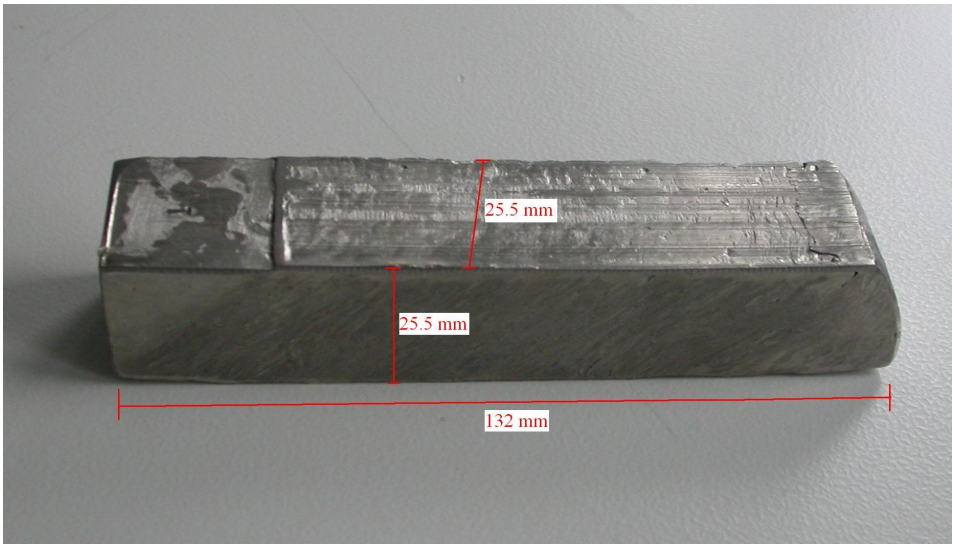

Figure 3.2.: The as-received ECAP nickel billet after ECAP process.

3.2. Specimen preparation

3.2.1. Specimens for mechanical tests

Specimens for tensile and fatigues experiments were cut by wire spark erosion from the PED NC nickel plates or ECAP UFG nickel billets. The geometries of the tensile specimens and fatigue specimens are shown in figure 3.3 and figure 3.4, respectively. The specimens from the PED nickel are about 1.3-1.8 mm thick, depending on the preparation of the PED plates. For the ECAP nickel, the tensile specimens are 2 mm thick and the fatigue specimens are 3 mm thick. Specimens for microindentation measurements are small pieces with no special geometries.

3.2.2. Surface preparation

Mechanical polishing and electropolishing were used for the specimen surface preparation. All specimens were prepared by fine mechanical grinding with the grinding papers from Grade 600 to Grade 4000. The surface of the specimens which are only for the mechanical testing was well prepared by the mechanical polishing. However, to obtain the

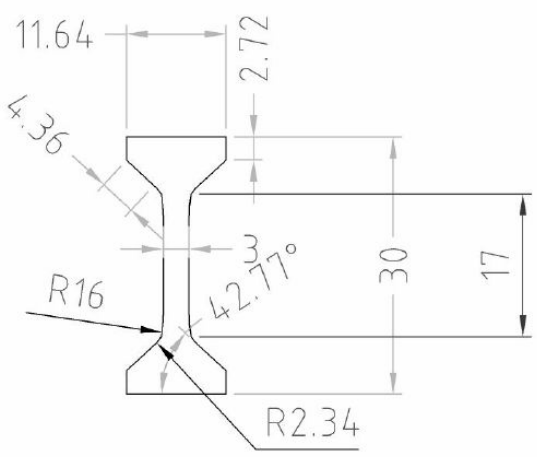

Figure 3.3.: Specimen geometry for the tensile tests.

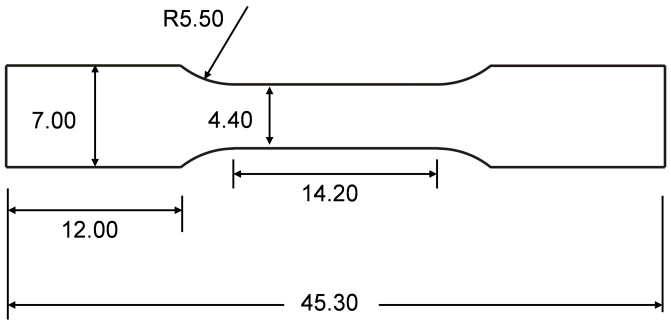

Figure 3.4.: Specimen geometry for the fatigue experiments.

defect-free surfaces for the microstructural analysis, the deformed layer introduced by mechanical grinding must be removed by electropolishing. The electrolyte used in the electropolishing for nickel in this work is a solution mixed of 98% H_2SO_4 and methanol. The parameters for electropolishing are listed in table 3.1.

3.3. Microstructural analysis

Analysis of the microstructures provides the insights to understand the micromechanisms of the deformation in the mechanical tests. With the modern high resolution electron microscopes the microstructures can be analyzed down to the nanoscale. In this work, three scanning electron microscopes (SEM), i.e. CamScan CS44, JEOL JSM–7000 F and Dual Beam Strata™ 235 (FEI), were used to analyze the surface microstructures of

parameter	value
solution	53 ml 95% H_2SO_4 plus 947 ml Methanol
voltage	32-35 V
flow rate	12-16
time	30-60 s

Table 3.1.: Parameters for the electropolishing.

the investigated objectives, according to the different requirements. Secondary electron images and backscattered electron images were taken for the surface analysis and microstructural analysis. Electron backscattered diffraction (EBSD) was used for gathering of the information about grain size, grain size distribution, grain orientations and grain boundary misorientations.

The specimen surface was also analyzed using atomic force microscope (AFM). Figure 3.5 shows an AFM image of the surface microstructure of the ECAP nickel on the y-plane. However, the surface preparation for the AFM characterization was not always satisfying. Besides, there was no detailed information about the misorientations at the grain boundaries and the textures by AFM analysis. Therefore, further microstructural analysis was carried out using the electron microscopes.

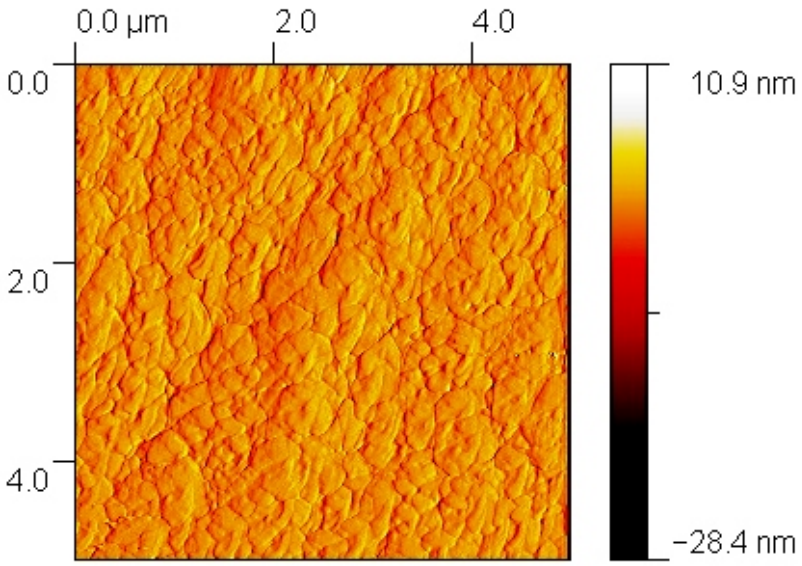

Figure 3.5.: Surface microstructure of the ECAP nickel characterized by AFM. This image is for an ECAP nickel specimen with route C on the y-plane.

3.4. Heat treatment

Heat treatments were performed to achieve the different desired microstructures. The specimens were annealed in vacuum ($< 10^{-5}$mbar) and cooled in a cooling chamber quickly after the pre-set annealing time. In this work, different grains sizes and grain size distributions were designed, from nanograins, ultrafine grains to coarse grains. In order to obtain the aimed size of the growing grains, the appropriate annealing temperature should be selected. Therefore, a series of pre-experiments were conducted for choosing the appropriate annealing temperatures with the anticipated grain sizes, which are shown in table 3.2. Finally, two annealing temperatures were selected by considering the ultimate grain size and the grain growth rate, i.e. 250℃ and 500℃, which are equivalent to $0.3T_m$ and $0.45T_m$, respectively, where $T_m = 1455$℃ is the melting temperature for nickel.

When annealing the PED NC nickel at 250°, a continuous grain growth from nanograins to ultrafine grains occurred, with the transition bimodal microstructure mixed with nanograins and ultrafine grains (NC/UFG). It took 15 min to heat the specimens from room temperature to 250° and then different holding times were chosen for controlling the 'bimodality' of the grain size distribution.

When annealing the PED nickel at 500°, two different methods were used. The first one was to heat the specimens with nanograins directly to 500° and then to hold them at this temperature for different annealing times. For the second method the specimens with nanograins were heat treated at 250° as the first stage with a long holding time, to get a transition state with the ultrafine grains. Then the UFG specimens were heat treated at 500° for different times. Complicated annealing phenomena - normal and abnormal grain growth - were observed. It took 15 min to heat the specimens to 250° and 40 min to heat the specimens to 500°.

According to the pre-experiments, the ECAP UFG nickel was annealed only at 250° with different holding times. The as-received ECAP nickel had the starting grain size in the UFG range which was similar to that of the PED UFG nickel, which had been achieved by annealing the NC nickel at 250°. After ECAP process the UFG nickel was in a severely deformed state, therefore, a quite different annealing phenomenon at this temperature occurred as that for the PEC NC nickel. The bimodal microstructure mixed with ultrafine grains and coarse grains (UFG/CG) was obtained. It was found that the heat treatment of the ECAP UFG nickel was more sensitive to the annealing temperature and the annealing time comparing to the PED nickel. Besides, the bimodal

temperature	PED NC nickel	ECAP UFG nickel
600 °C	–	no survival UFG grains
550 °C	–	no survival UFG grains
500 °C	proper temperature for abnormal grain growth	no survival UFG grains
400 °C	fast grain growth average grain size ∼ 600 nm	–
350 °C	–	no survival UFG grains
320 °C	fast grain growth average grain size ∼ 500 nm	–
300 °C	–	no survival UFG grains
270 °C	bimodal NC/UFG, selectable temperature	–
260 °C	–	bimodal microstructure, but too quick
250 °C	bimodal NC/UFG, selected temperature	proper annealing temperature for UFG/CG
240 °C	–	hardly bimodal microstructure observed
230 °C	–	no grain growth observed
200 °C	–	no grain growth observed
180 °C	–	no grain growth observed

Table 3.2.: Pre-experiments for the selection of the annealing temperatures, to obtain the desired microstructures.

UFG/CG microstructure was strongly influenced by the starting UFG microstructures formed in the ECAP process.

In order to obtain a better understanding of the annealing process in-situ heat treatment in SEM was conducted. The in-situ heat treatment equipment used in this work was developed after Noll, who annealed the PED NC nickel and observed the abnormal grain growth phenomena [*Noll*, 2006]. Figure 3.6 shows the experimental set-up, which is a modified heating system from Fa. Kammarath & Weiss GmbH. The specimen is fixed on the heating plate and the heating table is installed in SEM. The annealing temperature is controlled by the electric current. A cooling system is adopted in order to protect the SEM detectors and to help lower the system temperature.

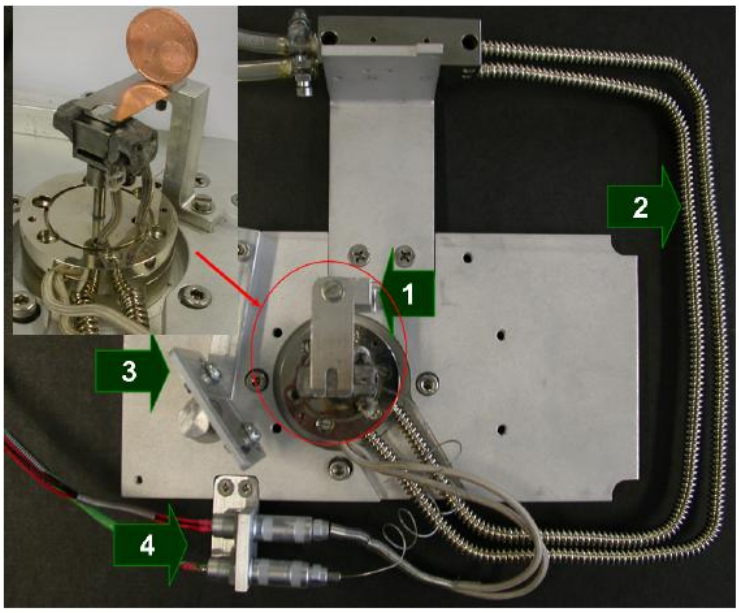

(a)

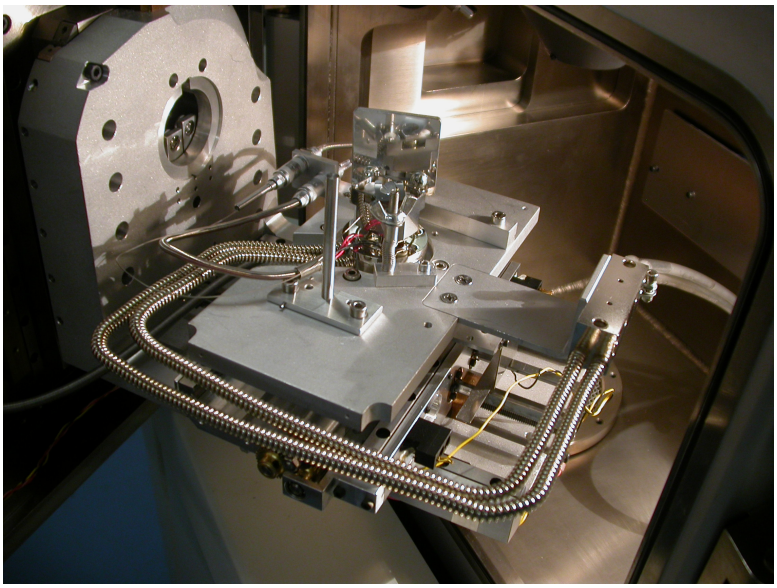

(b)

Figure 3.6.: (a)Experimental setup for the in-situ heat treatment. (1) sample holder, (2) cooling system, (3) EDX shielding and (4) electrical contacts. (b) In-situ annealing setup in SEM.

3.5. Mechanical property measurements

3.5.1. Microindenatation

Microhardness was measured for the strength of the materials. Microindentation measurements were carried out with a Vickers hardness testing machine (Leica VWHT-MOT). There were different maximum loading forces available from 49 mN to 19 N. All the measurements were performed at room temperature with a holding time for 15 s. At least ten indents were conducted to each specimen.

3.5.2. Tensile tests

Tensile tests were performed to obtain the stress-strain curves for the ECAP specimens with different microstructures. As there were only three PED NC plates available, tensile tests had not been carried out for the PED nickel. All tensile tests were performed with a hydraulic testing machine Fa. SCHENCK TREBEL at room temperature controlled by LabVIEW programs. The strain-controlled mode was used with a strain rate of $0.01\%\mathrm{s}^{-1}$.

3.6. Fatigue experiments

Fatigue experiments were conducted to the PED and ECAP nickel, with help of the artificially initiated microcracks by focused ion beam (FIB). For metallic materials the fatigue cracks initiate at the preferring sites for the stress concentration during the cyclic loading. In this work we start directly with the microcracks which serve as the stress concentration sites to investigate the fatigue behaviour and the crack resistance of the different microstructures.

FIB is a very powerful tool to manipulate the specimen surface microscopically, without influencing the rest of the materials. The application of the microcracks by FIB was firstly developed by Schaef, who introduced the microcracks into the coarse grained CMSX-4 alloy and investigated the crack propagation in relevance to the grain orientations [*Schaef*, 2010; *Marx et al.*, 2010; *Schaef et al.*, 2011; *Schaef and Marx*, 2012]. A great advantage of the FIB technique is to prepare the microcracks with different lengths, which are with the accuracy in micrometers. Besides, other parameters such as microcrack shapes, depth, orientations and positions can also be accurately controlled. In this work microcracks with the geometry shown in figure 3.7 are initiated on the

specimen surface by FIB. The surface geometry of the microcracks is with a high aspect ratio, in order to obtain a high stress concentration locally at the crack tips.

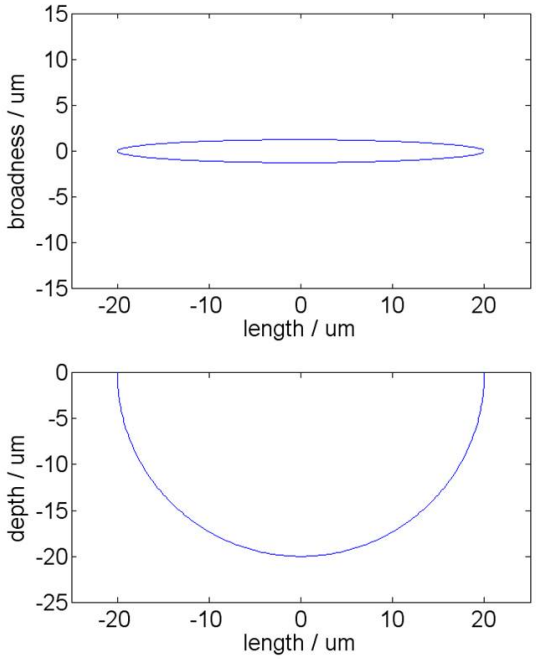

Figure 3.7.: Surface and depth profile of the artificial FIB cracks.

The fatigue behaviour of the PED nickel with different microstructures were investigated. A hydraulic testing machine Instron 8511 was used for the fatigue experiments in this work. It was found in the pre-experiments that the fine grained PED nickel is very sensitive to the microstructural imperfections such as the micro-pores which has been introduced in the electrodeposion process. Therefore, initiating the artifical microcracks is a very useful method to investigate the fatigue behaviour, espeically the crack resistance, of the PED nickel with different microstructures. The microcracks were stable under the lower stress amplitudes. They began to grow when the stress amplitude is increased and then induce the ultimate fatigue fracture.

In order to concentrate on the influence of the microstructures, the other experimental parameters were held constant. The FIB cracks were initially perpendicular to the loading direction with the crack length of 100 μm. The specimens were then loaded under the load-controlled mode by a sinusoidal signal with the loading ratio R $= -1$ and loading frequency 2Hz. The incremental stress amplitudes were applied: when there was no crack propagation observed under a given stress amplitude after $100,000$ fatigue cycles, a higher stress amplitude was then used in the further loading. Replica technique was used to observe the crack propagation and the crack growth length was measured

after the given fatigue cycles. It was found that the NC/UFG microstructure showed an improved crack resistance over the monomodal NC or monomodal UFG microstructure. For a better understanding to this phenomenon, in-situ fatigue experiment was performed to the bimodal PED NC/UFG nickel. The influence of the nanograins and ultrafine grains to the crack propagation was directly observed.

For the ECAP nickel the FIB microcracks were also initiated on the specimen surface. This kind of material is characterized with the microstructure containing strong microstructural textures which have been cause by the severe plastic deformation in the ECAP process. The textures are usually along the direction about 45° to the specimen border. Therefore, microcracks of different length were initiated with different orientations relating to the microstructural textures (figure 3.8). The microcracks in figure 3.8a and figure 3.8c are approximately parallel and perpendicular to the direction of the microstructural textures and the microcrack in figure 3.8b is vertical to the loading direction.

The ECAP nickel specimens having the UFG microstructure or bimodal UFG/CG microstructure, with the FIB microcracks on the specimen surface, were cyclically loaded under the load-controlled mode by a sinusoidal signal with the loading ratio $R = -1$ and loading frequency $2 - 5$Hz. Sometimes the term stress-controlled mode is also used in this work because the microcracks has little influence to the whole cross-sectional area. With help of the Replica technique the crack propagation was observed and the crack growth length was measured after the given fatigue cycles. The specimens were taken out from the testing machine after a certain number of cycles, and the crack propagation and the microstructural evolution along the crack propagation path were directly investigated in SEM.

Actually, it has been found that although the microcracks in the ECAP nickel specimens propagated with increasing fatigue cycles in the fatigue experiments, they did not grow to a critical length and then induced the ultimate fracture. In other words, the ECAP UFG nickel is not sensitive to the microcracks. In order to investigate the crack propagation behaviour of the ECAP UFG nickel, macro-notches with the length in the millimeter range were initiated, at the edge of the specimen by wire spark erosion (Mode I Notch) (figure 3.9) or in the middle of the specimen by vertical spark erosion (Mode II Notch) (figure 3.9). To obtain a sharp tip of the notches, the Mode I Notch tip was further sharpened by the surgical blade and the Mode II Notch tip was sharpened by FIB. The notched specimens were then investigated in the fatigue experiments, similarly to the specimens with microcracks in their surface.

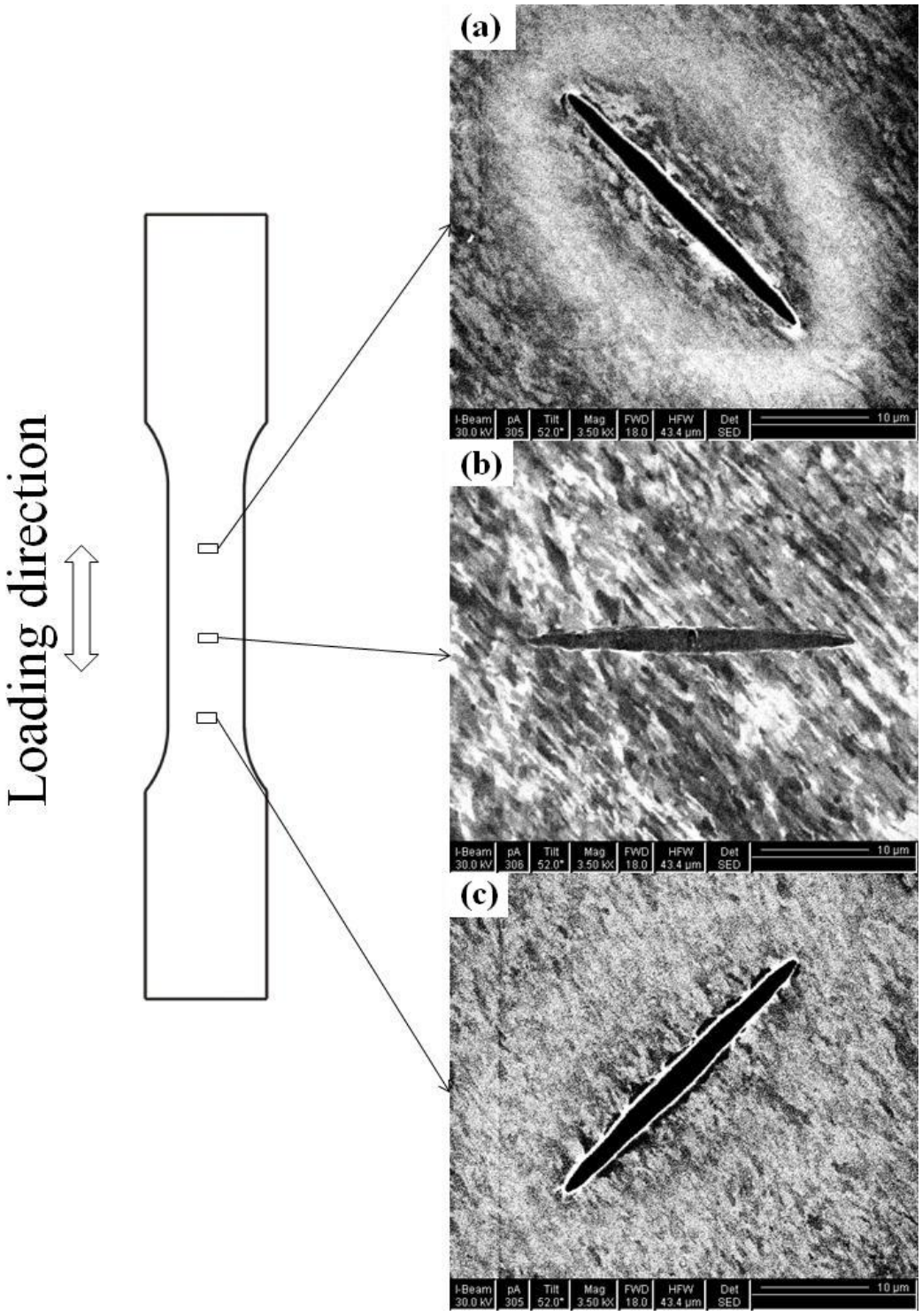

Figure 3.8.: Microcracks initiated by FIB on the surface of ECAP UFG nickel. The microcracks are introduced with different orientations relating to the microstructural textures and loading direction in (a), (b) and (c).

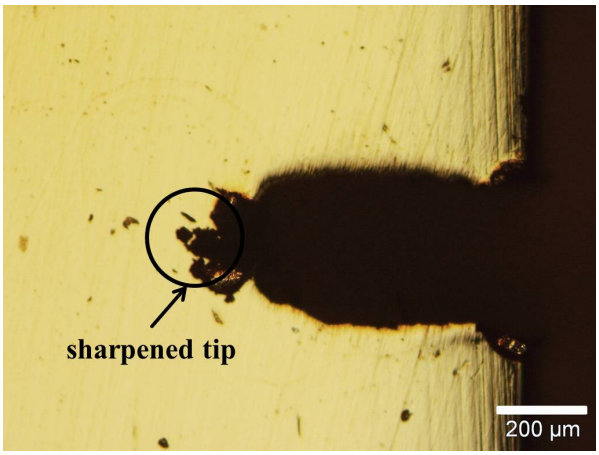

Figure 3.9.: Micro-notch at one edge of the specimen, introduced by wire spark erosion (Mode I Notch). The notch tip is sharpeend by the surgical blade.

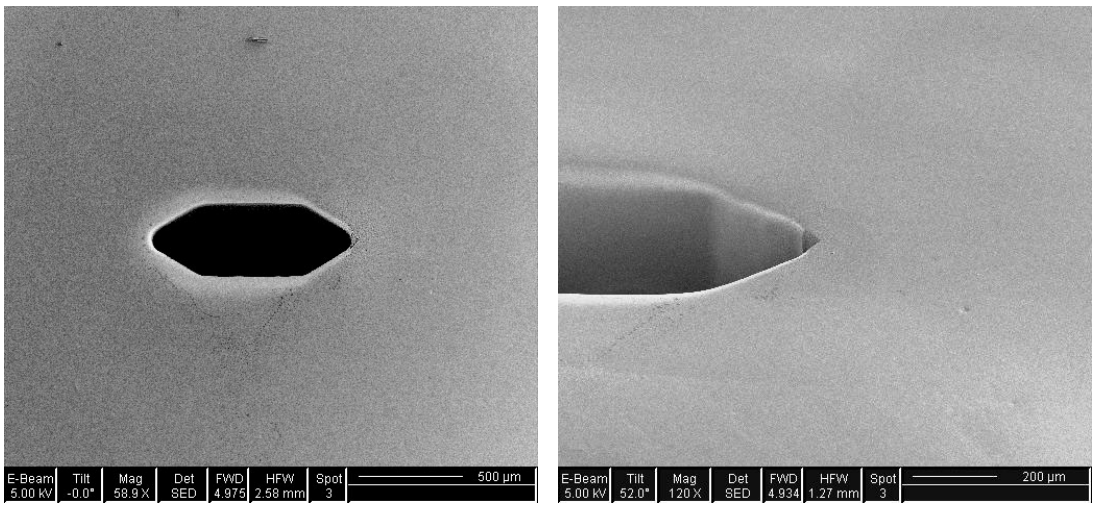

(a) **(b)**

Figure 3.10.: (a) Micro-notch in the middel of the specimen, introduced by vertical spark erosion (Mode II Notch). (b) One notch tip is sharpened by FIB.

4. Results

4.1. Microstructural characterization

Figure 4.1 shows the SEM image of the microstructure of the as-received PED NC nickel. It is difficult to determine the mean grain size quantitatively according to this image due to the SEM resolution. However, it can be seen that the grain size is well below ~ 30 nm with some exceptions of larger grains, but all the grains are of the grain sizes in the NC range (below 100 nm). This result is similar to the characterization of the NC nickel conducted by Yang with different methods(AFM, TEM and XRD), who used the similar starting materials in his work. The PED NC nickel has nanograins separated by high angle grain boundaries, and there is low dislocation density inside the grains [*Yang*, 2006].

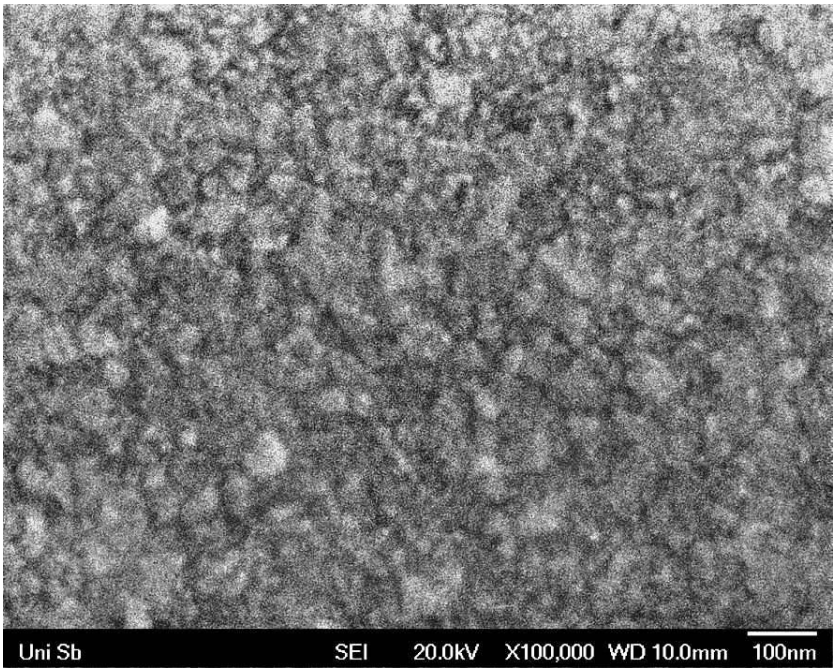

Figure 4.1.: Secondary electron image of the surface microstructure of the as-received PED NC nickel.

For the ECAP UFG nickel, it is important to define the different surfaces of the ECAP billet, which is shown in figure 2.2 schematically. The investigation of the ECAP UFG materials is usually concentrated on the y-plane, which is parallel to the direction of shear deformation during the ECAP process. Figure 4.2 shows the SEM images of the microstructures on the y-plane for the ECAP UFG nickel with an area about $25 \times 15\ \mu m^2$, with the figure 4.2a and figure 4.2b for route C and route E, respectively. It is shown that the grain size is in the UFG range for both routes. For the route C specimen, the grains are mainly of the elongated form, consisted of bands of subgrains along the direction about 45° to the image border which was induced by the simple shear during the ECAP process. For the route E specimen, there is mixture of areas of directional elongated grains like the route C and areas with homogeneous distributed grains. Further characterization on the microstructures was carried out by the EBSD measurements. The cubic specimens were cut from the ECAP billet for both routes and the three surfaces in the x-, y- and z-plane were analyzed (figure 4.3). Figure 4.3a shows the color-coded orientation map for the route C specimen, revealing the strong textures consisted of clusters of the elongated grains. Figure 4.3b shows that there are more homogeneous equiaxed grains for the route E specimen. Actually there are also areas with elongated grains for the route E specimen as shown in figure 4.2b, and their orientation map is similar to that in route C specimens. The grain sizes, which are listed in Table 4.1, are calculated according to the EBSD images using the line intercept method. More information about the microstructures of the ECAP UFG nickel is shown in Appendix B.

sample	plane	grain size (nm)
route C	X	377.5
	Y	277.6
	Z	458.0
route E	X	317.1
	Y	334.9
	Z	314.0

Table 4.1.: Grain size of UFG nickel on different ECAP planes, using the line intercept method.

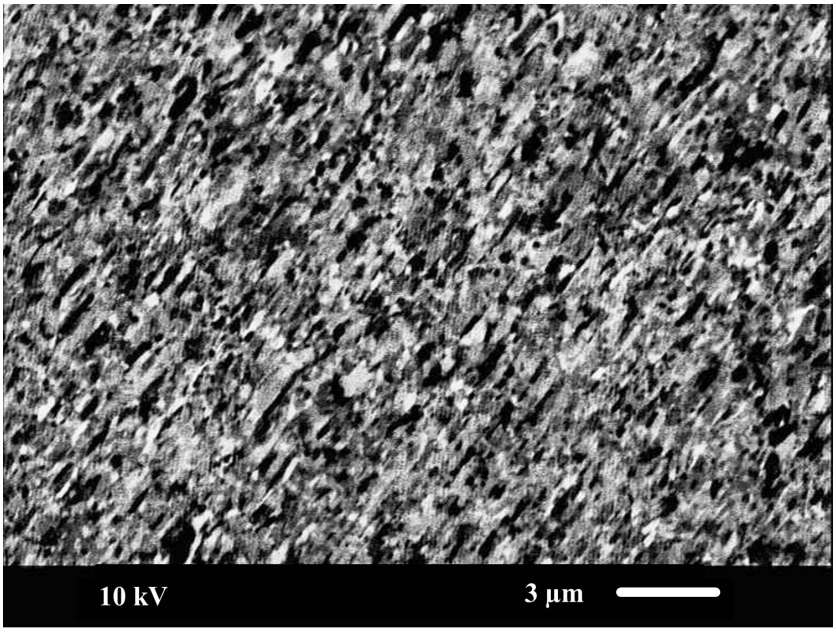

(a)

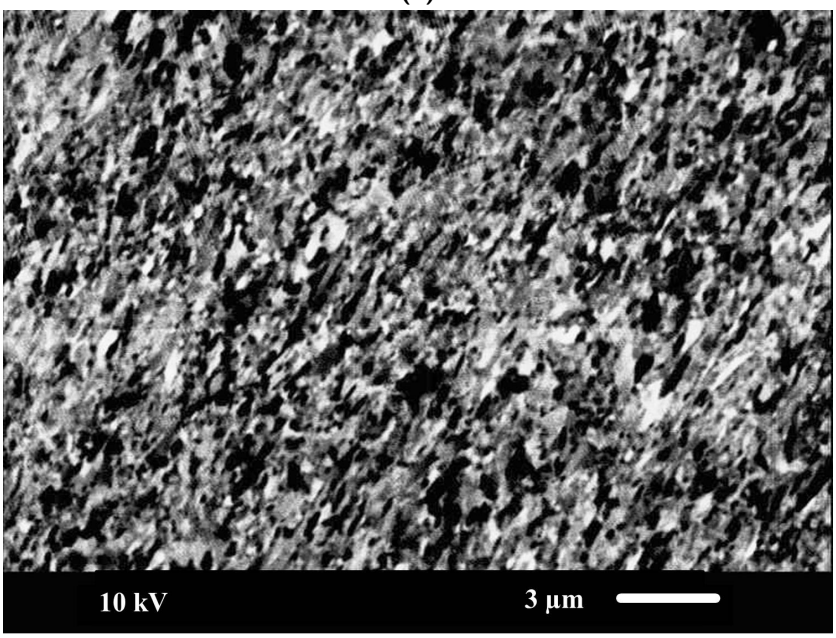

(b)

Figure 4.2.: Secondary electron images of the y surface of the as-received ECAP UFG nickel processed with eight passes by (a) route C and (b) route E.

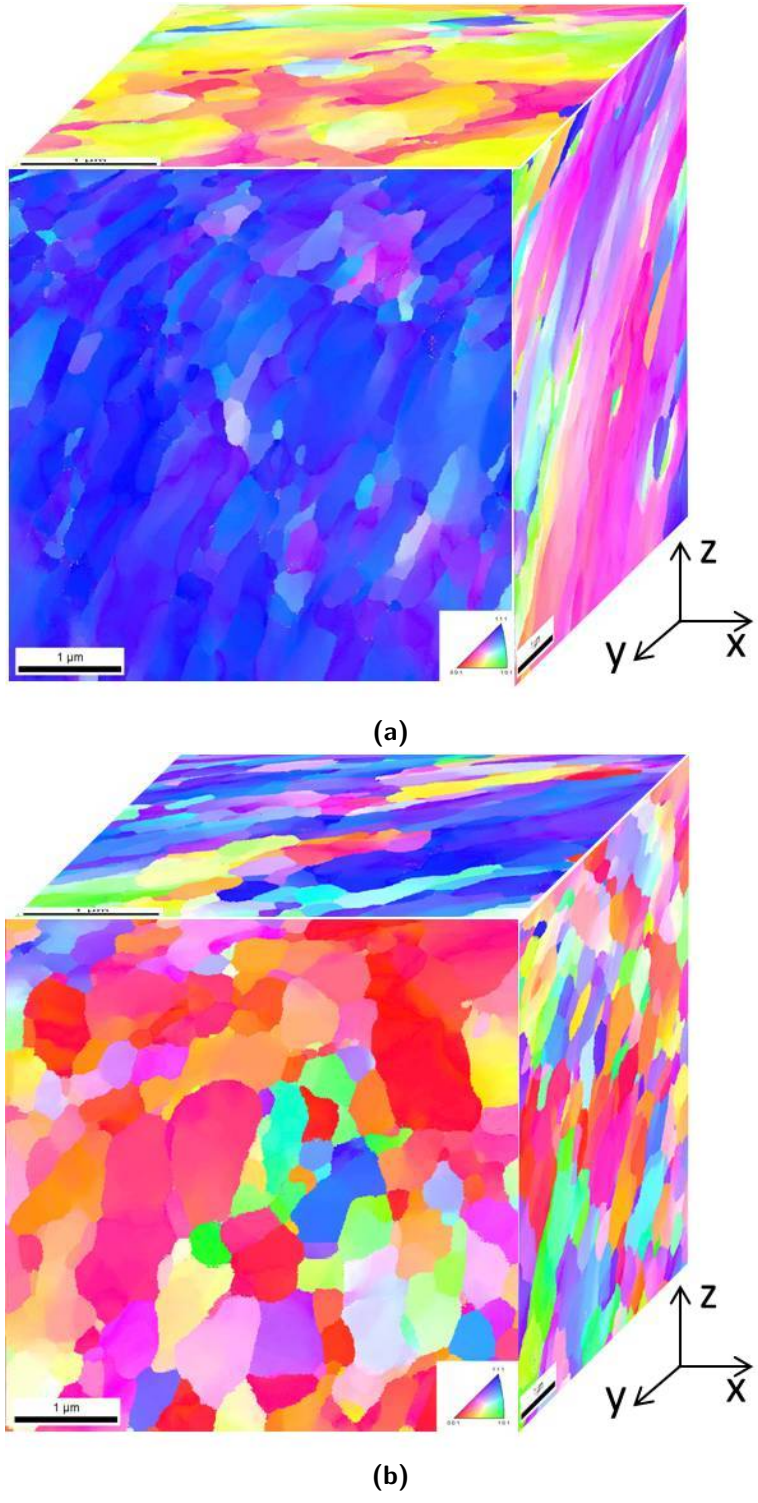

Figure 4.3.: EBSD characterization of the as-received ECAP UFG nickel processed with eight passes by (a) route C and (b) route E.

4.2. Microstructures after heat treatment

4.2.1. PED nickel annealed at 250 °C

The PED NC nickel was annealed at 250 °C to obtain the bimodal NC/UFG microstructure. Figure 4.4 shows the microstructural evolution with the increasing annealing time, in which all the subfigures are with the same magnification. It was found that grain growth began to take place in the first 20 min (figure 4.4(a)-(c)), but there was only a quite low volume fraction of the new growing grains in the UFG range. However, the volume fraction of the ultrafine grains increased quickly in the following annealing time (figure 4.4(d)-(h)). There were almost no nanograins when the specimen was annealed at this temperature for relatively long time, e.g. 180 min in figure 4.4(i). An overview of the annealing parameters and the corresponding volume fraction and the mean grain size of the ultrafine grains are listed in Table 4.2.

sample	Annealing temperature (°C)	Annealing time (min)	volume fraction of grown grains	mean grain size of the grown grains (μm)
p3.2	250	10	1.2%	0.071
p2.2	250	20	10.3%	0.210
p5.2	250	25	35.2%	0.259
p4.2	250	30	55.8%	0.294
p5.1	250	35	80.2%	0.308
p1.2	250	40	83.9%	0.339
p4.1	250	55	89.2%	0.367
p3.2	250	180	99.4%	0.372
p1.1	250	300	100%	0.390

Table 4.2.: An overview of the volume fraction and the mean grain size of the grown grains for PED NC nickel annealed at 250 °C

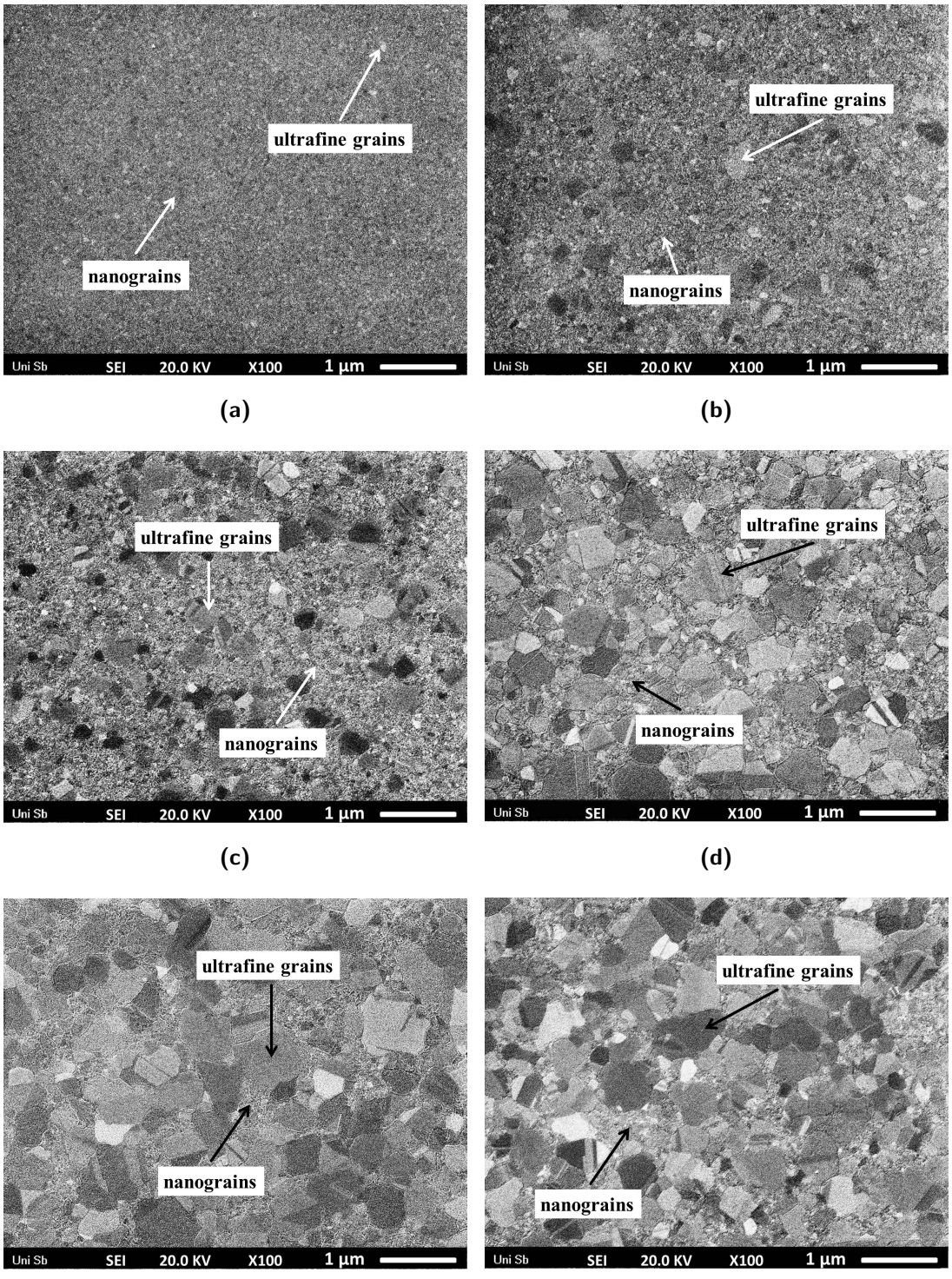

Figure 4.4.: Microstructure evolution of PED NC nickel annealed at 250° for different times. (a) 10 min, (b) 20 min, (c) 25 min, (d) 30 min, (e) 35 min, (f) 40 min, (g) 55 min, (h) 180 min.

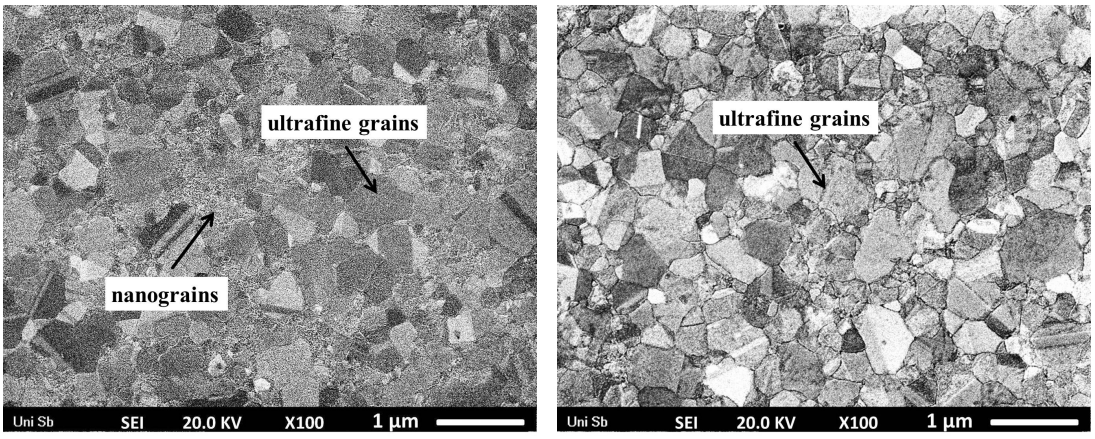

(g) **(h)**

Figure 4.4.: Microstructure evolution of PED NC nickel annealed at 250° for different times (continued).

In order to examine if the grain growth was homogeneous in the whole specimen, the microstructure on the cross section of the bimodal microstructural specimen which was annealed at 250 °C for 25 min, was investigated (figure 4.5). Figure 4.5a shows the surface microstructure, while figure 4.5b shows the grain distribution in the cross section. It can be seen that the distribution of the nanograins and the ultrafine grains is quite homogeneous both on the surface and the cross section. The bimodality, which represents the volume fractions of the coarser grains and the finer grains, is also similar to each other on the surface and in the cross section. Therefore, characterization of the microstructure on the specimen surface can represent the microstructure of the whole specimen.

The mean grain size of the growing grains increases slightly with increasing annealing time, which is shown in Table 4.2. After a long annealing time at 250 °C, the monomodal UFG microstructure with the mean grain size 390 nm has been reached. This mean grain size is quite similar to that of the as-received ECAP UFG nickel, both for route C and route E. Unlike the ECAP UFG nickel, there are dominant high angle grain boundaries and low dislocation density in the annealed PED UFG nickel.

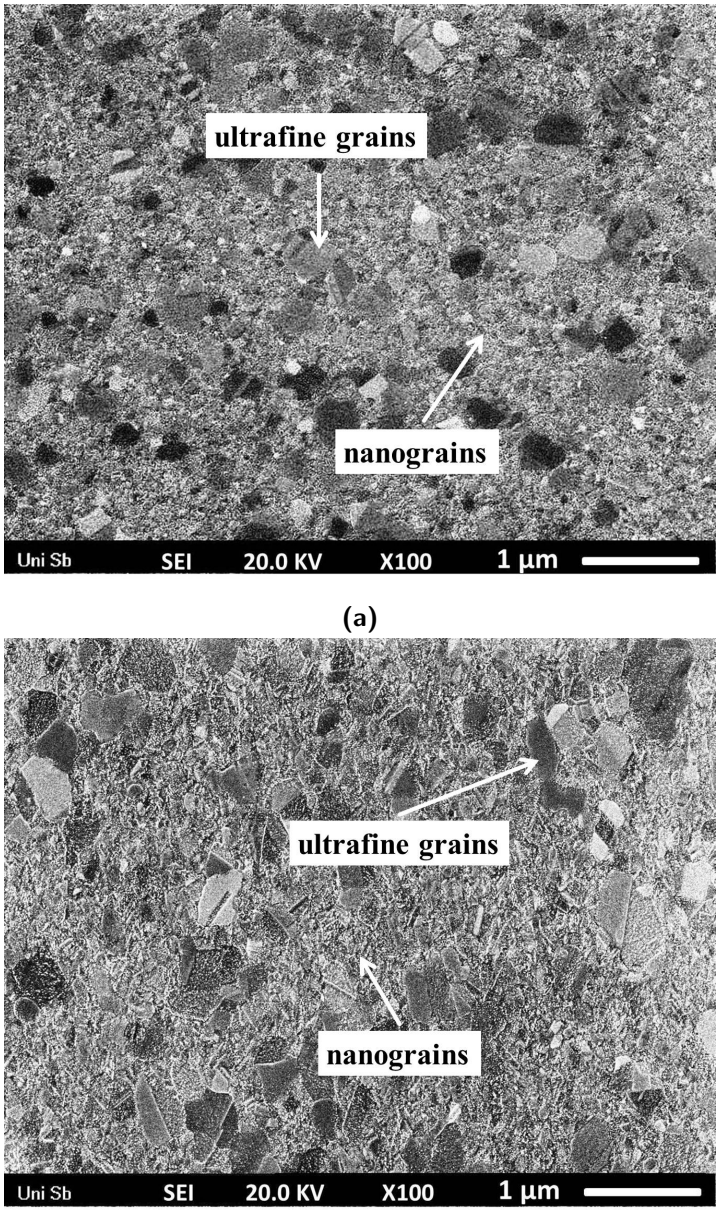

Figure 4.5.: Comparison of grain size distribution (a) on the surface and (b) on the cross section. The sample has the bimodal grain size distribution, which is annealed at 250 °C for 25 min.

4.2.2. ECAP nickel annealed at 250 °C

The ECAP UFG nickel was heat treated at 250 °C to obtain the bimodal UFG/CG microstructure. While the grains after ECAP process are in the severely deformed state, recovery and recrystallization are the main processes during the annealing, which is unlike the grain growth for the PED NC nickel at this temperature. Heat treatment of the ECAP UFG nickel is very sensitive to the temperature. The bimodal UFG/CG microstructure was also obtained by annealing the UFG ECAP nickel specimens at 260 °C, however, the recrystallization process was much faster than annealing at 250 °C. Figure 4.6 shows the bimodal microstructure obtained by annealing the ECAP UFG nickel at 260 °C for 30 min.

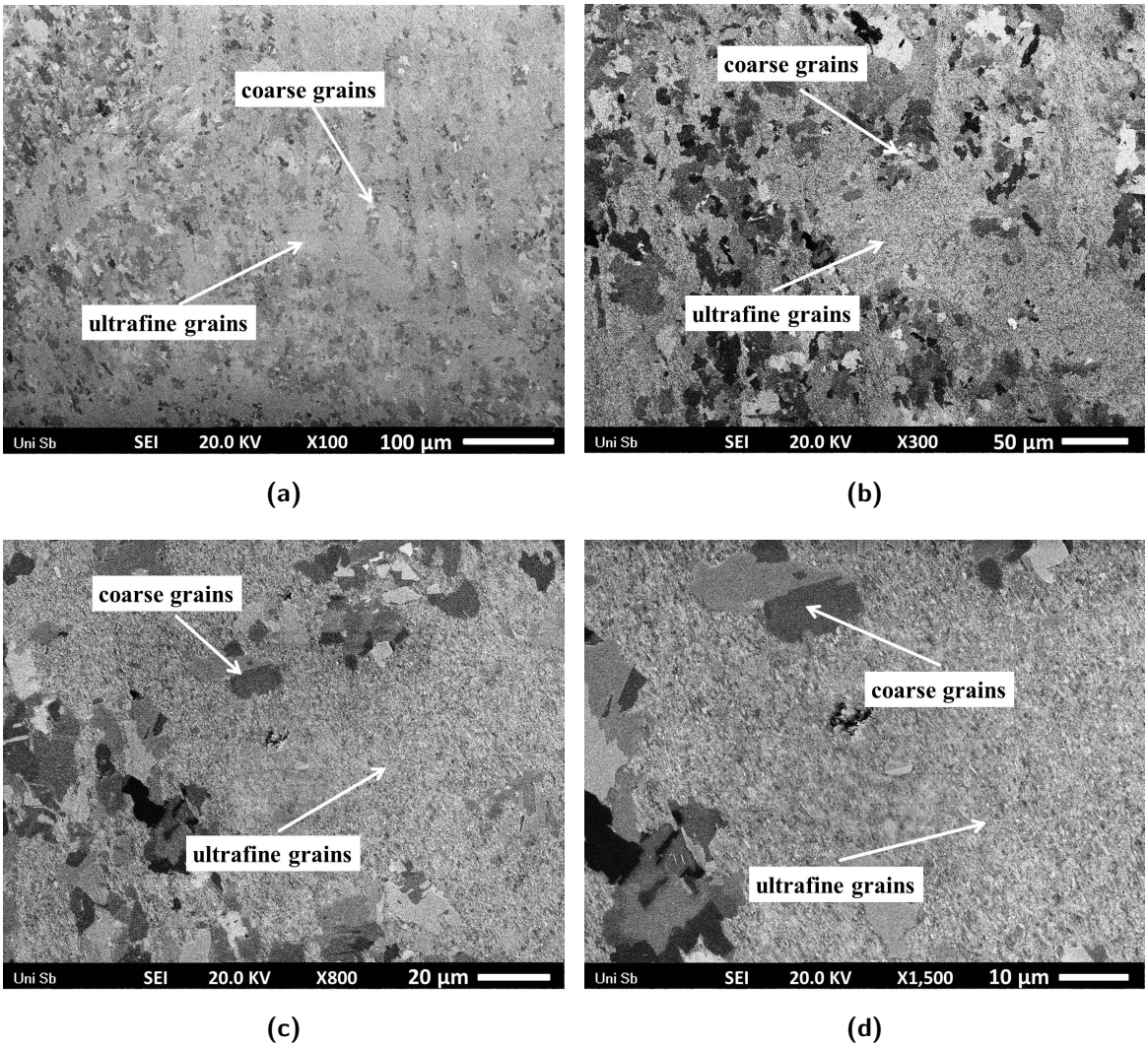

Figure 4.6.: The bimodal microstructure achieved by annealing the 8C ECAP UFG nickel at 260 °C for 30 minutes.

Therefore, the temperature 250 °C was selected as the annealing temperature for the ECAP UFG nickel. Figure 4.7 shows SEM images of the bimodal microstructure with different magnifications when an ECAP UFG nickel specimen was annealed at 250 °C for 50 min. Analysis on the grain size according to figure 4.7c reveals that the mean grain size is about 6.13 μm with a standard deviation of 2.20 μm.

It is obvious that the recrystallization of the ECAP nickel is significantly influenced by the microstructures formed in the ECAP process. Although the specimen is processed with route E in figure 4.7, the growing coarse grains are along the direction which is the shear direction in the last pass of the ECAP process. It is known that recovery and recrystallization are competing processes as both are driven by stored energy of the deformed state. Once recrystallization has occurred and the deformation substructure has been consumed, then no further recovery can occur. Conversely, recovery lowers the driving force for recrystallization and influences the recrystallization process. However, the division between recovery and recrystallization is sometimes difficult to define, because recovery mechanisms play an important role in nucleating recrystallization. Subsequent grain growth after recrystallization takes place further in the annealing process. Actually recrystallization textures should form when severely deformed metals are annealed. But the development of an annealing texture does not cease when recrystallization is complete. It continues during grain growth and the final texture, which has been altered by grain growth, is not necessarily representative of the texture present when primary recrystallization is complete.

In consideration of the whole annealed specimen in figure 4.7, the part of the UFG areas can carry on the properties of the UFG materials with higher strength and the growing coarse grains provide the improved ductility. The bimodal grain size distribution combines the properties of the ultrafine grains and the coarse grains.

To obtain more information about the recrystallization process of the severely deformed ECAP nickel, the bimidal UFG/CG microstructure was characterized by the EBSD measurement. Figure 4.8 shows the results for an annealed route C ECAP nickel specimen. Similar to the results for the specimens by route E, the growing coarse grains are along the shear direction in the last pass of the ECAP process. Taking figure 4.7 as reference, the CG areas and the UFG areas were investigated separately. It was found that the ultrafine grained area stayed unchanged during the annealing process, comparing with the EBSD image of the as-received UFG nickel on the y-plane by route C in figure 4.3a. In the areas of growing coarse grains, there are still ultrafine grains which have not been 'consumed' in the annealing process, as marked in figure 4.8b. The coarse grained areas are separated mainly by HAGBs and there is no recrystallization

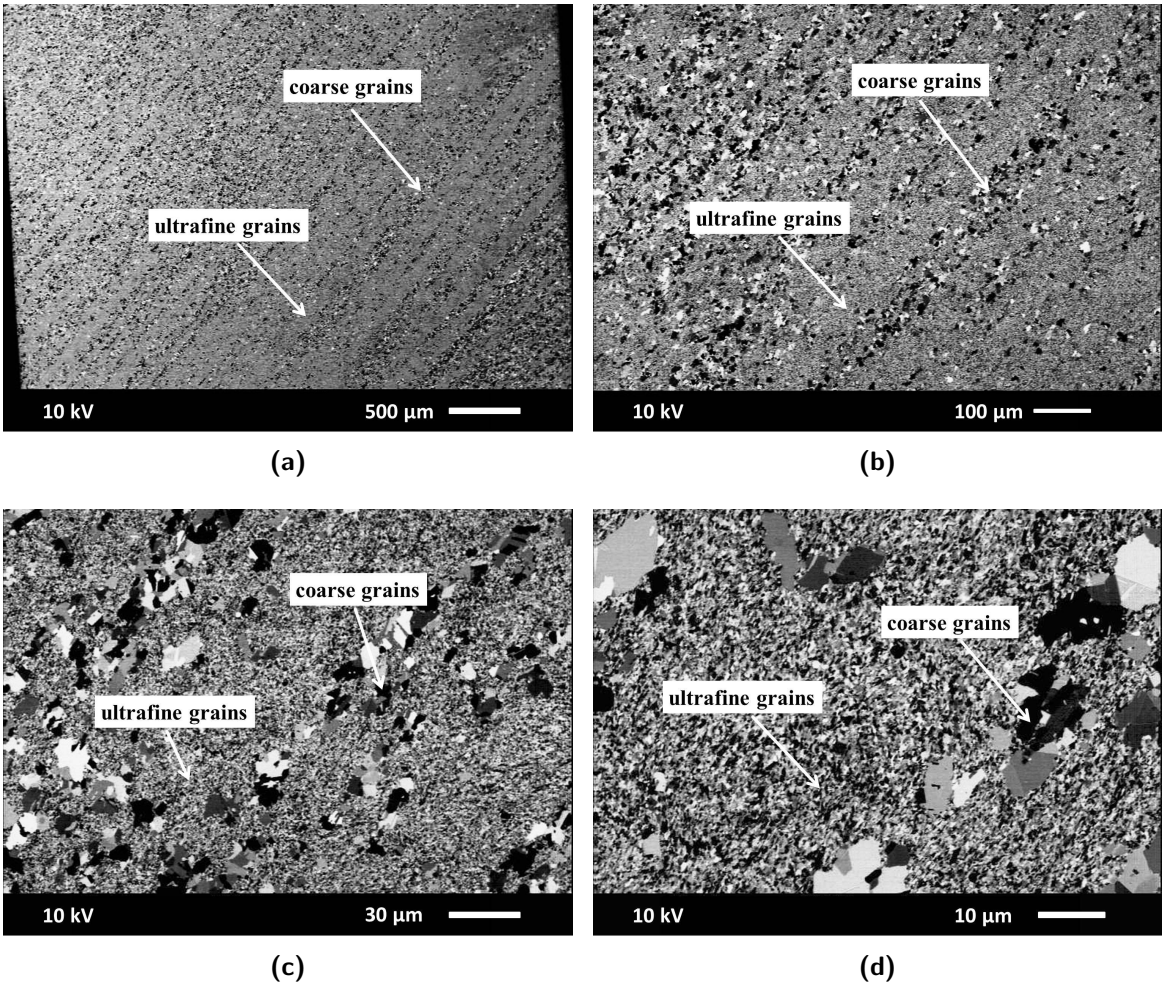

Figure 4.7.: SEM images of bimodal microstructure achieved by annealing the 8E ECAP UFG nickel at 250 $°C$ for 50 minutes.

textures in them, according to analysis by the EBSD image.

Figure 4.9 shows the pole figure for the heat treated specimen, which are analyzed from the EBSD data of figure 4.8. Figure 4.9a shows the pole figure of the UFG areas corresponding to figure 4.8a. Comparing with the pole figure of the as-received route C ECAP nickel (figure B.2a), the distribution of the ultrafine grains is quite similar, showing strong microtextures. Figure 4.9b depicts the orientation distribution of the CG areas. The thick points, which are clusters of series points having the same orientation, represent the coarse grains in figure 4.8b, showing relatively random distribution. This indicates that the recrystallization texture has been altered by the subsequent grain growth during the annealing process. The thin points represent for the ultrafine grained areas. A closer comparison of the two subfigures shows that the distribution of thin points in figure 4.9b overlaps very well to the orientation distribution in figure 4.9a. This proves again that some of the UFG areas 'survived' in the annealing process.

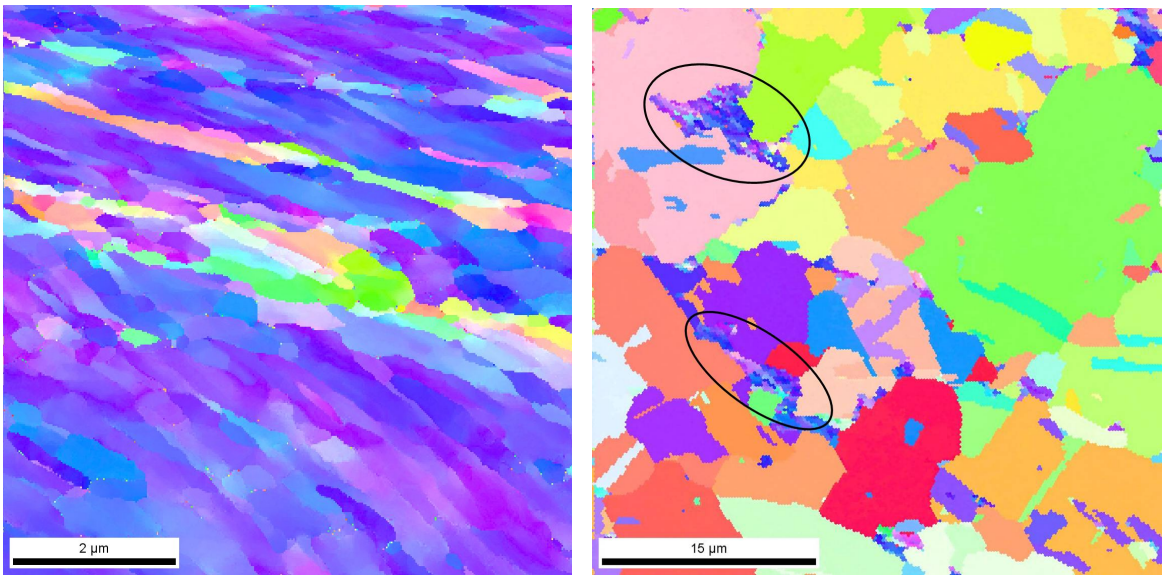

Figure 4.8.: EBSD images of the bimodal microstructure from 8C ECAP UFG nickel, showing the selected areas of (a) ultrafine grains and (b) coarse grains.

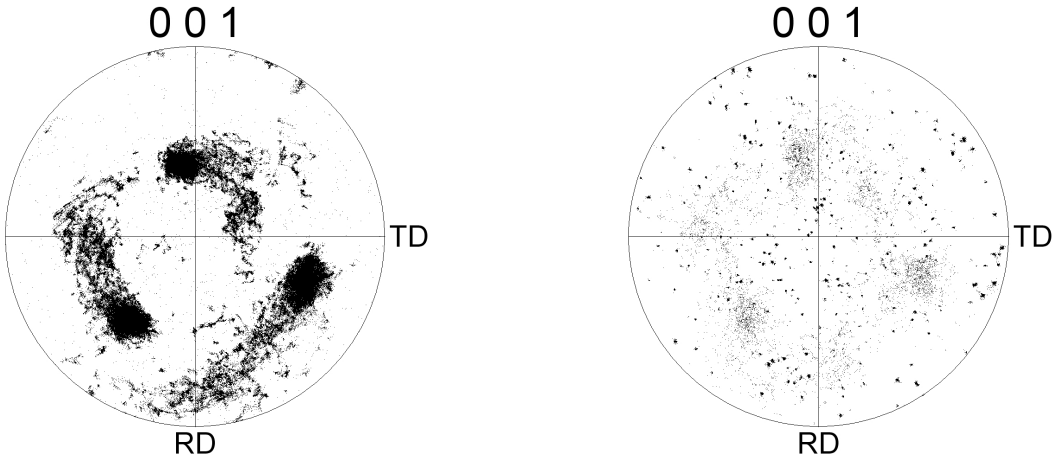

Figure 4.9.: Comparison of the pole figure of (a) the UFG area and (b) the CG area of the annealed ECAP nickel.

4.2.3. PED nickel annealed at 500 °C

The bimodal UFG/CG microstructures were obtained by heat treating the ECAP UFG nickel at 250 °C. However, annealing of the PED NC nickel at this temperature only caused the nanograins growing to the ultrafine grains. Therefore, the bimodal UFG/CG microstructure based on the PED NC nickel is anticipated by annealing the PED specimens at higher temperatures.

The first relevant results are shown in figure 4.10 and figure 4.11. The as-received PED NC nickel was firstly annealed at 250 °C for 180 min and the homogeneous microstructure of ultrafine grains formed. After then this specimen was annealed at 500 °C for 30 min. The specimen was annealed in vacuum and the surface microstructure was directly characterized in SEM after the heat treatment (figure 4.10). It is found that there are extremely large grains, which is caused by the abnormal grain growth. The grain boundaries of the large grains are of a jagged form, which can be observed clearly under larger magnifications (figure 4.10b and figure 4.10c). The jagged grain boundaries might be influenced by the surface effect in the annealing process. Analysis of the volume fraction of the large grains shows the value about 25.6 %. However, after preparing the specimen with grinding and electropolishing to eliminate the surface effect, the microstructure is totally different from that on the surface. Firstly, the volume fraction of the large grains, about 75.0%, is much higher than that on the surface microstructure. Secondly, the grain boundaries of the large grains are smoother, which are not the jagged form as on the surface. Thirdly, the mean grain size of the ultrafine grains is also slightly larger. Therefore, the specimens are firstly grinded and electropolished before the microstructures are characterized in the later work.

In the following, two groups of specimens, which were cut from two different PED plates, were annealed at 500 °C. Two different methods were applied to heat treat these specimens. The fist was the one-step method: directly to anneal the NC specimens at 500 °C. The second was the two-step method which divided the annealing process in two steps: to anneal the NC specimens at 250 °C for long time to initiate the UFG microstructure as a transition state, and then to anneal the UFG specimens at 500 °C. It was found that the two methods used in the heat treatment showed no influence to the ultimate microstructures for the specimens from the same PED plate. However, the grain growth phenomena were totally different for the specimens from the different PED plates, although synthesizing parameters and conditions for the two PED plates had been held identically in the PED process according to the producer (Appendix A).

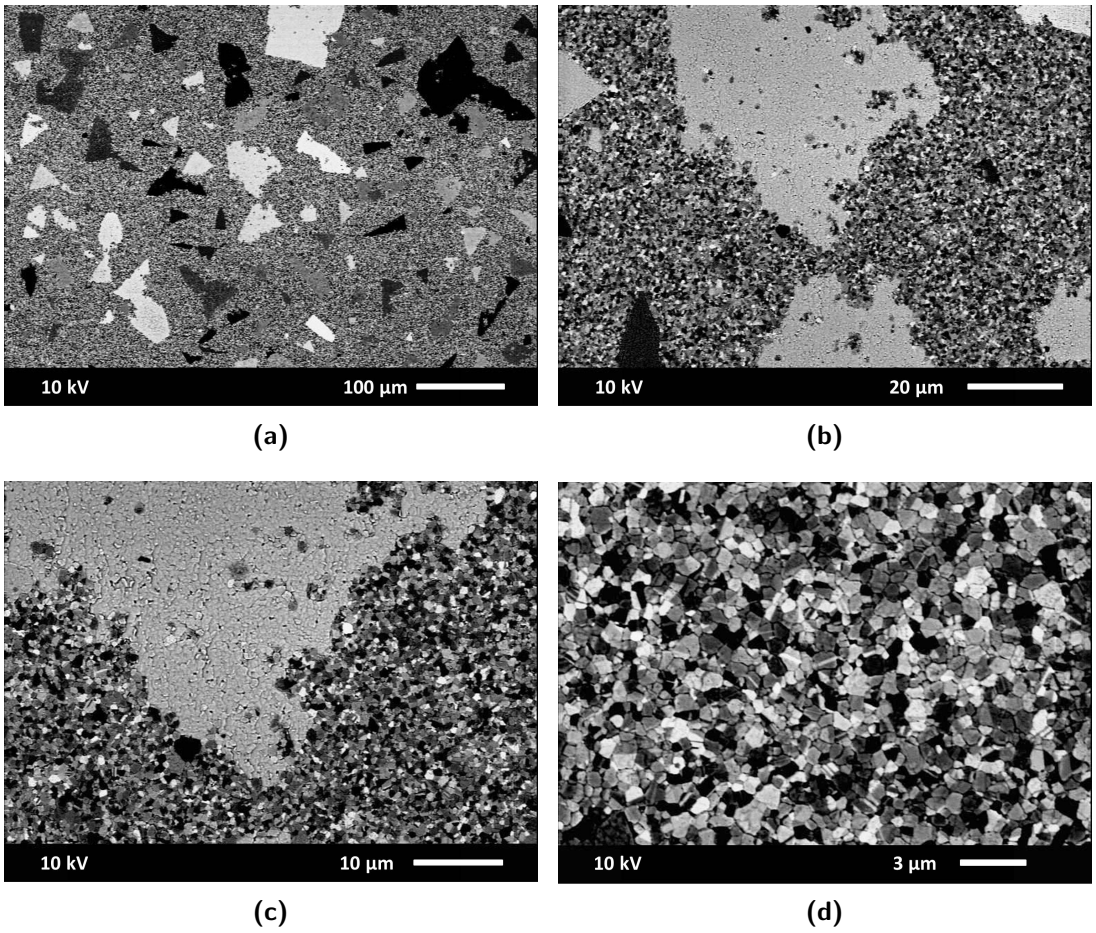

Figure 4.10.: Abnormal grain growth of the PED NC nickel, heated at 500°C for 30min. The specimen was not polished showing the surface microstructure.

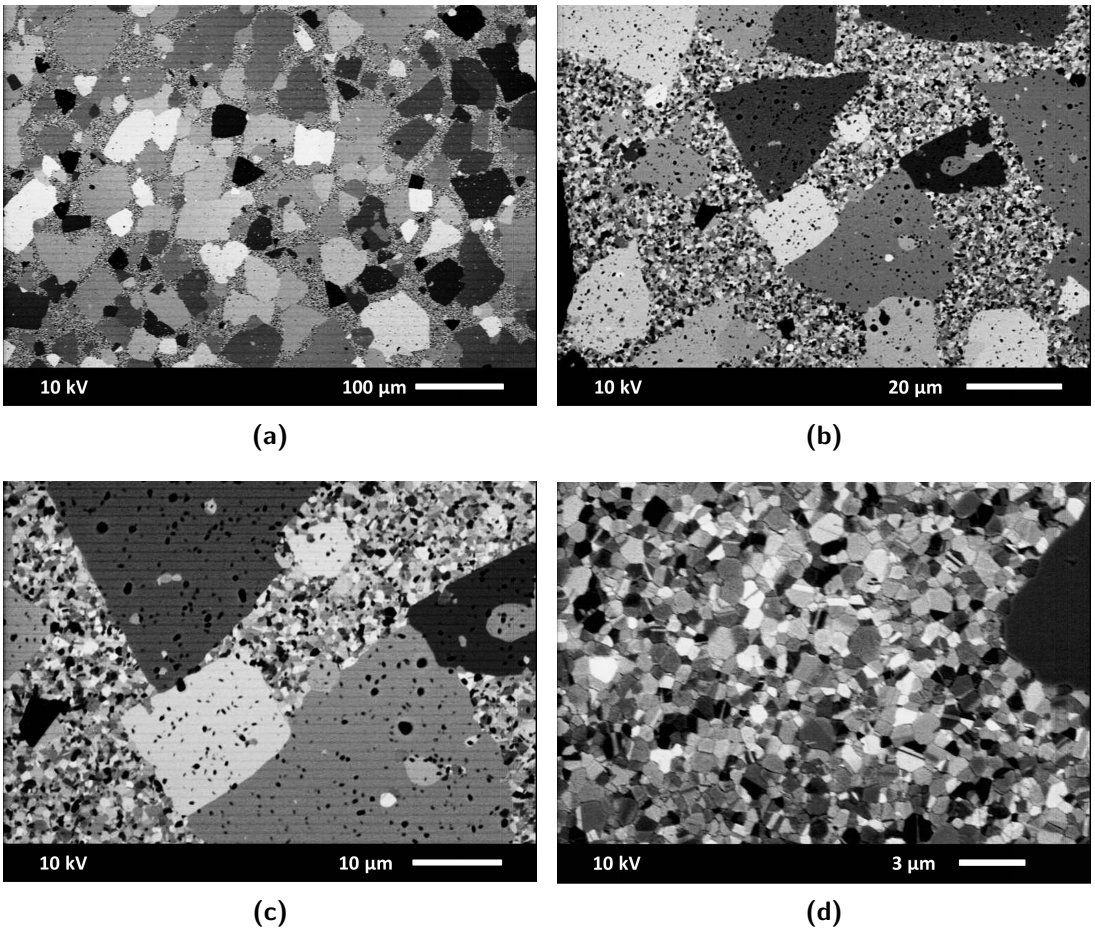

Figure 4.11.: Abnormal grain growth of the PED NC nickel, heated at 500°C for 30min. The specimen was polished to remove the surface influence.

PED plate 1

A series of specimens cut from the PED NC plate No.74 were firstly annealed at 250 °C for 300 min and a homogeneous microstructure of ultrafine grains was received. These specimens were further annealed at 500 °C, with different annealing times. The microstructural evolution with the annealing time is shown in figure 4.12. In order to show the grains clearly for different specimens, there are different magnifications in the subfigures.

In the first 20−30 min there was only continuous grain growth happening (figure 4.12a and 4.12b), where the largest grains were about $7 - 8$ μm. Actually the first extremely large grains, which were the abnormal growing grains, were observed after 30 min. However, this phenomenon was only occasional and not representative. The discontinuous grain growth, i.e. abnormal grain growth, was widespread to the whole specimen after 60 min. With further increasing the annealing time, the sum and the mean grain size of the abnormal growing grains both increased rapidly. There were only discrete areas, where the fine grains still existed, after 300 min (figure 4.12f). In this subfigure some areas with the fine grains (but not all the fine grained areas) are marked out with the red polygons. Further observation on the fine grained areas showed that the mean grain size was in the micrometer range. A comparison of the fine grained areas to the transition UFG microstructure after annealing at 250 °C is shown in figure 4.13.

The above specimens were annealed with the transition state, where the as-received PED NC specimens had been firstly annealed at 250 °C for 300 min to achieve the homogeneous UFG microstructure. The as-received PED NC specimens were also directly heat treated at 500 °C. However, the microstructures were quite identical to the above results with a transition annealing (figure 4.14). This result indicates that the final microstructures after heat treatment at 500 °C are not affected by the starting microstructures (NC or UFG) when the other annealing parameters are held the same.

A summary of this series of specimens from the PED plate No.74 annealed at 500°C is listed in table 4.3. It is also observed that there are plenty of annealing twins in the normal growing grains which is a common phenomenon for the fcc metals in the grain growth process. However, they are considered as a substructure inside the individual grains, and not counted as the effective points when using the line intersection method to calculate the grain size in this work.

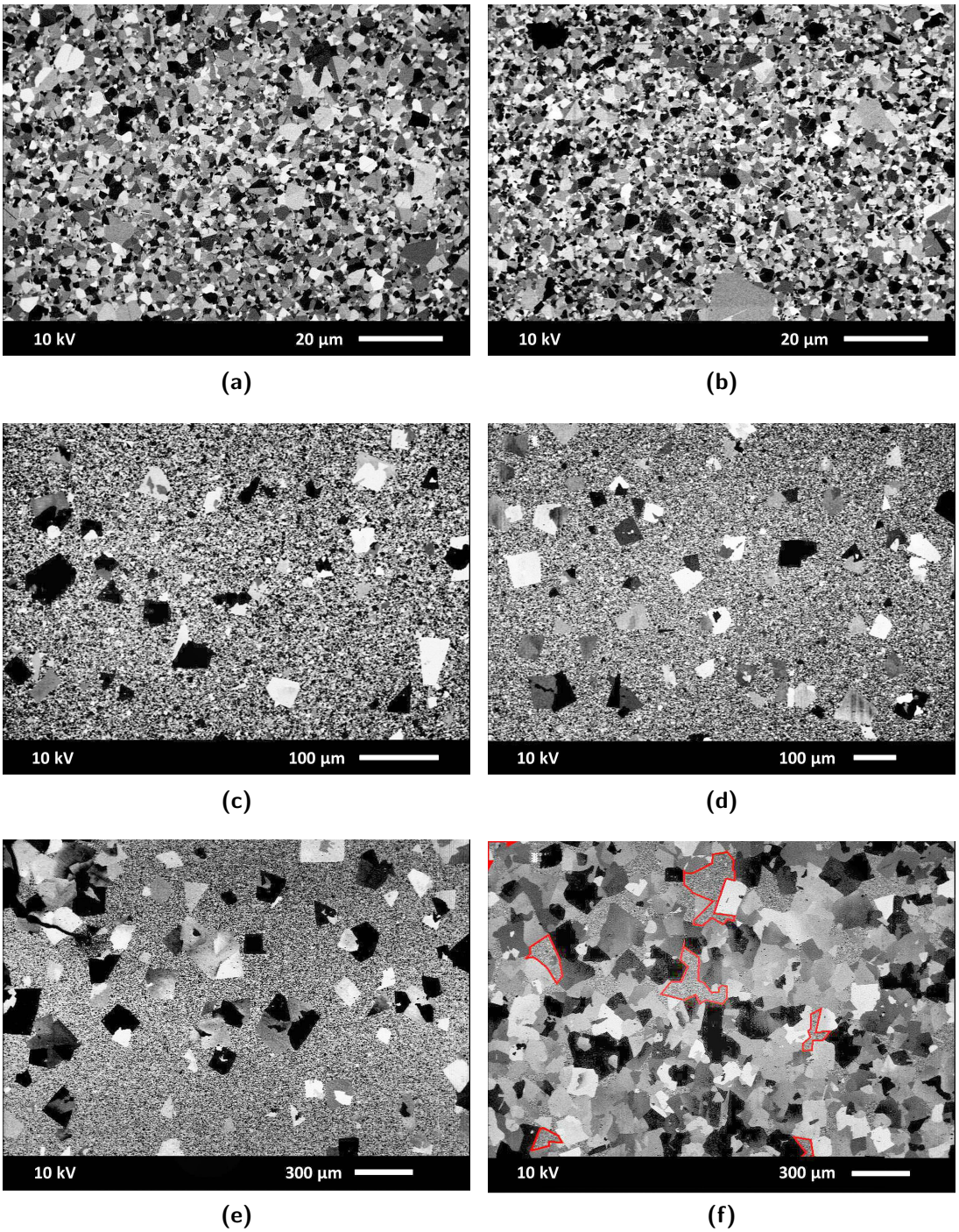

Figure 4.12.: Microstructure evolution of PED NC nickel annealed at 500° for different times. (a) 20 min, (b) 30 min, (c) 60 min, (d) 120 min, (e) 180 min, (f) 300 min. *Some finer grained areas are marked with the red polygons in subfigure (f).

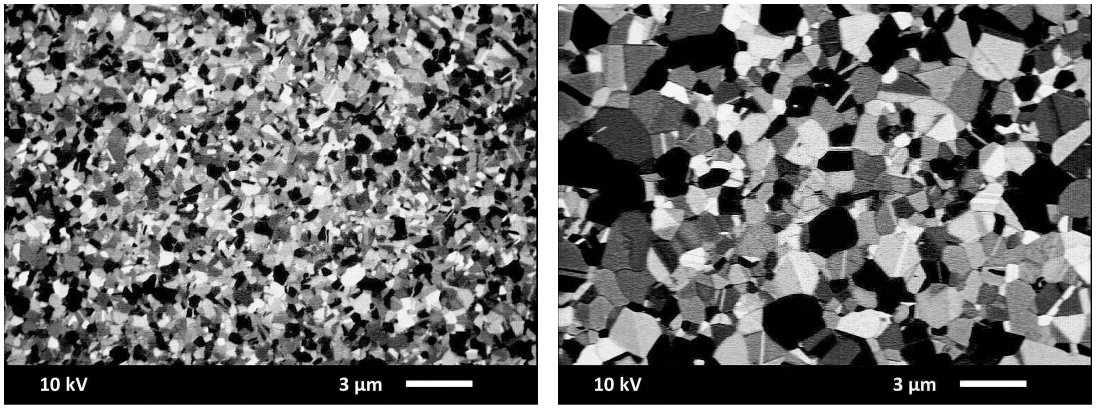

Figure 4.13.: Comparison of (a) the ultrafine grained area in the homogeneous UFG microstructure with (b) the fine grained area after annealing at 500 °C.

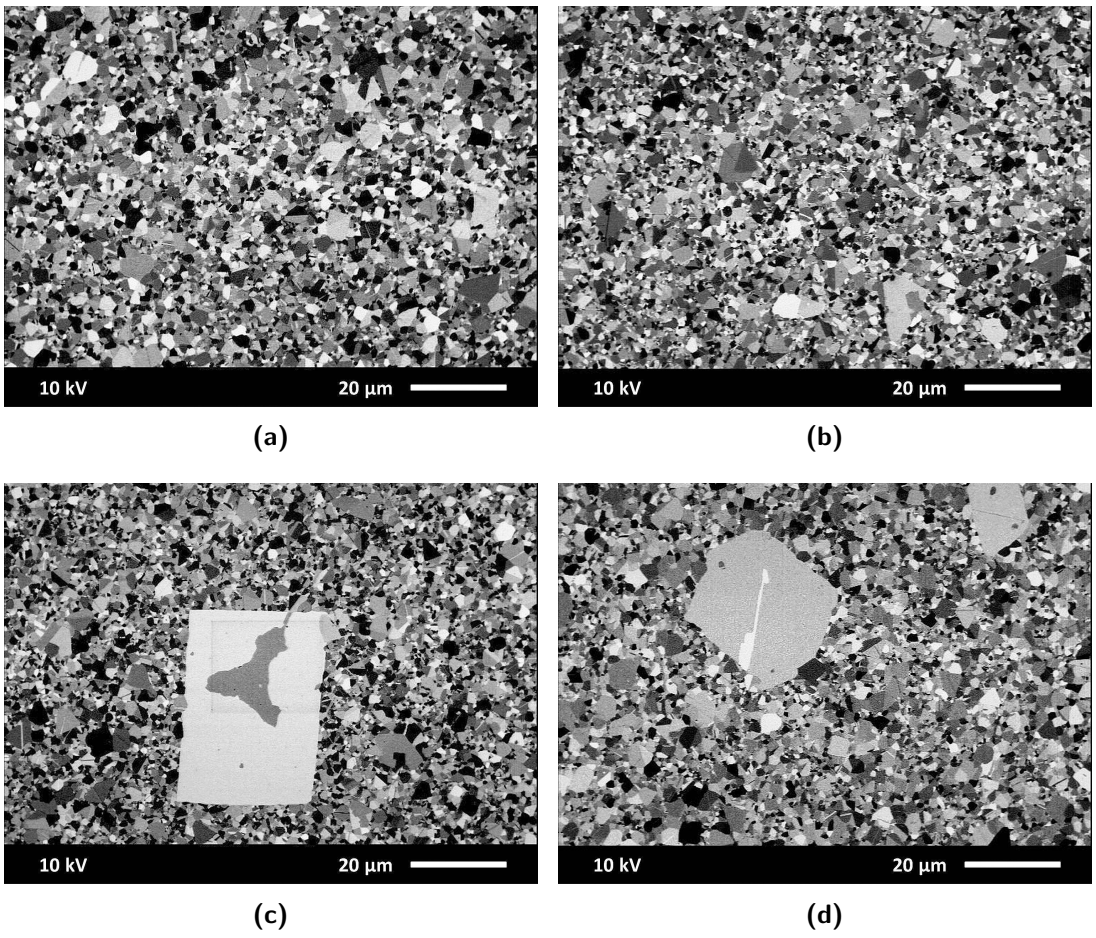

Figure 4.14.: Comparison of the microstructures of the annealed PED nickel at 500 °C for (a)(b) 20 min and (c)(d) 30 min, (a)(c) with and (b)(d) without a transition annealing at 250 °C.

sample	Annealing time (min)	volume fraction of coarse grains	mean grain size of coarse grains (μm)	mean grain size of fine grains (μm)	250 °C annealing
p1	20	5.37%	6.046	1.245	yes
p2	20	3.51%	6.287	1.185	no
p3	30	7.18%	6.075	1.244	no
p4	30	9.60%	6.860	1.252	yes
p5	60	13.54%	21.88	1.187	yes
p6	120	16.94%	33.06	1.463	yes
p7	180	35.84%	118.65	1.637	yes
p8	300	92.91%	125.87	1.611	yes

Table 4.3.: A summary of the heat treatments for PED NC nickel specimens from the plate No.74 annealed at 500 °C

PED plate 2

A second series of specimens cut from the PED NC plate No.90 were also annealed at 500 °C, with different annealing times. Abnormal grain growth was not observed until annealing the specimens after long time such as 240 min. Nevertheless, there were only very few abnormal growing grains, which were of extremely large grain size (figure 4.15a). The abnormal growing grains were also observed in the specimen annealed 360 min (figure 4.15b). Inasmuch as these observations, the abnormal grain growth was not a general phenomenon for this series of specimens.

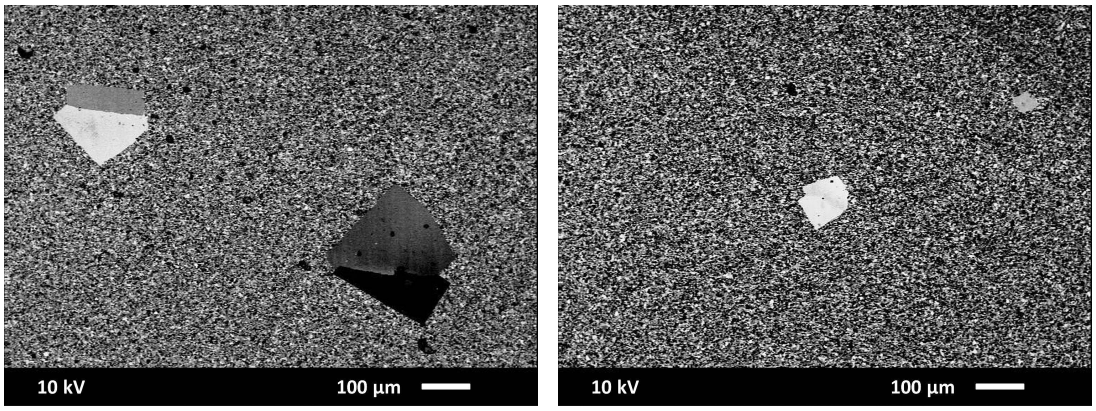

Figure 4.15.: Abnormal grain growth for samples cut from PED No.90 annealing for (a) 240 min and (b) 360 min.

During the heat treatment of these specimens, continuous grain growth was the main phenomenon. Surprisingly, the annealing time played a marginal role in the annealing process. It was because that it took relatively long time (40 min) to heat the specimens to 500°C. When there was no abnormal grain growth in the annealing process, the grain size of the normal growing grains depended only on the annealing temperature if there was enough time to finish the normal grain growth. The mean grain sizes were some larger than that in the fine grained areas for the specimens from the PED plate No.74 (figure 4.16). A summary of this series of specimens from the PED plate No.90 annealed at 500°C is listed in table 4.4.

In order to obtain better understanding to what happened in the annealing process, further analysis on the grain size and the grain size distribution was conducted. Figure 4.17 shows the mean grain size and their standard deviations for specimens with different annealing times. It can be seen that the grain size changes little with the annealing time. There is a special point marked with red square, which represents the

sample	Annealing time (min)	mean grain size (μm)	standard deviation (μm)	abnormal grain growth
p3	10	1.530	0.965	no
p3 (*)	10	1.801	1.191	no
p1	40	1.736	1.282	no
p6	60	1.840	1.245	no
p4	90	1.812	0.982	no
p9	240	1.870	1.070	very few abnormal growing grains
p5	360	1.920	1.223	very few abnormal growing grains

Table 4.4.: A summary of the heat treatments for PED NC nickel specimens from the plate No.90 annealed at 500 °C. (*) Data for the cross section of the specimen.

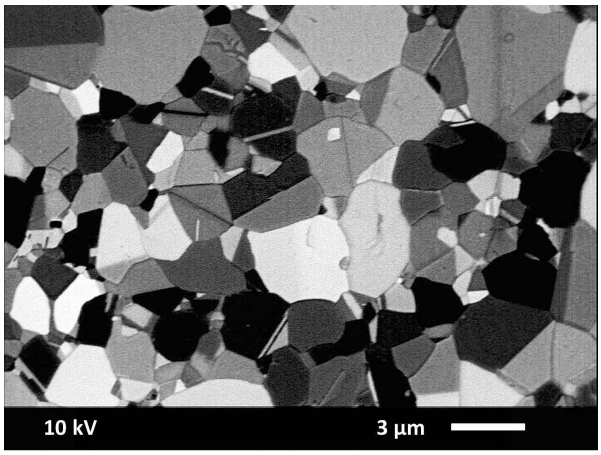

Figure 4.16.: Grain growth of the samples cut from PED No.90 annealed at 500 °C.

grain size from the cross section of the specimen annealed for 10 min. The mean grain size in the cross section is consistent with that in the surface. Actually there is a relatively broad distribution of the grain size, which is represented by the large error bars in the plot. A closer description of the grain size distribution is shown in figure 4.18. The standard distribution according to the grain size is calculated. The grain size obeys the Gauss distribution, which reflects the continuous grain growth during the annealing process. The mixture of all the curves indicates that there is little difference in the grain size and grain size distribution for the specimens annealed for different times.

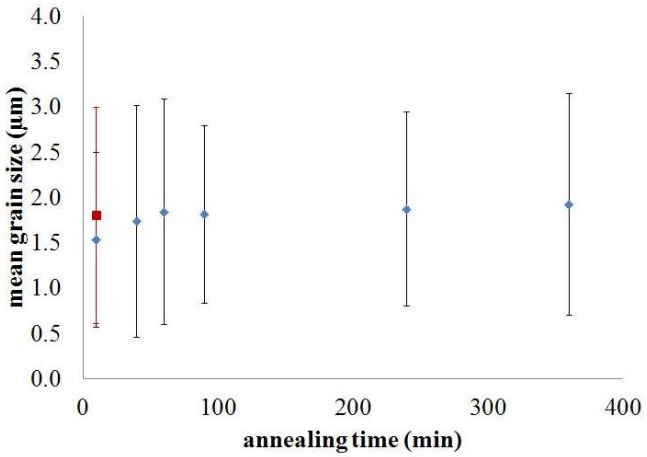

Figure 4.17.: Mean grain size with the standard deviation for samples with increasing annealing time.

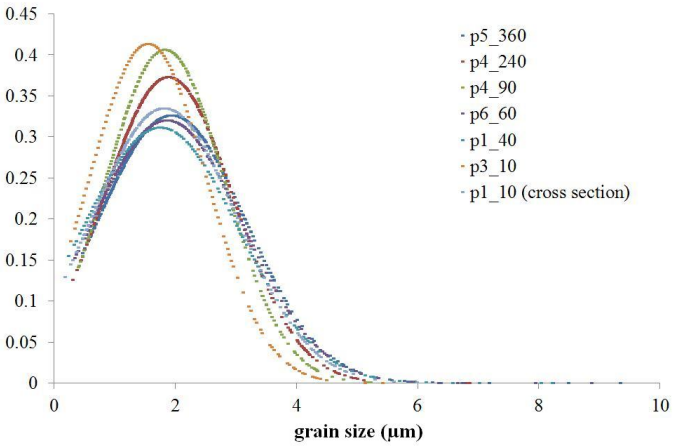

Figure 4.18.: Grain size distribution for samples with different annealing time, where the standard distribution according to the grain size was calculated.

4.3. Microhardness

Microhardness was measured for the PED and ECAP nickel with different microstructures, which had been achieved by appropriate heat treatments as shown in section 4.2. A summary of the microhardness to the as-received and heat-treated PED and ECAP nickel is listed in table 4.5.

sample	microstructure	microhardness (HV)
PED	monomodal NC	488
	bimodal NC/UFG	319
	monomodal UFG	286
	bimodal micron area	159 - 192
	bimodal CG area	91 - 96
ECAP	UFG (route C)	262
	UFG (route E)	258
	bimodal UFG area	229
	bimodal CG area	93

Table 4.5.: Microhardness of nickel specimens according to the microstructures and material processing methods. *The HV value for the bimodal PED NC/UFG nickel was measure from the specimen with the volume fraction about 50% for each phase.

The as-received PED NC nickel with the mean grain size about 30nm has the highest mean HV value of 488. The bimodal NC/UFG nickel, which is composed of nanograins and ultrafine grains with the volume fraction of about 50% for each phase, shows the microhardness about 319. It can be seen that this bimodal microstructure has the microhardness much closer to the monomodal UFG microstructure (HV 286) than to the monomodal NC microstructure (HV 488).

After heat treatment at 500 °C, different microstructures have developed for the specimens from the different PED plates. The specimens from the PED plate No.74 exhibit the bimodal microstructures combining the matrix grains ($\bar{d} > 1$ μm) and extremely coarse grains, while the specimens from the PED plate No.90 show only the monomodal grain size distribution ($\bar{d} > 1.5$ μm). Actually there are no UFG microstructures in these specimens. The values of the microhardness measurements show that these specimens exhibit no high strength anymore. Therefore, they are not further investigated with the fatigue experiments.

The microhardness values for the as-received ECAP UFG nickel are HV 262 for the route C specimens and HV 258 for the route E specimens. Upon the microstructural

analysis it has been found that the as-received ECAP UFG nickel has the similar mean grain size to the annealed PED UFG nickel, but there are totally different grain boundary properties and the inside dislocation densities. However, the microhardness values of these specimens are quite similar, depending only on the grain size.

After annealing the ECAP UFG nickel at 250 °C, the bimodal UFG/CG microstructures are obtained. The microhardness value of the UFG matrix areas is similar to that of the as-received ECAP UFG nickel. The microhardness value for the growing coarse grains is HV 93 which is similar to the abnormal growing coarse grains in the PED nickel.

4.4. Tensile tests

As the local microindentation tests could only qualitatively estimate the materials' strength, tensile tests were carried out to obtain the stress-strain relationship of the materials. However, as there were not enough PED nickel plates available, tensile tests were only performed to the ECAP nickel specimens at room temperature using a hydraulic testing machine with a strain rate of 10^{-2} s^{-1}.

Figure 4.19 shows the stress-strain curves for the ECAP nickel specimens with different microstructures. The as-received ECAP UFG nickel exhibits the highest strength, $\sim$ 700 MPa, both for route C and route E. Due to the high density of dislocations inside the grains, the ECAP UFG nickel shows little hardening effect, and necking was observed at about $2-3\%$ strain. The annealed specimen No.1, in which no grain growth was observed, exhibits a decreasing strength with little change in ductility. The annealed specimens (No.2, No.3 and No.4) are characterized with the bimodal microstructures, which are mixtures of ultrafine grains and coarse grains with different volume fractions. The specimen No.2 displays the strength comparable to the specimen No.1, but much improved ductility. With increasing volume fractions of the coarse grains, the ductility of the specimens No.3 and No.4 increases further but the strength decreases at the same time. The stress-strain curve for the CG nickel is also shown in the figure, for a comparison means. The tensile tests for the annealed specimen No.4 and the CG nickel were interrupted because the limitation for the displacement measurement of the testing machine was achieved, therefore, the curves are further extended with the dotted line.

It can be seen that the bimodal microstructure combines the strength and ductility of the material, where the small grains ensure the strength and the large grains provide the ductility. This is a method to search a compromise between the strength and ductility, because the increasing ductility sacrifices the strength, and vice versa.

The experimental data for the ECAP nickel are listed in table 4.6. There is difficulty to determine the yield strength and the uniform elongation for some specimens because of the data acquisition.

As there were no tensile tests conducted on the PED nickel, the experimental data in the literatures are used as reference. Table 4.7 shows the strength and ductility of the PED processed NC and UFG nickel by Hanlon [*Hanlon*, 2004] and Caveliere [*Cavaliere*, 2009], who both used the electrodeposited Ni foil of 99.9% purity from INTEGRAN^{TM} Corporation, Canada. It can bee seen that the PED NC nickel has the higher strength but relatively low ductility, and the PED UFG nickel shows the improved ductility but decreasing strength.

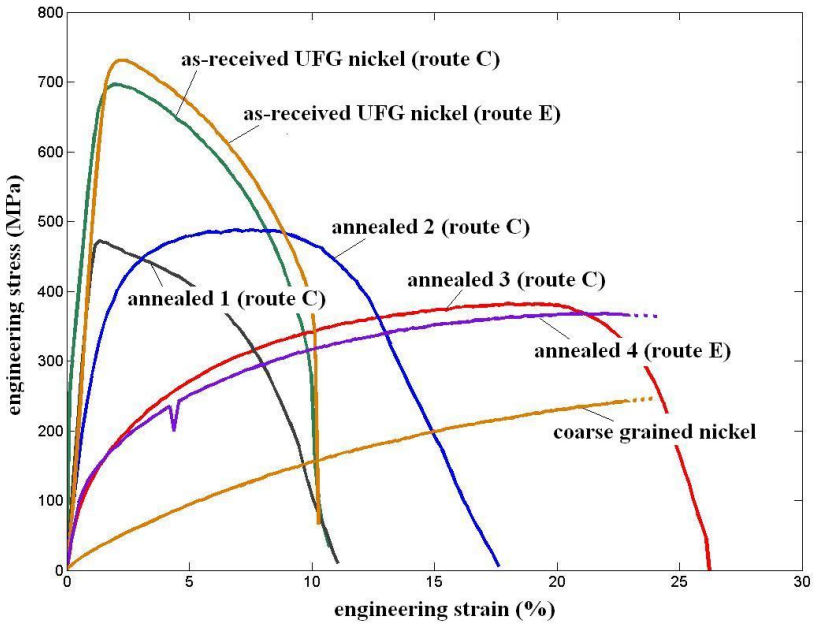

Figure 4.19.: Engineering stress-strain curves for the as-received ECAP UFG nickel and bimodal nickel with subsequent annealing.

sample	$\sigma_{0.2}$(MPa)	σ_{UTS}(MPa)	ϵ_{ue}	volume fraction of coarse grains (%)
UFG (route C)	680	700	2	0
UFG (route E)	700	730	2	0
UFG (annealed 1)	460	470	1.5	0
bimodal (annealed 2)	350	470	8 - 9	19.6 ± 7.0
bimodal (annealed 3)	100	380	20	39.4 ± 11.4
bimodal (annealed 4)	100	370	> 20	87.2 ± 2.8
CG	-	200	> 20	100

Table 4.6.: A list of yield strength $\sigma_{0.2}$, ultimate tensile strength σ_{UTS}, uniform elongation ϵ_{ue}, and volume fraction of coarse grains $\mathrm{X_V}$ for the samples in the tensile tests

material	grain size (nm)	$\sigma_{0.2}$ (MPa)	σ_{UTS} (MPa)	ϵ_{f}	refs.
NC nickel	20-40	930	–	3%	[*Hanlon*, 2004]
UFG nickel	300	525	–	10%	[*Hanlon*, 2004]
NC nickel	20	–	950	6%	[*Cavaliere*, 2009]
NC nickel	40	–	800	11%	[*Cavaliere*, 2009]
UFG nickel	270	–	500	15%	[*Cavaliere*, 2009]

Table 4.7.: Mechanical properties of the PED NC and UFG nickel. $\sigma_{0.2}$ is the 0.2% offset yield stress, σ_{UTS} is the ultimate tensile stress and ϵ_{f} is the strain to failure.

4.5. Fatigue experiments to different microstructures

Upon annealing the PED NC nickel and ECAP UFG nickel, we have received series of nickel specimens with different microstructures, i.e. different grain sizes and grain size distributions. Divided from the material processing, there are specimens originated from PED NC nickel with the microstructures from NC, NC/UFG, UFG to micron/CG, and specimens originated from ECAP UFG nickel with the microstructures UFG and UFG/CG. In-between, the UFG specimens from PED and ECAP have similar grain size but different grain boundary properties and dislocation densities inside the grains. In the last sections we know there is little difference in the microhardness of these two materials. However, how do these materials behave under cyclic loading, especially the crack resistance, is the main objective of the subsequent work.

4.5.1. PED NC, NC/UFG and UFG nickel with FIB microcracks

The fatigue experiments were conducted on the PED nickel specimens with different grain size distributions (NC, NC/UFG and UFG), in order to investigate the influence of the microstructures. The microcracks were initiated on the specimen surface, perpendicular to the loading direction. With this method, the fatigue crack resistance and crack growth rates of the different microstructures could be investigated. The microcracks, with the initial length of 100 μm, were introduced by FIB.

Actually, it was found in the pre-experiments that the PED nickel was very sensitive to the intrinsic imperfections, especially the micro-pores which had been introduced in the electrodeposition process. The specimens were fractured during the fatigue experiments due to the micro-pores with the scale about $300 - 500\mu$m, when the PED plates were not fully-dense prepared.

The microcracks propagated with increasing fatigue cycles and caused the ultimate fracture when they reached a critical crack length. Figure 4.20 shows the fracture surface of a NC nickel specimen. The specimen was cyclically loaded under the load-controlled mode with the equivalent stress amplitude of 400 MPa and loading ratio of $R = -1$ at a fatigue frequency of 2 Hz. The microcrack was not found to grow in the first 20,000 cycles. The specimen was fractured between $20,000$ and $30,000$ cycles, but no experimental data on the crack growth with increasing fatigue cycles had been recorded. Investigation of the fracture surface, which was perpendicular to the loading direction, revealed that the microcrack propagated along the initial crack direction at first (marked between the red line in figure 4.20a) and then the ultimate fracture

happened. Figure 4.20b shows clearly that the semicircular microcrack propagates 2-dimensionally along its radius on the fracture surface. However, there is no detailed information about the crack growth length with increasing fatigue cycles. Therefore, more carefully controlled experiments should be performed.

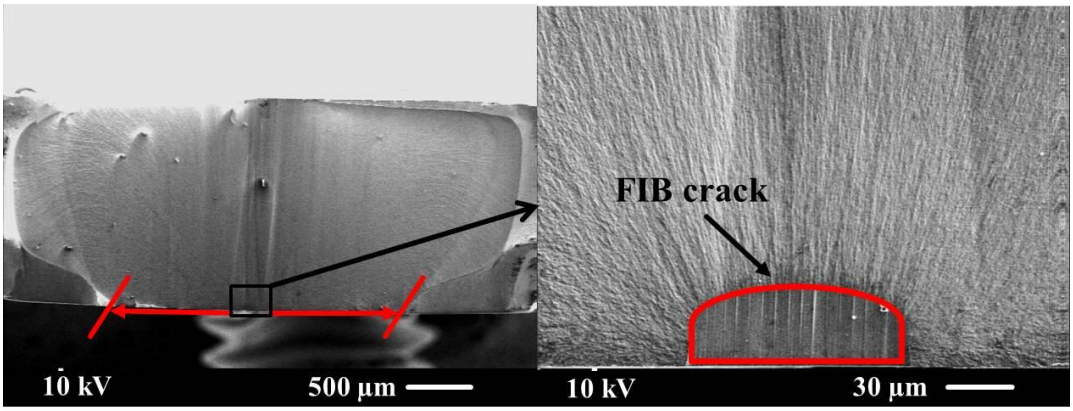

Figure 4.20.: (a) Fracture surface of the NC nickel specimen under 400 MPa, in which the stable crack growth is marked by the red arrowed line. (b) Crack growth starts from the FIB crack, propagating 2-dimensionally along the fracture surface.

Fatigue experiments with increasing stress amplitudes have been designed in which the nickel specimens were loaded from the lower stress amplitude. The specimens with different microstructures were investigated, starting with the same stress amplitude. For each stress, 100,000 fatigue cycles were planed. When there was no crack growth under a given stress after 100,000 cycles, the higher stress would be applied in the further fatigue cycles. The loading ratio was $R = -1$ and the load frequency was 2 Hz. The loading histories for the different microstructural specimens are shown in figure 4.21.

There was no crack propagation under 200 MPa and 250 MPa for all the NC, NC/UFG and UFG nickel specimens. The microcracks began to grow under 300 MPa for both the NC and UFG nickel specimens, and the ultimate fracture happened after $\sim 102,000$ and $\sim 87,000$ cycles for the two microstructures, respectively. Meanwhile, there was no crack growth detected in the bimodal NC/UFG nickel specimen after $100,000$ cycles under 300MPa. The bimodal NC/UFG nickel specimen was loaded under 350 MPa for 200,000 cycles. It was because the microcrack was observed to have propagated after $100,000$ cycles under this amplitude. However, there was no further propagation of the microcrack for the next $100,000$ cycles (figure 4.22). Therefore, the specimen was loaded under the higher stress of 400 MPa further and fractured after $\sim 45,000$ cycles. A summary of the loading history for these specimens is listed in table 4.8.

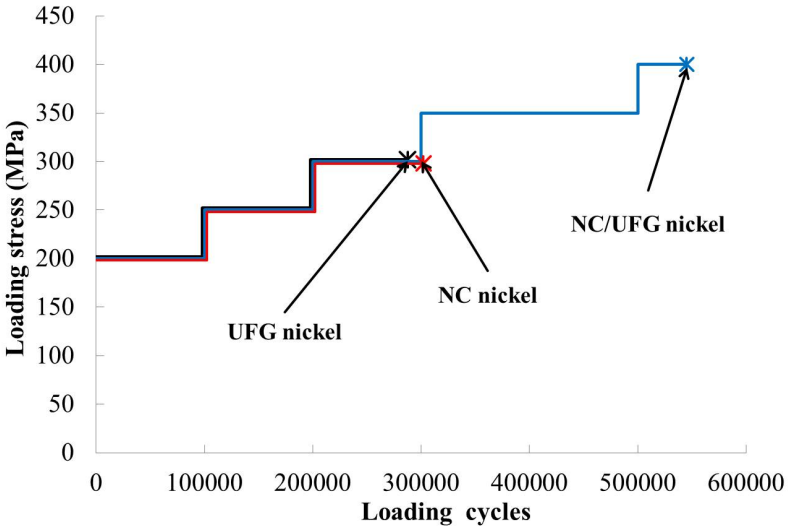

Figure 4.21.: Loading history of pre-cracked PED nickel with different microstructures.

stress amplitude	Microstructure		
	NC	UFG	NC/UFG
200 MPa	100,000 cycles no crack growth	100,000 cycles no crack growth	100,000 cycles no crack growth
250 MPa	100,000 cycles, crack tip $\sim 3\mu$m growth	100,000 cycles, crack tip $\sim 5\mu$m growth	100,000 cycles no crack growth
300 MPa	$\sim$ 102,000 cycles fractured	$\sim$ 87,000 cycles fractured	100,000 cycles no crack growth
350 MPa			200,000 cycles, crack tip 7 $\sim 8\mu$m growth
400 MPa			$\sim$ 45,000 cycles fractured

Table 4.8.: A summary of the loading history of the PED nickel with different microstructures

The cracks propagated along the initial crack direction which was perpendicular to the loading direction. The NC nickel had the highest strength and there was a long stable crack growth stage for the NC nickel specimen. Figure 4.23 shows the overview of the crack growth of a NC nickel specimen. The microcrack propagated steadily along the initial direction and deviated from this direction when the crack length was large. When the crack was long, it could not propagate steadily anymore and fracture happened. Observation of the fracture surfaces for the different microstructures shows more detailed information about the crack propagation process (figure 4.24).

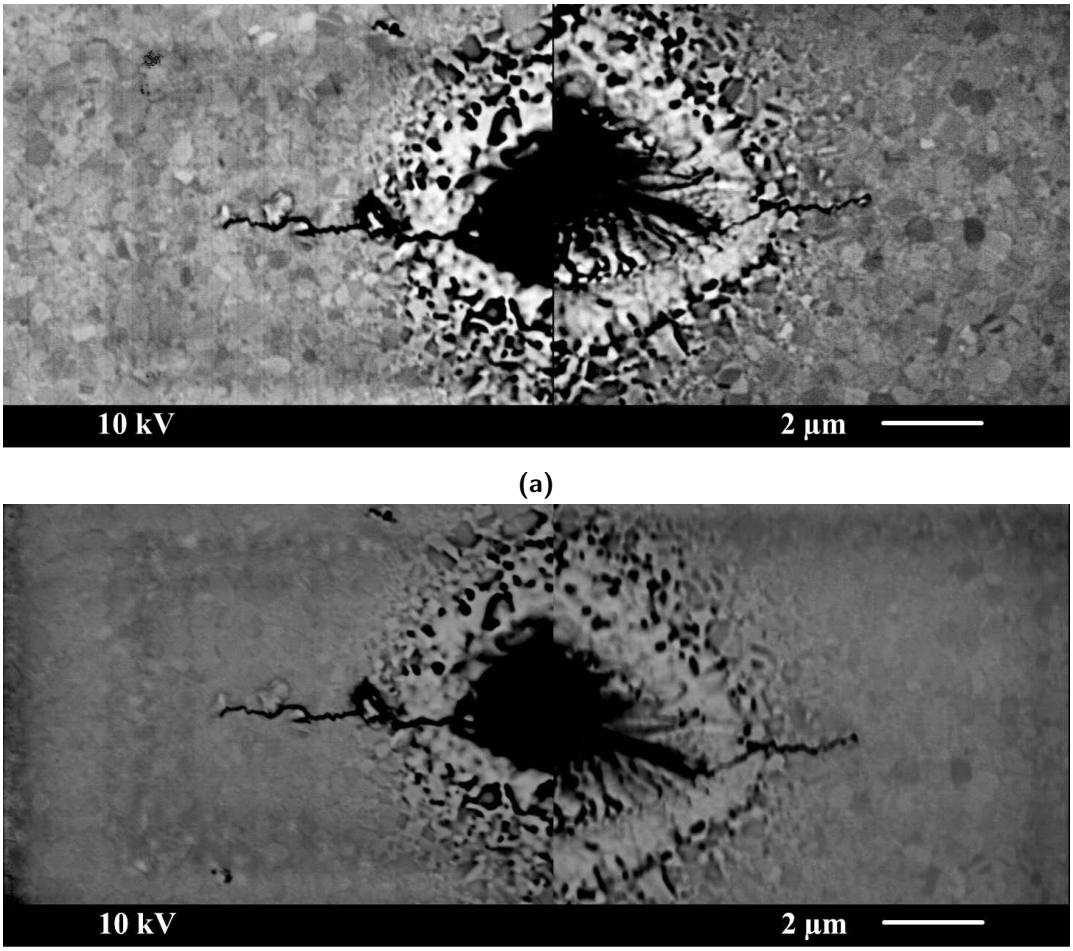

Figure 4.22.: SEM images of the crack tip of in the bimodal NC/UFG nickel under 350 MPa after (a) 100,000 cycles and (b) 200,000 cycles. There was no crack propagation in the second 100,000 cycles under 350 MPa for the bimodal NC/UFG nickel.

Figure 4.24a shows the fracture surface of the NC nickel specimen. Comparing to the fracture surface in figure 4.20, they are quite similar. However, more detailed information about the crack propagation has been gathered in this specimen. The 2-dimensional crack-front is clearly indicated by the traces in the fracture surface. Figure 4.24b shows the fracture surface of the bimodal NC/UFG nickel specimen. There is a clear boundary between the stable crack growth area and the unstable fracture. Figure 4.24c shows the fracture surface of the PED UFG nickel specimen. The fracture surface seems to be a mixture of the brittle fracture and ductile fracture.

It was found that when the specimens with different microstructures were identically prepared, the microcrack in the bimodal NC/UFG nickel began to grow under the higher stress amplitudes. It indicates that the bimodal NC/UFG nickel has higher

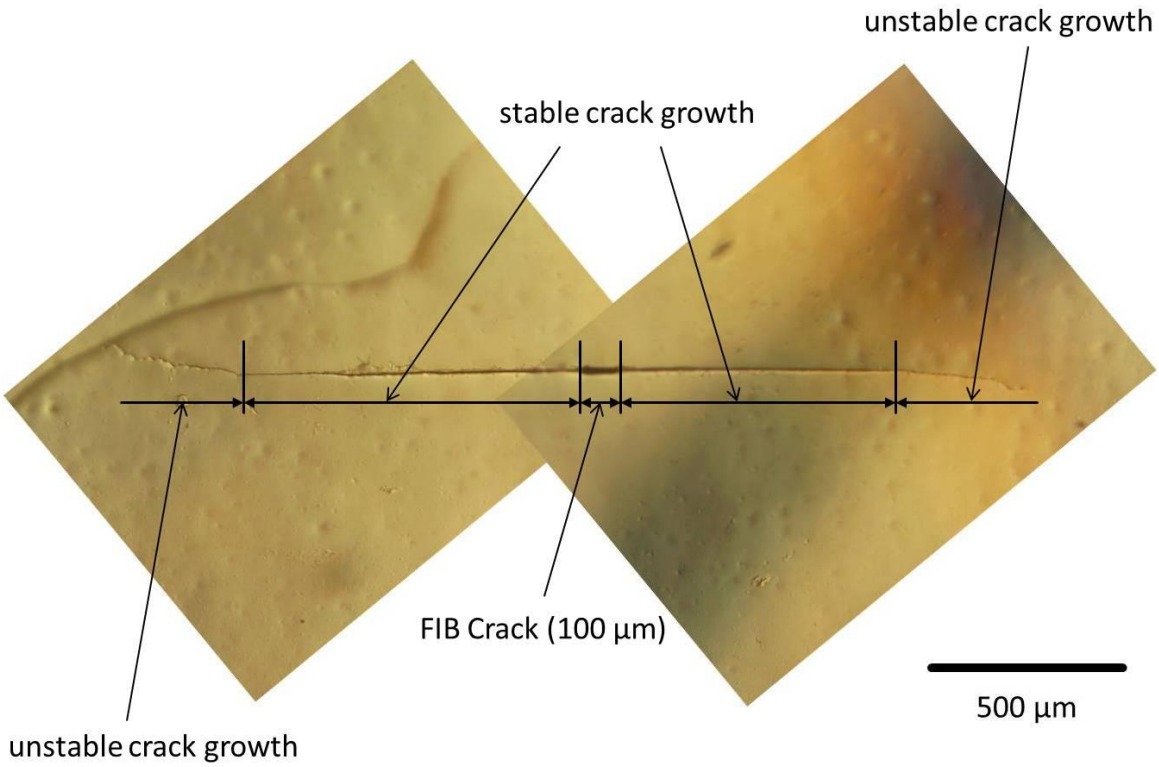

Figure 4.23.: Overview of the surface microcrack growth of the as-received PED NC nickel.

crack resistance than the monomodal NC or UFG nickel. Therefore, developing the bimodal NC/UFG microstructure which is the mixture of the nanograins and ultrafine grains is an effective method to improve the fatigue performance of the fine grained materials.

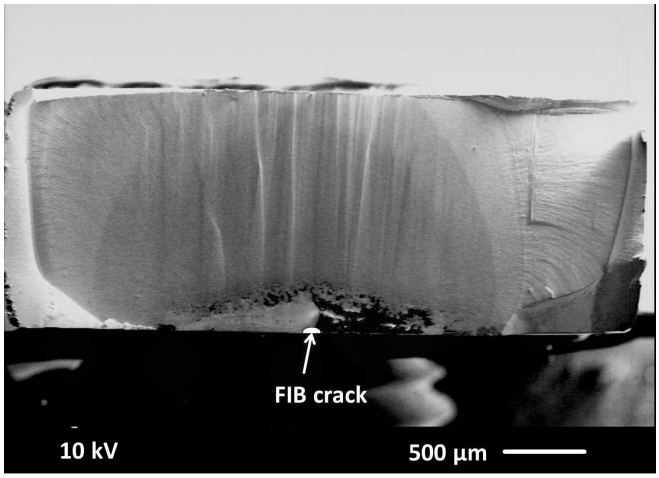

(a)

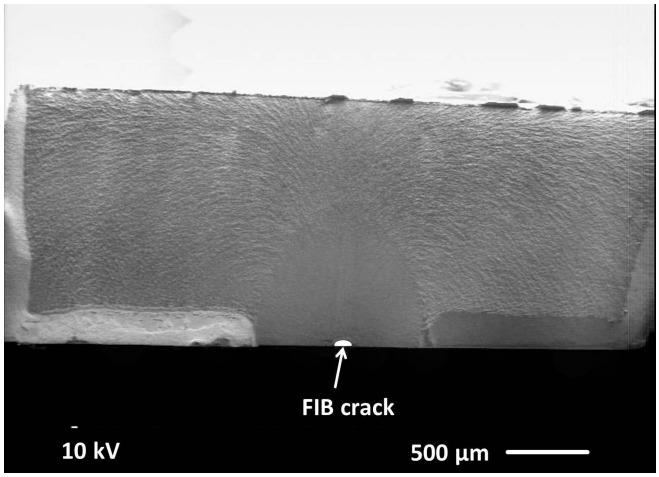

(b)

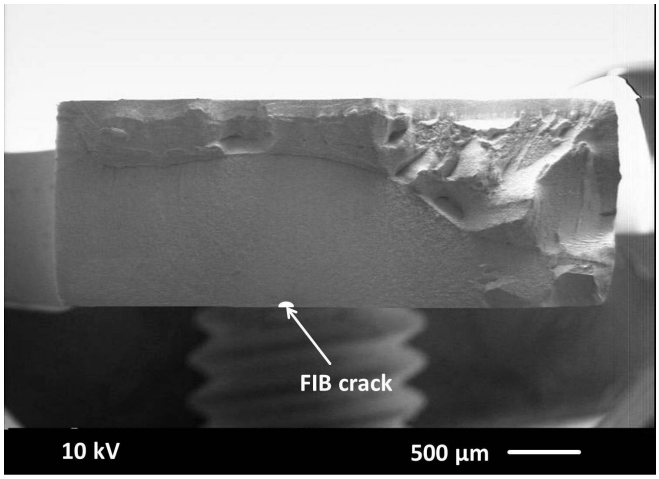

(c)

Figure 4.24.: Overview of the crack surface for different microstructures from PED nickel. (a) as-received NC nickel, (b) bimodal NC/UFG nickel and (c) UFG nickel.

4.5.2. In-situ fatigue experiment of the bimodal PED NC/UFG nickel

It has been shown in the last section that the bimodal NC/UFG nickel exhibits the improved fatigue crack resistance. To understand how the nanograins and the ultrafine grains in the bimodal microstructure influence the crack growth during the fatigue loading, an in-situ fatigue experiment was performed with the bimodal NC/UFG nickel. The specimen had been firstly loaded in an ex-situ fatigue experiment for 70,000 cycles and there was a total crack length of $\sim 500\ \mu$m. The loading history of the in-situ fatigue experiment is shown in figure 4.25. The specimen was loaded with increasing stress amplitudes with the loading ratio of R = −1. When there was no crack growth observed under a stress amplitude after the designed fatigue cycles, a higher stress amplitude was applied. Besides, the specimen was also then loaded with the loading ratio of R = 0.1, to investigate the influence of the loading ratios to the crack propagation.

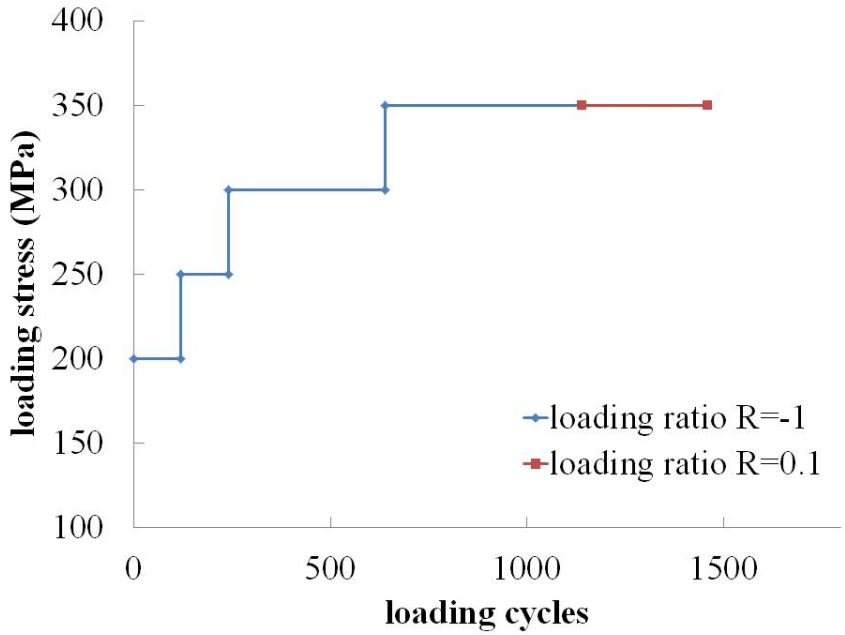

Figure 4.25.: Loading history of the in-situ fatigue test for the bimodal NC/UFG nickel. The blue line shows the fatigue loading with R=-1 and the red line shows the loading with R=0.1.

It was found that the crack didn't propagate under the loading stress from 200 MPa to 300 MPa. The crack began to grow until the loading stress was increased to 350 MPa, which was the same as the loading stress in the ex-situ fatigue experiment. It was

estimated that the crack would propagate under a higher stress intensity factor because the in-situ fatigue experiment was conducted in vacuum. The crack propagated with increasing loading cycles and the crack growth behaviour at one crack tip is shown in figure 4.26 for the loading ratio R = −1 and in figure 4.27 for the loading ratio R = 0.1. More information about the in-situ crack propagation at the other crack tip is shown in Appendix C.

Although the crack propagated under both loading ratios in the in-situ cyclic loading, there was some difference in the crack propagation behaviour. The deformed area was smaller under R = −1 where alternative tension and compression were applied to the specimen than that of R = 0.1 where the specimen was loaded only under tension. However, there was contamination from the pump oil in the SEM chamber. A layer of carbon film formed with increasing exposing time in SEM, which prevented further observation of the crack propagation. However, the deformed area around crack tip is clearly demonstrated after the plasma cleaning of the specimen surface (figure 5.29).

4.5.3. ECAP UFG nickel with FIB microcracks

The fatigue performance of the as-received ECAP UFG nickel, both route C and route E, has been investigated. Based on the detailed characterization of the microstructures it is known that the grain size in the ECAP nickel specimens is about 300 − 400 nm after the ECAP process but there are strong microtextures and high density dislocations inside the grains. The dislocation density has not measured directly in this work, but it is an inevitable consequence after the severe plastic deformation during the ECAP process and also has been proved in the literatures [*Zhao et al.*, 2004; *Murata et al.*, 2008; *Reihanian et al.*, 2008; *Janecek et al.*, 2012].

Artificial FIB microcracks with the lengths of 40 μm and 100 μm were introduced on the specimen surface. The load-controlled mode with the loading ratio R = −1 was applied in the fatigue experiments when not specially emphasized. The smooth specimens with the surface microcracks were loaded under different stress amplitudes.

The microcracks was found to grow with the increasing fatigue cycles, however, the specimens were fractured not because of the crack propagation. A sudden fracture happened always after certain number of fatigue cycles. A Wöhler curve is plotted for the different specimens and shown in figure 4.28. It is maybe not exactly suitable to use the data according to the testing specimens with microcracks on the surface. However, the specimens are fractured not because of these microcracks. As the applied stress amplitudes (max. 500 MPa) were below the yield strength of the ECAP UFG nickel,

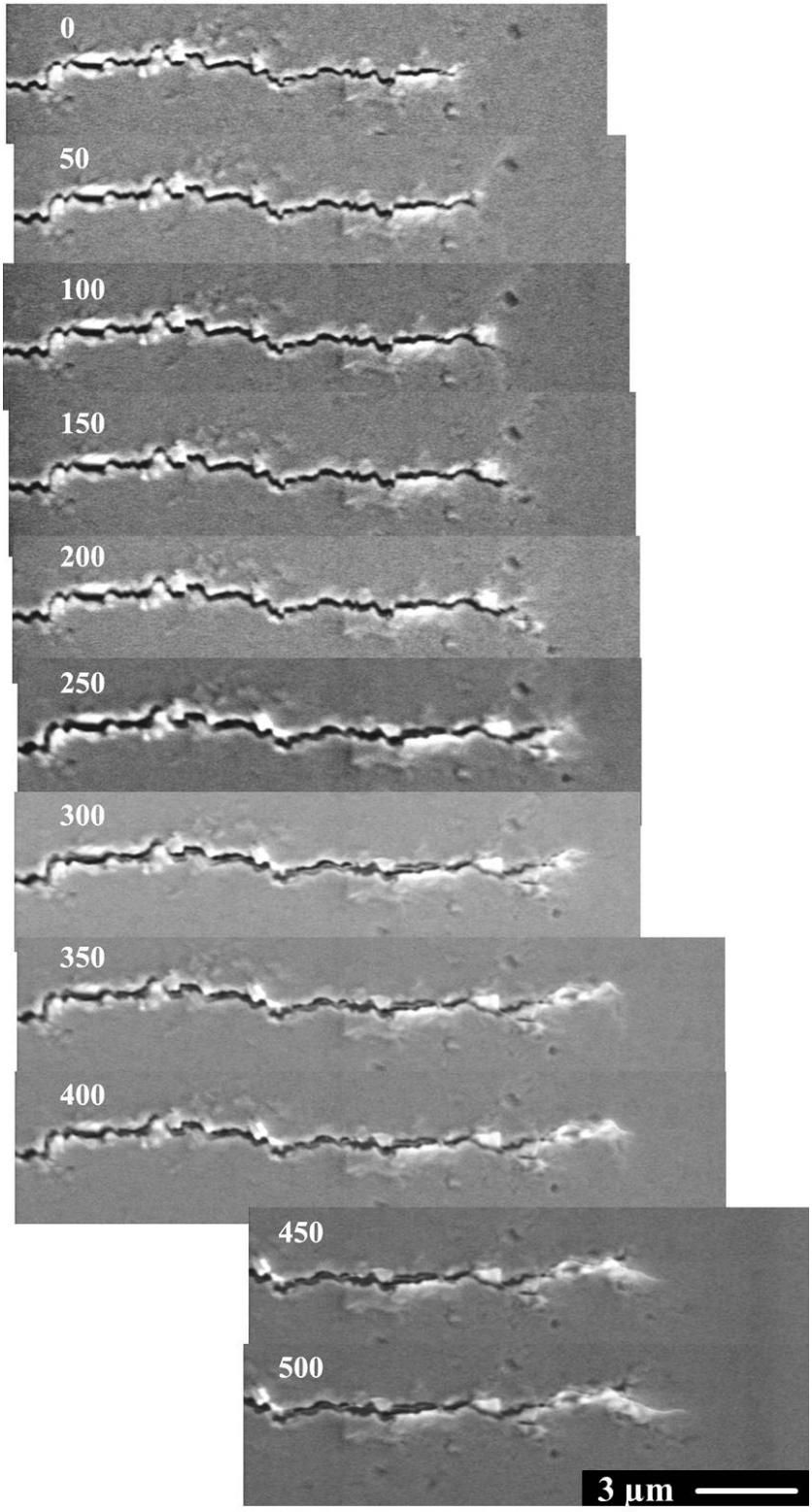

Figure 4.26.: In-situ crack propagation with increasing fatigue cycles under 350 MPa with R = −1.

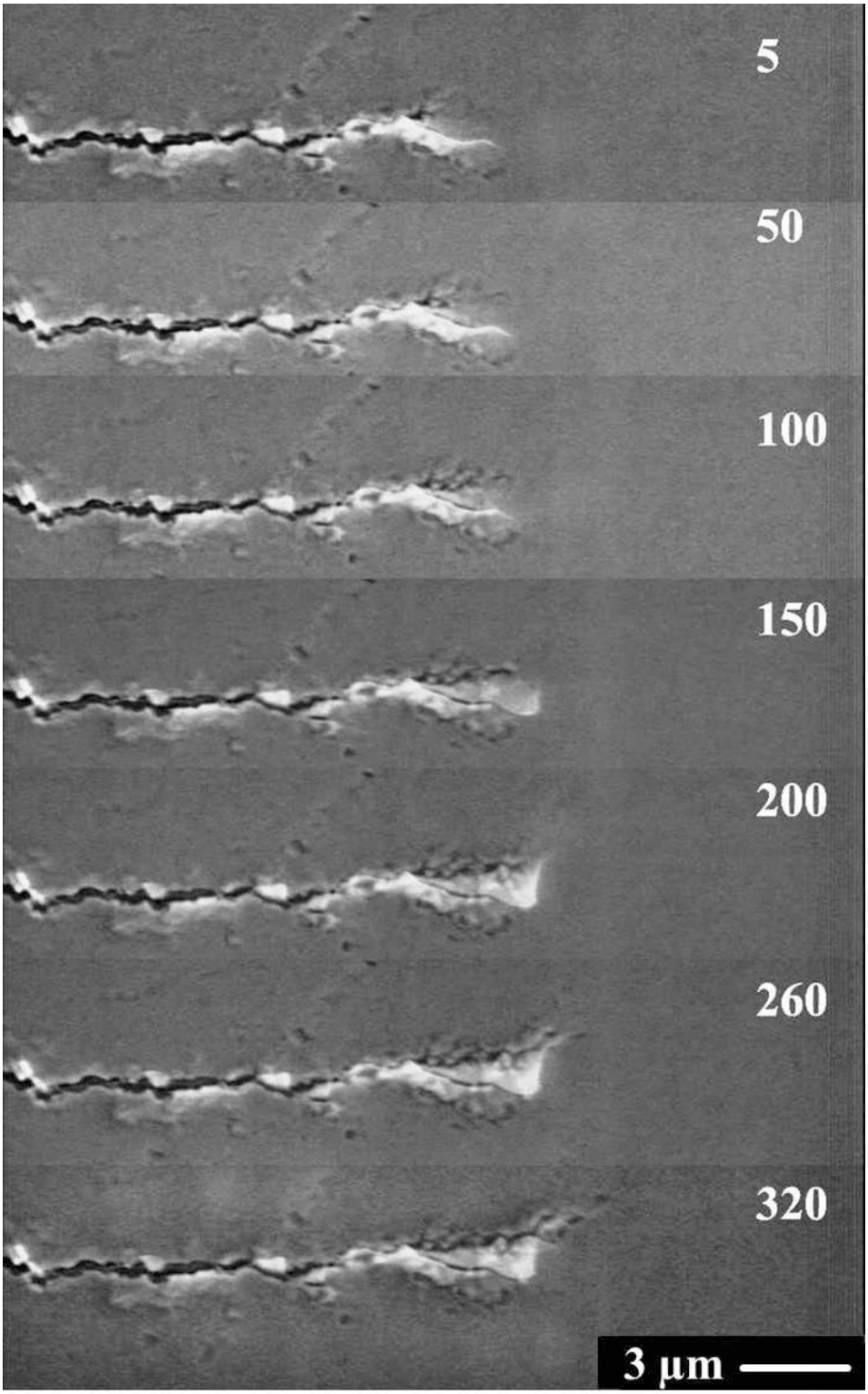

Figure 4.27.: In-situ crack propagation with increasing fatigue cycles under 350 MPa with R = 0.1.

there was nominally only elastic deformation during the cyclic loading. Therefore, the fatigue life of the as-received ECAP UFG nickel, both route C and route E, follows well the tendency in the high cycle fatigue (HCF) range in the Woehler curve. It is known that the Wöhler curve in the HCF range can be described by the Basquin equation:

$$\frac{\Delta\sigma}{2} = \sigma'_f(2N_f)^b \tag{4.1}$$

where the σ'_{f} is the fatigue strength coefficient which corresponds often to monotonic fracture strength, with a fairly good accuracy, and b is the fatigue strength exponent or Basquin exponent which, for most metals, is in the range of -0.05 to -0.12 [*Suresh*, 1998]. According to the experimental data, σ'_{f} equals 1445 MPa and b is -0.1259. Taking $\sigma_{\mathrm{f}} = 715$ MPa from the tensile tests, there is relatively large difference between the fatigue strength coefficient and the monotonic fracture strength. Such difference has also been reported by some other author for different UFG metals [*Vinogradov et al.*, 2003a; *Lukas et al.*, 2007; *Wang et al.*, 2008a]. Analyzing the Basquin equation, the higher calculated fatigue strength coefficient σ'_{f}, instead of the monotonic fracture strength σ_{f}, is corresponding to the increasing fatigue life when the same $\Delta\sigma/2$ and Basquin exponent are used. This result is consistent with the literatures that the NC and UFG materials show an improved fatigue resistance to their CG counterparts in stress-controlled HCF tests [*Agnew et al.*, 1999; *Vinogradov et al.*, 2001; *Hoeppel et al.*, 2002, 2006; *Goto et al.*, 2008, 2009]. There are also measuring points for the CG nickel and the bimodal UFG/CG nickel shown in the plot. It can be seen that the CG nickel specimen has a considerably low fatigue life comparing to the UFG nickel under the load controlled fatigue experiments. The measuring points for the bimodal UFG/CG nickel specimens lie on the tendency line, but the specimens have not fractured after one million cycles.

Although the microcracks did not growth to a critical length, inducing the ultimate fracture, they were found to propagate with increasing loading cycles during the fatigue experiments. The initial microcracks by FIB were with different orientations, i.e. vertical to the loading direction, and with 45° or −45° angles to the loading direction (figure 3.8).

It was found that the unique microstructures formed in the ECAP process showed significant influence to the crack propagations. For route C the ECAP billets were rotated by 180° between each pass, and there was only one main shear direction during the ECAP process. Although the FIB microcracks had different initial orientations, they all propagated along the bands of the elongated grains which was actually along

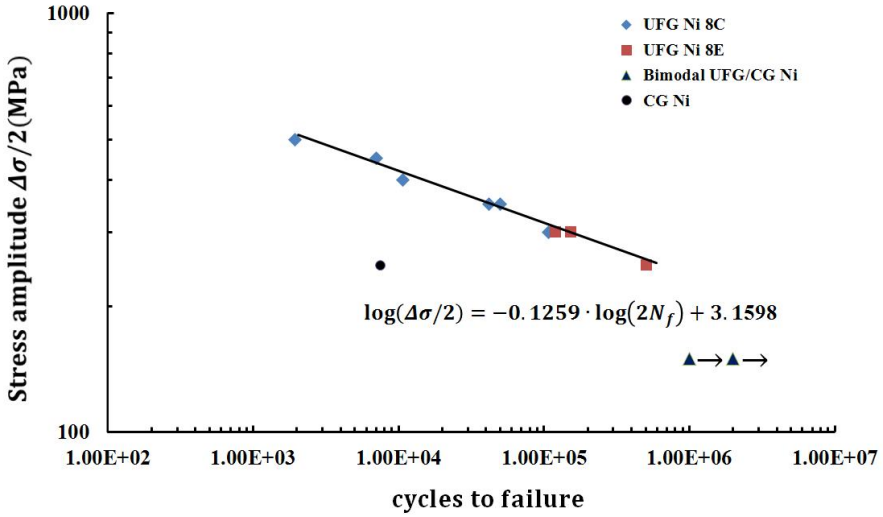

Figure 4.28.: Woehler curve for the ECAP UFG nickel specimens, with reference points of CG nickel specimen and bimodal nickel specimen.

the shear direction in the ECAP pass (figure 4.29). The crack propagation was quite different to that in the UFG nickel specimens annealed from PED NC nickel where the crack propagated vertical to the loading direction during the fatigue experiments.

The ECAP billet processed by route E was rotated by a combination of 180°, 90°, 180° and 270°, four passes as a circle. It is shown in the microstructural characterization in section 4.1 that the microstructure of the route E specimen is more complicated than that of the route C specimen, because there are mixed areas of elongated grains and homogeneous equiaxed grains (figure 4.2). Therefore, the microcracks also propagated in a more complicated manner comparing to the route C specimens, depending on the microstructures around the crack tip. When there were the elongated grains around the crack tip, the microcracks propagated similar to the route C specimens as shown in figure 4.29 . However, when the microstructure around the crack tip was relatively homogeneous, the FIB cracks propagated along the direction perpendicular to the loading direction which was similar to the PED UFG nickel, shown in figure 4.30.

Nucleation of new cracks in the specimen surface was found to the main cause for the fracture of ECAP UFG nickel. Figure 4.31 reveals the well-developed fatigue markings which are shear bands along the direction of the elongated grains. However, the length and distance of the shear bands are much larger than the average grain size of the ECAP UFG nickel. Shear bands formed during the cyclic loading due to the strain localization. When they reached a critical length, fracture happened.

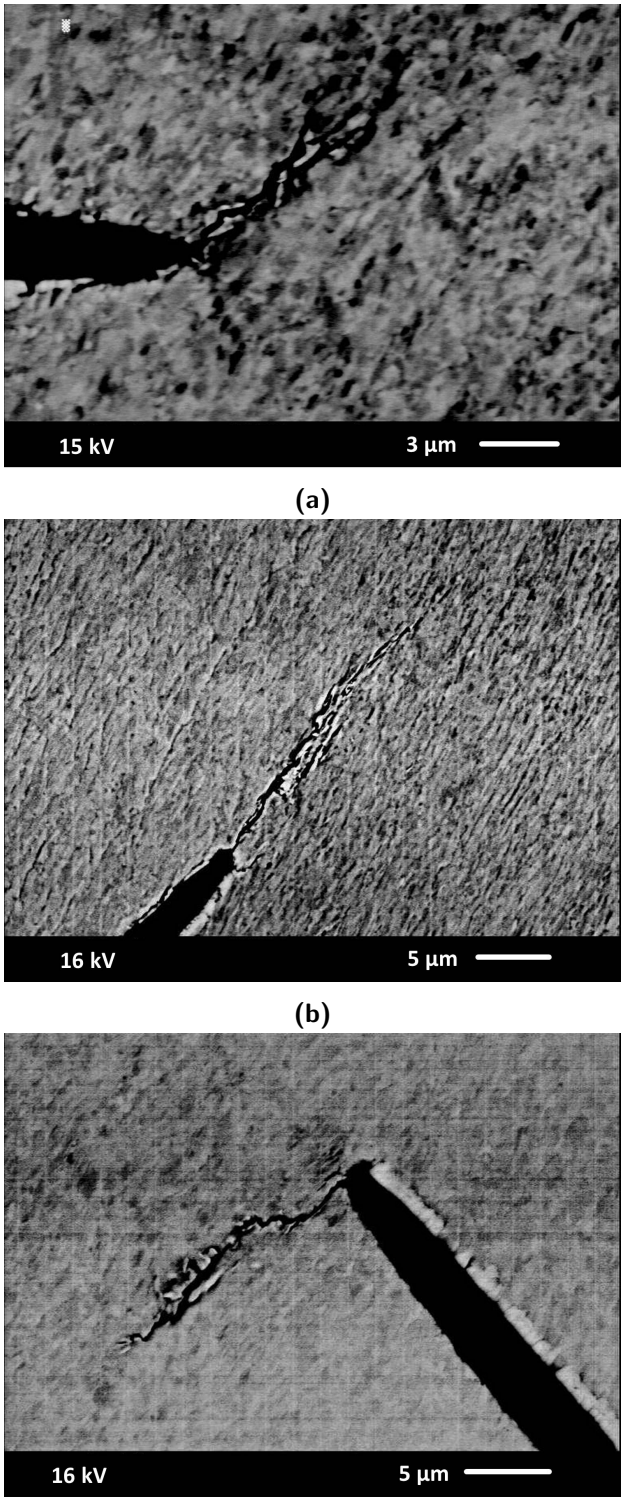

Figure 4.29.: Propagation of the FIB cracks with different initial orientations during the fatigue loading.

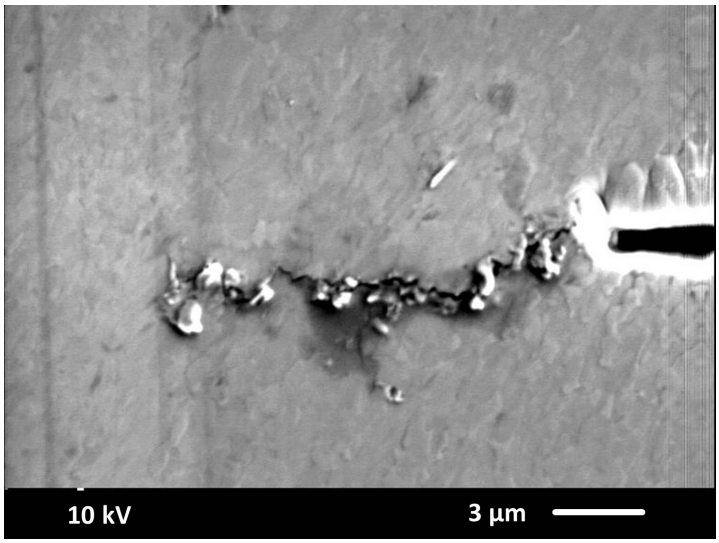

(a)

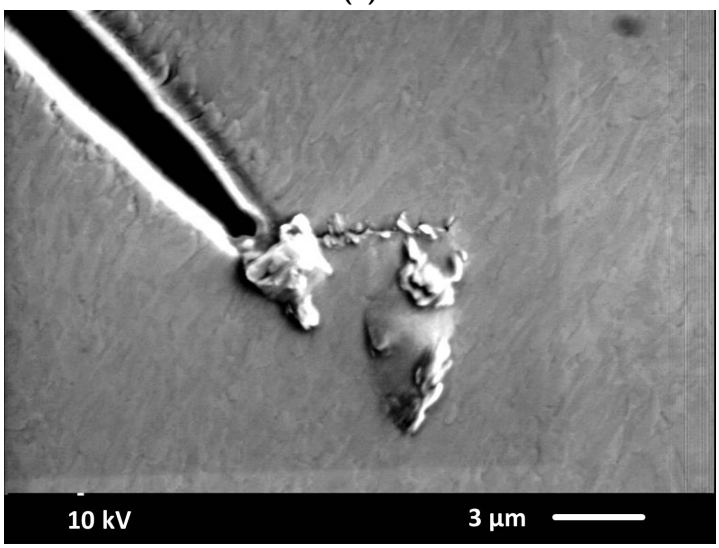

(b)

Figure 4.30.: Microcracks propagated perpendicular to the loading direction in the 8E ECAP specimen where the microstructures are relatively homogeneous, although the initial cracks have different orientations.

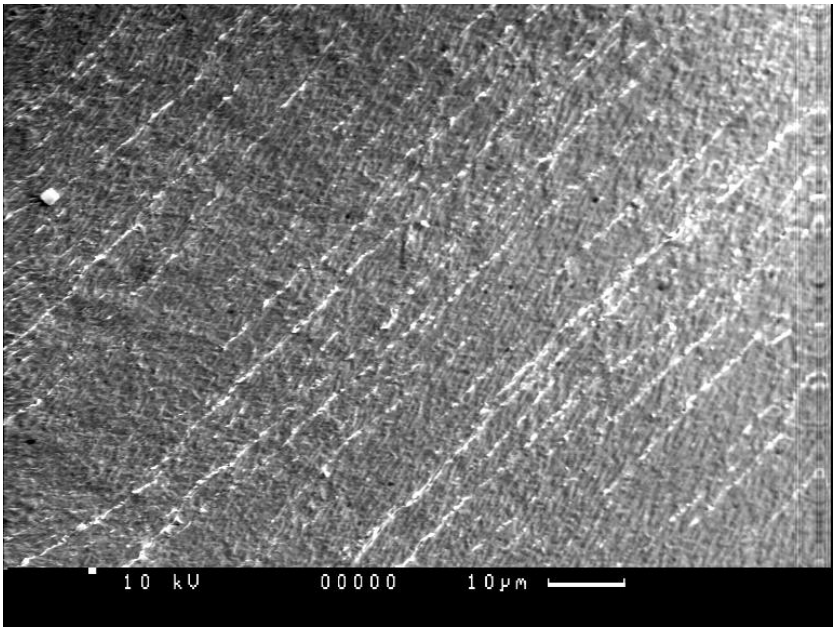

(a)

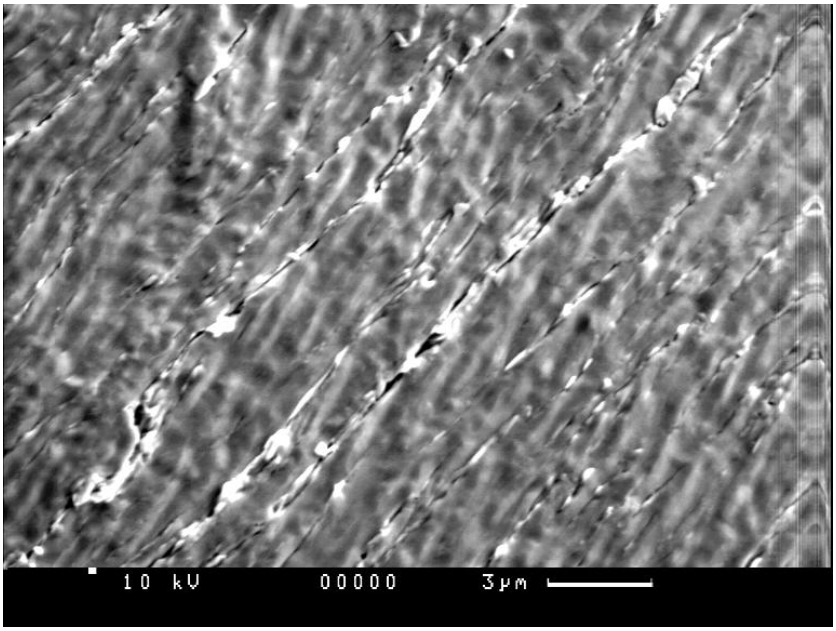

(b)

Figure 4.31.: Surface shear bands of the cyclic deformed ECAP UFG nickel.

4.5.4. ECAP UFG nickel with macro-notches

Because the microcracks initiated by FIB did not grow to the critical length inducing the ultimate fracture, the macro-notches were introduced in the ECAP nickel specimens, in order to investigate the crack growth and fracture behaviour of the ECAP nickel.

The first method to initiate macro-notches was by wire spark erosion to introduce the macro-notch at one edge of the specimen (Mode I Notch). In figure 4.33 a macro-notch with an initial length about 700 μm was initiated at the specimen edge for a route E specimen. The notch was sharpened with surgical blade. The specimen was then loaded cyclically under a displacement-controlled mode with amplitude $\mathrm{d} = 0.037\,\mathrm{mm}$, which was equivalent to $\epsilon = 2 \times 10^{-3}$, and $\mathrm{R} = -1$. The notch was firstly found to grow after $12,000$ cycles and then propagated further with increasing loading cycles until the fracture happened. The crack growth length is plotted with the fatigue cycles as shown in figure 4.32. It can be found that the crack propagates with an accelerated growth rate with increasing crack length under the constant strain.

The microstructure of the ECAP nickel by route E is characterized as the mixed areas of directional elongated grains and homogeneous equiaxed grains. The crack tip propagates through the different areas either preferably along the direction of the elongated grains or perpendicular to the loading direction which has been shown by the microcracks in section 4.5.3. Figure 4.33a exhibits the overview of the crack propagation in which the crack length is over 60% of the specimen width. The crack growth direction is inclined against the direction perpendicular to the loading direction, showing more significant geometry effect of the macro-notches. There is increasing plastic deformation influenced areas around the crack tip with the increasing crack length, upon observation of the surface profile around the crack growth path (figure 4.33b).

The macro-notches were also initiated with vertical spark erosion in the middle of the ECAP specimens (Mode II Notch), with the length from 500 μm to 1000 μm. One tip of the notches was further sharpened with FIB. Then the notched specimens were loaded in load-controlled mode with the equivalent stress amplitude of 200 MPa and loading ratio $\mathrm{R} = -1$. It was found that the sharped crack tip by FIB began to propagate earlier, because of the high stress concentration. Analyzing the crack growth behaviour it was quite similar to the specimen with the notch at one side, i.e. the crack propagated with an accelerated growth rate with increasing crack length under the constant load.

Figure 4.34 shows the crack growth after $40,000$ cycles for a route C specimen with the initial notch length 1000 μm. The first crack growth was observed after $5,000$ cycles for the right sharpened notch tip, and after $10,000$ cycles for the left notch tip. The

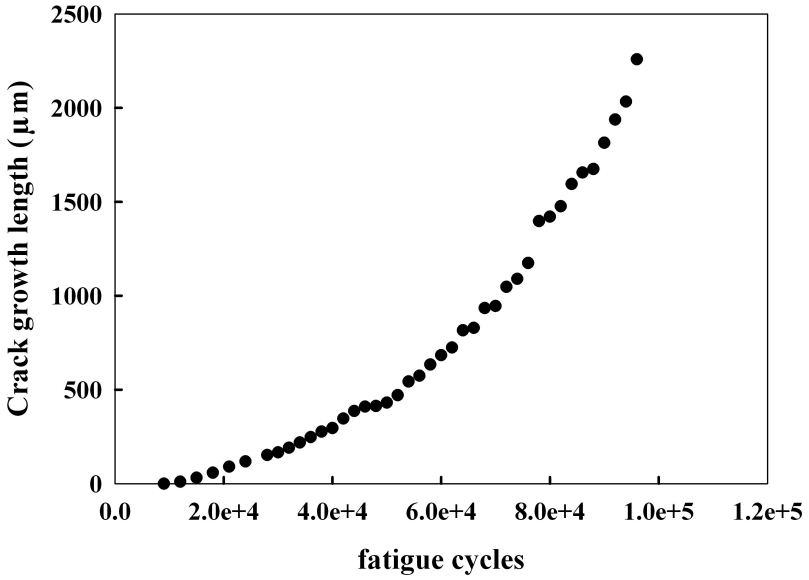

Figure 4.32.: Experimental data for the crack growth length with the fatigue cycles for the macro-notched specimen.

initial propagation directions for the two crack tips were different. The left crack tip propagation was mainly influenced by the microstructure and was along the direction of the elongated grains. There was additional influence from the crack geometry for the right crack tip and the crack propagated inclining perpendicular to the loading direction. However, with increasing crack length the propagation directions of the two tips approached to to the same direction, i.e. along the elongated grains, indicating that the influence of the microstructures became predominant. Surface shear bands along the direction of the elongated grains, which were caused by the strain localization, were also found along the crack growth path, as shown in figure 4.34. Comparing to the smooth specimens or specimens with microcracks in which formation of the surface shear bands was the causing for the ultimate fracture, propagation of the micro-notches was the reason for the fracture of the notched specimens.

Microstructural analysis of the fatigue specimens revealed that grain coarsening, i.e. dynamic recrystallization was the micromechanism responsible to the plastic deformation during the fatigue experiments. Figure 4.35 shows a backscattered image around the crack growth path for a Mode I Notched specimen. Comparing the areas above and below the marked line there are two areas with different grain sizes. The grains stay stable like the as-received ECAP grains above the line, with elongated grains. Figure 4.34 shows the dynamic recrystallization occurring around the crack tip for a Mode

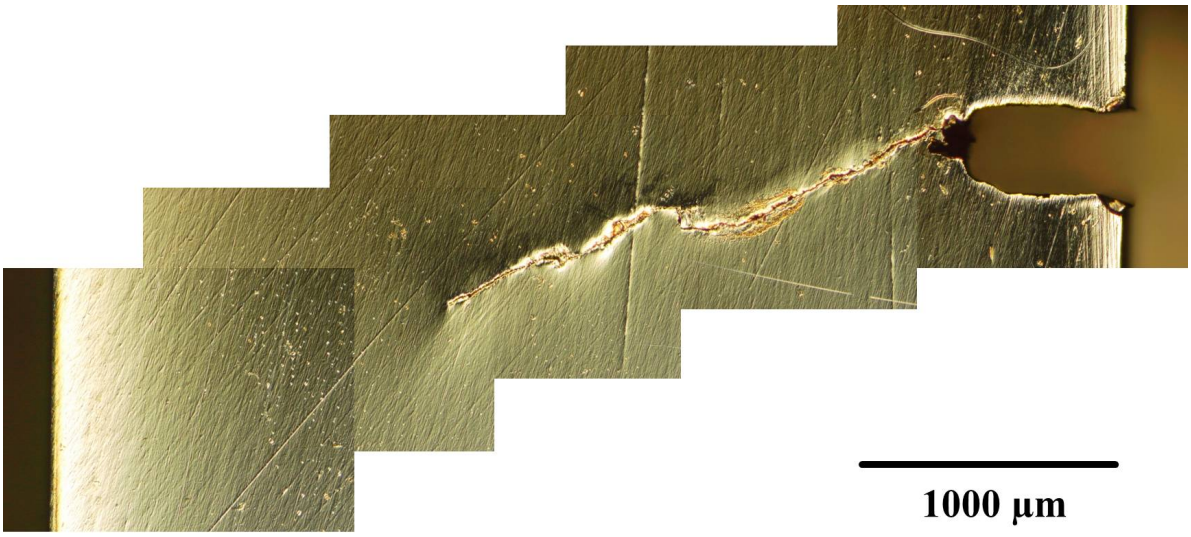

(a)

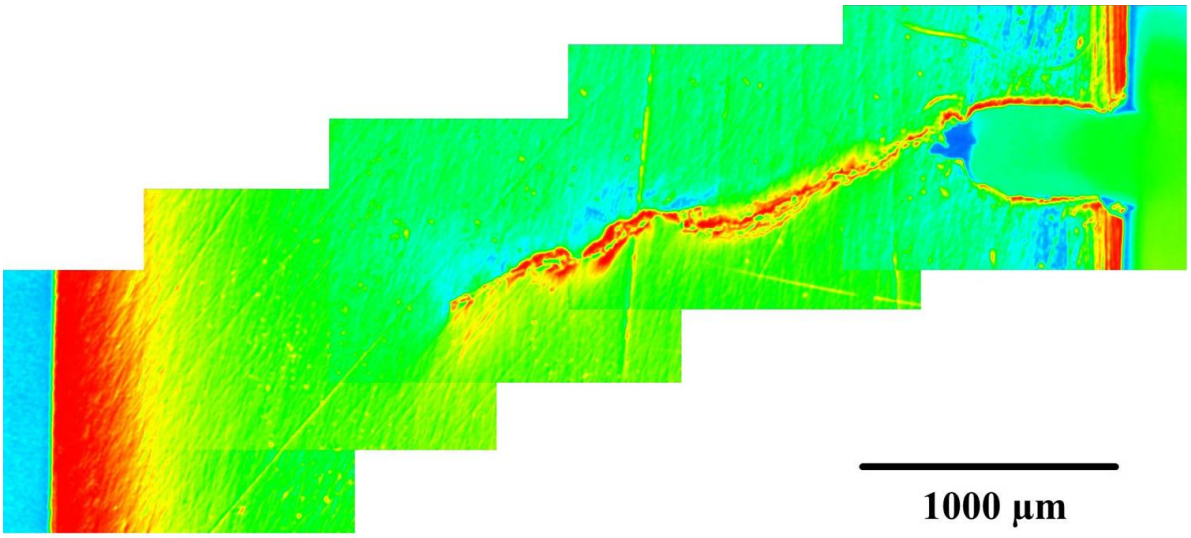

(b)

Figure 4.33.: (b) Overview of the crack propagation of the macro-notch across the specimen (notch at the right edge). (b) Analysis of the plastic deformation influenced zone according to the surface analysis.

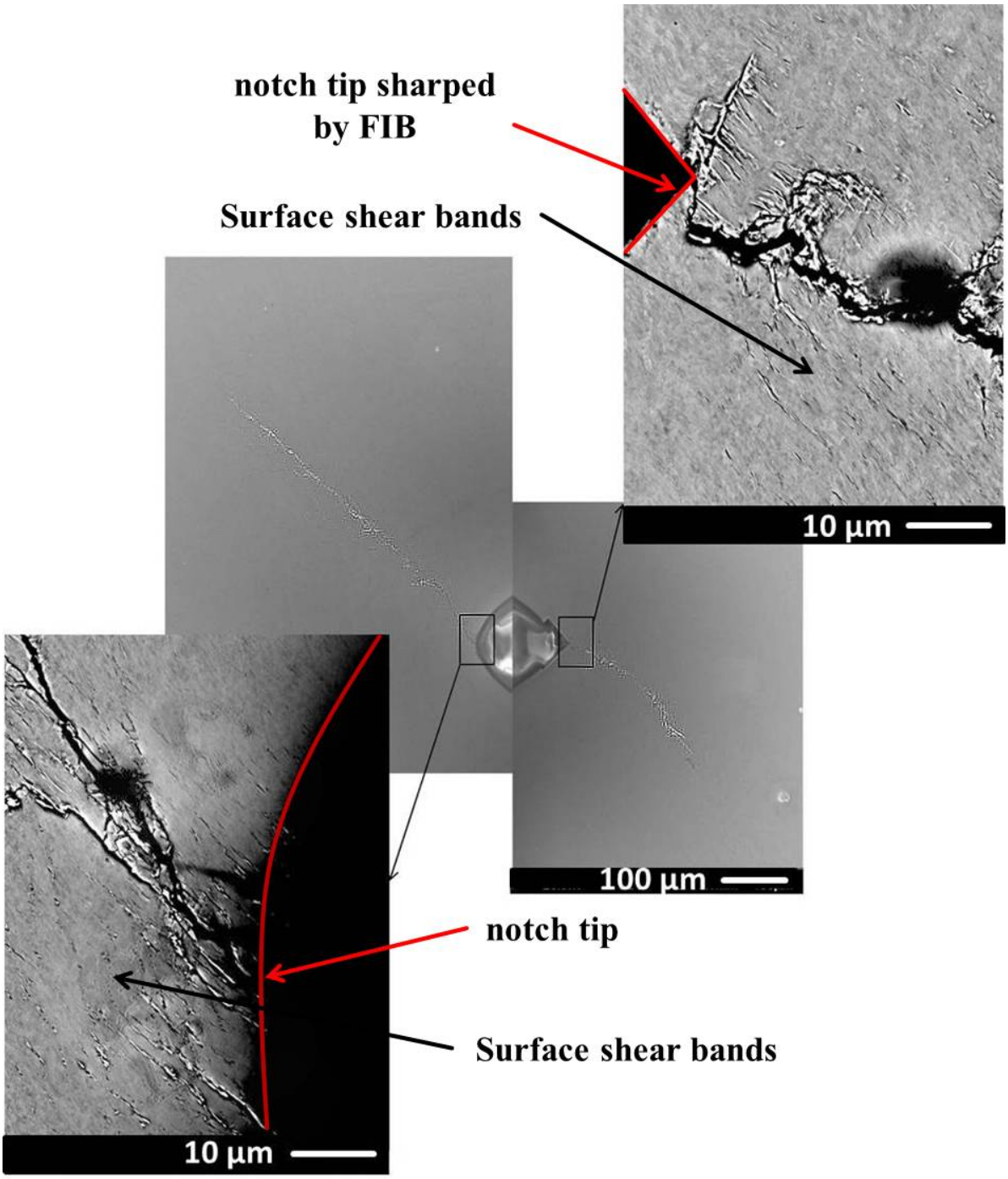

Figure 4.34.: Crack propagation of the notch with the initial length of 1000 μm, with a detailed observation at the notch tip areas.

II Notched specimen. The crack tip was the stress concentrated area during the fatigue loading, and the area around the crack tip was characterized by the most severely plastic deformation influenced zone. When dynamic recrystallization could not ensure the local plastic deformation, the crack propagated.

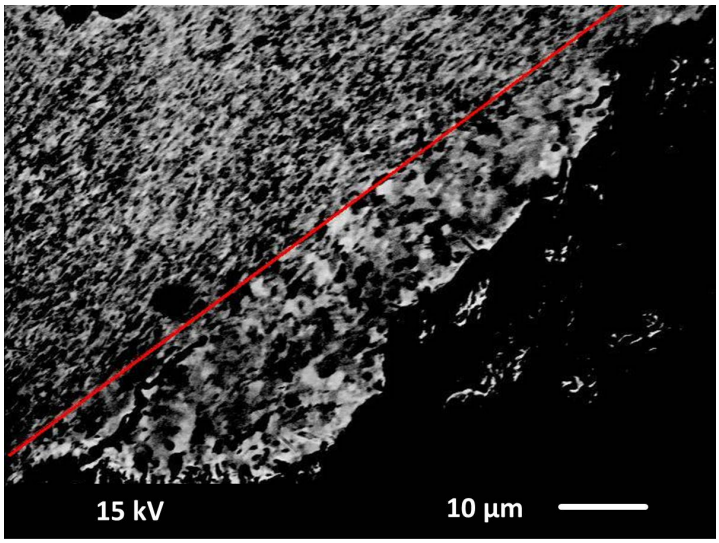

Figure 4.35.: Dynamic recrystallization along the crack growth path for a Mode I Notched specimen.

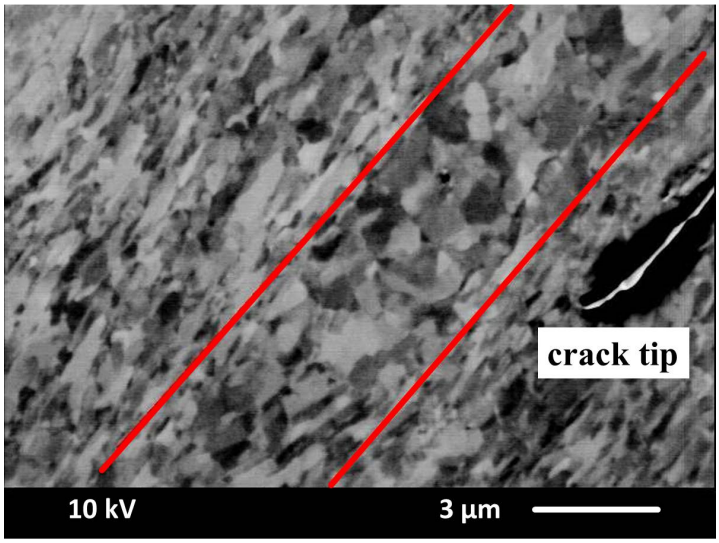

Figure 4.36.: Dynamic recrystallization around the crack tip for a Mode II Notched specimen.

4.5.5. Fatigue behaviour of the bimodal ECAP UFG/CG nickel

The fatigue behaviour of the bimodal UFG/CG nickel was investigated. Annealing the ECAP UFG nickel specimens, coarse grains formed with different volume fractions (section 4.2.2). Microcracks with length 100 μm were initiated by FIB on the specimen surface and then the specimens were cyclically loaded with the load-controlled mode under 150 MPa with R=-1. The results of the tensile tests in section 4.4 showed that the yield stress of the bimodal UFG/CG nickel decreased with increasing coarse grains. The loading amplitude was selected to ensure that the loading stress was lower than the yield stress of the bimodal UFG/CG nickel. Actually the loading stress was higher than the yield stress of the bimodal nickel specimen with high volume fraction of coarse grains, however, it was still utilized for all the bimodal UFG/CG specimens, which were cyclically loaded till $500,000 \sim 600,000$ cycles.

An overview of the crack propagation for different specimens is shown in figure 4.37 in which there are increasing volume fractions of the coarse grains in subfigures (a), (b) and (c). The deformed coarse grains are marked by the arrows in figure 4.37a and figure 4.37b. In figure 4.37c only the undeformed coarse grains are marked with the arrows and the deformed coarse grains are characterized with the deformmation bands inside. It can be seen that the plastic deformation concentrates in the coarse grains. Actually, the coarse grains have been found to be deformed after the first 10,000 cycles and the plastic deformation is accumulated inside these grains in the form of slip lines and then extrusions.

Figure 4.38 shows the coarse grain at the crack tip deforming with the increasing fatigue cycles. The local plastic deformation is more severe at the left half grain where the crack tip is located (figure 4.38a), and induces the slip lines. The slip lines widespread into the whole coarse grain and extrusions form with increasing fatigue cycles (figure 4.38b,c and d). Besides, it seems that the ultrafine grains around the coarse grain are stable and no deformation has been found inside them. The coarse grains elsewhere around the microcrack are also found to be deformed and the severity of the deformation depends on the local stress and the grain size. Those coarse grains in which severe plastic deformation is accumulated behave as the potential sites for initiation of new cracks during the fatigue experiment. Although there is accumulating plastic deformation inside the coarse grains with increasing fatigue cycles, all the specimens in which there are with different volume fractions of the coarse grains are found to hold up with further loading.

Figure 4.39 shows more detailed information about the different areas around the

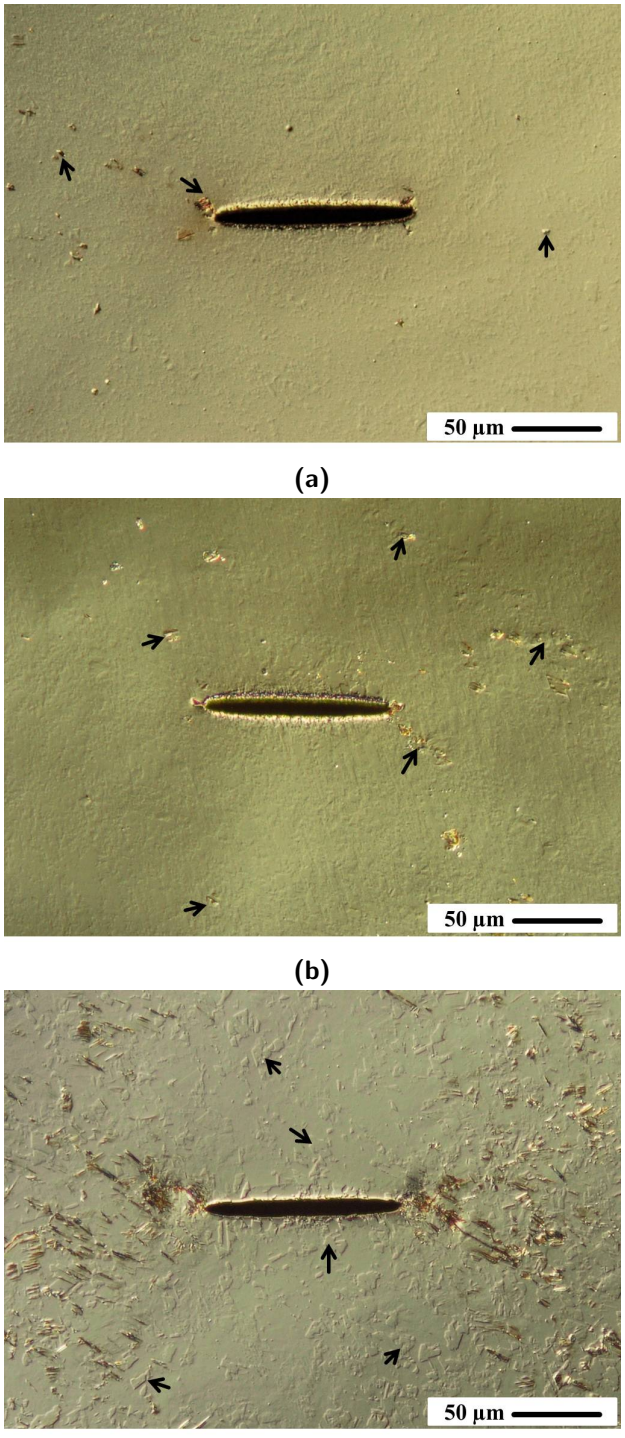

Figure 4.37.: Overview of the crack propagation in the annealed ECAP UFG/CG nickel specimens, in which there are increasing volume fractions of the coarse grains in (a), (b) and (c). The coarse grains are marked with the arrows in figure (a) and (b). In (c) only the undeformed coarse grains are marked with the arrows and the deformmation bands inside.

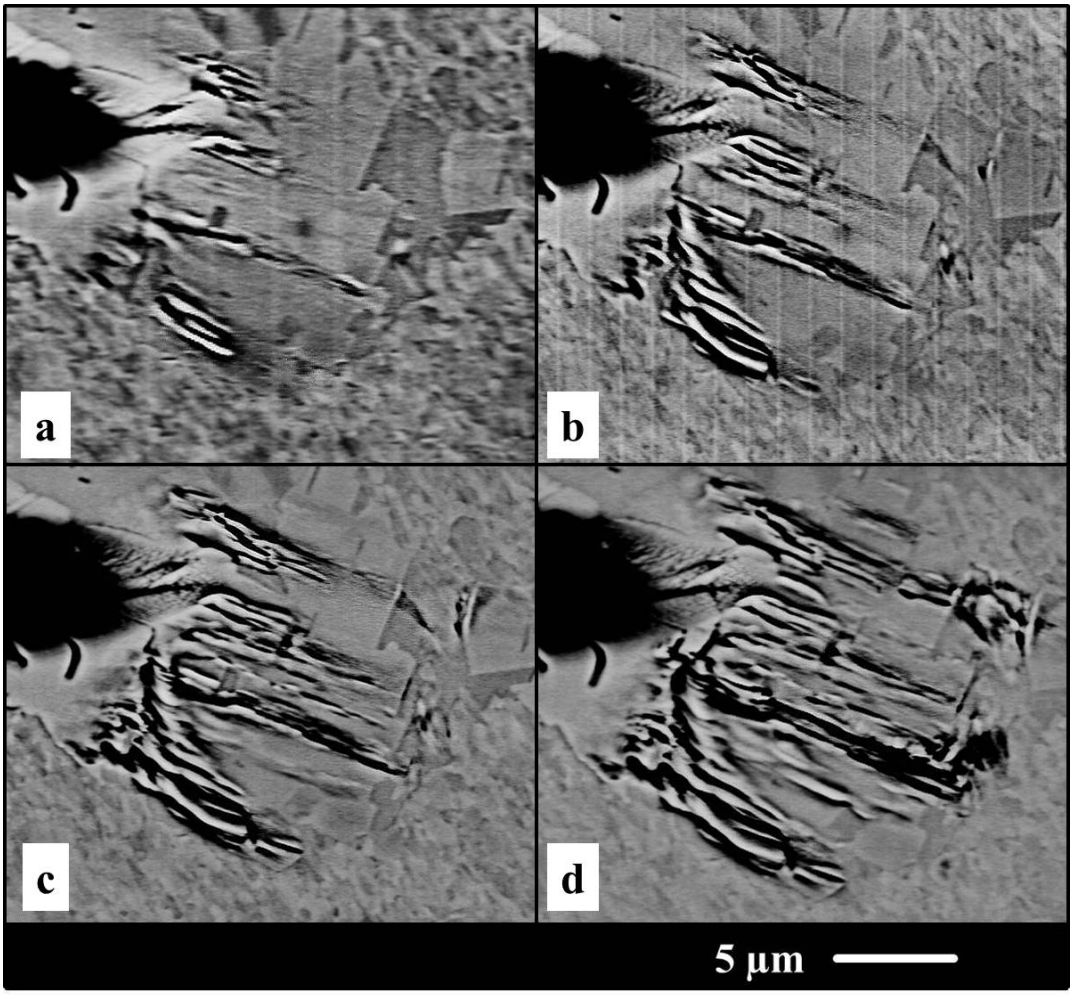

Figure 4.38.: Deformation of the coarse grain at the crack tip with increasing fatigue cycles. The specimen was loaded under 150 MPa for (a) 20,000, (b) 80,000, (c) 180,000 and (d) 500,000 cycles.

crack tip for the specimen which is corresponding to figure 4.37a. The coarse grains near the crack tips are the most strongly deformed (points A and B) due to the high stress concentration at the crack tip, which is similar to that in figure 4.38. Besides, the crack tip propagates slowly further due to the high local plastic deformation (point E). There are deformation bands inside the coarse grains, which are with some distance to the microcrack (point E). Actually, these grains could represent the coarse grains in the whole specimen, which are less or not influenced by the microcrack. There is no plastic deformation in the coarse grains (point C) which are directly along the middle round of the microcrack, because the microcrack middle edge behaves as a free surface where no stress concentration occurs.

Figure 4.40 shows the formation of the surface cracks that induces the ultimate frac-

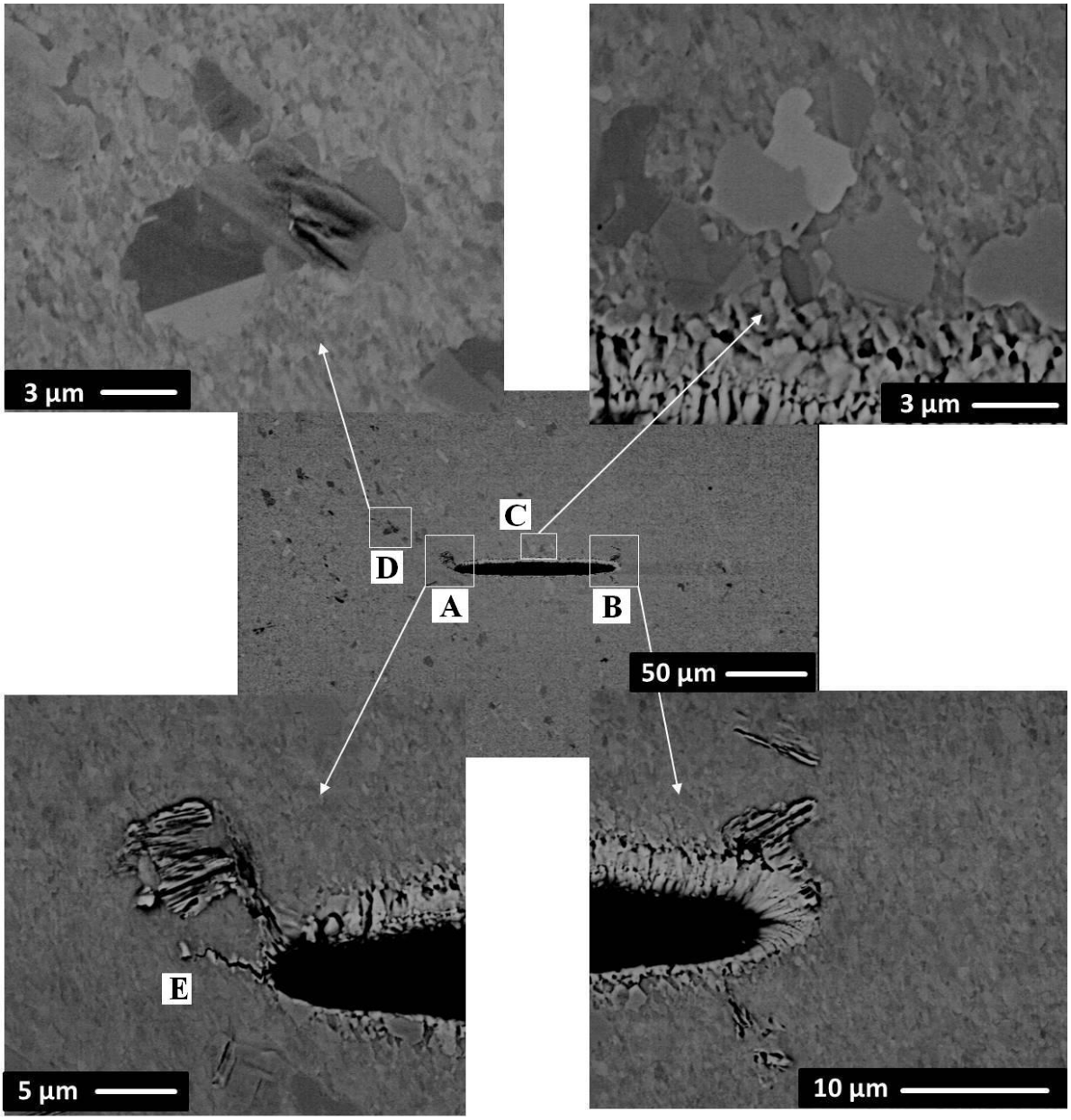

Figure 4.39.: SEM image of the different areas around the microcrack after cyclical loading, which is corresponding to the figure 4.37a.

ture of the bimodal ECAP UFG/CG nickel. The specimen was overloaded only for several fatigue cycles (the stress amplitude has not been measured). The coarse grains are those with strongly slip lines inside. Surface cracks in the UFG areas are found to along the direction of the elongated grains and the significantly deformed coarse grains are combined by these surface cracks. This result indicates that when the coarse grains in the bimodal UFG/CG microstructures can not endure the total plastic deformation, the ultrafine grains are involved suffering the plastic deformation. Surface cracks then form in the UFG areas due to the low capacity of the ultrafine grains for the dislocation movements. Therefore, when designing the bimodal UFG/CG microstructures, the volume fractions of the coarse grains should be considered in combining the strength and the ability of plastic deformation (ductility) of the materials.

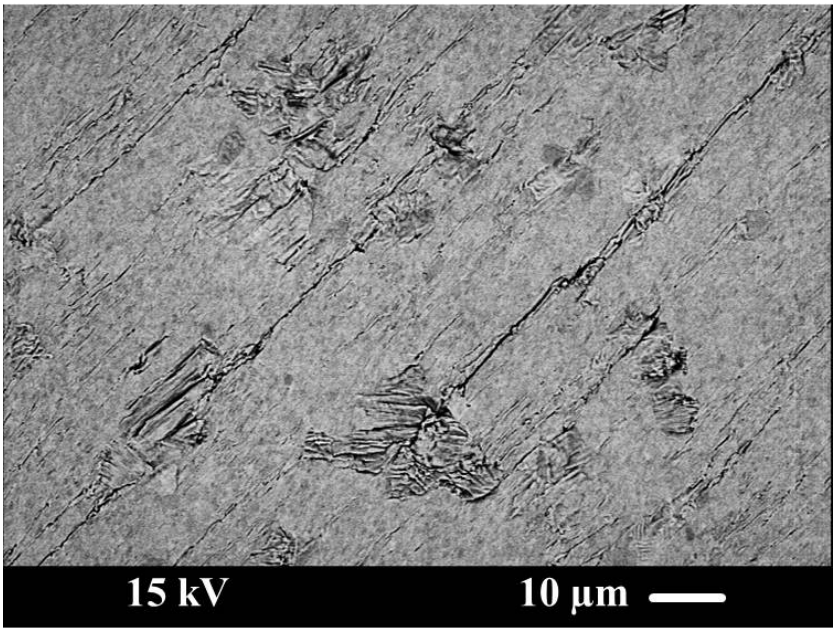

Figure 4.40.: Formation of the surface cracks inducing the ultimate fracture in the bimodal ECAP UFG/CG nickel.

5. Discussion

5.1. Initiation of bimodal NC/UFG microstructure from PED NC nickel

It is of great importance to understand the grain growth process during the annealing, because the materials properties, in particular the mechanical properties, are significantly influenced by the grain size and grain size distribution. In materials for structural applications at lower temperatures, small grain sizes are beneficial for optimizing the strength and toughness. However, the low ductility is usually a problem for the fine grained materials, therefore larger grain sizes are required to improve the materials' ductility. A good understanding of grain growth during heat treatment is a prerequisite to control the microstructures and thus the mechanical properties of metals and ceramics during solid state processing.

The concept of bimodal microstructures is applied to combine strength and ductility of the materials in this work. Starting with the monomodal nanocrystalline grains, the bimodal microstructure mixing nanograins and ultrafine grains was achieved by annealing the PED NC nickel at 250°C, which was a continuous grain growing process (section 4.2.1). The nanograins were growing totally into the UFG range after longer annealing time. There was over 99 % of ultrafine grains after 180 min and no nanograins were detected after 300 min. Curves describing the relationship between the annealing time and the volume fraction and mean grain size of the growing ultrafine grains in the annealing process are plotted according to the data in Table 4.2 and are shown in figure 5.1. It can be seen that the measuring points of the volume fraction and the mean grain size both obey an S-shape, which is quite similar to the curve for the fraction of the recrystallized areas with the annealing time (figure 2.20), although the as-received PED NC nickel is not in a deformed state.

The S-shaped curve, which describes the volume fraction of the growing grains with the annealing time, can be described using the JMAK model. Analysis according to the JMAK equation 2.2 is conducted and the calculated equation is described as:

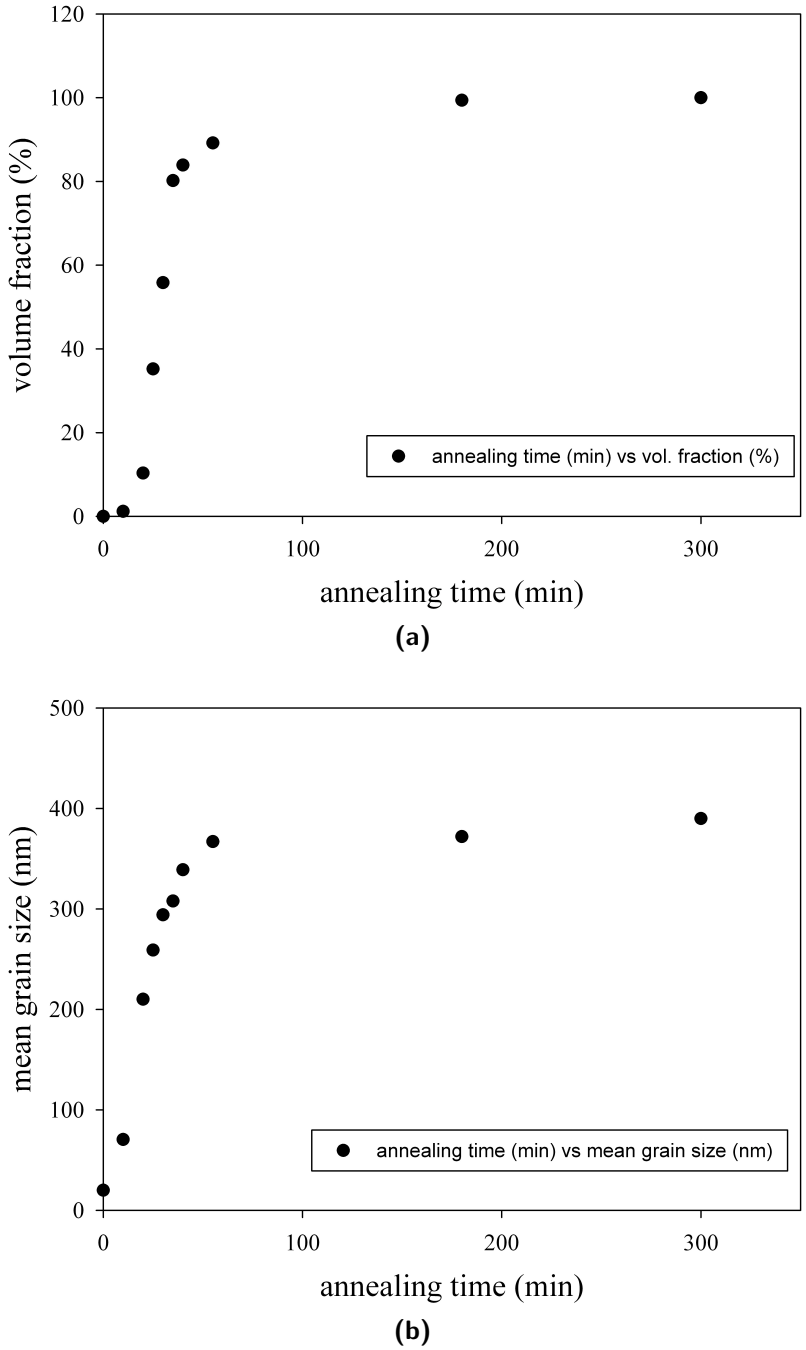

Figure 5.1.: (a) Volume fraction and (b) mean grain size of the growing ultrafine grains with the increasing annealing time in the heat treatment process of NC PED nickel at 250℃.

$$X_V = 1 - exp(-4.3927 \cdot 10^{-7} t^{4.252}) \tag{5.1}$$

with the JMAK exponent n = 4.252. This model matches the experimental data well (figure 5.2a), especially for the initial stages (figure 5.2b). The ideal JMAK exponent is **4**, in which the growing grains are assumed to grow in three dimensions and the nucleation and growth rates are constant [*Humphreys and Hatherly*, 2004]. The calculated JMAK exponent **n** is little larger than **4** in this work, which implies the probable increasing nucleation and (or) growth rates in the annealing process. Although the as-received PED NC nickel is not in the deformed state, the grain growth still obeys the JMAK model for the recrystallization quite well.

The grain size is analyzed according to the Burke and Turnbull model, which is described in equation 2.7. The grain growth exponent **n** varies when the data volume is differently considered (figure 5.3). Similar to the volume fraction of the growing grains, the calculated curve matches very well the experimental data when only the initial 40 min are considered. Actually, there seems to be a saturating value of the grain size with increasing annealing time. In this means, the mean grain size changes little after 55 min, and the grain growth exponent is 1.492 when calculating the experimental data to this moment. An overview of dependence of the fitted grain growth exponents to the data volume is shown in table 5.1.

annealing time (min)	mean grain size (nm)	grain growth exponent **n**	constant c_2
40	339	1.155	14.58
55	367	1.492	27.40
180	372	3.610	102.00
300	390	4.574	124.14

Table 5.1.: The calculated grain growth exponent for the low temperature annealing of the PED NC nickel, according to different data volume.

The driving force of the grain growth comes from the reduction in the grain boundary energy. The main factors which influence the grain growth are temperature, solutes and particles, specimen size and microstructural textures. Grain growth, in which the nanograins are growing into the ultrafine grains for the PEC NC nickel at 250℃, involves the migration of high angle grain boundaries of the NC nickel and the kinetics is strongly influenced by the grain boundary mobility. The grain boundary mobility depending on the temperature is usually found to obey the the Arrhenius type relationship $M = M_0 exp(-Q/RT)$, in which Q is the activation energy. The driving force for

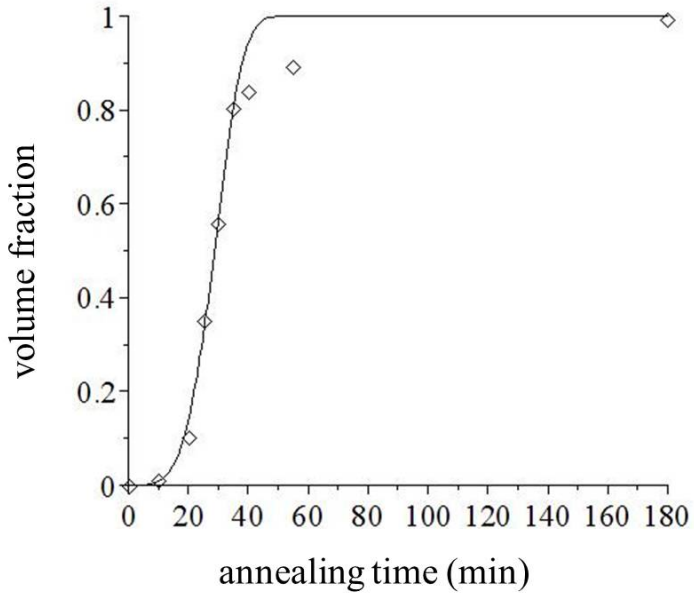

(a)

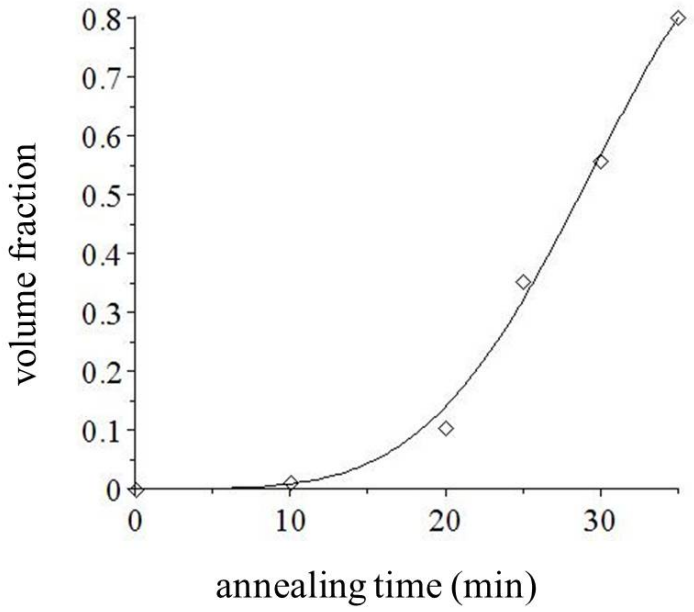

(b)

Figure 5.2.: (a) Volume fraction of the grown grains with increasing time, calculated according to the JMAK equation. (b) Comparison of the JMAK model with the experimental data in the initial 35 min.

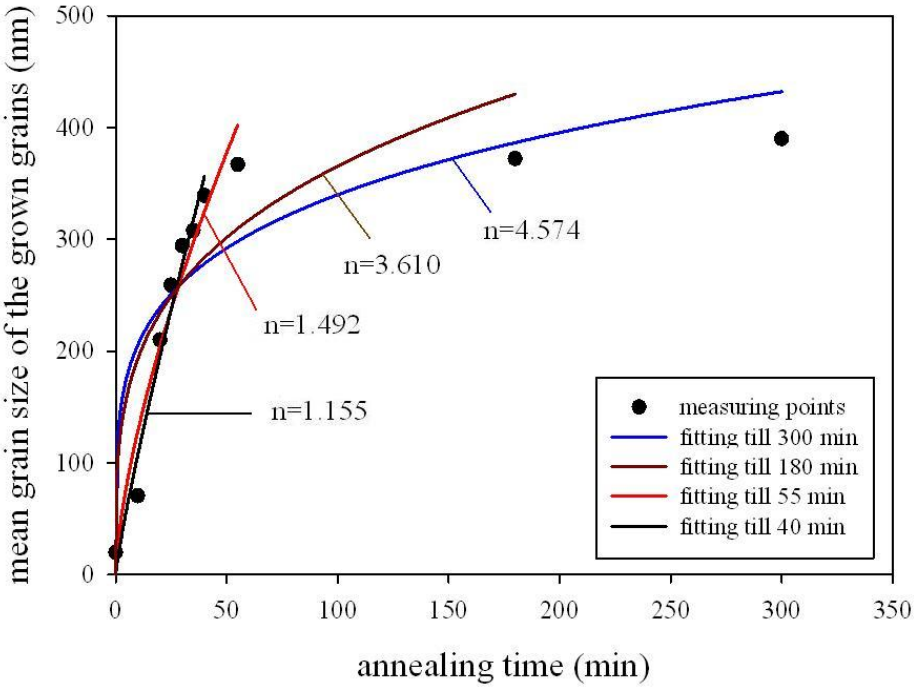

Figure 5.3.: Analysis of the grain growth according to the Burke and Turnbull model.

grain growth is usually small, and significant grain growth is often found only at very high temperatures. The annealing temperature is 250℃ in this work and the grain size of the growing grains is limited in the UFG range (< 400nm). The effect of the solutes or second-phase particles has not been considered, because the PED nickel used in this work is of high purity in which no other impurities have been detected using EDS in the high resolution SEM. Actually, the effect of the solutes or particles are of great importance to the grain growth, therefore, it should be investigated more carefully in the future work. It has been found that when the growing grains have the grain size comparable to the specimen thickness, the rate of grain growth will diminish [*Humphreys and Hatherly*, 2004]. But the grain sizes of the growing grains are only in the UFG range in this work and they would hardly be influenced from the specimen scales. Strong textured materials contain high volume fraction of low angle grain boundaries which possess low grain boundary energies which will reduce the driving force for the grain growth. However, although there are growing textures along the growing direction in the PED process, they are found to show little effects to the grain growth. This has been proved in section 4.2.1 in which the mean grain size in the cross section is found quite identical to that in the specimen surface.

Concluding remarks

Annealing the PED NC nickel at relatively low temperature, i.e. at 250°C in this work, is a continuous grain growth process, in which the nanograins are growing to the ultrafine grains. The microstructures between monomodal nanograins and monomodal ultrafine grains, i.e. bimodal NC/UFG microstructure, are achieved by controlling the annealing time. The grain growth process is driven by the energy stored in the form of grain boundaries. The mean grain size follows the Burke and Turnbull model well, when a limiting grain size is assumed. The volume fraction of the growing grains is also analyzed, applying the JMAK model for recrystallization. Nevertheless, the model and the experimental data are fitting very well. However, this annealing process is semi-quantitative, because of the difficulty in controlling the annealing time. Besides, the chemical PED processing inevitably brings impurities into the samples. Diffusion of the impurities in the fine grained materials will influence the annealing process when different starting samples are used.

5.2. Initiation of bimodal UFG/CG microstructure from ECAP UFG nickel

The bimodal UFG/CG microstructures have been obtained by annealing the ECAP UFG nickel at 250°C (section 4.2.2). Due to the complex starting microstructures of the ECAP materials, different factors will influence the annealing process, i.e. the formation and distribution of the growing coarse grains, which will be discussed in this section. Firstly, the influence of the temperature and annealing time will be investigated. Secondly, the effects of the microtextures are studied. Finally, an in-situ annealing experiment is conducted, directly to observe the recrystallization process.

5.2.1. Influence of the annealing temperatures

Specimens of the ECAP UFG nickel are annealed at different temperatures and with different annealing times which are shown in figure 5.4. The heating rate for the high temperature is slower due to the limitation of the heat treatment furnace. All specimens are held at the setting temperature for 60 min. Figure 5.5 shows the annealing results of different temperatures. The grain size distributions for all specimens exhibit the 'bimodal' microstructures, surprisingly. However, the specimens, except annealed at 250°C, have quite large grain sizes and show no superior strength anymore, according to the microhardness measurements.

There are high volume fraction of low angle grain boundaries and strong microtextures after severe plastic deformation in the ECAP process, which has been characterized in section 4.1. Upon annealing the ECAP UFG nickel at elevated temperatures, the material usually recrystallizes continuously, with the driving force in form of the stored energy in the LAGBs. The grain sizes are not constant in the specimens, shown as the 'bimodal' microstructures in figure 5.5. This phenomenon occurs because the different areas within the specimen recrystallizes at different rates due to the different local stored energy, therefore the final grain sizes and grain size distributions are not homogeneous around the whole specimen. Altering the heating rate might change the balance of the nucleation and growth in recrystallization, thus might influence the final grain size and the grain size distribution. However, the temperature is the critical factor that determines the ultimate largest grain size. The bimodal UFG/CG microstructure has also been achieved by annealing the specimen at 260°C which is shown in figure 4.6. However, there is already high volume fraction of the growing coarse grains after 30 min. Therefore, the lower temperature 250°C is selected by considering the balance of the

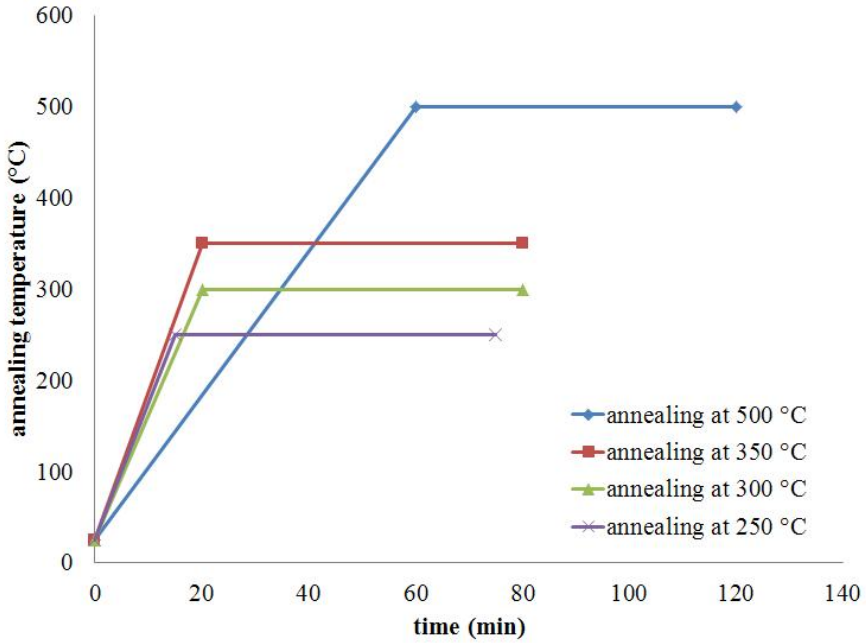

Figure 5.4.: The heating history of the ECAP specimens at different temperatures.

grain size and grain growth rate.

When annealing the PED NC nickel at 250°C, continuous grain growth takes place. The ultrafine grains are the ultimate microstructure and stable at this temperature. But the ultrafine grains in the ECAP nickel would recrystallize into the coarse grains when annealing at this temperature. This is because the driving force for the grain growth in PED NC nickel is from the grain boundary energy and the recrystallization in the ECAP UFG nickel is driven by the stored energy in the cold deformation in the form of dislocations. The magnitude of the stored energy in the dislocations is substantially larger than that associated with the grain boundary [*Humphreys and Hatherly*, 2004; *Rollett et al.*, 2007]. Therefore, the mixing microstructure of ultrafine grains and coarse grains forms by annealing the ECAP UFG nickel at 250°C, in which discontinuous annealing phenomena, i.e. primary recrystallization, takes place.

5.2.2. Influence of the annealing time

Recrystallization of the ECAP UFG nickel is found to be a semi-empirical process. There are no statistical results achieved by analyzing the experimental data. The volume fraction and the mean grain size do not obey the existing theories and models for recrystallization, because of the complexity of the microstructural properties. After

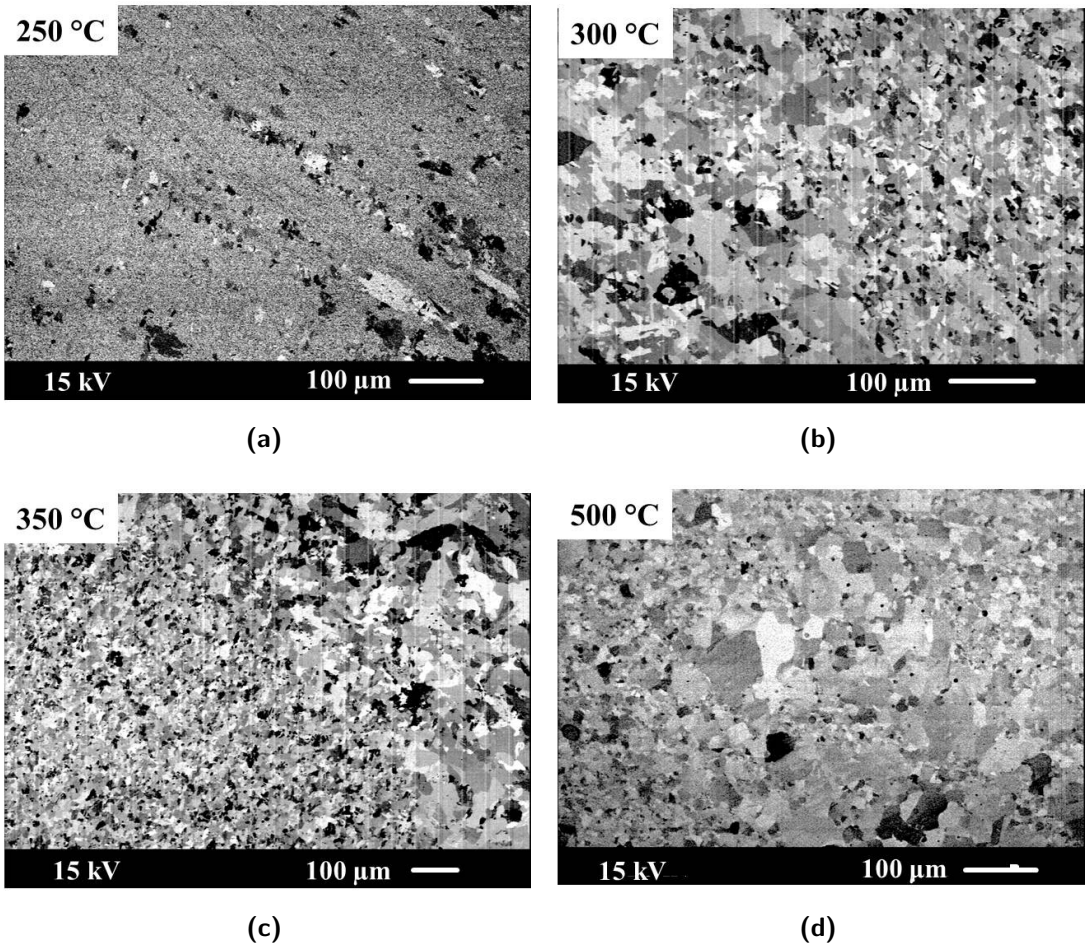

Figure 5.5.: Influence of the annealing temperature to recrystallization of the ECAP UFG nickel. (a) 250°C, (b) 300°C, (c) 350°C and (d) 500°C.

eight passes of the ECAP process the microstructures, especially in the grain boundaries, are quite inhomogeneous, which make the subsequent annealing process complicated.

Generally, a minimum annealing time, e.g. 50 min − 60 min, at 250°C is needed to obtain the bimodal UFG/CG microstructure. There is some deviation of the annealing time for different specimens to achieve the bimodal microstructures when the other annealing parameters are held constant. This is due to the inhomogeneity of the UFG microstructures in different areas in the ECAP billet, although the microstructures observed in SEM, especially the mean grain sizes, are quite homogeneous in different specimens. The initial coarse grains of te billets before the ECAP process seem to play an important role in the heat treatment of the ECAP UFG nickel. The boundaries between the recrystallized and not recrystallized areas correspond well to the grain boundaries of the original coarse grains which have been elongated by the severe shearing in the

ECAP process.

With the same annealing time there appear different microstructures, from almost no coarse grains to bimodal microstructure to almost all coarse grains, which causes great difficulty in the analysis of the heat treatment on the ECAP UFG nickel. However, there is also another phenomenon that the previous annealing shows little influence to the subsequent annealing when the specimen is heat treated again. This 'no memory' effect makes it possible to initiate the bimodal UFG/CG microstructures from the ECAP UFG nickel.

When annealing the ECAP nickel for long time, e.g. 300 min, at 250°C, more complicated grain size distribution is obtained (figure 5.6). The grain size distribution exhibits a 'trimodal' microstructure in which there are areas with typically three different mean grains sizes, as marked in the image. There are ultrafine grains in area '1' which are not recrystallized during the annealing. The areas '2' is characterized by the coarse grains with the mean grain size about 6 μm which is the 'normal grain size' of the coarse grains in the bimodal UFG/CG microstructure when annealing ECAP UFG nickel at 250°C. The mean grain size in area '3' is about 15 μm which is only observed in the specimens after long annealing time. Furthermore, the boundaries between the areas with different grain sizes form elongated large grains, which indicates the influence of the initial coarse grains before ECAP process.

There is also observing influence by the ECAP routes on the annealing process, where the ECAP UFG nickel with route E recrystallizes comparably faster than route C when the other annealing parameters are held the same. However, whether the route E specimens recrystallizes 'earlier' must be investigated in the further work. Besides, there is influence from the specimen geometry, mainly the specimen size. The volume fraction of the recrystallized areas is usually higher in the smaller specimens, when the other parameters are held constant.

5.2.3. Correlation between the microtextures and recrystallization

In order to investigate the influence of the microtextures on the recrystallization process, a 'map' of the microhardness (HV) of an ECAP specimen is drawn, which is consisted of the microhardness at the indenting points with the distance 200 μm $\times$ 250 μm to each other. Figure 5.7 shows the HV map in which the mesh points correspond to the measured points. Figure 5.8a displays the same area as in figure 5.7 but without the mesh points, showing the image more clearly. The microhardness of the ECAP UFG nickel is between HV250 and HV300. It is found that there is a preferred direction

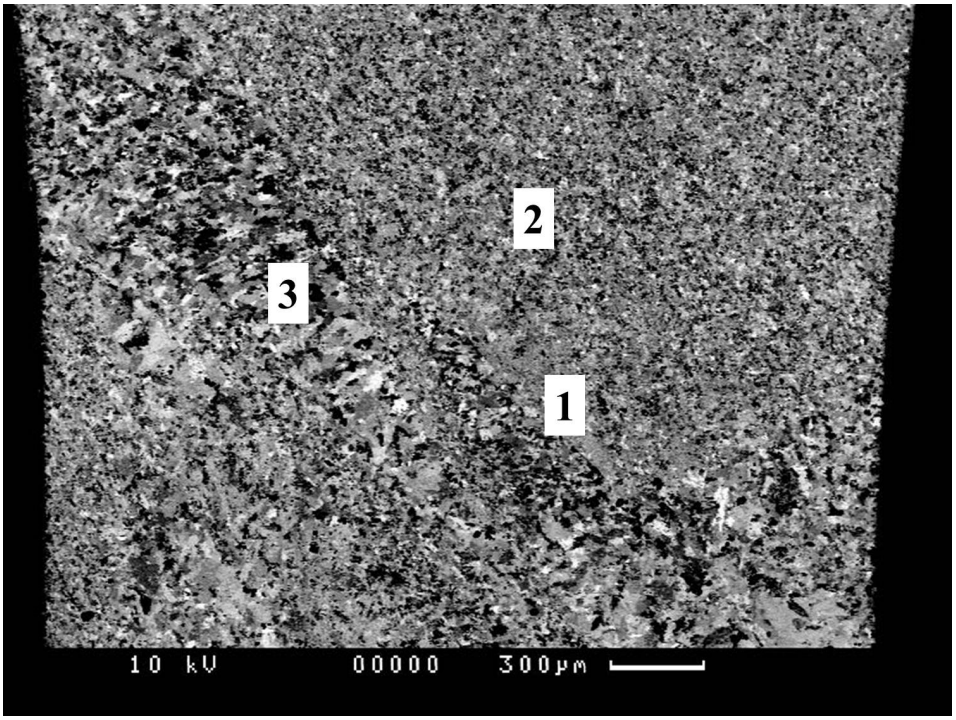

Figure 5.6.: 'Trimodal' grain size distribution of the ECAP nickel annealed for 300 min at 250°C.

along the elongated grains of the microhardness, which reflects the direction of the microtextures in the ECAP materials. The specimen is heat treated at 250°C for 50 min, to form the bimodal UFG/CG microstructure. Figure 5.8b shows the recrystallized UFG/CG microstructures corresponding to the indented area in figure 5.8, in which the UFG areas are marked with the black arrows and the CG areas are marked with the white arrows.

The coarse grains forming during the annealing process come from the primary recrystallization and subsequent grain growth. Comparing the HV map and the bimodal microstructure after annealing, the recrystallized areas overlaps well the areas with the higher HV values. It seems that the areas with higher HV values begin to recrystallize earlier or easier. Actually, the driving force of the primary recrystallization stems from the stored energy in the form of dislocations during the cold work, which refers to the severe plastic deformation in the ECAP process. Therefore, the areas with higher HV values might possess more stored energy in the ECAP process, and made the primary recrystallization occur easier.

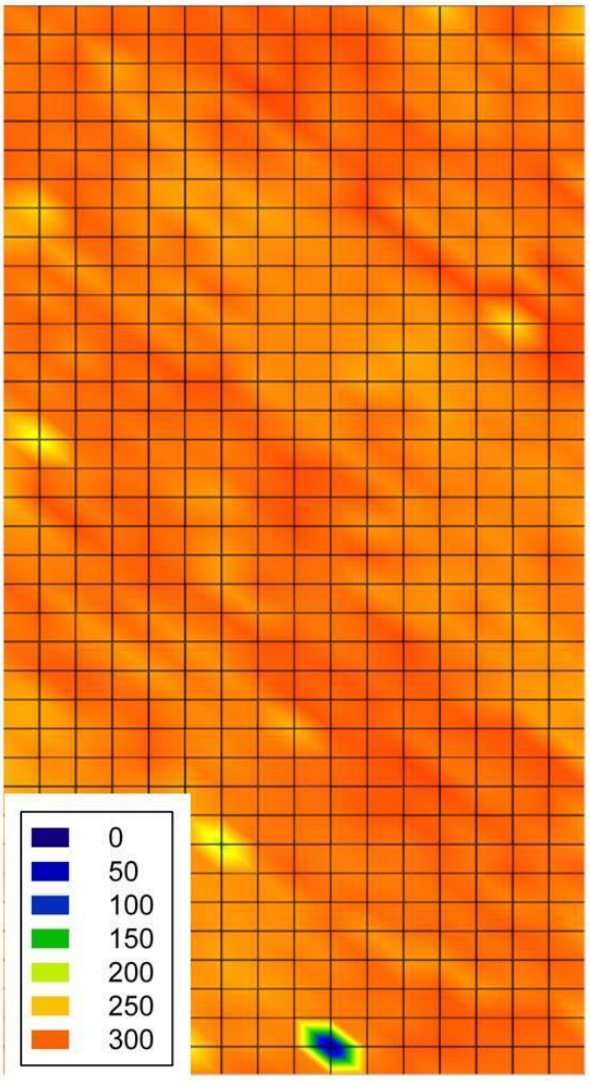

Figure 5.7.: Microhardness map of the with route C processed ECAP UFG nickel, with and without mesh points.

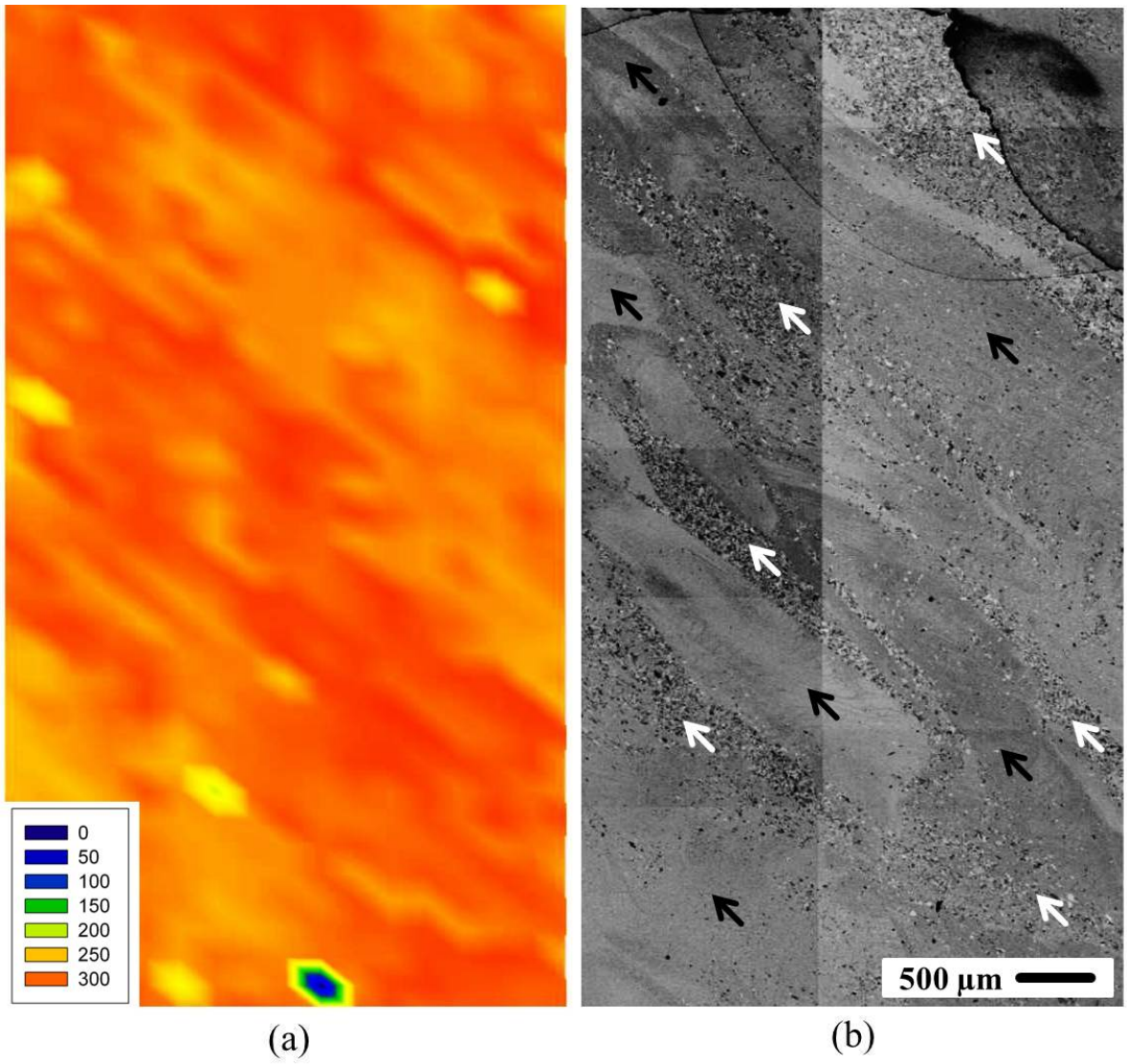

Figure 5.8.: Comparison of (a) the microhardness map with (b) the forming bimodal UFG/CG microstructure in which the UFG areas are marked with the black arrows and the CG areas are marked with the which arrows.

5.2.4. In-situ annealing of the ECAP nickel

In order to understand the recrystallization process of the ECAP UFG nickel more clearly, an in-situ annealing experiment was carried out. The annealing temperature in ex-situ heat treatment was taken as reference, however, there was no recrystallization observed at this temperature in the in-situ annealing. This might be due to the relatively small heating area of the in-situ annealing setup and the strong heat dissipation in the SEM chamber. Therefore, temperature was elevated to 290°C, and then recrystallization began to be observed. The recrystallization process with the increasing annealing time is shown in figure 5.9. The images show clearly the two stages of the primary recrystallization: **nucleation** which corresponds to the first appearance of new grains in the microstructure and **growth** during which the new grains replace the deformed materials. Although these two events occur consecutively for any particular grain, both nucleation and growth might be occurring at any time throughout the specimen.

The specimen is further investigated after the in-situ annealing (figure 5.10). The bimodal UF/CG microstructure is similar to that after the ex-situ annealing, where the recrystallized grains concentrate in some special areas, which correspond to the coarse grains before the ECAP processing, presumably. After new polishing of the specimen the surface microstructure could be seen more clearly and there showed a larger volume fraction of the recrystallized areas. There is due to the surface effect to the recrystallization which could be observed more clearly in the images with larger magnifications (figure 5.10b and figure 5.10d). Actually, the surface effect has already been shown for the PED nickel annealed at higher temperature in section 4.2.3 (figure 4.10 and figure 4.11).

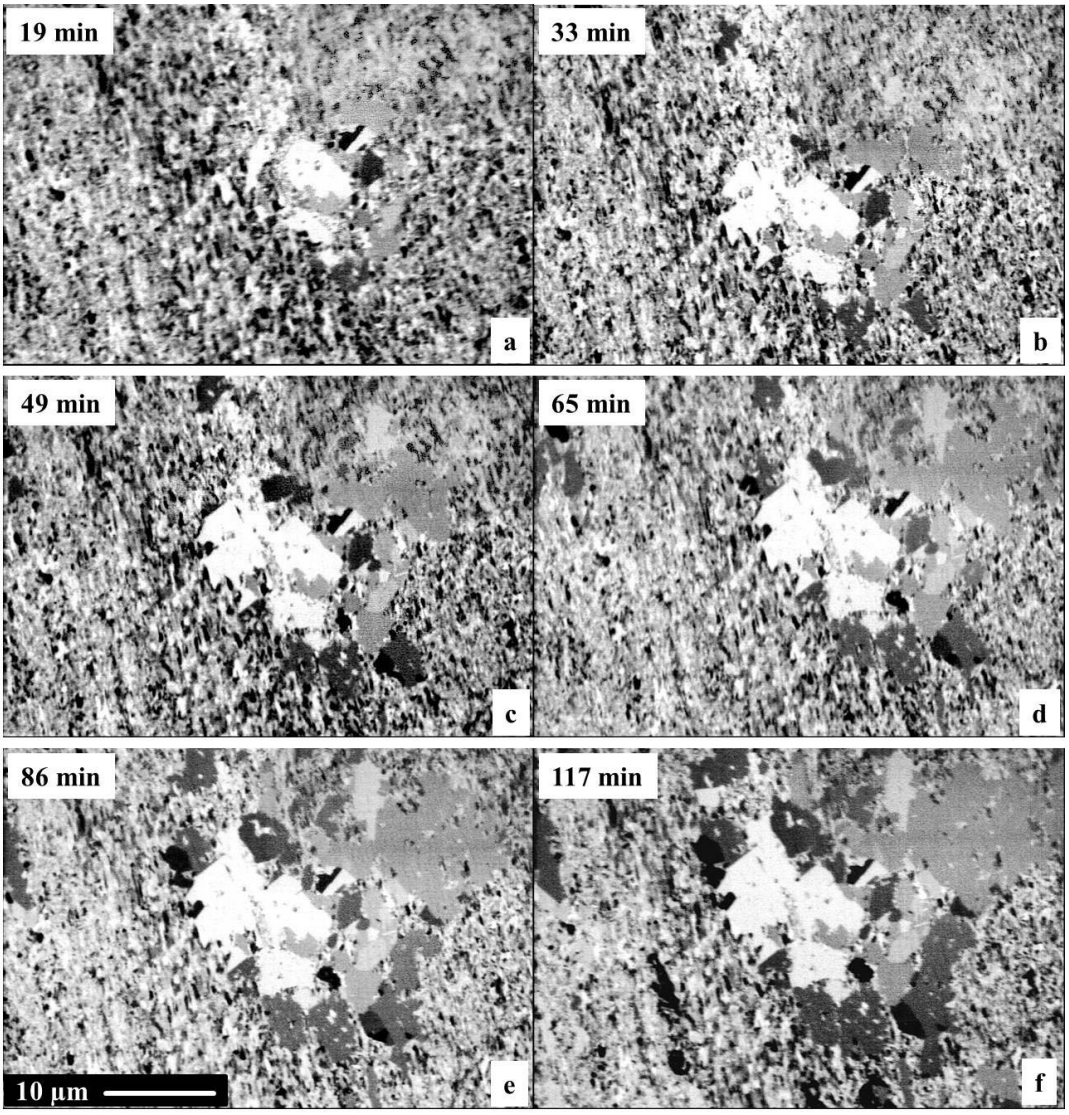

Figure 5.9.: Recrystallization of ECAP UFG nickel with increasing annealing time during in-situ heat treatment experiment in the SEM. (a) 19 min, (b) 33 min, (c) 49 min, (d) 65 min, (e) 86 min and (f) 117 min.

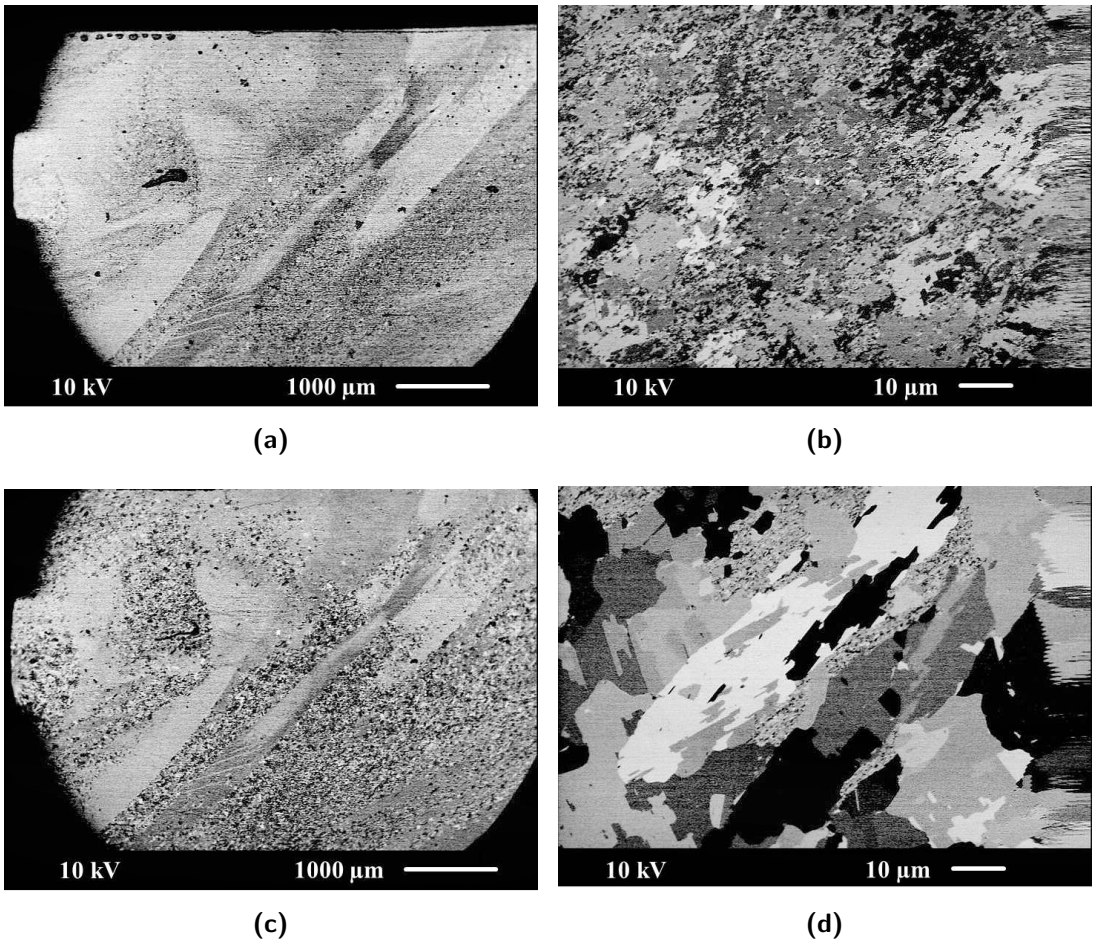

Figure 5.10.: SEM image of the bimodal UFG/CG microstructure after the in-situ annealing. (a)(b) direct after in-situ annealing experiment and (c)(d) specimen newly electropolished.

5.2.5. Conclusion to the annealing of ECAP UFG nickel

The bimodal UFG/CG microstructures are initiated by annealing the ECAP UFG nickel at 250°C. Controlling the annealing time, maybe by repeated annealing, the volume fraction of recrystallized coarse grains could be approximately controlled. It is found that the areas with higher HV values are the preferred sites for recrystallization, with the aid of the microhardness map. This is presumably due to the higher stored energy in these areas. In-situ annealing experiments reinforce the understanding of the recrystallization process of the ECAP UFG nickel, which is typically a discontinuous annealing phenomenon. The bimodal UFG/CG microstructures combine the strength and ductility of the materials, which has been shown by the tensile tests (section 4.4). However, it is difficult to achieve the homogeneous UFG/CG microstructures by annealing the ECAP UFG nickel directly, due to the complexity of the starting microstructures of the ECAP UFG nickel. Therefore, new methods are needed to achieve the bimodal microstructures. A potential method - heat treating the ECAP UFG nickel by laser beam (Appendix D) - is in progress.

5.3. Normal and abnormal grain growth of PED nickel at elevated temperature

When annealing the PED NC nickel at elevated temperature 500°C, two different phenomena, i.e. abnormal grain growth and normal grain growth, occurred using two different initial PED plates (plate No.74 and plate No.90), as stated in section 4.2.3. However, the two PED plates were synthesized with the same parameters and conditions according to the producer (Appendix A).

Abnormal grain growth occurred when annealing the specimens from PED plate No.74. There were two different ways to anneal the specimens at 500°C: the one-step method with which the as-received PED NC nickel specimens were annealed directly at 500°C; and the two-step method with which the PED NC nickel was annealed firstly at 250°C for long time (e.g. 300 min) to obtain the monomodal UFG microstructure and then the UFG nickel specimens were annealed at 500°C. The volume fraction and the mean grain size of the abnormal growing grains are plotted in figure 5.11. Abnormal grain growth is also known as the secondary recrystallization. however, when analyzing the abnormal grain growth phenomenon here analogue to the primary recrystallization, it can be seen that the curve for the volume fraction of the abnormal growing grains and annealing time follows the S-shape not so well. Actually, the simple exponential function

$$X_V = 7.1782 \cdot e^{0.0085 \cdot t} \tag{5.2}$$

fits the experimental data of the volume fraction of the growing grains well (figure 5.11a). However, developing the model for the abnormal grain growth is outside the scope of this work and the simple exponential law is accepted to describe the experimental data. At the same time, the classical law governing the grain growth (equation 2.7) cannot describe the grain growth kinetics for the abnormal grain growth process. There is no suitable function found to relate the mean grain size of the abnormal growing grains with the annealing time very well.

However, quite different results were detected for the other PED plate No.90 which was synthesized with the same parameters and conditions as the PED plate No.74. Abnormal grain growth was only found for the specimens from the PED plate No.90 after quite long annealing time (240 min and 360 min). Comparing the mean grain size of the normal growing grains it is larger in the specimens for the plate No.90 than that in specimens from the PED plate No.74 (figure 5.12). There is more abnormal

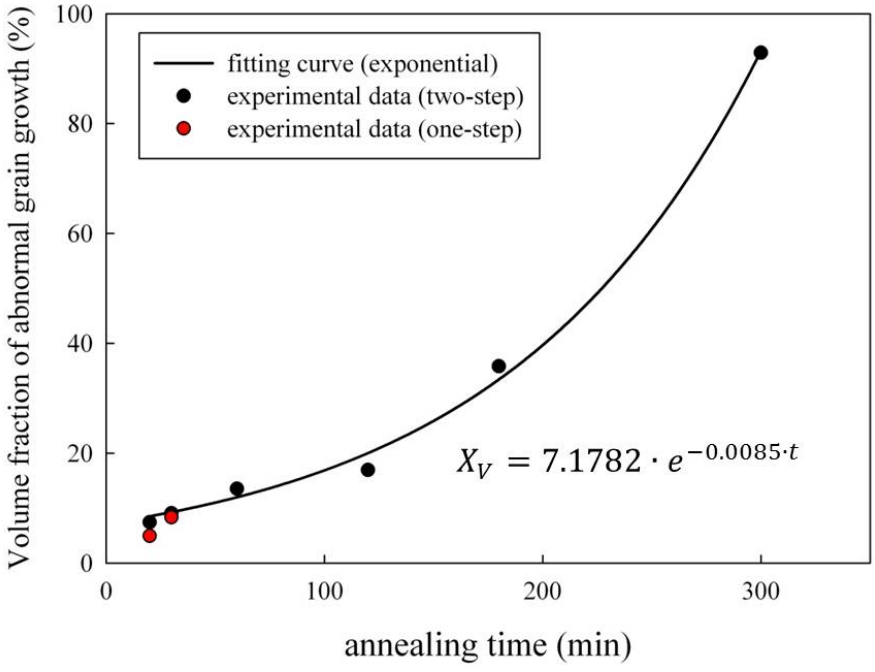

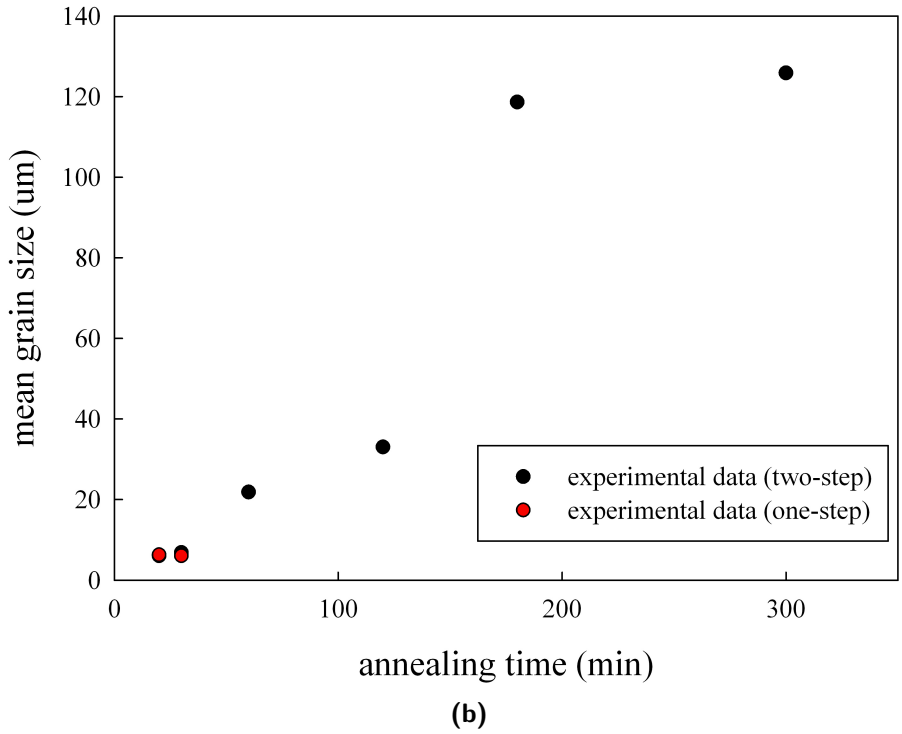

Figure 5.11.: (a) Volume fraction and (b) mean grain size of the ultrafine grains formed in the annealing process at 250℃ with increasing time.

grain growth in specimens from the plate No.74 but the mean grain size of the normal growing grains is smaller, while there is little abnormal growth occurring in specimens from the plate No.90 but the mean grain size of the normal growing grains is larger. It is concluded that normal grain growth and abnormal grain growth are competing processes during the annealing. When the abnormal grain growth favors, the normal growth is inhibited; and vice versa.

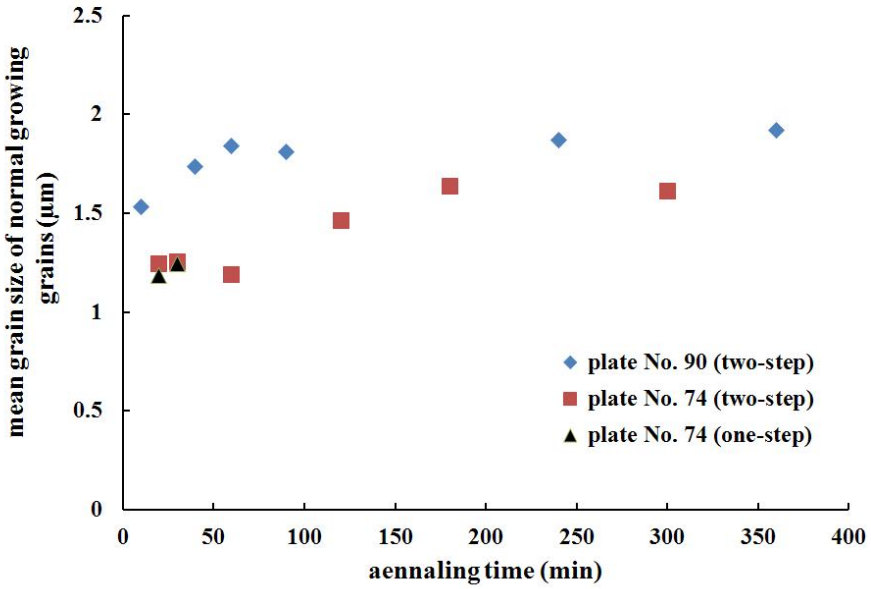

Figure 5.12.: Comparison of the mean grain size of the normal growing grains for plate No.90 and plate No.74 at 500 °C.

According to Riontino et al. abnormal grain growth takes place when particular conditions, such as impurities or slight plastic deformation, interfere with the simpler process of normal growth [*Riontino et al.*, 1979]. However, the experimental results by Randle and Horton showed that abnormal grain growth occurred easier in pure metals which was inconsistent with the classical theories for the mechanism of abnormal growth. In their work the nickel specimens with known purities (99.5% and 99.999%) were investigated and the results showed that there was more pronounced abnormal grain growth observed in a pure Ni than in an impure Ni specimen [*Randle and Horton*, 1994].

The results for the annealing experiments at 500 °C were unexpected, because the parameters and conditions in the synthesizing process for the both PED plates were held the same. The nickel samples processed by PED in this work are of high purity, as controlled in the synthesizing process. It is unavoidable of the impurities in the

chemical process for the PED plate synthesizing. However, there are no detectable impurities with the EDS detection in a high resolution SEM for both PED plates. It has not been found experimentally in which plate there are more impurities. Besides, it is also impossible to distinguish the two PED plates by the impurities using the existing theories because there are different statements according to the different researching groups. Therefore, to obtain a better understanding in the annealing process for the PED NC nickel with the normal and abnormal grain growth at elevated temperatures, more detailed works based on the impurities should be conducted in the future work.

Concluding remarks

When annealing the PED NC nickel at elevated temperature, i.e. at 500℃ in this work, continuous (normal) and discontinuous (abnormal) grain growth occur. The normal and abnormal grain growth are competing processes. In the specimens with abnormal grain growth, the mean grain size of the normal growing grains is slightly smaller than that in the specimens without abnormal grain growth. As the abnormal grain growth is also considered as the secondary recrystallization, the JMAK model is used to analyze the volume fraction of the growing grains, but the calculated curve is not so satisfying to the experimental data. The annealing time plays a marginal role in the continuous grain growth process, because there is a limiting grain size for the normal grain growth at a given temperature. It is also found that the initial microstructure, i.e. NC or UFG PED nickel, does not influence the ultimate annealing microstructures at the elevated temperature.

5.4. Influence of the microstructures to the microhardness

Microhardness is often used to reflect the resistance to the plastic deformation. Microindentation tests reveal the materials' strength according to the microhardness values and the materials' ductility based on the deformation around the indents. Pile-up and sink-in are the common phenomena for the materials with strain hardening. Observation of the indented area helps to understand the plasticity of the researching objectives. In a low strain hardening metal or alloy, plastically displaced material tends to flow up to (and pile-up against) the faces of the indenter due to the incompressibility of plastic deformation. On the other hand, for high strain hardening materials, the plastically deformed region is pushed out from the indenter with the imprint sinking below the initial surface level. The resultant impressions for pile-up and sink-in are 'barrel-shaped' and 'pin-cushion-like', respectively (figure 5.13) [*Giannakopoulos and Suresh*, 1999].

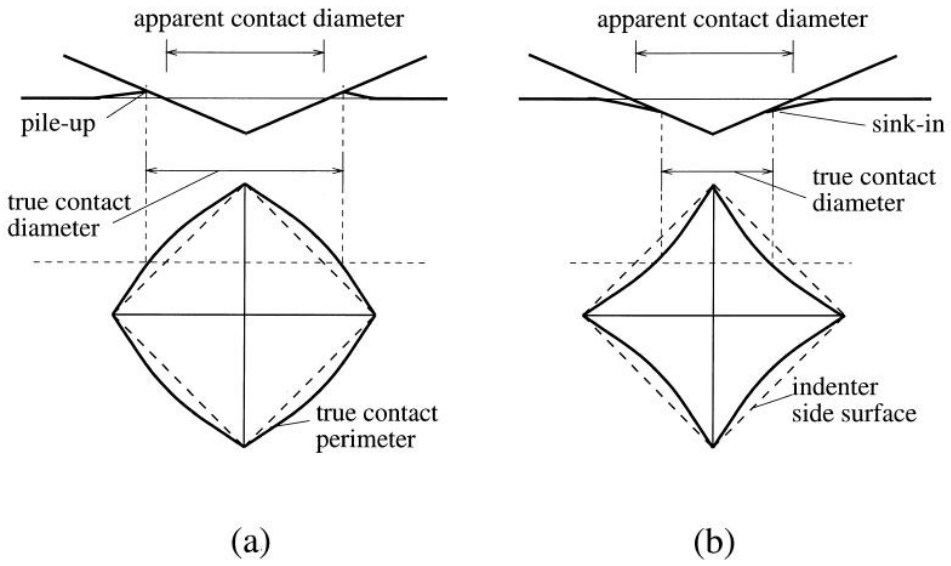

Figure 5.13.: Schematic illustrations of (a) pile-up and (b) sink-in around a indenter [*Giannakopoulos and Suresh*, 1999].

Table 4.5 shows the microhardness values to the corresponding microstructures. For the fine grained specimens such as the PED NC, NC/UFG and UFG nickel although low indenting force is applied in the indenting test, the indents are much larger then the grain size. Therefore, it is more appropriate to consider the microhardness as a 'quasi-global' mechanical property then a 'local' property for the fine grained materials.

Observing the microhardness (HV 318.6) for the bimodal NC/UFG microstructure with 50% volume fraction for both the nanograins and ultrafine grains, the microhardness is more influenced by the ultrafine grains in the NC/UFG microstructure.

Figure 5.14 shows the detailed information of the indented points of the NC, NC/UFG and UFG microstructures of the PED nickel specimens, where the same loading forces are used for the different microstructures. The NC nickel has the highest strength and shows almost no plastic deformation (pile-up or sink-in) around the indents. The indents are 'barrel-shaped' for the NC/UFG and UFG nickel and pile-ups are shown in the topography images. This result indicates the low strain hardening effect of the ultrafine grains. The plastic deformation in the NC/UFG nickel around the indents, which is comparable to that in the monomodal UFG nickel, indicates the preferred effect of the ultrafine grains in this microstructure under microindentation.

The microhardness for the coarse grains is a local property, because the indents are located inside the single grains. Figure 5.15 shows the indented points in the different areas in the micron/CG microstructure. 'Barrel-shaped' or 'pin-cushion-like' indents are observed in the different areas in the specimen, which are located in the low strain hardening micron grains and high strain hardening coarse grains, respectively. The HV value is added by the two components from the two separate phases, which is totally different from that in the fine grained materials.

The ECAP UFG nickel, both for route C and route E, has the similar mean grain size of the PED UFG nickel, however, the other microstructural characteristics are quite different. The HV values for these UFG nickel are similar to each other, which indicates that the microhardness is mainly determined by the grain size and less influenced by the other microstructural properties. Figure 5.16 shows an indent for the ECAP nickel. The microtextures influence the HV values little, but they have strong effect on the plastic deformation around the indents. There are many deformation 'fringes' parallel to the direction of the elongated grains which indicates the strong 'barrier-effect' of the high angle grain boundaries.

Figure 5.17 shows the experimental data about the microhardness for different nickel specimens, considering only the grain size. The trend that the microhardness increases with decreasing the grain size follows the Hall-Petch relationship. A fitting curve considering all grain sizes is plotted in which the Hall-Petch equation $HV = 124.36 + 20.749 \cdot d^{-0.5}$ is derived. However, it seems that it is more appropriate to divide the experimental values into two different ranges according to the grain size. For the grain size above and below 390 nm, the Hall-Petch relationship $HV = 74.533 + 41.146 \cdot d^{-0.5}$ and $HV = 208.46 + 15.316 \cdot d^{-0.5}$ are deduced. This result is in accordance to the work of

Yang in our institute who concentrated in a continuous grain size spectrum [*Yang*, 2006; *Vehoff et al.*, 2008]. The different slopes of the Hall-Petch plots are regarded as an indirect evidence of the transition in the deformation mechanism with the decreasing grain size. The volume fraction of the grain boundaries increases fast with decreasing grain size (figure 2.3), therefore, the grain boundary mediated mechanisms play increasing role in the plastic deformation of the fine grained materials.

Concluding remarks

From the above discussions, it can be concluded that the grain size is the main factor that determines the microhardness of a material with the monomodal grain size distribution. Comparing the pile-ups around the micro-indents for the UFG PED and ECAP nickel, plastic deformation of the both UFG materials is strongly influenced by the grain boundary properties. For the bimodal microstructures, the microhardness is significantly influenced by the grain size distributions. The microhardness is mainly determined by the UFG phase for the bimodal NC/UFG nickel, and it is the sum of the two components in the two different phases for the bimodal UFG/CG or micron/CG nickel. The microhardness is a quick method to know the materials' strength, maybe qualitatively the ductility, however, it is not enough to describe the materials' mechanical properties.

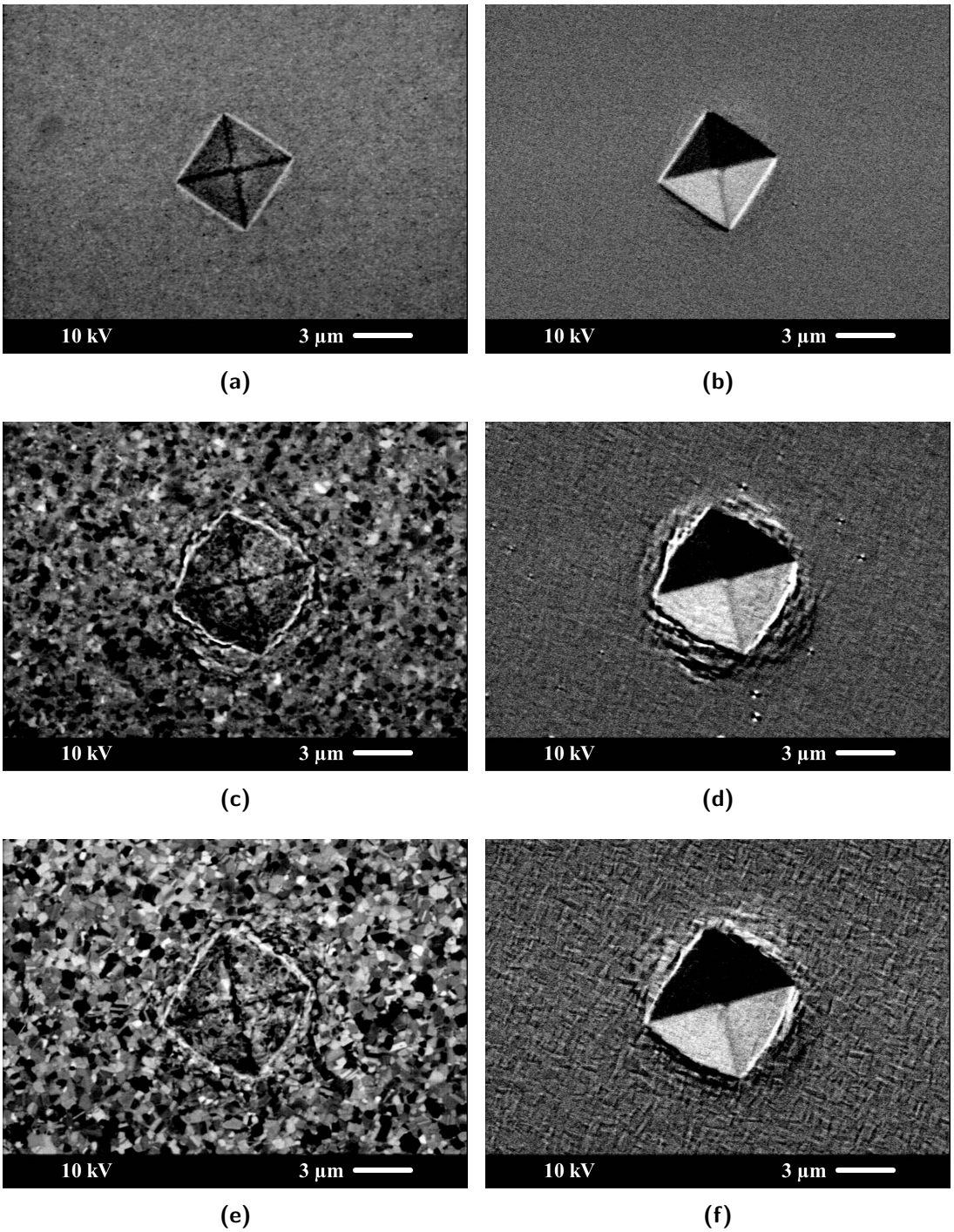

Figure 5.14.: SEM images for the indents of the microindentation tests for the (a)(b) NC, (c)(d) NC/UFG and (e)(f) UFG nickel, showing the (a)(c)(e) microstructure and (b)(d)(f) surface topography.

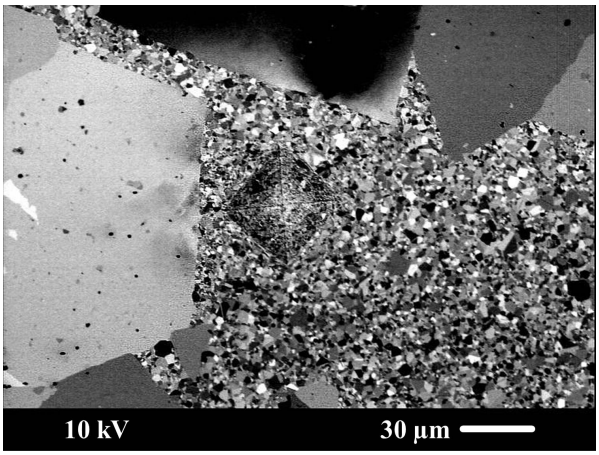

(a)

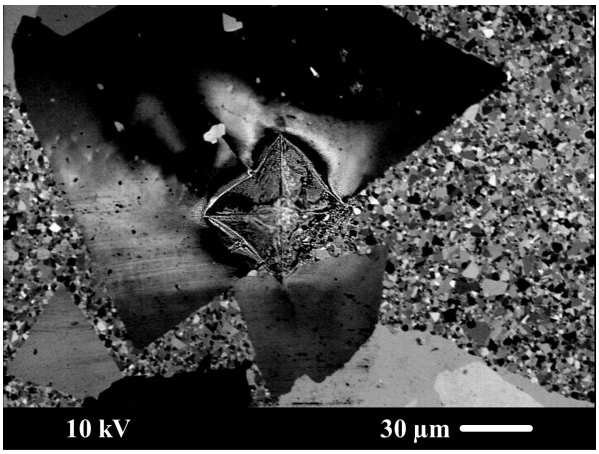

(b)

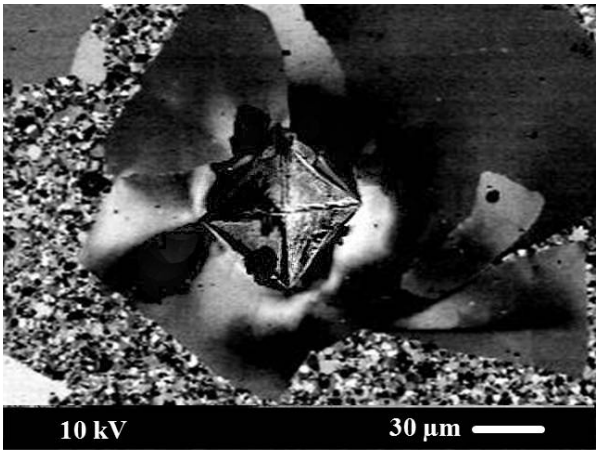

(c)

Figure 5.15.: SEM images for the indents in different areas in the micron/CG microstructures. (a) micron grained area, (b) transition area and (c) coarse grained area.

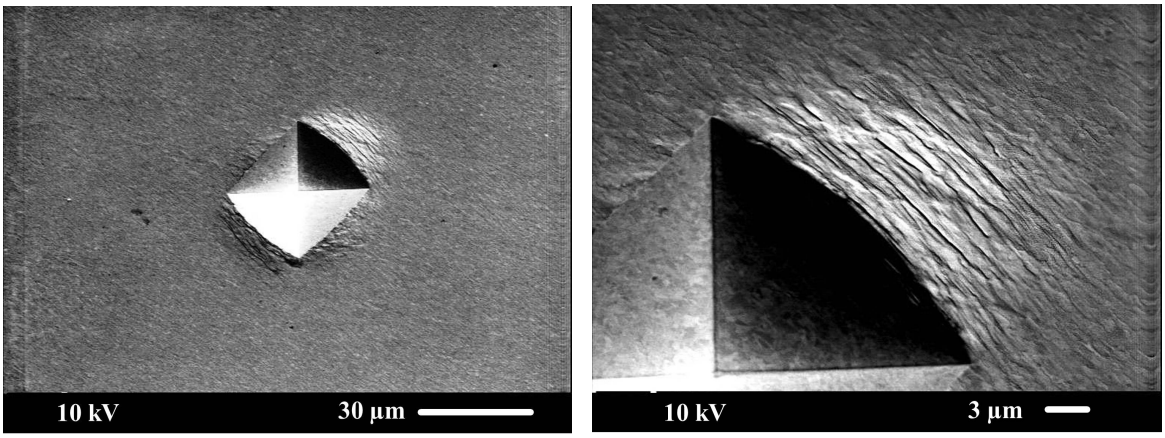

Figure 5.16.: Microhardness indents for the ECAP UFG nickel processed by route C.

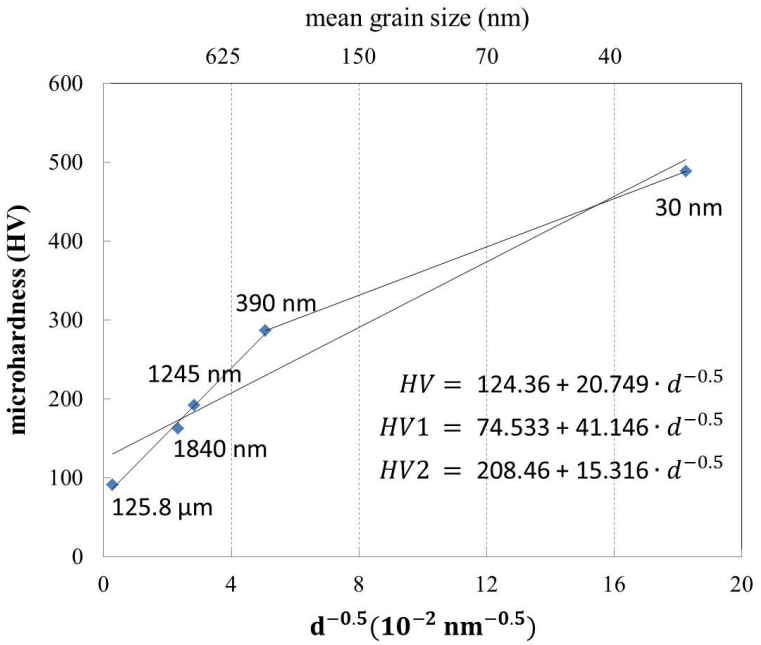

Figure 5.17.: Microhardness vs. mean grain size, analyzed based on the Hall-Petch relationship.

5.5. Influence of the microstructures to the tensile properties

Tensile tests on a series of the ECAP specimens with different microstructures (UFG, UFG/CG and CG) are carried out and the results are shown in figure 4.19. There is a continuous change in the strength and ductility with the increasing volume fraction of the coarse grains. Similar work was conducted by Zhao et al. with ECAP processed UFG copper in which the homogeneous bimodal microstructures mixed of the original ultrafine grains and recrystallized coarse grains were achieved [*Zhao et al.*, 2011]. However, the homogeneous bimodal microstructures were not achievable in this work although the same starting UFG microstructures as in the literature were applied. The distribution of the recrystallized coarse grains were strongly influenced by the microtextures from the ECAP process, more accurately to say, influenced by the original coarse grains before the ECAP process, as shown in figure 4.7.

The yield strength decreases, while the uniform elongation increases with increasing volume fraction of the recrystallized coarse grains. It is suggested from some authors that the rule-of-mixtures relationship can be used to describe the yield strength and uniform elongation [*Han et al.*, 2005; *Gubicza et al.*, 2007; *Zhao et al.*, 2011]:

$$\sigma = (1 - X_V)\sigma_{UFG} + X_V\sigma_{CG} \tag{5.3}$$

$$\epsilon = (1 - X_V)\epsilon_{UFG} + X_V\epsilon_{CG} \tag{5.4}$$

where σ_{UFG} and σ_{CG} are the yield strengths, and ϵ_{UFG} and ϵ_{CG} are the uniform elongation values of the UFG matrix and coarse grains, respectively. However, the yield strength of the bimodal nickel with higher volume fractions is difficult to be determined in this work, because of the early yielding of the coarse grains areas. Nevertheless, an analysis on the ultimate tensile strength is conducted based on the rule-of-mixtures based on the data in Table 4.6 (figure 5.18). It can be qualitatively assessed that the rule-of-mixtures correlates the mechanical properties to the volume fraction of the recrystallized coarse grains not so well due to the inhomogeneous distribution of the two different phases. Taking consideration of the annealed specimens No.3 and No.4, in which the volume fraction of coarse grains are $39.4 \pm 11.4\%$ and $87.2 \pm 2.8\%$, the stress-strain curves are quite similar to each other (figure 4.19).

The deformed surfaces of the bimodal UFG/CG nickel are investigated in SEM after

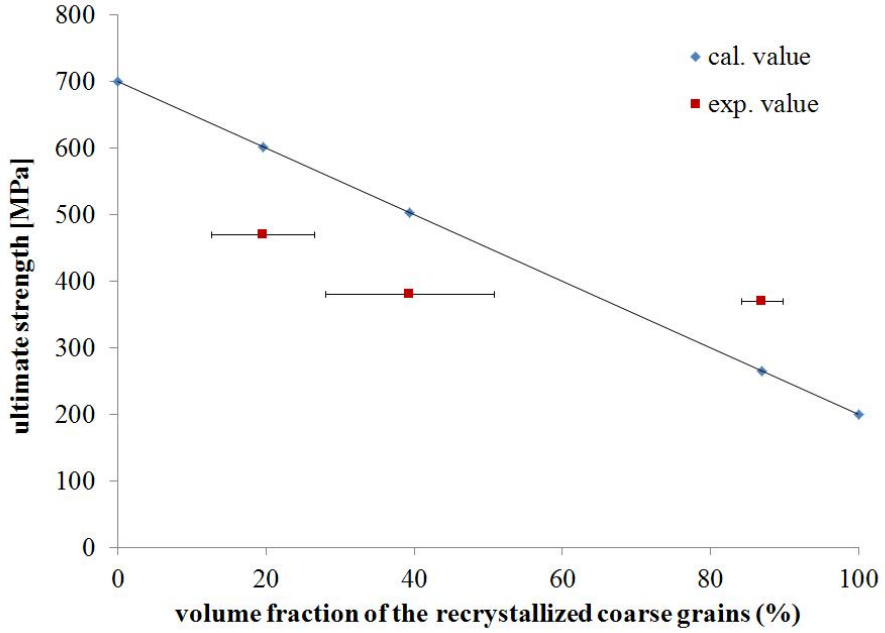

Figure 5.18.: The measured ultimate strength of the bimodal UFG/CG nickel with different volume fraction of the recrystallized coarse grains, compared with the calculated values based on the rule-of-mixtures relationship.

the tensile tests. Figure 5.19a,b, Figure 5.19c,d and Figure 5.19e,f are corresponding to the specimens with $19.6 \pm 7.0\%$, $39.4 \pm 11.4\%$ and $87.2 \pm 2.8\%$ volume fraction of coarse grains after the strain of 10.5%, 20% and 23%, respectively. Secondary electron images and backscattered electron images are both displayed, in order to show the surface deformation and corresponding microstructures clearly. It can be observed that the plastic deformation occurs preferentially in the coarse grained areas. For the specimen with 19.6% coarse grains, it has the strength about 500 MPa and 10% homogeneous elongation. The deformed coarse grained areas are pointed out by the black arrows, and the UFG matrix stays undeformed. Despite there are only few coarse grains in the specimen, the plastic deformation still concentrates there. The bimodal UFG/CG specimens exhibit increasing ductility when the volume fraction of the coarse grains increases. The specimen of 39.4% coarse grains has a homogeneous elongation about 20%. Strong plastic deformation takes place in the coarse grains (figure 5.19c). The UFG areas next to the coarse grains begin to deform and the other UFG areas still stay undeformed. However, in the specimen with even higher volume fraction of coarse grains (e.g. 87.3%) there are slip bands in the UFG areas. This is because the coarse grains can not endure all the plastic deformation inside themselves and there is very strong local deformation around the UFG areas.

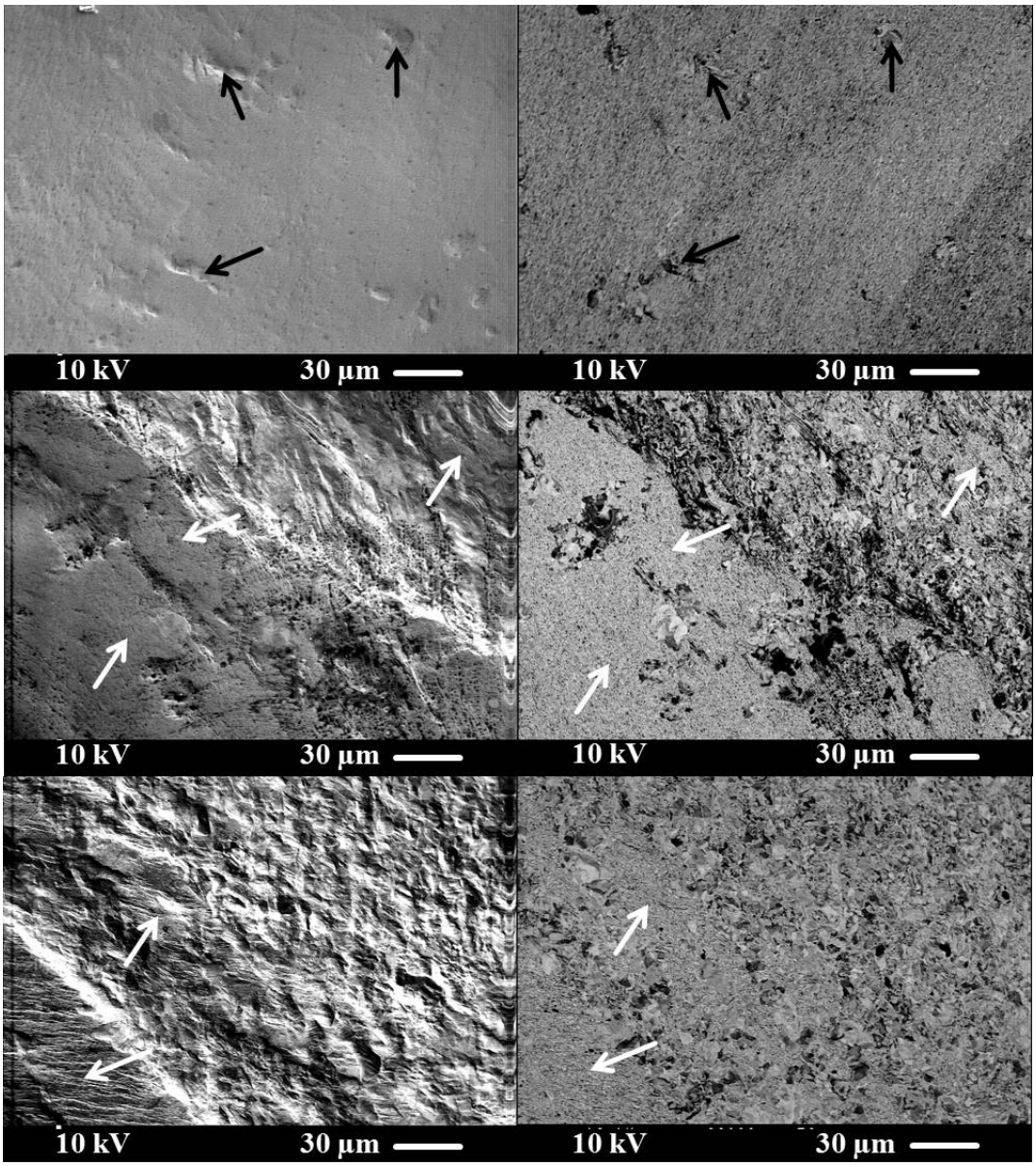

Figure 5.19.: SEM images of the deformed surfaces of the bimodal UFG/CG nickel after tensile experiments. (a)(c)(e) secondary electron images and (b)(d)(f) backscattered images, with the white arrows showing the CG areas and black arrows showing the UFG areas.

It is concluded that the bimodal UFG/CG microstructures, annealed from the ECAP UFG nickel, combine the strength of the ultrafine grains and the ductility of coarse grains. With a proper volume fraction of the coarse grains, the bimodal microstructure balances the mechanical properties, such as enhanced yield strength and ultimate tensile strength, and considerable ductility compared to their monomodal CG or UFG counterparts. The plastic deformation concentrates in the CG areas, even if there is only low volume fraction of the coarse grains. There are deformation bands formed in the UFG areas when large local plastic deformation occurs.

However, due to the complexity of the initial microstructures of the ECAP nickel it is difficult to achieve the bimodal microstructures with homogeneous distribution of the recrystallized coarse grains upon normal annealing. New method, i.e. annealing with the laser beam, has been attempted (Appendix D). The advantage of the laser treatment is that the annealed areas can be controlled, even the orientation. The disadvantage is that only the microstructures on the surface area can be modified and the grain sizes show multiple distributions in the heat influenced areas.

Concluding remarks

Introducing coarse grains into the UFG matrix of the ECAP nickel improves the ductility of the material, but with the loss in strength at the same time. It is a compromising concept of the bimodal microstructures to combine the materials' strength and ductility. Nevertheless, it is a promising method to adjust the two main mechanical prosperities of the materials, according to the practical applications. The complexity in the initial microstructures, i.e. microtextures, different dislocation densities in different areas, of the ECAP nickel makes it difficult to obtain a homogeneous mixture of the ultrafine grains and the coarse grains.

5.6. Influence of the microstructures of PED nickel to the fatigue properties

5.6.1. Crack growth behaviour of different microstructures

The experimental results indicate that microstructures of the fine grained PED nickel significantly influence the crack growth behaviour, thus the fatigue properties. It is shown in section 4.5.1 that the PED nickel with different microstructures (monomodal NC, bimodal NC/UFG and monomodal UFG) is sensitive to the microcracks in the fatigue experiments. Figure 4.21 shows that, although the strength of the NC nickel is much higher than that of the UFG nickel, the microcracks begin to propagate at the same applied fatigue stress for the two microstructures. At the same time, the bimodal NC/UFG nickel in which there is about 50% volume fraction for both the nanograins and ultrafine grains shows much lower strength than the NC nickel and only minor higher strength than the UFG nickel, according to the microhardness measurements. However, the microcrack in the specimen begins to grow at a much higher fatigue stress, and considerably improved damage tolerance is observed for the bimodal NC/UFG nickel.

When the crack begins to grow under a constant stress amplitude, the crack growth rate is found to follow the accelerating trend with increasing fatigue cycles (figure 5.20). However, the experimental results show totally different fatigue crack growth behaviours for the NC and UFG nickel than found by Hanlon et al. in figure 2.16. In their work, the crack in the NC nickel was found to propagate faster than that in the UFG nickel when all the experimental conditions were held constant [*Hanlon*, 2004]. The different results are observed because different starting cracks are applied. The macro-notches with the length 1 mm were introduced in the literature and the microcracks with the length 100 μm are initiated in this work. It is demonstrated that the microstructures having higher strength possess the better crack resistance to the microcracks. Besides, it is shown in the figure that there is no crack propagation for the bimodal NC/UFG nickel under 300 MPa. The microcrack begins to grow under 400 MPa, with an increasing crack growth rate.

Among the three microstructures, the bimodal NC/UFG nickel is found to have the improved damage tolerance, which is attributed to the combination of the high strength and improved ductility. The nanograins and ultrafine grains ensure the strength and ductility respectively in the bimodal microstructures. Actually, combining the strength and ductility to obtain the better damage tolerance for the fine grained materials, was also achieved by some others but with different methods [*Sangid et al.*, 2011; *Singh*

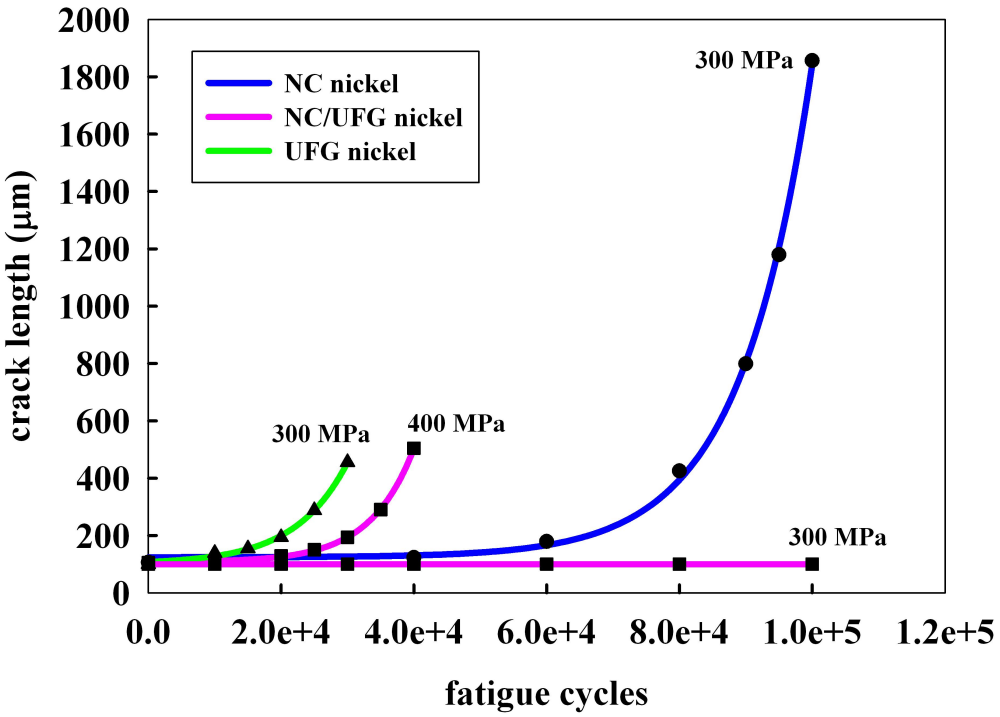

Figure 5.20.: The total crack length as a function of the number of fatigue cycles for the PED NC, NC/UFG and UFG nickel. The initial stress for crack growth is 300 MPa for the NC and UFG nickel. The microcrack in the NC/UFG nickel begins to propagate under 400 MPa.

et al., 2011].

To understand the crack growth resistance of the different microstructures, the crack growth rates are analyzed as the function of the stress intensity factor (figure 5.21). The ΔK_I is calculated using the geometry factor for the semi-circular crack form for simplification, although the crack depth profiles are becoming semi-elliptical as the cracks grow. Comparing the experimental results with the different regimes of fatigue crack propagation, it seems that they lie mainly in the regime I, although the crack propagation rates are much higher than 10^{-6} mm/cycle. It is known that crack propagation depends on the microstructures and the flow properties of the materials, and the crack growth rate is sensitive to the materials' grain size in regime I [*Suresh*, 1998]. Taking the last measuring point for the UFG nickel as a reference where ΔK_I is 7.5 MPa $m^{1/2}$, the crack growth rates are $2 \cdot 10^{-5} - 5 \cdot 10^{-5}$ mm/cycle, i.e. $20 - 50$ nm/cycle, for the different fined grained microstructures. Therefore, the effect of the grain size, i.e. the microstructure, is unavoidable to the crack growth rate. It is demonstrated in figure 5.21

that the microcracks grow faster in the monomodal NC nickel and the monomodal UFG nickel than that in the bimodal NC/UFG nickel. Among them, the UFG nickel shows the highest crack growth rate under the same stress intensity factor. It is concluded that the NC nickel exhibits higher resistance to the microcracks than the UFG nickel, and the bimodal NC/UFG nickel performs as the best among the three microstructures when fatigued against the microcracks.

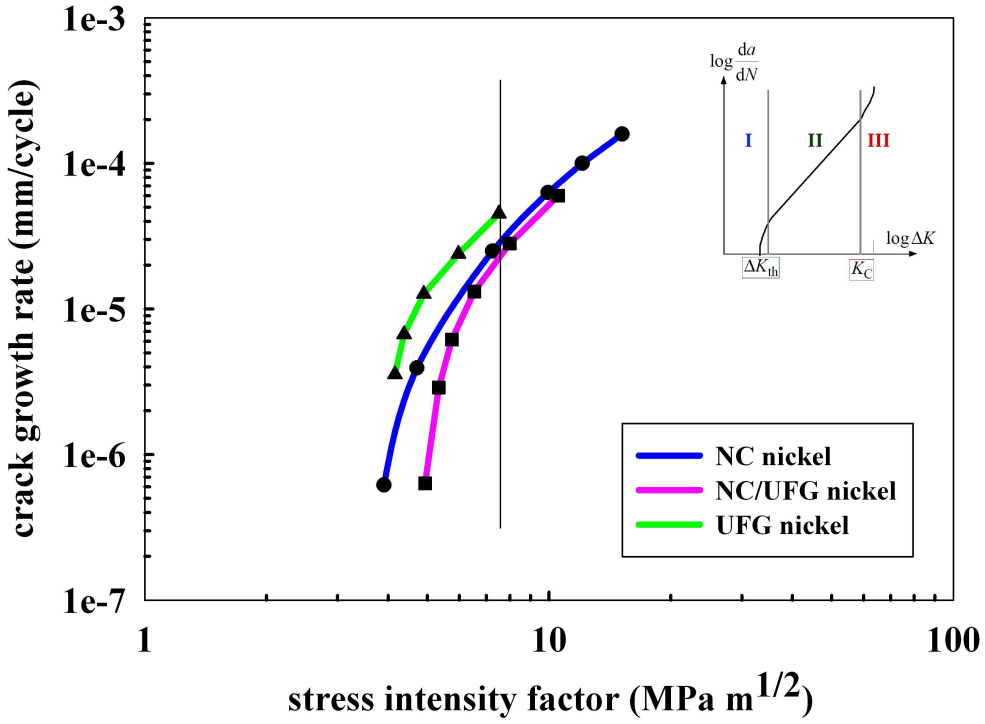

Figure 5.21.: Crack growth rate of the NC, NC/UFG and UFG nickel according to ΔK_I calculated based on the experimental data in figure 5.20.

An overview of the crack growth path on the specimen surface for the monomodal NC nickel in the optical microscope is shown in figure 4.23. The crack propagates along the initial direction which is perpendicular to the applied stress. When the crack length becomes large, unstable crack growth occurs where the crack propagation deviates from the initial direction till ultimate fracture happens. Similar surface crack growth paths are observed for the bimodal NC/UFG nickel and the monomodal UFG nickel in which there are shorter stable crack growth length.

Further observation of the stable crack propagation is carried out with a SEM as shown in figure 5.22 in which the subfigures (a)(b), (c)(d) and (e)(f) are corresponding to the NC, NC/UFG and UFG nickel, respectively. The backscattered electron images show the microstructure explicitly and the secondary electron images show the surface topologies clearly.

The figures show clearly that the nanograins and ultrafine grains behave differently in the crack propagation. There is no plastic deformation observed in the NC nickel, because the grains are too small for dislocation movement. The crack grows directly along the grain boundaries, i.e. the crack propagates intercrystallinely during the fatigue experiments. The surface areas along the crack paths are rarely influenced and no micro-extrusions form during the crack propagation (figure 5.22b). Therefore, the NC nickel shows the brittle manner in the fracture.

The ultrafine grains along and around the crack path in the UFG nickel are found to be plastically deformed as indicated by the slip lines inside the grains, however, with different severities. The crack propagated either intercrystallinely or intracrystallinely in the UFG nickel, depending on the severity of plastic deformation occurring in the corresponding grains (figure 5.22e). The ductility of the UFG nickel is improved because of the deformation capacity of the ultrafine grains, but the strength of the material is lower comparing to the NC nickel. The microcracks in the monomodal NC and monomodal UFG nickel specimens begin to grow at the comparable stress amplitude, either in beneficial of the high strength or the improved ductility. Furthermore, the NC nickel with higher strength exhibits the better damage tolerance to the microcracks (figure 5.20 and figure 5.21). There are lots of micro-extrusions observed in the ultrafine grains along the crack growth path in the secondary electron image, which indicates the severity of the deformation inside the grains (figure 5.22f).

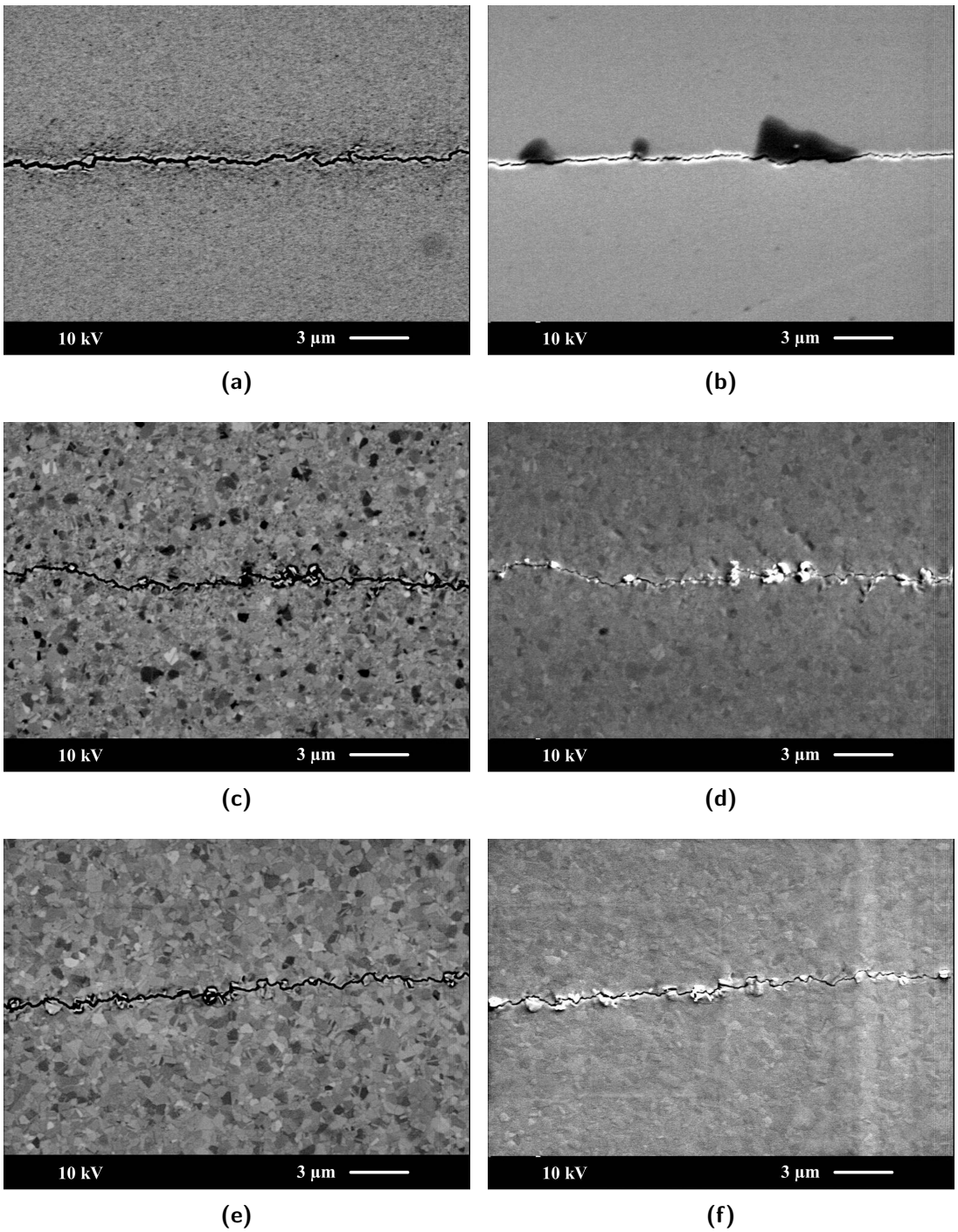

Figure 5.22.: Backscattered and secondary electron micrographs of the crack propagation in (a)(b) NC nickel, (c)(d) NC/UFG nickel and (e)(f) UFG nickel.

The microcracks propagate intercrystallinely along the nanograins and less deformed ultrafine grains, and intracrystallinely through the severe plastically deformed ultrafine grains in the bimodal NC/UFG nickel. Due to the deformation capacity of the ultrafine grains, the NC/UFG nickel shows better ductility than the NC nickel. Meanwhile, the strength of the NC/UFG nickel is higher than that of the UFG nickel. The combination of strength, which is originated form the nanograins, and ductility, which is ensured by the ultrafine grains, induces a higher microcrack growth resistance than the monomodal NC or UFG nickel. Similarly to that in the UFG nickel, there are micro-extrusions on the specimen surface in the severely deformed ultrafine grains along the crack path, as shown in the secondary electron image in figure 5.22d.

Figure 5.23 shows the backscattered electron image of crack propagation path in the bimodal NC/UFG nickel using a high resolution SEM. It shows clearly the areas of the nanograins and ultrafine grains. The grains along the crack propagation path are marked out according to their characteristics and crack growth modes where the intercrystalline crack growth along the nanograins are marked with the violet lines, the intercrystalline crack growth along the ultrafine grains are marked by the cyan-blue polygons and the intracrystalline crack growth througth the ultrafine grains are marked with the red polygons. The ultrafine grains behave differently according to their grain size. Besides, the severity of the deformation of the ultrafine grains decreases with the increasing distance to the crack path. The plastically deformed grains are characterized by the activated slip bands inside the grains. Actually, the grains with slip bands inside are those ultrafine grains around the crack path which have comparably larger grain sizes. The ultrafine grains with the annealed twins inside behave as the 'hard' grains, in which no plastic deformation is detected.

An overview of the fracture surfaces is shown in figure 4.24. The cracks propagate along the initial directions, both by the specimen surface and in the depth. Figure 5.24 shows the fracture surface of the stable crack propagation area down to the grain size level. Intercrystalline crack propagation is clearly observed for the nanograins. Meanwhile, the mixed mode of intercrystalline and intracrystalline crack growth is revealed in the bimodal NC/UFG nickel and in the monomodal UFG nickel where the intercrystalline and intracrystalline crack growth along the ultrafine grains are marked with the cran-blue and red polygons, respectively. Besides, pure intercrystalline crack propagation in monomodal UFG nickel is observed when the overload fracture happens, in which there is no observing plastic deformation in the ultrafine grains (figure 5.25).

Finally, the crack growth profile in the fracture surface is investigated after the specimens have failed via fracture, as shown in figure 5.26. The initial crack profile is

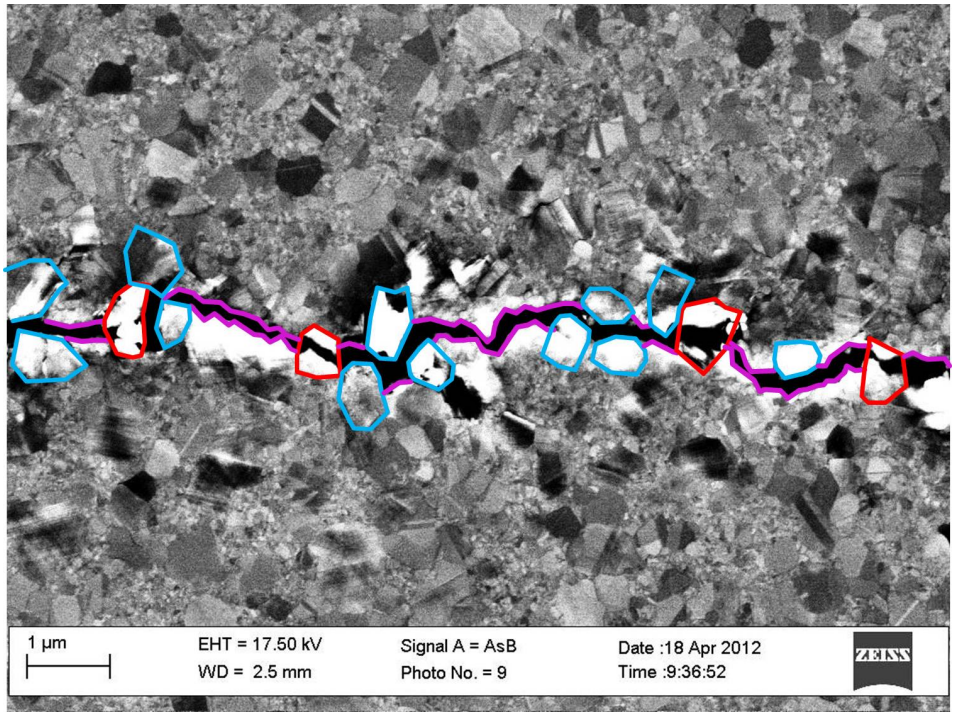

Figure 5.23.: Image of the crack propagation path using high resolution SEM in the bimodal NC/UFG nickel in which the intercrystalline crack growth along the nanograins are marked with the bright violet lines, the intercrystalline crack growth along the ultrafine grains are marked by the cyan-blue polygons and the intracrystalline crack growth througth the ultrafine grains are marked with the red polygons.

semi-circular (a:c=1:1). However, analysis on the fracture surface reveals that the crack growth rates along the specimen surface and along the depth are different, i.e. the crack propagation rates are heterogeneous along the different directions in the fatigue experiment. The ratios of the surface crack length and the crack depth are

$$(\frac{a}{c})_{(NC)} = \frac{1040\ \mu m}{1329\ \mu m} \approx \frac{4}{5} \tag{5.5}$$

$$(\frac{a}{c})_{(NC/UFG)} = \frac{492\ \mu m}{872\ \mu m} \approx \frac{3}{5} \tag{5.6}$$

$$(\frac{a}{c})_{(UFG)} = \frac{1329\ \mu m}{1072\ \mu m} \approx \frac{6}{5} \tag{5.7}$$

for the NC, NC/UFG and UFG nickel, respectively. The crack growth rate along the specimen surface is faster than that along the depth for the NC and NC/UFG nickel and the opposite result is found for the UFG nickel.

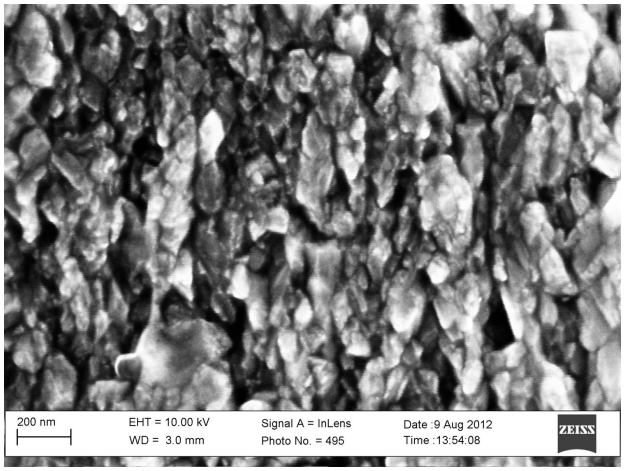

(a)

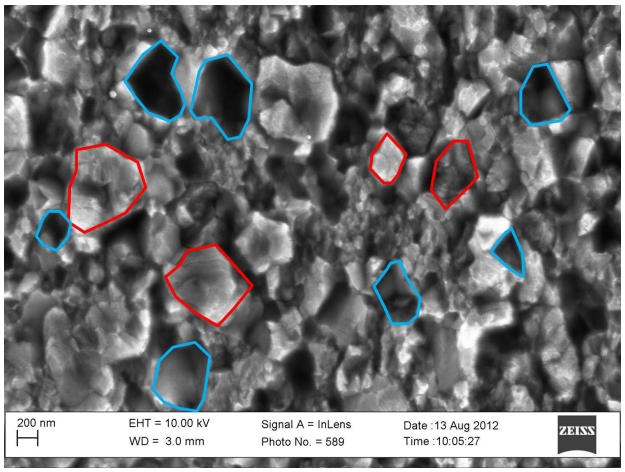

(b)

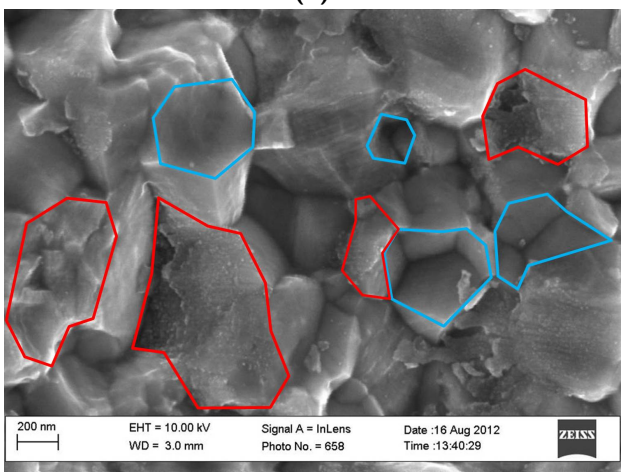

(c)

Figure 5.24.: High resolution SEM images of the fracture surface for the (a) NC nickel, (b) the NC/UFG nickel and (c) the UFG nickel. The intercrystalline and intracrystalline crack growth along the ultrafine grains are marked with the cran-blue and red polygons, respectively

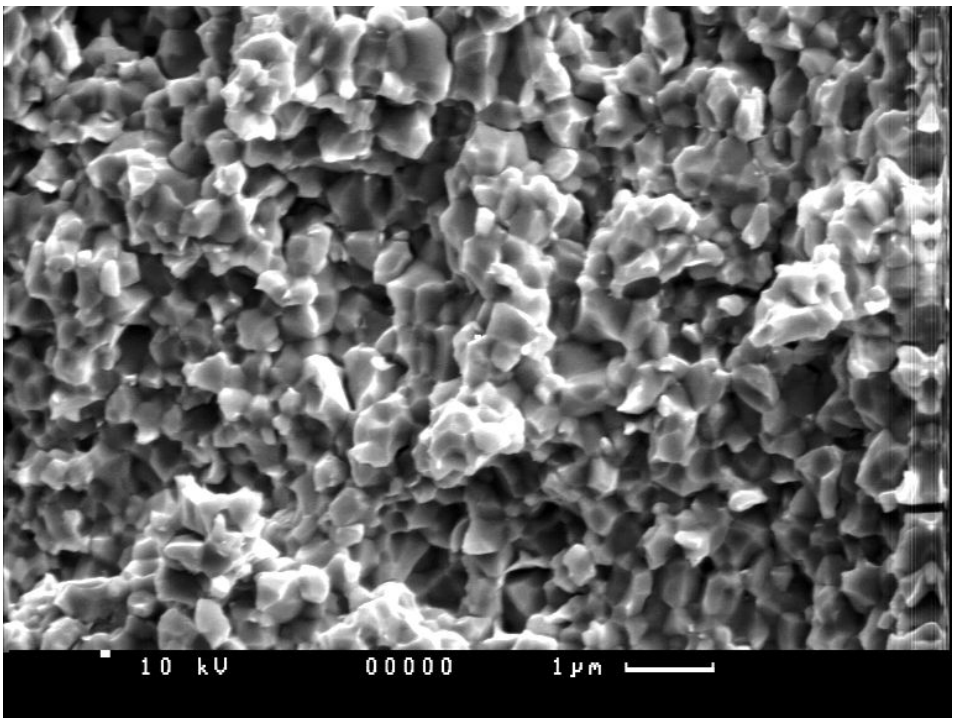

Figure 5.25.: Intercrystalline crack growth in the UFG nickel by overload fracture.

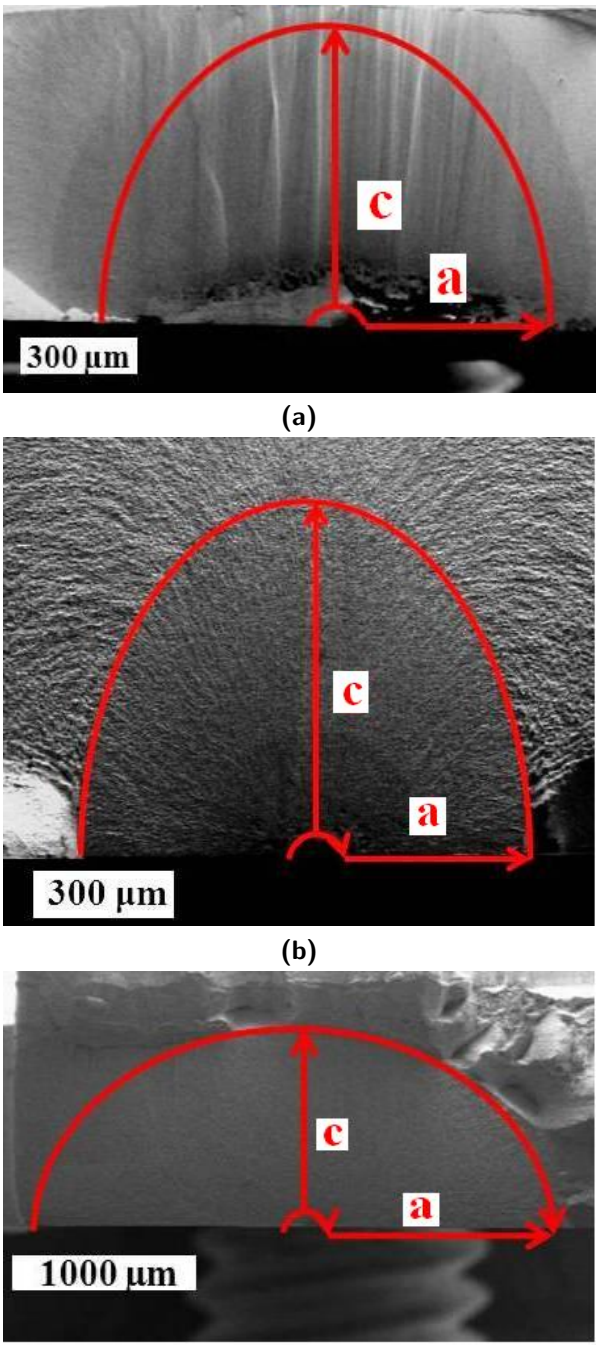

Figure 5.26.: Crack growth profiles in the fracture surfaces for (a) NC, (b) NC/UFG and (c) UFG nickel.

Concluding remarks

Fatigue behaviour, especially the fatigue crack resistance, of the fine grained nickel with different microstructures (monomodal NC, bimodal NC/UFG and monomodal UFG), is investigated with the aid of the FIB initiated microcracks on the specimen surface. The specimens with different microstructures are fractured due to the growth of the microcracks. Despite large difference in the strength of the monomodal NC and the monomodal UFG nickel, the microcracks in the two microstructures begin to grow at similar fatigue stress. The monomodal NC nickel is of the highest strength but lacking of the capacity for the plastic deformation, and the monomodal UFG nickel behaves in the opposite way. Therefore, the fatigue crack resistance of the materials is determined simultaneously by their strength and ductility. The bimodal microstructure mixed of the nanograins and ultrafine grains exhibits the highest fatigue crack resistance among the three microstructures. The combined high strength of the nanograins and high ductility of the ultrafine grains ensure the better fatigue performance of the bimodal NC/UFG nickel.

5.6.2. In-situ fatigue experiment for the bimodal NC/UFG nickel

In order to understand the role of the nanograins and ultrafine grains in the microcrack propagation, the in-situ fatigue experiments were conducted. As shown in section 4.5.2, the bimodal NC/UFG nickel specimen was firstly loaded in ex-situ fatigue experiment and the microcracks began to grow under the stress amplitude 350 MPa. After 70,000 cycles, the crack propagated 192.89 μm from the left crack tip and 181.30 μm from the right crack tip, i.e. there was the total crack length of $\sim$ 500 μm (474.19 μm).

The crack began to grow under 350 MPa in ex-situ fatigue experiment and propagated to about 500 μm before the in-situ experiment. The main difference between the in-situ and ex-situ fatigue experiments was that the specimens were loaded in vacuum or in air. Therefore, the environmental effect should be considered when comparing the stress effect on the crack growth. Water vapor in air is known to accelerate the fatigue crack growth rate for many metals and alloys [*Pao et al.*, 2009; *Vasudevan and Sadananda*, 2009]. Considering only the concept of the stress intensity factor (ΔK_I), an equivalent stress about 160 MPa could cause the crack to propagate further. However, the crack began to grow until the stress amplitude was increased to 350 MPa. It was because that the chemical effect in the laboratory air was eliminated in the vacuum condition in the SEM. Therefore, higher stress was required to induce the crack to propagate in the in-situ fatigue experiment.

Figure 5.27 shows the crack opening under different stresses from tension 300 MPa to compression -300 MPa. It can be seen that the crack is open to different extend under tension and closed under compression. Actually the crack tip is already closed under tension, as indicated in the figure under 200 MPa.

The in-situ crack propagation is shown in section 4.5.2. Due to the shield of the contamination deposition in the SEM chamber the crack propagation, relating to the microstructures, is not very clearly revealed with increasing loading cycles. However, the crack growth in the first 250 cycles under 300 MPa with $R = -1$ is shown detailedly in figure 5.28. In this circumstance the crack travels along an ultrafine grain firstly and then goes through the nanograins. It can be seen that it takes about 200 cycles for the crack going around the ultrafine grain ($\sim$ 1.5 μm) and only 50 cycles propagating approximately the same distance through the nanograins, which is marked between the lines. It is the first direct observation that the ultrafine grains behave as the stronger obstacle for the crack propagation than the nanograins. Therefore, introducing the ultrafine grains into the nanograined matrix is a viable method to improve the materials crack propagation resistance.

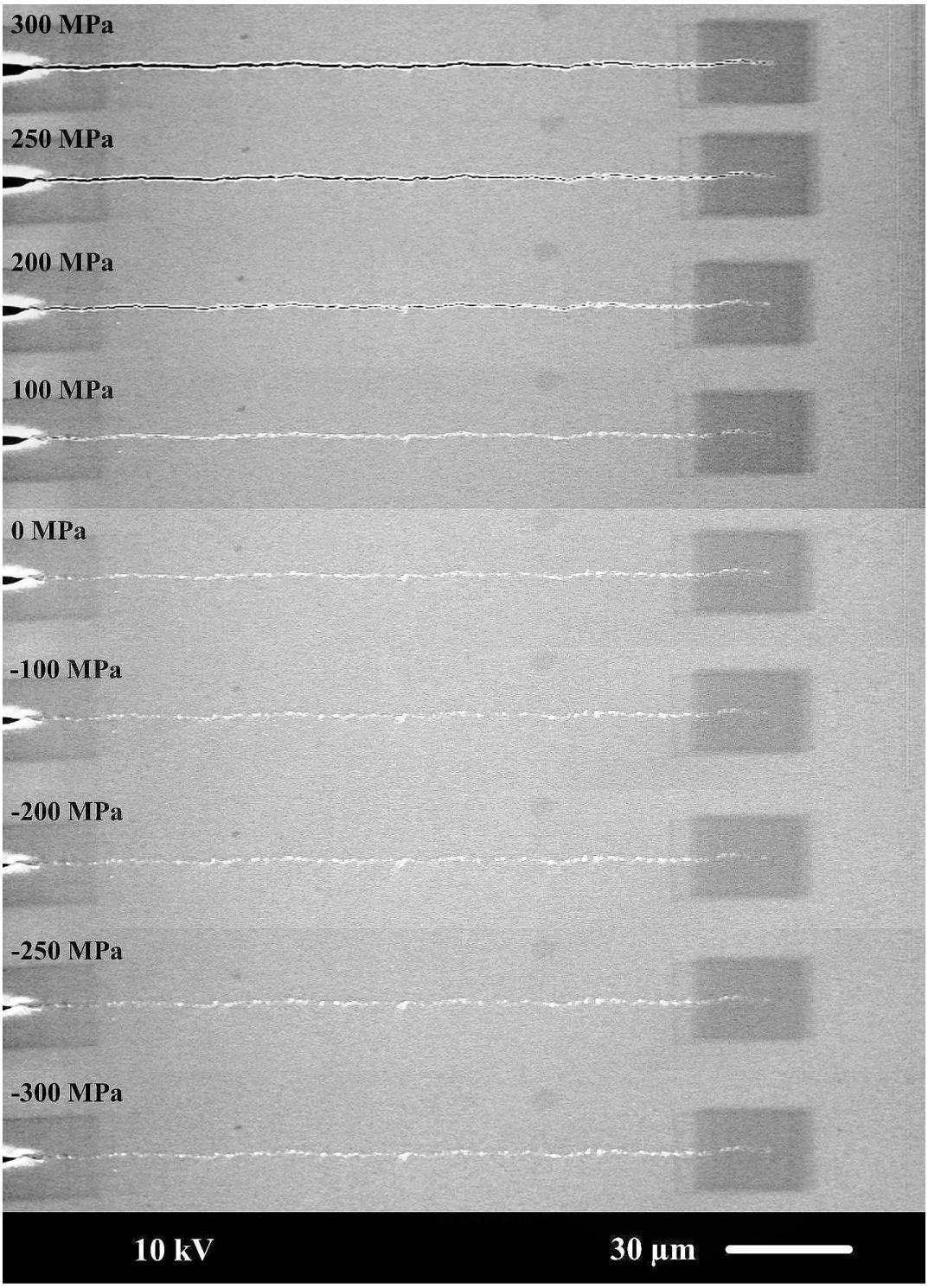

Figure 5.27.: The microcrack opening and closure under different stresses in the in-situ fatigue experiment.

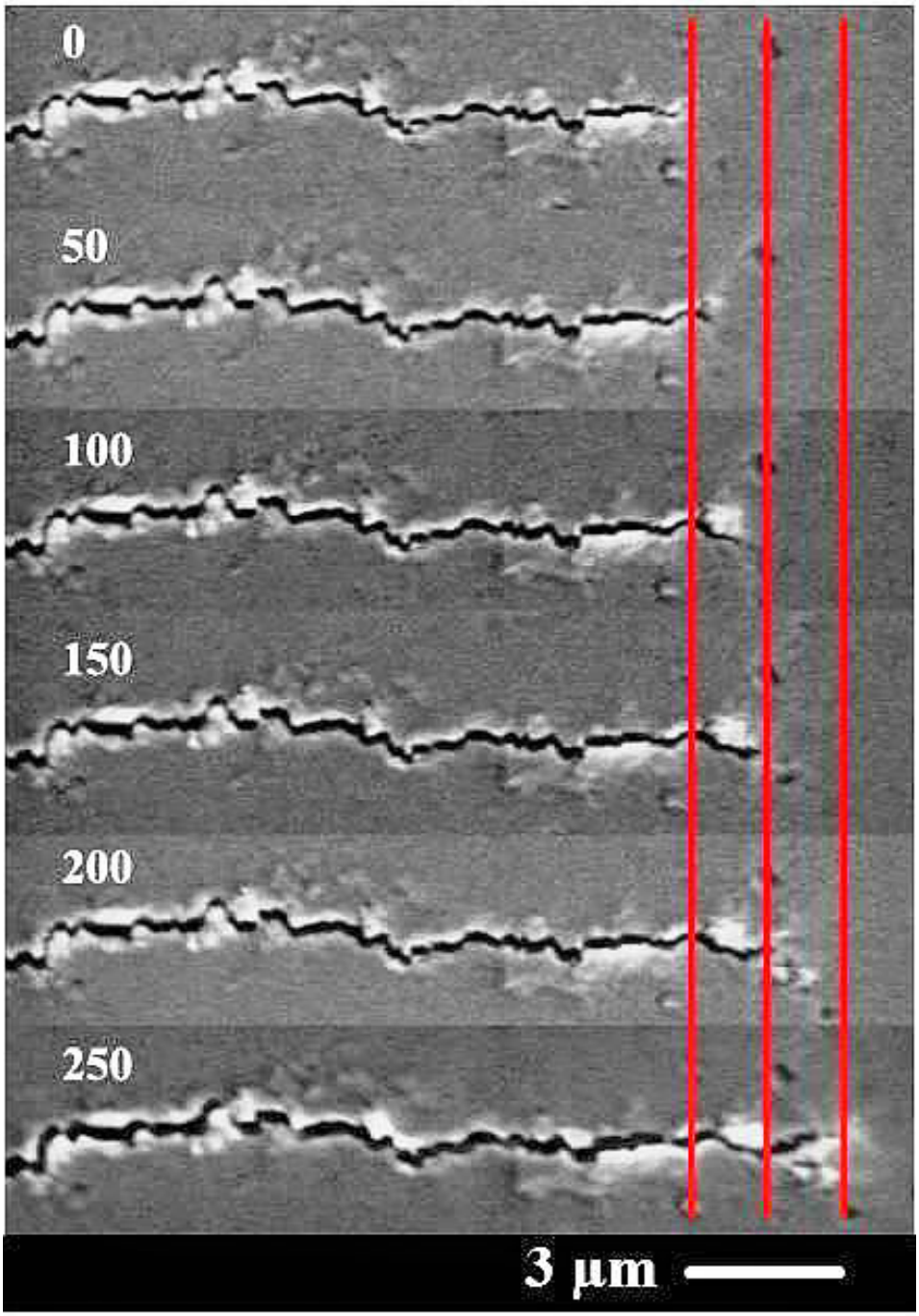

Figure 5.28.: In-situ observation of the crack propagation through the ultrafine grain and the nanograins. This specimen was loaded under 300 MPa with the loading ratio R=-1.

A post observation was conducted after the specimen surface had been cleaned with the plasma cleaning system (Gatan Solarus^{TM} model 950). Figure 5.29 shows the crack propagation path in the in-situ fatigue test after the surface cleaning. Crack growth with the two different loading ratios is exhibited, which is marked by the lines. The area marked with the rectangle is the transition area between two different loading ratios. Because of the resolution of the SEM and the shielding of the surface contamination, the microstructures could not be directly shown in figure 4.26 and figure 4.27. The crack propagation under the two different loading ratios can be distinguished, because the plastically influenced areas around the crack tip are different with the two different ratios, i.e. there is larger influenced area under the loading ratio R = 0.1.

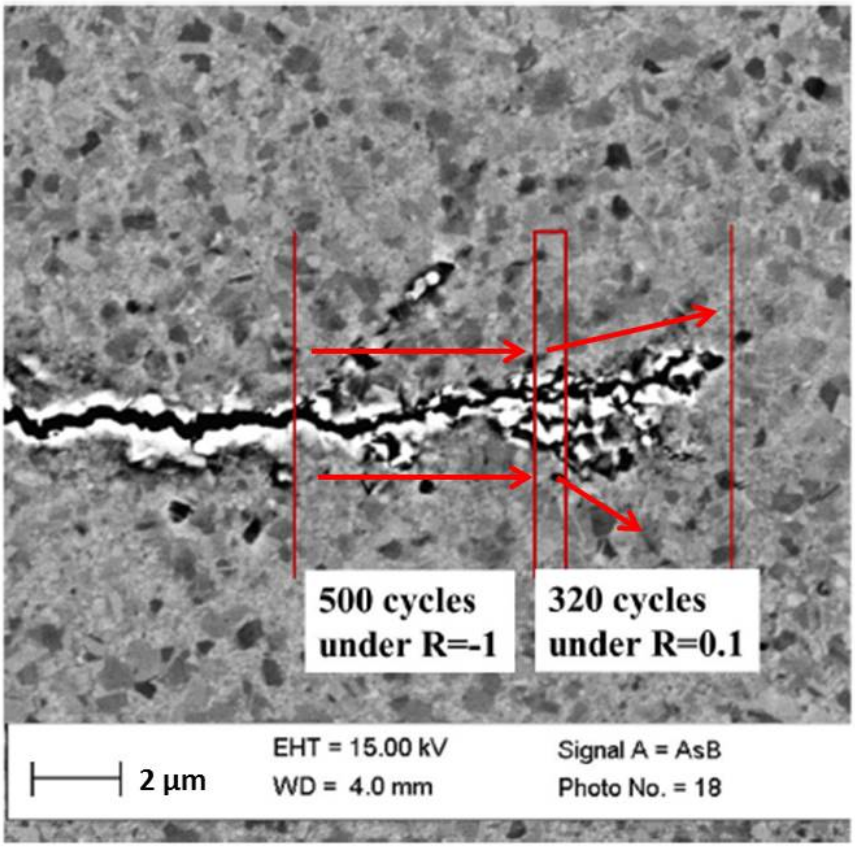

Figure 5.29.: Observation of the crack growth area in high resolution SEM after the surface cleaning.

The crack growth rates in the in-situ fatigue experiment are shown in figure 5.30. It can be seen that the crack growth rate in vacuum is slower under the given stress intensity factor, due to the elimination of the chemical effect comparing with the ex-situ test in air. Besides, the crack growth rate in vacuum seems to be little affected

by the loading ratio. When the specimen is loaded in vacuum, the chemical effect is not considered. The actual cyclic loading range is the key factor affecting the cyclic displacements at the crack tip. The full applied load range is not always experienced by the crack tip, as the crack tip may close prior to the minimum load, which is shown in figure 5.27 that the crack tip is closed under 100 MPa. The crack tip is shielded from the effects of a part of the load cycle, which is commonly referred as the crack closure. The significance of crack closure is that it acts as a shielding mechanism for the load, which reduces the effective stress intensity factor range at the crack tip:

$$\Delta K_{eff} = K_{max} - K_{open}. \tag{5.8}$$

The effective stress intensity factor range ΔK_{eff} only accounts for the portion of the stress intensity factor range above the crack opening level K_{open}. In this means, the effective stress range for the loading ratios $R = -1$ and $R = 0.1$ is comparably identical. Therefore, the crack growth rates in the in-situ fatigue experiment for the two loading ratios are also similar to each other.

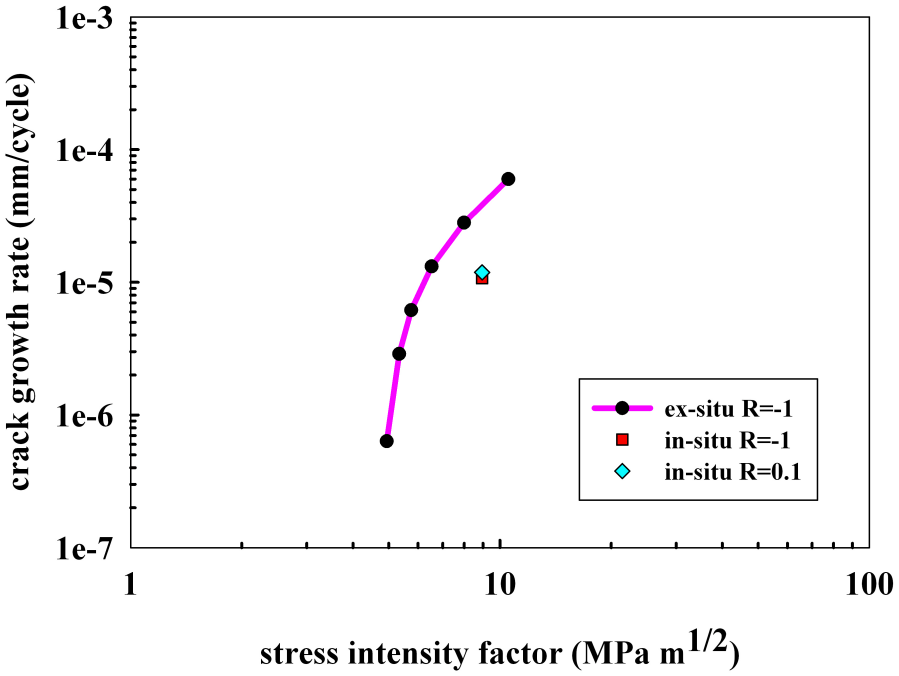

Figure 5.30.: Analysis of the crack growth rate of the in-situ fatigue experiment. The results are compared with that for the bimodal NC/UFG nickel in the ex-situ fatigue experiment.

5.6.3. Conclusions to the fatigue properties of the fine grained PED nickel

In this section we have discussed the fatigue behaviour of the NC, NC/UFG and UFG nickel. The crack growth is investigated with increasing fatigue cycles and the crack growth rate is analyzed according to the stress intensity factor. It is found that the bimodal NC/UFG nickel has higher fatigue crack resistance than the monomodal NC or UFG nickel, i.e. the microcrack in the bimodal NC/UFG nickel begins to grow at the higher stress amplitude and the crack growth rate is slower at a given ΔK_I. The improved fatigue performance is beneficial from the bimodal microstructure combining the high strength (nanograins) and the considerable ductility (ultrafine grains).

The deformation mechanisms of the different microstructures of the fine grained nickel are schematically summarized in figure 5.31. The crack propagates in the NC nickel intercrystallinely, due to the limiting capacity of the nanograins for the plastic deformation. The crack propagation is along the grain boundaries, accompanied by the possible grain boundary sliding or rotation. In the bimodal NC/UFG nickel, the nanograins behave in the same way as in the NC nickel. But the ultrafine grains behave more complicatedly, depending on the grain size and the distance to the crack tip. Slip bands form in the ultrafine grains which have relatively larger grain size and are near the crack tip. There is no deformation observed in the ultrafine grains including the annealing twins (figure 5.23), which indicates that the twins behave similar as the grain boundaries, increasing the strength of the materials. It was also indicated by some authors that the twins increased not only the materials strength but also the ductility [*Lu et al.*, 2005, 2009], but the increasing ductility by twins is not detected in this study. Actually, the crack tip travels preferably along the grain boundaries, especially when the crack is short and the local plastic deformation influenced zone is small. However, some ultrafine grains in front of the crack tip deform severely with increasing strain localization so that the crack goes through these grains intracrystallinely. Upon observation in the in-situ fatigue experiment, it is demonstrated directly that the ultrafine grains behave as the strong obstacle and the nanograins as the weak obstacle for the crack propagation. The ultrafine grains are deformed similarly in the monomodal UFG nickel to that in the bimodal NC/UFG nickel. However, due to the lack of the nanograins with high strength there is larger plastic deformation influenced area around the crack tip which causes the crack to propagate faster in the UFG nickel.

Summarily, introducing the ultrafine grains into the nanograined matrix is an effective way to improve the materials' crack growth resistance and fatigue performance.

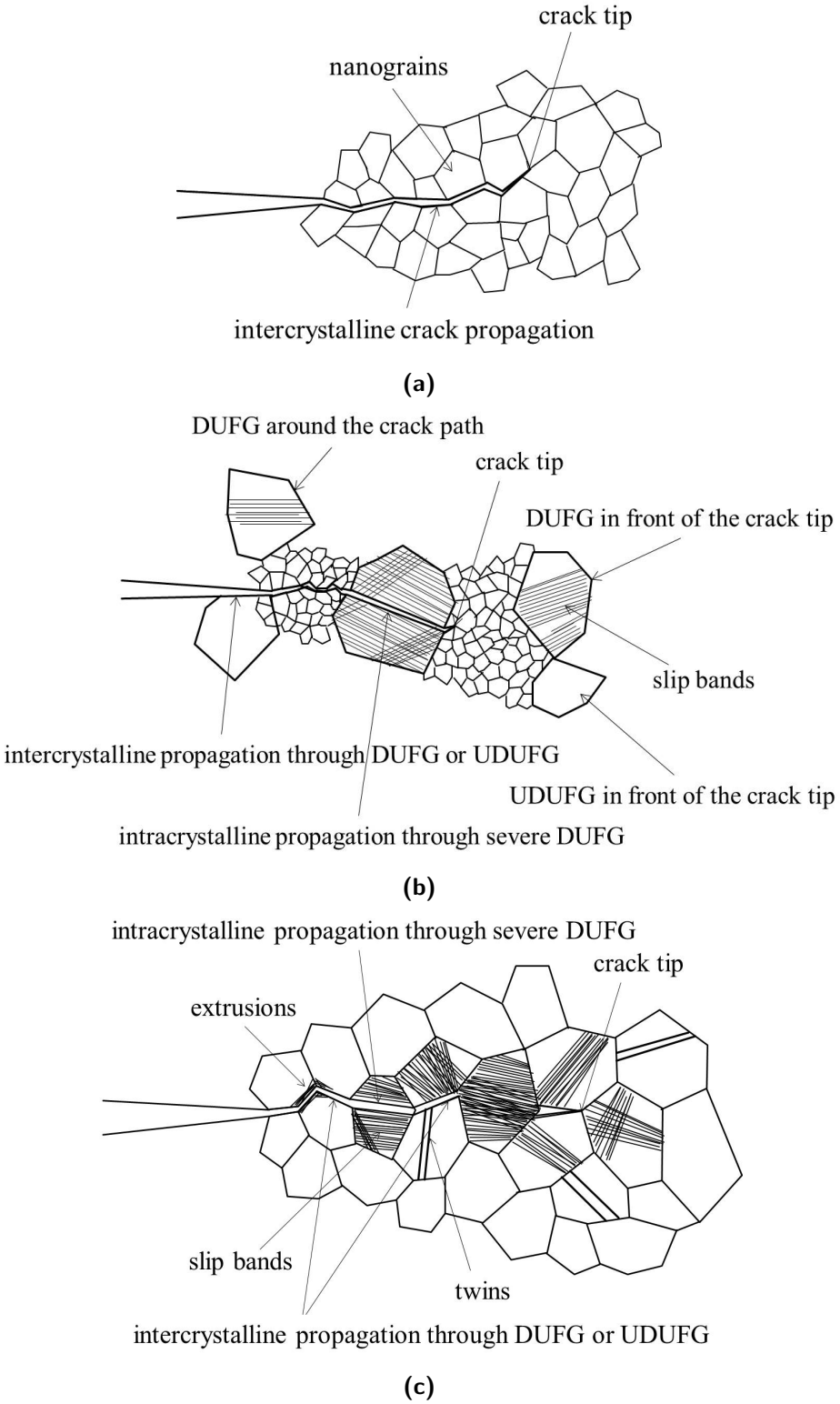

Figure 5.31.: Schematic description of mechanisms to the crack propagation for the (a) NC nickel, (b) NC/UFG nickel and (c) UFG nickel. (DUFG: deformed ultrafine grain; UDUFG: undeformed ultrafine grain).

5.7. Influence of the microstructure of ECAP nickel to the fatigue properties

The as-received ECAP UFG nickel has the grain size which is equivalent to that of the annealed PED UFG nickel. However, after initiation of the microcracks on the specimen surface they behave quite differently in the fatigue experiments. The PED UFG nickel is sensitive to the microcracks, and is fractured during the cyclic loading because of the microcrack propagation. But the ECAP UFG nickel is not sensitive to the microcracks. Although the microcracks propagate during the fatigue loading, they do not grow to a critical length and induce the ultimate fracture. In the following, the microcrack propagation and the fracture behaviour of the ECAP nickel will be discussed separately.

5.7.1. Fatigue of the ECAP UFG nickel with microcracks

The microcracks, initiated by FIB on the specimen surface, propagates with the increasing loading cycles in the fatigue experiments. It is found that the crack growth is significantly affected by the initial microstructures and also by the loading stress. The two different kinds of the ECAP UFG nickel specimens which are processed by route C and route E have similar but also unique microstructures, as shown in section 4.1, which inevitably influences the crack growth behaviour. When different loading amplitudes are applied, the interaction between the crack tip and the microstructures is also influenced.

Influence of the ECAP routes

The microstructure of the ECAP UFG nickel processed by route C is of predominant elongated grains along the direction about 45° to the specimen borders on the y-plane. The appearance of the microstructure on the y-plane of the ECAP billet after four passes is schematically described in figure 5.32, using the model for grain refinement in the ECAP process by Langdon [*Langdon*, 2007]. After eight passes this microstructure is reinforced as the repeated process of the following four passes. It can be seen that the boundaries of the elongated subgrains are the preferential sites, allowing the microcrack to propagate, as shown in figure 4.29.

Similar analysis according to the model by Langdon for the ECAP route E is shown in figure 5.33. It can be seen that the microstructure after eight passes of route E is very

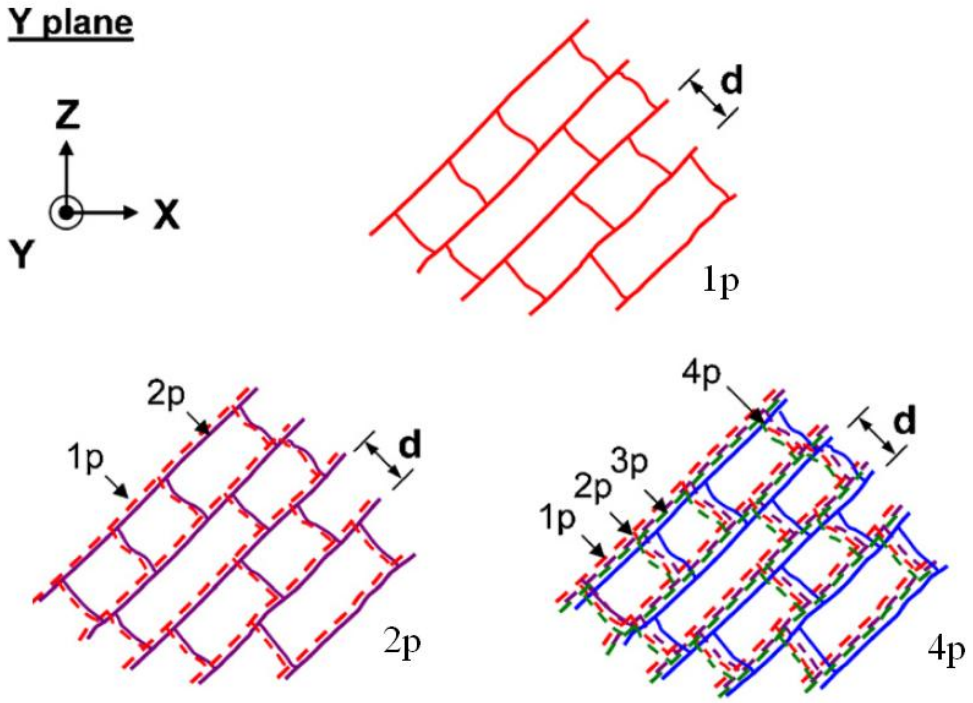

Figure 5.32.: Model for grain refinement in ECAP of route C where subgrain bands formed [*Langdon*, 2007].

complicated. Actually it was expected that route E would be an improved ECAP route over route C to improve the subgrain structures. However, it is found that the route E can only partially improve the subgrain properties, but also induce more complicated microstructures. The microstructure is detailed characterized in section 4.1 in which the mixed areas of microstructural textures and homogeneous equiaxed grains are observed. Therefore, there are different modes of the microcrack propagation: growing along the direction of the elongated grains or growing perpendicular to the loading direction which is similar to the annealed PED UFG nickel, where high angle grain boundaries are dominant (figure 4.30).

Influence of the stress amplitudes

The applied stress is also found to influence the crack growth in the fatigue experiment. It is observed that there are increasing plastically deformed areas around the crack tip when higher stress amplitudes are introduced. Under the highest applied stress of 500 MPa, the crack propagates not only along the elongated grains, but also along the direction which has an equivalent angle to the loading direction in the other side

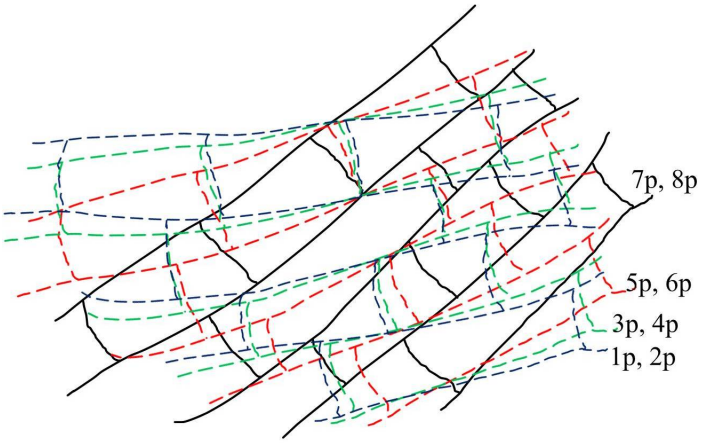

Figure 5.33.: Schemeatical description of the microstructure of the ECAP route E specimen, using the model for grain refinement in figure 5.32.

(figure 5.34). At the same time, the microcrack propagates only along the direction of the elongated grains when the lower fatigue stresses are applied.

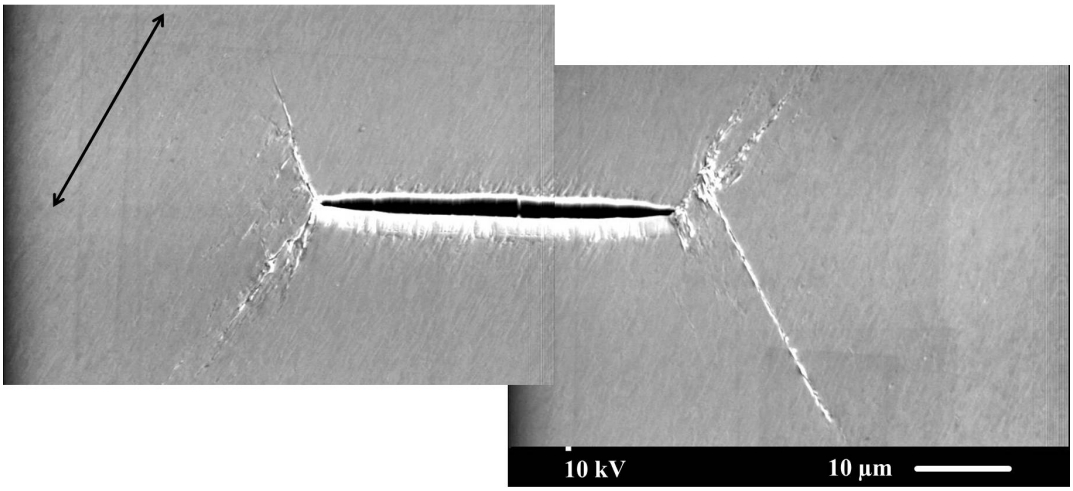

Figure 5.34.: Crack propagation in the ECAP UFG nickel processed with route C under high stress amplitude in the fatigue experiment. The direction of the elongated grains is marked with the arrow.

An experiment in which the increasing stress amplitudes were applied was carried out to investigate the influence of the stress amplitude to the microcrack propagation. The crack growth length is shown in figure 5.35, with increasing fatigue cycles under different stress amplitudes. It is found that the crack does not propagate under the low stress with the amplitude 100 MPa. The microcrack begins to grow under 150 MPa. However, it seems that there is a saturating value for the crack growth under a given stress as the

crack growth suspends after certain number fatigue cycles. The microcrack propagates further when even higher stress is applied. The specimen is fractured quickly when the high fatigue stress is applied. It is concluded that the applied stress influences the microcrack growth marginally, but affects the fatigue life of the specimens significantly by initiation of the new critical cracks.

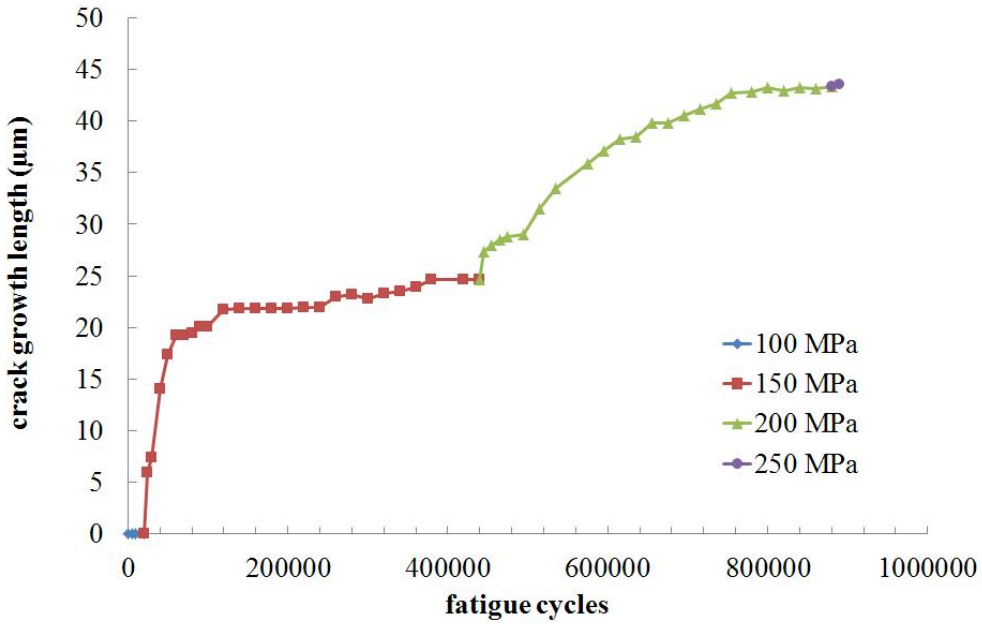

Figure 5.35.: Crack propagation with increasing stress amplitudes for the ECAP UFG nickel.

Fracture behaviour

The microcracks in the ECAP UFG nickel propagate with the increasing fatigue cycles in the fatigue experiments, but they do not grow to the critical length to cause the ultimate fracture, in other words, they are not decisive to the fatigue life of ECAP UFG nickel. The ECAP UFG specimens are fractured in a sudden manner that there is no stable crack propagation phase detected. Surface observation reveals the well-developed fatigue markings which follow the last ECAP shear plane, whose average length and distance substantially exceeds the average grain size of the ECAP UFG nickel (figure 4.31). This observation indicates that the formation of the surface shear bands along the direction of the elongated grains, i.e. the shear plane of the last ECAP pass, is the decisive mechanism for the nucleation and propagation of the surface cracks, causing the ultimate fracture.

Investigation on the fracture surface reveals the quick propagation of the crack which induces the fracture. Figure 5.36 shows the fractograhpy in which crack growth corresponding to each loading cycle and the crack growth direction are illustrated clearly. Figure 5.36a depicts the crack propagation perpendicular to the specimen surface, and figure 5.36b is for the crack propagation along the other direction in the fracture surface.

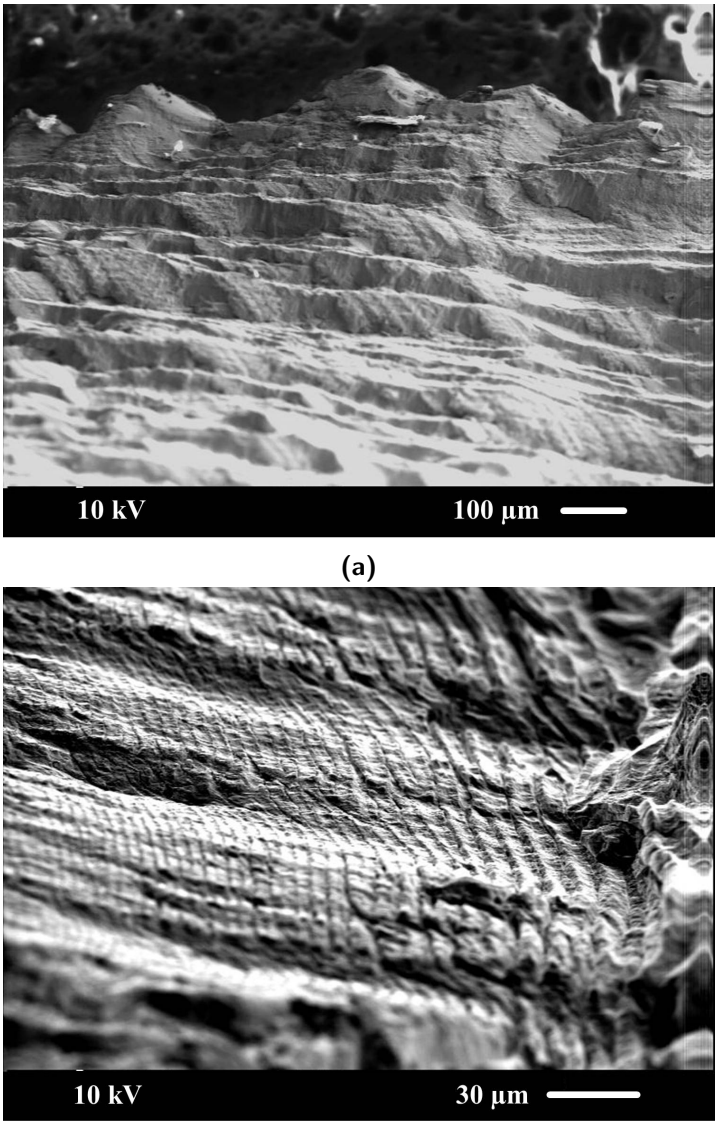

Figure 5.36.: Fracture surface of the ECAP UFG nickel showing the quick crack propagation inducing the ultimate fracture.

Deformation and fracture mechanism

The ECAP UFG nickel has the similar grain size to the PED UFG nickel, but the other microstructural characteristics such as the grain boundary properties and the dislocation densities inside the grains are totally different. As a consequence, the two kinds of UFG nickel behave completely differently in the fatigue crack propagation. There are slip bands forming in the ultrafine grains of the PED nickel, which are contributed to the plastic deformation. However, the slip bands are not observed in the ultrafine grains in the ECAP nickel, which indicates the limiting deformation capacity of this kind of ultrafine grains.

EBSD measurements have been conducted to investigate the microstructural evolution during the fatigue experiment. Figure 5.37 shows the crack tip area of the ECAP UFG nickel before and after the fatigue experiment under the low fatigue stress, where the initial crack direction is vertical to the loading direction. The selected area is investigated with EBSD before the fatigue loading and after $100,000$ cycles under 200 MPa. The crack propagates along the direction of the microstructural textures, which is marked within the two straight lines. The microstructure of the UFG nickel is stable and undergoes marginal changes during the fatigue experiment. The different colors in the EBSD images representing the orientations of the grains change slightly when carefully comparing the corresponding grains in the two images. Besides, the black vectors marking the position of the selected grains to the crack tip are compared before and after the fatigue loading. Overlapping the two subfigures, the starting points and ending points of the corresponding grains are marked by the black vectors, as shown in the image. This indicates that there is slight grain rotation occurring during the fatigue loading, which compensates the limiting deformation capacity of the ultrafine grains of the ECAP nickel.

When increasing the stress amplitude in the fatigue experiments, there is more severe local plastic deformation around the crack tip. In this situation the above mentioned fatigue mechanism can no longer hold for the plastic deformation process. Meanwhile, a new mechanism, i.e. dynamic recrystallization, is detected, as shown in figure 4.35 and figure 4.36. The slight coarsening grains are observed around the crack tip or along the crack growth path on the specimen surface. This is because there is more severe local plastic deformation around the crack tip or the micro-extrusions, inducing dynamic recrystallization occurring there.

When there is even higher strain localization, surface shear bands, which are associated with the micro-extrusions, are found to form along the shear plane of the last

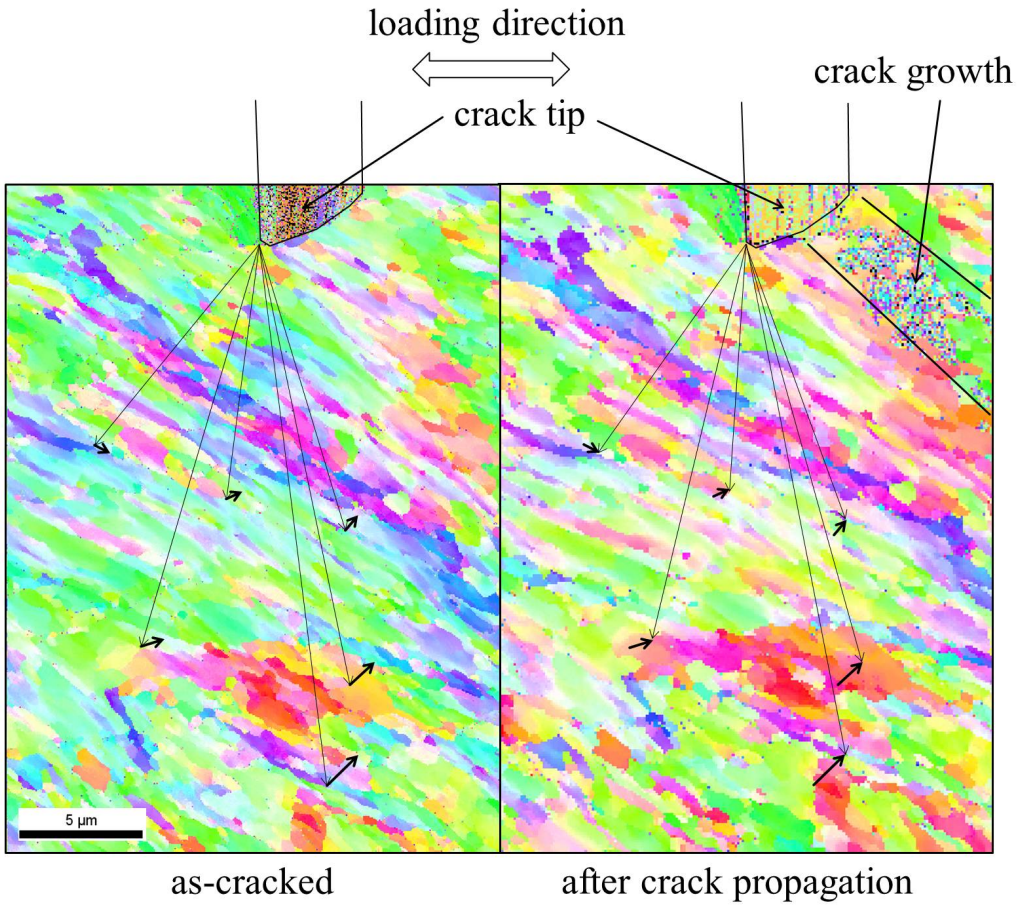

Figure 5.37.: Microstructural evolution during the fatigue loading using EBSD. The relative displacements of the selected grains are analyzed according to the vectors.

ECAP pass. There is observing grain coarsening between the extrusions, as marked between the line in figure 5.38, which indicates that dynamic recrystallization is also partially the mechanism for the plastic deformation. When this mechanism can not ensure the total plastic deformation, the surface shear bands, thus extrusions, form. The microcrack propagation is found not to be the decisive factor inducing fracture in the ECAP UFG nickel. Instead, the new forming surface cracks, which are caused by the surface shear bands, are the causing for the ultimate fracture.

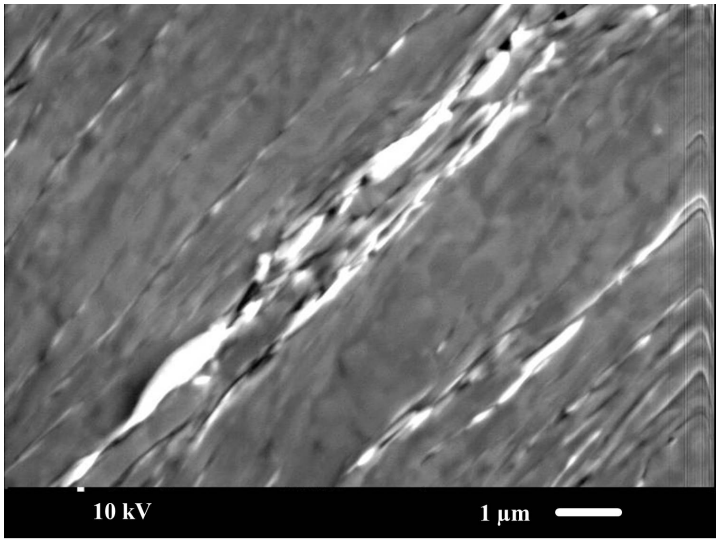

(a)

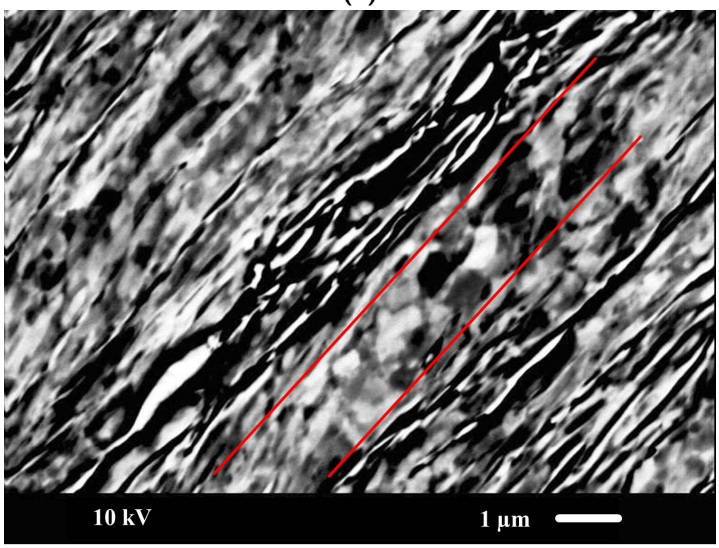

(b)

Figure 5.38.: (a) Surface shear bands and extrusions of the severely deformed ECAP UFG nickel. (b) Dynamic recrystallization between the extrusions, as marked by the lines.

5.7.2. Fatigue of the notched specimens

The microcracks initiated by FIB are found to be too small in dimension to induce the ultimate fracture for the ECAP UFG nickel. Therefore, the macro-notches with large length scale are introduced with two different methods, as shown in section 4.5.4.

The specimens with the micro-notch at one edge (Mode I Notch) are loaded with the displacement-controlled mode and the crack propagates in an accelerating manner (figure 4.32). The overview of the crack propagation for this kind of specimens is shown in figure 4.33. It can be seen that the crack propagation is influenced not only by the microstructure but also from the geometry of the notch. The crack tip travels in the path mediated by the microstructure which makes the crack grow along the direction of the microtextures, and by the notch geometry which provides the favored direction perpendicular to the loading direction. The macro-notch propagates with increasing fatigue cycles, inducing the ultimate fracture of the ECAP UFG nickel.

Figure 5.39a depicts the crack growth rate according to the stress intensity factor ΔK_I which is in quite good consistence to the results for UFG nickel by Bansal et al [*Bansal et al.*, 2005]. Figure 5.39b exhibits the crack growth rate according to ΔK_I for the ECAP UFG nickel and the PED UFG nickel. It shows clearly that there is a considerably higher threshold of the stress intensity factor for the crack growth of the ECAP UFG nickel which proves that the ECAP UFG nickel is not sensitive to the microcracks. Besides, the UFG nickel has much lower crack growth rates in consideration of ΔK_I.

Observation on the crack propagation path shows that the deformation field around the crack tip is becoming larger with the increasing crack length (figure 4.33b). It has been discussed in section 5.7.1 that dynamic recrystallization occurs during the fatigue experiment for the ECAP UFG nickel when there is relatively severe local plastic deformation. This phenomenon has been observed much more clearly for the notched specimens, which has been shown in figure 4.35 and figure 4.36. This is because there is much larger local deformation field and strain localization around the crack tip for the macro-notches. When dynamic recrystallization could not ensure the total plastic deformation, the crack then propagates, instead of formation of the surface shear bands.

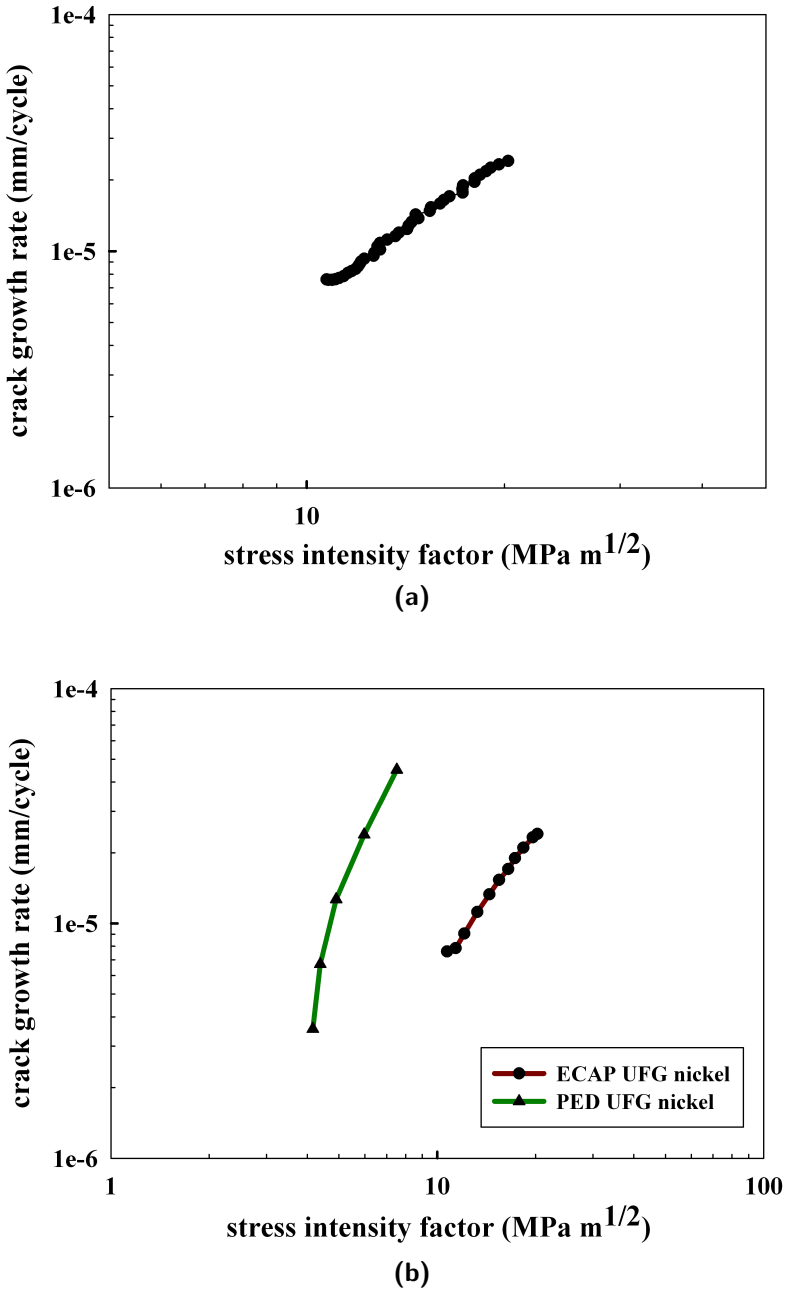

Figure 5.39.: (a) Fatigue crack growth rate as the function of ΔK_I of the edge notched ECAP UFG nickel and (b) Comparison of the crack growth rates of the PED UFG nickel and ECAP UFG nickel according to ΔK_I.

5.7.3. Fatigue of the ECAP bimodal UFG/CG nickel

The fatigue behaviour of the annealed ECAP UFG nickel, i.e. bimodal UFG/CG nickel in which there are different volume fractions of the coarse grains, has been investigated (section 4.5.5).

The deformed surface around the microcracks is shown in figure 4.37. The loading stress is lower than the yield stress of the UFG nickel but higher than that of the CG nickel (figure 4.19). Therefore, the fatigue response of the bimodal nickel, with more or less coarse grains, is quite similar to each other: the plastic deformation concentrates in the coarse grains. Considering the areas around the microcracks, there is the most local plastic deformation around the crack tip. The accumulation of the dislocation movements which is in form of the formation of the slip lines inside the coarse grains is directly observed (figure 4.38). This is the main mechanism of the plastic deformation of the bimodal UFG/CG nickel in the fatigue experiments. The severity of the deformation in the coarse grains decreases with the increasing distance between the crack tip and the corresponding coarse grains until the influence of the microcrack disappears. However, there is no deformation in the coarse grains around the middle edges of the microcrack, this is because that the microcrack behaves as a free surface where no stress concentration occurs. Actually, not only the coarse grains around the microcracks, but also the coarse grains in the whole specimen take part into the plastic deformation in the fatigue experiments. They behave quite similar to those coarse grains around the microcracks, but without the effect of strong strain localization by the crack tip and without the 'shield-effect' by the crack edges.

The deformation of the bimodal UFG/CG nickel is more obvious in the specimens where high volume fraction of the coarse grains exists. Figure 5.40 shows the crack growth from the two crack tips which can be used to describe the formation of the critical surface cracks inducing the ultimate fracture when higher loading stresses are applied. Slip bands form in the coarse grains and the extrusions come out with increasing fatigue cycles. When the ultrafine grains around the coarse grains can not hold up due to the severe plastic deformation, the extrusions in the coarse grains combine together and the surface cracks form. With accumulation of such surface cracks, there comes a crack with the critical length which causes the ultimate fracture.

Conclusively, introducing the coarse grains into the UFG matrix can improve the ductility of the material, because the coarse grains have the good capacity ensuring the plastic deformation. In the fatigue tests, the coarse grains are effective sites where the plastic deformation concentrates, even though there are very few coarse grains dis-

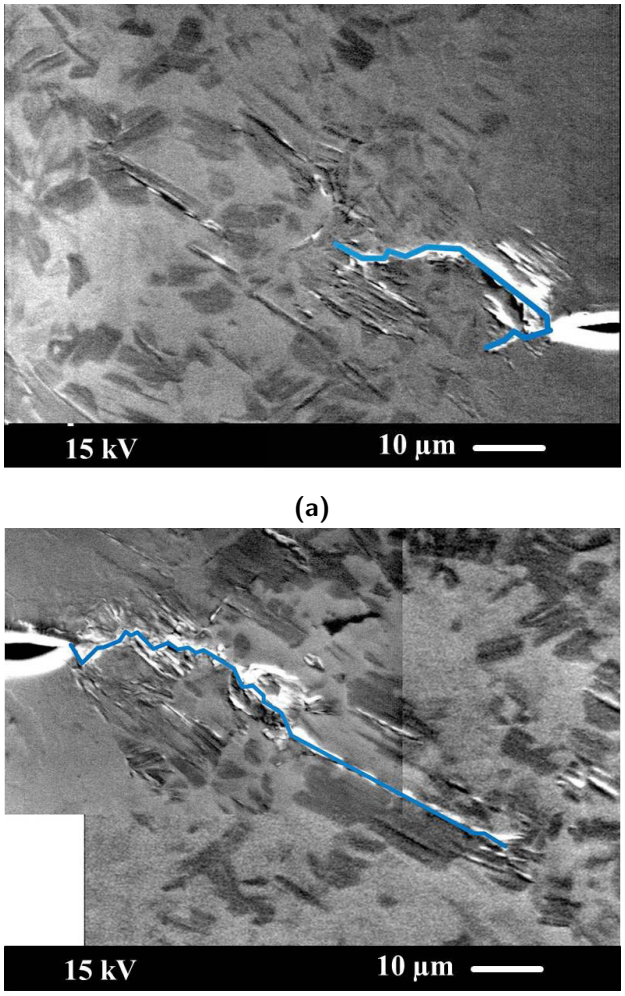

Figure 5.40.: Crack propagation in the bimodal UFG/CG nickel with high volume fraction of coarse grains for (a) the left crack tip and (b) the right crack tip.

tributing in the microstructures. The quantity of coarse grains to be introduced into the UFG matrix depends on the applications in which more strength or more ductility is required. However, the quantitative investigation on the fatigue behaviour, correlating the bimodality to the strength and ductility, has not been conducted and is suggested as the subject in the future work.

5.7.4. Conclusions to the fatigue properties of the ECAP nickel

In this section we have discussed the fatigue behaviour of the ECAP UFG nickel, which is of the unique microstructures due to the severe plastic deformation. Similar to the

fatigue experiments for the PED nickel, microcracks have been introduced on the specimen surface by FIB. Although the grain size is similar to that of the low temperature annealed PED UFG nickel, the fatigue response and crack growth behaviour are totally different.

The microcracks propagate during the fatigue loading, but they do not grow to a critical length and then cause the ultimate fracture. The sudden fracture happens after a quantity of fatigue cycles, depending on the fatigue stress (figure 4.28). Therefore, the ECAP UFG nickel is not sensitive to the microcracks and the nucleation and propagation of new cracks is the critical factor for the ultimate fatigue fracture. The different ECAP routes influence the microstructures of the as-processed UFG nickel and consequently the crack growth behaviour, depending on the local microstructures around the crack tip. The ECAP nickel with route C is of dominant microtextures consisted by elongated grains (figure 4.2a and figure 5.32) and the microcracks grow mainly along this direction. At the same time, the ECAP nickel with route E is of a more complicated microstructure which is combined of the elongated subgrains and the homogeneous ultrafine grains with high angle grain boundaries (figure 4.2b and figure 5.33). Therefore, the microcrack propagates either along the direction of the microtextures or perpendicular to the loading direction. The influence of the applied stress shows marginal effect to the propagation of the microcracks, but significant influence to the fatigue life due to the formation of the critical surface cracks.

Upon the analysis to the EBSD images it is found that slight grain rotation is the main mechanism for the small local deformation around the microcrack tip under the low fatigue stresses. When there is more severe local plastic deformation, i.e. loading the specimens under the higher fatigue stresses or introducing the macro-notches, dynamic recrystallization is the responsible mechanism. However, formation of the surface shear bands and thus the surface cracks is the main mechanism for the ultimate fracture of the ECAP UFG nickel when even higher strain localization takes place.

Introducing coarse grains into the UFG matrix improves the ductility, i.e. the capacity of plastic deformation of the UFG nickel. Plastic deformation concentrates in the coarse grains in which the accumulation of the dislocation movements induces the formation of slip bands and then the extrusions inside the coarse grains. The critical surface cracks form by combining the local extrusions inside the coarse grains when the UFG matrix can not hold up due to the severe strain localization. However, quantitative experiments based on the volume fraction of the coarse grains and the fatigue stress have not been carried out and should be further investigated in the future work.

6. Conclusion and Outlook

6.1. Conclusions

The as-received PED NC and ECAP UFG nickel have low ductility because of the low capability of their grains to accumulate dislocations, e.g. due to the smallness of the grain size of the PED NC nickel and the high initial dislocation density of the ECAP UFG nickel, which motivates the researching objectives in this thesis: improving the ductility of the fine grained materials and the fatigue response. The concept of the bimodal microstructure is employed and effort has been given to initiate the bimodal microstructure on the basis of the as-received PED NC nickel and the ECAP UFG nickel. The key contributions of this thesis can be summarized as follows:

1. The novel bimodal NC/UFG microstructure, e.g. mixture of the nanograins and the ultrafine grains, is initiated by a low temperature annealing of the PED NC nickel. It is successful to obtain the bimodal NC/UFG microstructures with different volume fractions of the nanograins and the ultrafine grains. The continuous grain growth process in the low temperature heat treatment is driven by the energy stored in the form of grain boundaries. The nanoscale grain growth kinetics is analyzed, qualitatively obeying the JMAK model for the bimodality and following the Burke and Turnbull model for the grain size.

2. The annealing process of the PED nickel at the elevated temperature is investigated. It is found that if normal or abnormal grain growth occurs depending on the starting PED plates, which indicates the significant influence of the electrodeposition process. Normal and abnormal grain growth are competing processes: when one process occurs, the other one will be inhibited. The bimodal micron/CG microstructures are initiated when abnormal grain growth occurs. The volume fraction of the abnormal growing grains abeys not the JMAK model so well but follows approximately the exponential law, although the abnormal grain growth is known as the secondary recrystallization. It is also found that the initial grain

size, i.e. the NC or UFG PED nickel, does not influence the ultimate annealing microstructures at the elevated temperature. As the grains are no longer in the UFG range after this annealing, there are no improved strength properties for the bimodal micron/CG microstructures anymore which is proved by the microindentation measurement.

3. The bimodal microstructure UFG/CG is obtained by annealing the ECAP UFG nickel at low temperature. The driving force of this discontinuous grain growth process, more accurately primary recrystallization, comes from the stored energy in the form of dislocations by the severe plastic deformation in the ECAP process. The coarse grains are forming during the annealing process, due to the much higher driving force comparing to the PED NC nickel. With proper controlling of the annealing time, maybe repeated annealing, the bimodality could be approximately controlled. Besides, the initial coarse grains before ECAP seem to have significant influence to the recrystallization process. The improved ductility is achieved due to the bimodal grain size distribution by some loss in the strength, according to the tensile stress-strain measurements.

4. The fatigue response of the fine grained PED nickel with different microstructures, i.e. NC, NC/UFG and UFG, is investigated. After initiation of the microcracks by FIB on the specimen surface, the microstructure is found to have significant effect on the microcracks growth resistance and thus the fatigue fracture. Having the strength and ductility of the bimodal NC/UFG microstructure between the monomodal NC and the monomodal UFG microstructures, the specimens with the bimodal NC/UFG microstructures show much higher crack resistance. The combined high strength from the nanograins and improved ductility from the ultrafine grains ensure the better crack resistance of the bimodal NC/UFG nickel. The in-situ fatigue experiment shows the direct observation on the high crack resistance of the ultrafine grains in the NC/UFG microstructures. On the basis of the microstructural observation, the fatigue deformation and crack growth mechanisms are suggested for the different microstructures.

5. The fatigue response of the ECAP UFG and UFG/CG nickel is also investigated. It is found that the ECAP UFG is not sensitive to the microcracks, unlike the fine grained PED nickel. Although the microcracks propagate with increasing fatigue cycles, they do not grow to a critical length inducing the ultimate fracture. The initiation of the new surface cracks which is formed by the surface shear bands due

to the high strain localization is found to be the causing to the ultimate fracture of the ECAP nickel. The crack growth behaviour is further investigated with the macro-notches at the edge or in the middle of the specimens. The deformation mechanism is proposed according to the severity of the strain localization upon the microstructural observation.

6. The deformation mechanisms of two kinds of ultrafine grains are compared. Although the grain size of the as-received ECAP UFG nickel is similar to the low-temperature annealed PED UFG nickel, they behave quite differently during the fatigue loading. The ultrafine grains in ECAP nickel are with high dislocation density inside and separated mainly by LAGBs and show little capacity for the dislocation motion and accumulation. However, dislocation mediated mechanism is found in the ultrafine grains in the annealed PED nickel where slip bands form inside the grains.

6.2. Outlooks

The bimodal NC/UFG nickel is found to have better fatigue performance against the microcracks than the monomodal NC or UFG nickel. However, in this work fatigue experiments were only performed to the bimodal NC/UFG nickel specimens in which the volume fractions for each phase are approximately the same (50%). Investigation of the fatigue performance quantitatively correlating to the bimodality has not been carried out yet. The bimodal NC/UFG microstructures have been obtained with continuous bimodality (figure 4.4). Therefore, further investigation concentrating on the quantitative bimodality is of great interest: with which volume fraction of the ultrafine grains (or nanograins) the bimodal NC/UFG microstructure has the best fatigue performance! Besides, due to the limitation of the specimens, the tensile properties of the bimodal NC/UFG microstructure have not been investigated. Therefore, it is suggested that tensile tests be conducted in the future work.

Using FIB to introduce the microcracks in the specimen surface is of great advantage to control the crack parameters. The microcracks with different orientations were initiated for the ECAP UFG nickel, and there was no influence found by the crack orientations due to the insensitivity of the ECAP nickel to the microcracks and the strong effect of the microtextures. However, the fatigue behaviour of the fine grained PED nickel is strongly influenced, even determined, by the microcracks. Therefore, systematic investigation on the microcracks with different initial parameters is meaningful to

understanding the fatigue properties of the different fine grained microstructures, and to the practical applications of the fine grained materials in which micro-damages might exist.

The unique microstructures of the ECAP UFG materials influence the mechanical properties significantly. Therefore, further investigation based on the ECAP microstructures is suggested. Figure 6.1 shows the specimens which can be prepared directly correlating to the microstructures. The angle between the specimen border and the microstructural textures can be changed. In this image the two extreme situations with the specimen border parallel and vertical to the elongated grains are shown. With this method the influence of the ECAP microstructures to the materials properties and the correlated mechanisms can be more detailed investigated.

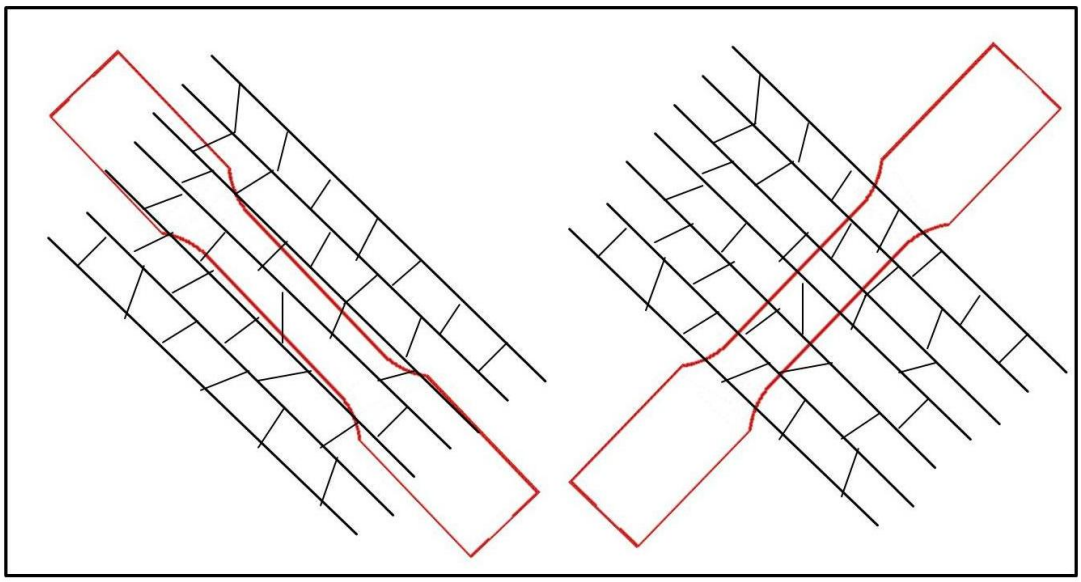

Figure 6.1.: Specimen preparation in correlation to the ECAP microstructure.

The complicated microstructures of the ECAP UFG nickel brings much difficulty into the heat treatment of these materials. The compromised strength and ductility have been achieved by the low temperature annealing, but the distribution of the bimodal NC/UFG microstructures is not satisfying. Therefore, new methodologies for the initiation of the bimodal microstructure based on the ECAP UFG nickel are required. One potential application is the surface treatment by the laser beam, to introduce the coarse grains into the designed areas. This process is like the opposite process of the surface mechanical attrition treatment (SMAT) in which a nanostructured surface layer on the

materials is introduced. Appendix D shows the first results on the heat treated surface of the ECAP UFG nickel by the scanning laser beam. It seems that there is a trimodal grain size distribution where different heat influenced zones were introduced by the laser beam.

Appendix A.

Parameters for the PED NC nickel

The NC nickel specimens in this work were produced with the PED technique. According to Schüler, who produced the PED NC plates, the parameters in the electrodeposition process are listed in Table A.1 for the basic electrolyte composition and in Table A.2 for the controlling parameters for the PED NC plates in this work.

component	concentration	function
nickel sulfamate	595 ml/l	
nickel chloride-6-hydrate	5 g/l	dissolving the anode
boric acide	35 g/l	pH-buffer agent
natrium lauryl sulfate	0.2 g/l	wetting agent

Table A.1.: The parameters for the basic electrolyte composition.

parameter	value
t_{on}	5 ms
t_{off}	10 ms
I_{pulse}	45mA/cm^2
grain refiner saccharin	0.4 g/l
grain refiner butynediol	0.02 g/l

Table A.2.: The controlling parameters in the electrodepostion process for the PED NC plates.

Appendix B.

Analysis of the microstructure of the ECAP nickel

The microstructures of the ECAP UFG nickel were characterized in section 4.1, where the backscattered electron images and EBSD images were shown. In this appendix some more detailed information is given about the grain boundaries and the textures.

It is reasonable to anticipate a high volume fraction of low angle grain boundaries (LAGBs) of the microstructure processed by ECAP, which is a natural consequence of the large numbers of excess dislocations introduced on the passages through the ECAP die. Figure B.1 shows the distribution of the misorientations on the y-planes of route C and route E specimens, analyzed from the EBSD measurement data in figure 4.3. There are dominant LAGBs in the specimen processed by route C, while the percent of high angle grain boundaries (HAGBs) is much higher for the route E specimens.

Study on the crystallographic orientations resulting from the ECAP process is of primary importance, especially since the crystallographic texture has a significant effect on many microstructure sensitive properties. Microtexture data, in the form of pole figure obtained from orientation imaging microscopy (OIM) measurements, are shown in figure B.2 from specimens prepared by route C and route E on the different planes (x, y, and z). The clusters of points indicate that there exists strong texture in the 8C ECAP UFG nickel, in all planes. Although the microstructure is more homogeneous in the 8E ECAP nickel, there are still relatively strong textures.

The texture with preferred orientations can be visualized more clearly in the inverse pole figure. Figure B.3 shows the inverse pole figure of the y-plane of the ECAP UFG nickel with two different routes, which are corresponding to the pole figure in figure B.2. The 8C ECAP UFG nickel has the preferred orientation all around the [111] direction, while the 8E ECAP UFG nickel shows a relatively preferred orientation near the [001]

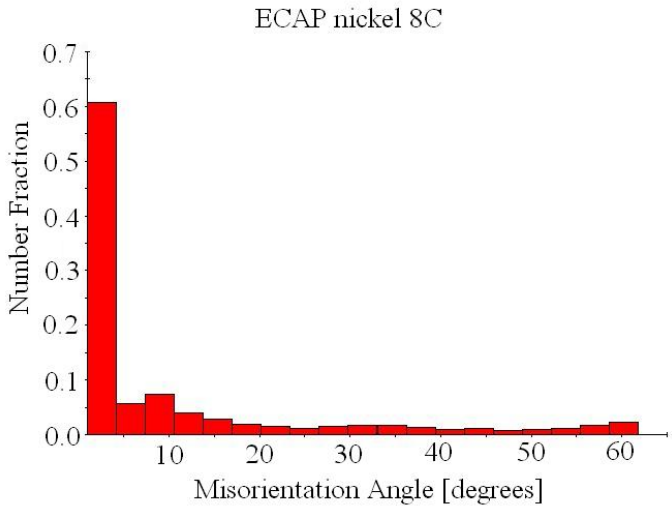

(a)

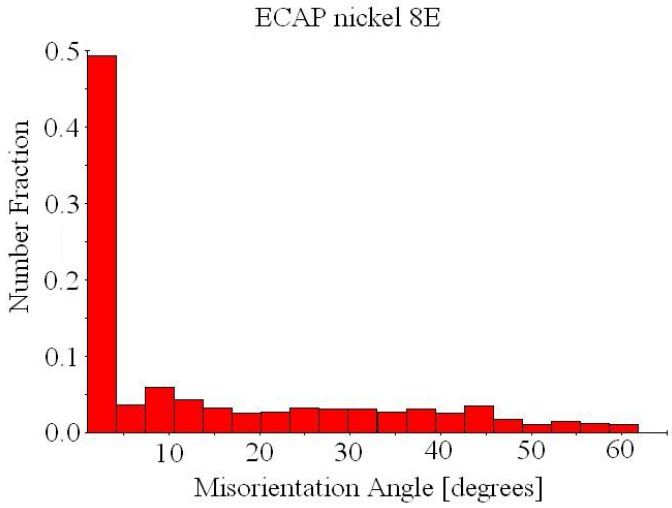

(b)

Figure B.1.: Distribution of the misorientation between grains of the as-received ECAP UFG nickel processed with eight passes by (a) route C and (b) route E.

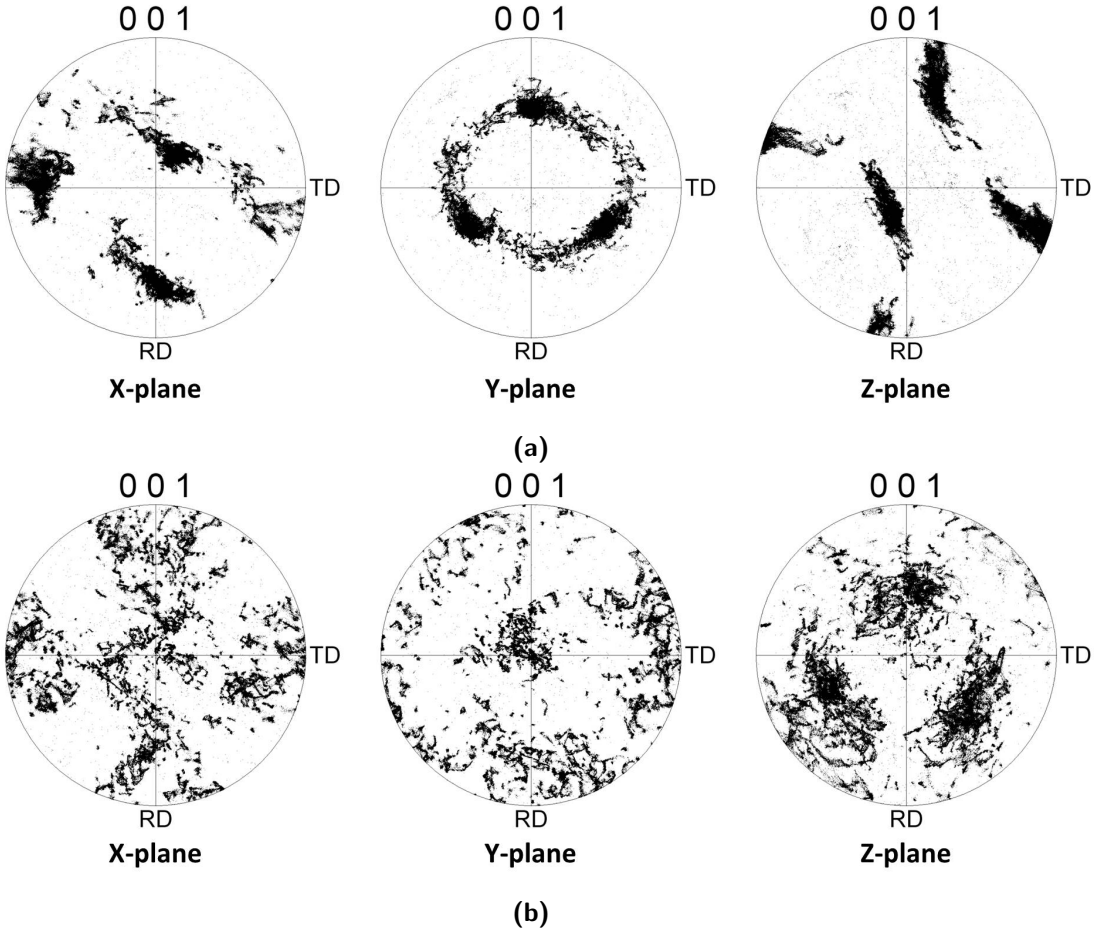

Figure B.2.: (001) pole figures on different planes of the as-received ECAP UFG nickel processed with eight passes by (a) route C and (b) route E.

direction.

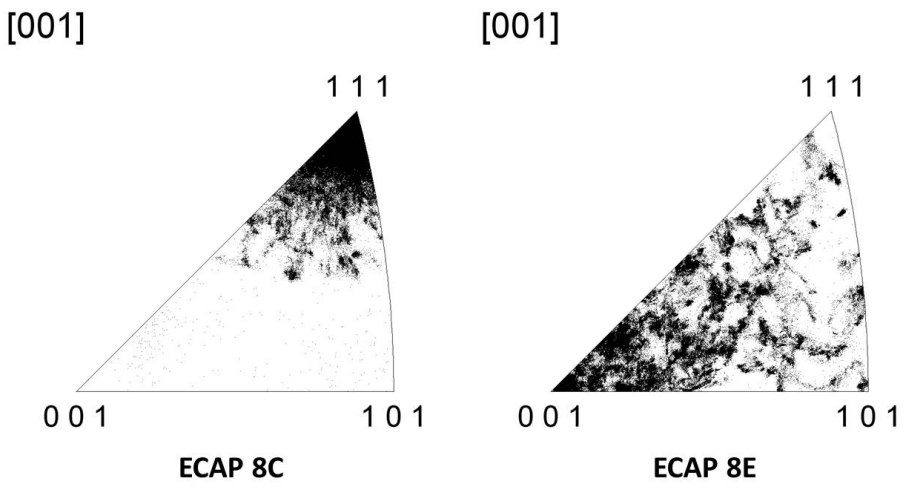

Figure B.3.: Inverse pole figure on the Y-planes of the two ECAP routes, corresponding to figure B.2.

Appendix C.

In-situ fatigue experiment of the bimodal NC/UFG nickel

The results of in-situ fatigue experiments for the bimodal NC/UFG nickel were shown in section 4.5.2 and 5.6.2, concentrated on the right crack tip. In this appendix some complementary results on the left crack tip will be shown.

Figure C.1 shows the crack propagation under 300MPa with the loading ratio R = −1. The crack tip began to grow from an ultrafine grain which was almost traveled around. The difference between the two crack tips was that right crack tip started from the nanograined area and propagated around an undeformed ultrafine grain. It can be observed that the ultrafine grain behaved as a strong obstacle for the crack propagation in which it took about 120 cycles for the crack traveling over this grain. The crack grew much faster in the next 60 cycles in the nanograined matrix.

Figure C.2 shows the total crack growth in the in-situ fatigue experiment, in which figure C.2a shows the result after 500 cycles with R = −1 and figure C.2b shows the subsequent crack propagation after 320 cycles with R = 0.1. Due to the surface contamination in the SEM chamber there was little information about the microstructures in the further measurements.

After the surface purification by the plasma cleaning the crack propagation was shown in correlation to the microstructures C.3. Similar to the results in section 5.6.2 there was larger plastic deformation influenced area with the loading ratio R = 0.1 than that with the loading ratio R = −1.

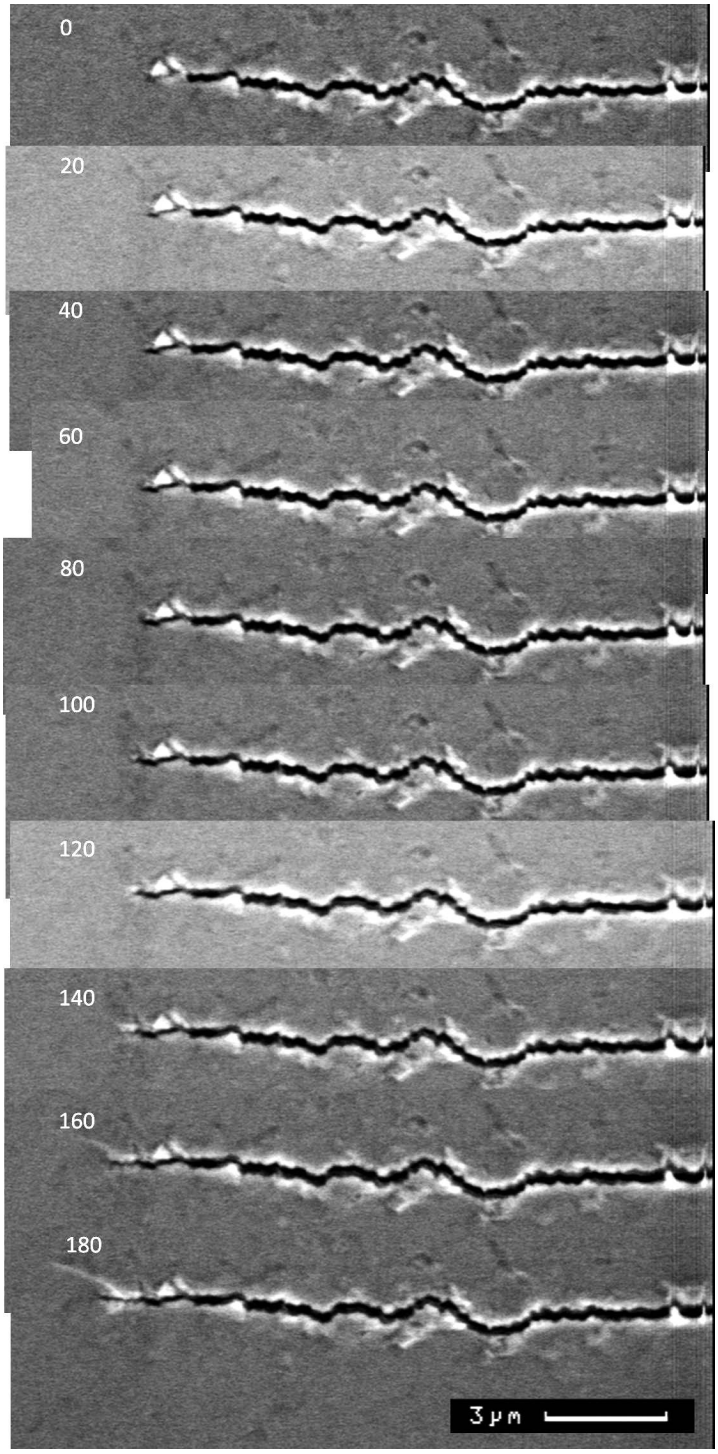

Figure C.1.: Crack propagation of the left crack tip in the bimodal NC/UFG nickel specimen in the in-situ fatigue experiment.

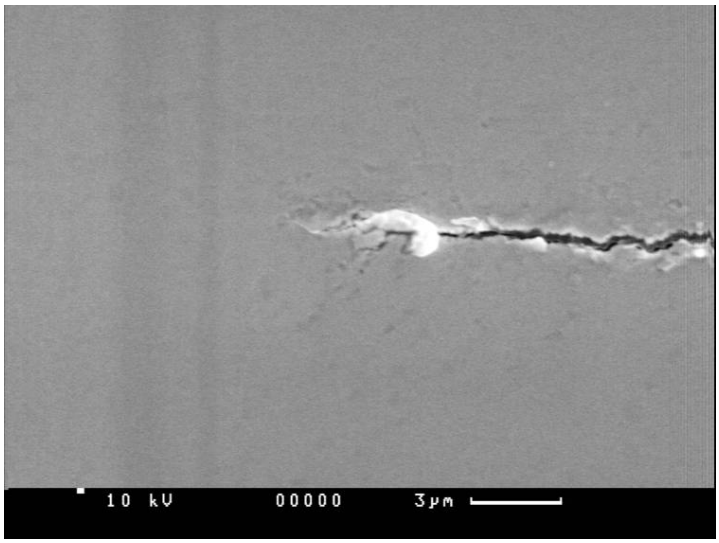

(a)

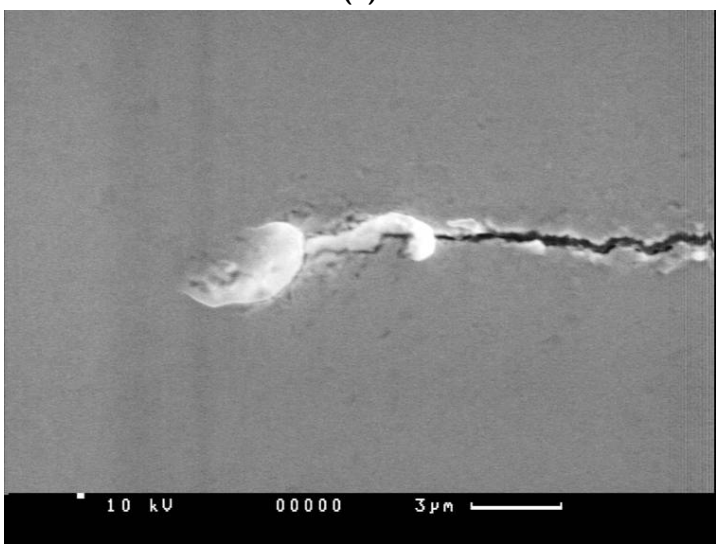

(b)

Figure C.2.: Overview of the crack propagation for the bimodal NC/UFG nickel in the in-situ fatigue experiment (the left crack tip). (a) after 500 cycles with R = −1 and (b) after 320 cycles with R = 0.1.

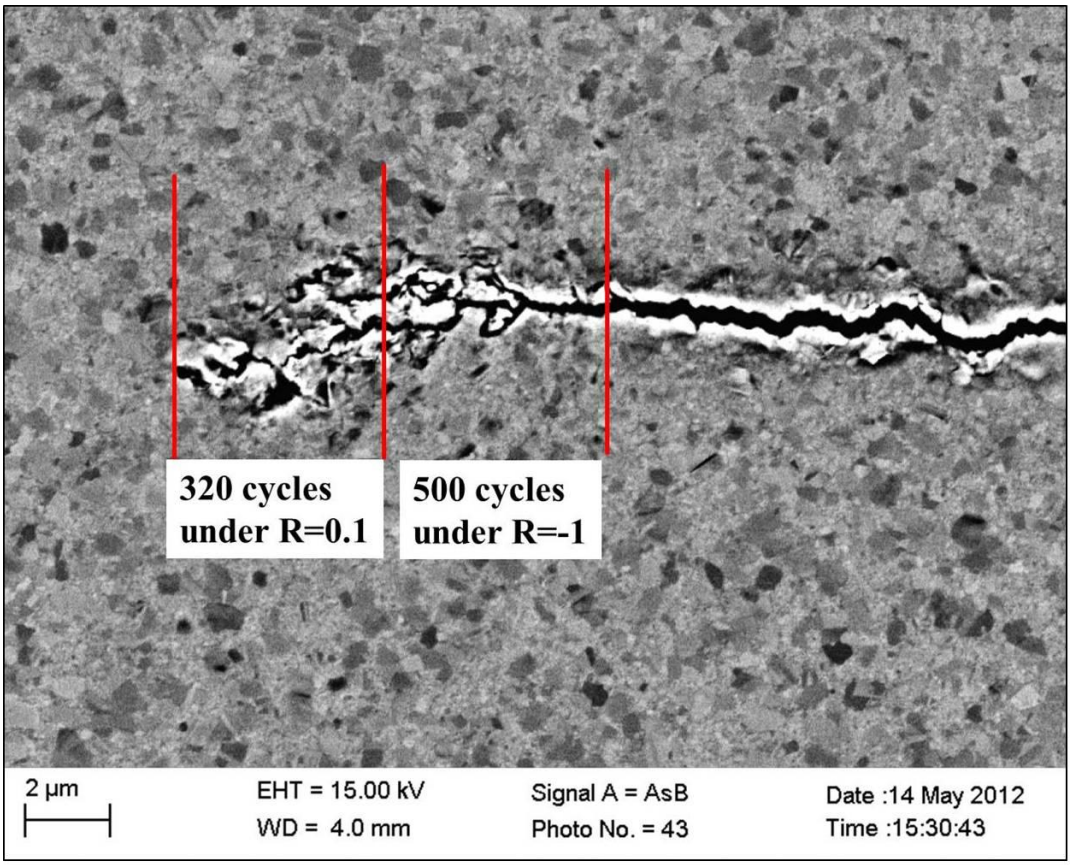

Figure C.3.: Overview of the crack propagation in the in-situ fatigue experiment, in correlation to the microstructures.

Appendix D.

ECAP nickel heat treated with laser beam

With the aim to control the grain growth areas the surface annealing with laser beam was conducted. The laser beam was controlled scanning over the specimen surface, in which different parameters such as the laser power, the specimen surface preparation, the focus of the laser beam and the scanning rate could be selected.

This experiment was conducted in the Institute of Functional Materials with the laser system Laserline LDM 500-20 which has the laser power of 500 W. As the heat absorption was influenced by the specimen surface toughness, the specimens were firstly grinded with the grinding papers to Grade 320 and Grade 800. It was found that the grain growth was more satisfying with the finer grinding.

The specimens were scanned with the focused and unfocused laser beam separately. With the two different modes the focused laser beam had a thinner scanning area but with higher heating intensity, while the unfocused laser beam had a wider scanning area but with lower heating intensity. After the laser scanning there were different grain growth areas depending on the distance to the middle of the laser beam, which could be described as the 'trimodal' grain size distributions. The analysis of the grain growth is shown in figure D.1 with the four special values: L1 as the width and D1 as the grains size of the center areas, L2 as the width of the whole heat influenced area and D2 as the grain size of the transition areas.

Table D.1 shows the overview of the experimental results, according to the scanning rates. It can be seen that the heat influenced areas and the average grain size both decreased with the increasing the scanning rate. However, the effect of the scanning rate became weaker with the growing scanning rate. Especially, the average grain sizes, both for the grain size in the center areas and in the transition areas, was less influenced

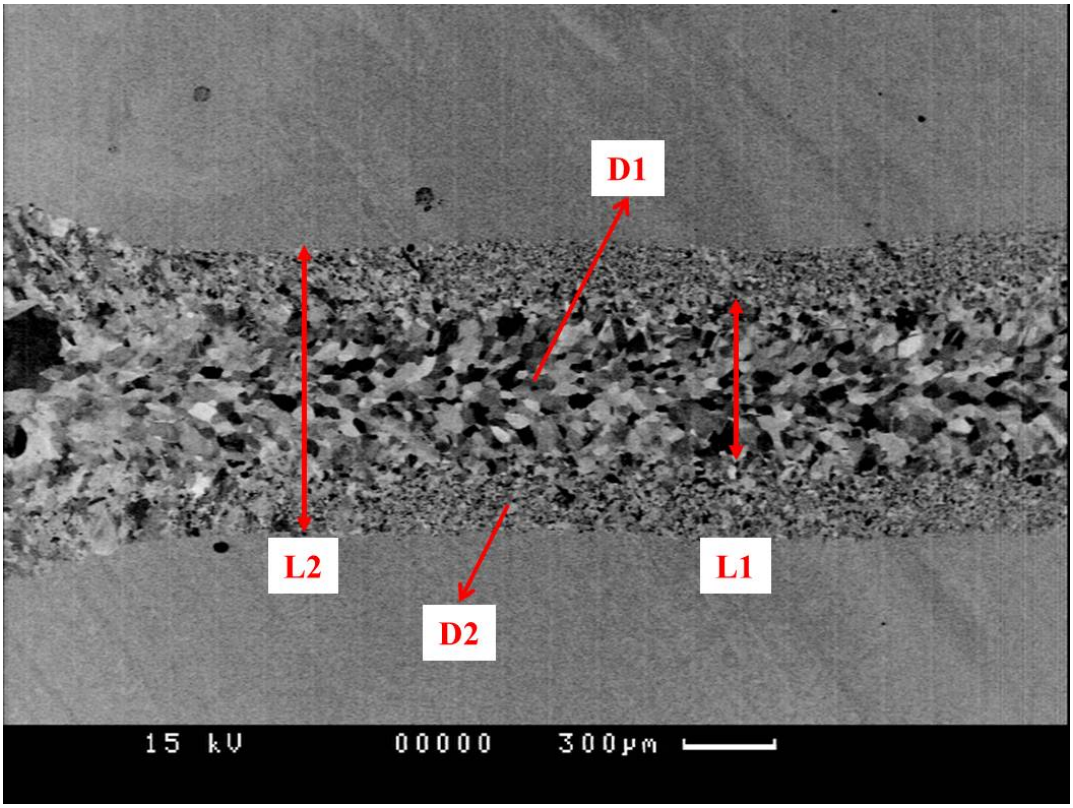

Figure D.1.: Analysis of the grain growth in the laser beam heat treated specimen.

by the scanning rate with the focused laser beam. Besides, although the focused laser beam had a thinner scanning area, the coarser grained areas were still larger than that with the unfocused laser beam, especially with the lower scanning rate. The unfocused laser beam seemed to be more efficient for this surface heat treatment, however the heat influenced areas were still too large comparing to the ultrafine grained matrix.

Upon the surface annealing with the laser beam the bimodal, or 'trimodal', microstructures were achieved. With this method the grain growth area and the grain size distribution can be controlled. However, in order to obtain more satisfying results with the designed bimodal microstructures a laser system with finer laser beam and lower power is needed.

laser beam	scanning rate (mm/min)	L1 (μm)	L2 (μm)	D1 (μm)	D2 (μm)
focused	500	933.61	1515.1	59.49	7.29
	1000	647.0	990.7	41.00	6.61
	5000	608.8	923.0	44.76	6.50
unfocused	500	706.7	1268.2	65.53	10.16
	1000	567.7	1036.4	37.98	4.38
	5000	505.6	901.4	28.48	3.91

Table D.1.: Experimental results of heat influenced area by the surface heat treatment with laser beam.

Bibliography

Agnew, S., and J. Weertman, Cyclic softening of ultrafine grain copper, *Mater*, *244*, 145–153, 1998.

Agnew, S., A. Y. Vinogradov, S. Hashimoto, and J. Weertman, Overview of fatigue performance of cu processed by severe plastic defor, *Journal of Electronic Materials*, *28*, 1038–1044, 1999.

Ahn, B., E. J. Lavernia, and S. R. Nutt, Dynamic observation of deformation in an ultrafine-grained al-mg alloy with bimodal grain structure, *J Mater Sci*, *43*, 7403–7408, 2008.

Aust, K., U. Erb, and G. Palumbo, Interfacial structures and properties, in *Mechanical properties and deformation behavior of materials having ultra-fine microstructures*, edited by M. Nastasi, D. M. Parkin, and H. Gleiter, p. 107, Kluwer Academic Publishers, 1993.

Azizi-Alizamini, H., M. Militzer, and W. Poole, A novel technique for developing bimodal grain size distribution in low carbon steels, *Scripta Materialia*, *57*, 1065–1068, 2007.

Bansal, S., A. Saxena, T. Hartwig, and R. R. Tummala, Fatigue and fracture behavior of nanocrystalline copper and nickel, in *Mixed mode, nano-or micro-scale on 11th International Conference on Fracture*, 2005.

Budrovic, Z., H. V. Swygenhoven, P. M. Derlet, S. V. Petegem, and B. Schmitt, Plastic deformation with reversible peak broadening in nanocrystalline nickel, *Science*, *304*, 273–276, 2004.

Cao, A., Y. Wei, and E. Ma, Grain boundary effects on plastic deformation and fracture mechanisms in cu nanowire: Molecular dynamics simulation, *Physical Review B*, *77*, 115,429–1–5, 2008.

Cavaliere, P., Fatigue properties and crack behavior of ultra-fine and nanocrystalline pure metals, *International Journal of Fatigue*, *31*, 1476C1489, 2009.

Cavaliere, P., and M. Cabibbo, Effect of sc and zr additions on the microstructure and fatigue properties of aa6106 produced by equal-channel-angular-pressing, *Materials Characterization*, *59*, 197–203, 2008.

Chai, G., Damage behavior of metallic materials under very high cycle fatigue, *Key Engineering Materials*, *348-349*, 237–240, 2007.

Chen, J., L. Lu, and K. Lu, Hardness and strain rate sensitivity of nanocrystalline cu, *Scripta Materialia*, *54*, 1913–1918, 2006.

Chen, Z., F. Liu, H. Wang, W. Yang, G. Yang, and Y. Zhou, A thermokinetic description for grain growth in nanocrystalline materials, *Acta Materialia*, *57*, 1466–1475, 2009.

Cheng, S., A. Stoica, X.-L. Wang, G. Wang, H. Choo, and P. Liaw, Fracture of ni with grain-size from nanocrystalline to ultrafine scale under cyclic loading, *Scripta Materialia*, *57*, 217–220, 2007.

Cheng, S., J. Xie, X.-L. Wang, J. Horton, D. Brown, H. Choo, and P. Liaw, Cyclic deformation of nanocrystalline and ultrafine-grained nickel, *Acta Materialia*, *57*, 1272–1280, 2009.

Dao, M., L. Lu, R. Asaro, J. D. Hosson, and E. Ma, Toward a quantitative understanding of mechanical behavior of nanocrystalline metals, *Acta Materialia*, *55*, 4041–4065, 2007.

El-Sherik, A., and U. Erb, Synthesis of bulk nanocrystalline nickel by pulsed electrodepostion, *Journal of Materials Science*, *30*, 5743–5749, 1995.

Erb, U., Electrodeposited nanocrystals: synthesis, properties and industrial applications, *Nanostructured Materials*, *6*, 533–538, 1995.

Fan, G., H. Choo, P. Liaw, and E. Lavernia, Plastic deformation and fracture of ultrafine-grained al-mg alloys with a bimodal grain size distribution, *Acta Materialia*, *54*, 1759–1766, 2006.

Farkas, D., M. Willemann, and B. Hyde, Atomistic mechanisms of fatigue in nanocrystalline metals, *Physics Review Letters*, *94*, 165,502–1 – 165,502–4, 2005.

Fougere, C., J. Weertman, and R. Siegel, Processing and mechanical behavior of nanocrystalline fe, *Nanostructured Materials*, *5*(2), 127–134, 1995.

Furukawa, M., Z. Horita, M. Nemoto, and T. Langdon, Review processing of metals by equal-channel angular pressing, *Journal of Materials Science*, *36*, 2835–2843, 2001.

Ganapathi, S., D. Owen, and A. Chokshi, The kinetics of grain growth in nanocrystalline copper, *Scripta Metallurgica et Materialia*, *25*(12), 2699–2704, 1991.

Giannakopoulos, A., and S. Suresh, Determination of elastoplastic properties by instrumented sharp indentation, *Scripta Materialia*, *40*(10), 1191–1198, 1999.

Gleiter, H., Nanocrystalline materials, *Progress in Materials Science*, *33*(4), 223 – 315, 1989.

Gleiter, H., Nanostructured materials: Basic concepts and microstructure, *Acta Materialia*, *48*, 1–29, 2000.

Godon, A., J. Creus, S. Cohendoz, E. Conforto, X. Feaugas, P. Girault, and C. Savall, Effect of grain orientation on the hall-petch relationship in electrodeposited nickel with nanocrystalline grains, *Scripta Materialia*, *62*, 403–406, 2010.

Goto, M., S. Han, T. Yakushiji, C. Lim, and S. Kim, Formation process of shear bands and protrusions in ultrafine grained copper under cyclic stresses, *Scripta Materialia*, *54*, 2101–2106, 2006.

Goto, M., S. Han, S. Kim, N. Kawagoishi, and C. Lim, Significance of non-equilibrium grain boundaries in surface damage formation of ultrafine-grained copper in high-cylce fatigue, *Scripta Materialia*, *57*, 293–296, 2007.

Goto, M., S. Han, T. Yakushiji, S. Kim, and C. Lim, Fatigue strength and formation behavior of surface damage in ultrafine grained copper with different non-equilibrium microstructures, *Inter*, *30*, 1333–1344, 2008.

Goto, M., S. Han, S. Kim, Y. Ando, and N. Kawagoishi, Growth mechanism of a small surface crack of ultrafine-grained copper in a high-cycle fatigue regime, *Scripta Materialia*, *60*(8), 729 – 732, 2009.

Gubicza, J., G. Dirras, P. Szommer, and B. Bacroix, Microstructure and yield strength of ultrafine grained aluminum processed by hot isostatic pressing, *Materials Science and Engineering: A*, *458*(1C2), 385 – 390, 2007.

Hall, E., The deformation and ageing of mild steel: Iii discussion of results, *Proceedings of the Physical Society. Section B*, *64*(9), 747–753, 1951.

Han, B., Z. Lee, D. Witkin, S. Nutt, and E. Lavernia, Deformation behavior of bimodal nanostructured 5083 al alloys, *Metallurgical and Materials Transactions A*, *36A*, 957–965, 2005.

Hanlon, T., Grain size effects on the fatigue response of nanocrystalline materials, Ph.D. thesis, Massachusetts Institute of Technology, 2004.

Hanlon, T., Y.-N. Kwon, and S. Suresh, Grain size effects on the fatigue response of nanocrystalline metals, *Scripta Materialia*, *49*, 675–680, 2003.

Hanlon, T., E. Tabachnikova, and S. Suresh, Fatigue behavior of nanocrystalline metals and alloys, *International Journal of Fatigue*, *27*, 1147–1158, 2005.

Hashimoto, S., Y. Kaneko, K. Kitagawa, A. Vinogradov, and R. Valiev, On the cyclic behaviour of ultra-fine grained copper produced by equi-channel angular pressing, *Materials Science Forum*, *312-314*, 593–598, 1999.

Higgins, G., Grain-boundary migration and grain growth, *Metal Science*, *8*, 143–150, 1974.

Hillert, M., On the theory of normal and abnormal grain growth, *Acta Metallurgica*, *13*(3), 227–238, 1965.

Hoeppel, H., and R. Valiev, On the possibilities to enhance the fatigue properties of ultrafine-grained metals, *Z. Metallkd*, *93*, 641–648, 2002.

Hoeppel, H., Z. Zhou, H. Mughrabi, and R. Valiev, Microstructural study of the parameters governing coarsening and cyclic softening in fatigued ultrafine-grained copper, *Philosophical Magazine A*, *82*(9), 1782–1794, 2002.

Hoeppel, H., M. Kautz, C. Xu, M. Murashkin, T. Langdon, R. Valiev, and H. Mughrabi, An overview: Fatigue behaviour of ultrafine-grained metals and alloys, *International Journal of Fatigue*, *28*, 1001–1010, 2006.

Hoeppel, H., M. Korn, R. Lapovok, and H. Mughrabi, Bimodal grain size distributions in ufg materials produced by spd: Their evolution and effect on mechanical properties, in *Journal of Physics: Conference Series 240*, 2010.

Huebner, P., R. Kiessling, H. Biermann, and A. Vinogradov, Fracture behaviour of ultrafine-grained materials under static and cyclic loading, *Int. J. Mater. Res.*, *97*(11), 1566–1570, 2006.

Humphreys, F., A unified theory of recovery, recrystallization and grain growth, based on the stability and growth of cellular microstructures - i. the basic model, *Acta Mater.*, *45*(10), 4231–4240, 1997.

Humphreys, F., and M. Hatherly, *Recrystallization and Related Annealing Phenomena, Second Edition*, ELSEVIER Ltd, 2004.

Janecek, M., J. Cizek, J. Gubicza, and J. Vratna, Microstructure and dislocation density evolutions in mgalzn alloy processed by severe plastic deformation, *J Mater Sci*, *47*, 7860–7869, 2012.

Jia, D., Y. Wang, K. Ramesh, E. Ma, Y. Zhu, and R. Valiev, Deformation behavior and plastic instabilities of ultrafine-grained titanium, *Applied Physics Letters*, *79*(5), 611–613, 2001.

Joshi, S., K. Ramesh, B. Han, and E. Lavernia, Modeling the constitutive response of bimodal metals, *Metallurgical and Materials Transactions A*, *37A*, 2397–2404, 2006.

Kirchheim, R., Grain coarsening inhibited by solute segregation, *Acta Materialia*, *50*, 413–419, 2002.

Koch, C., Optimization of strength and ductility in nanocrystalline and ultrafine grained metals, *Scripta Materialia*, *49*(7), 657 – 662, doi:10.1016/S1359-6462(03)00394-4, ¡ce:title¿Viewpoint Set No. 31. Mechanical Properties of Fully Dense Nanocrystalline Metals¡/ce:title¿, 2003.

Koch, C., K. Youssef, R. Scattergood, and K. Murtyg, Breakthroughs in optimization of mechanical properties of nanostructured metals and alloys, *Advanced Engineering Materials*, *7*(9), 787–794, 2005.

Komura, S., Z. Horita, M. Nemoto, and T. G. Langdon, Influence of stacking fault energy on microstructural development in equal-channel angular pressing, *J. Mater. Res.*, *14*(10), 4044–4050, 1999.

Korn, M., R. Lapovok, A. Boehner, H. Hoeppel, and H. Mughrabi, Bimodal grain size distributions in ufg materials produced by spd - their evolution and effect on the fatigue and monotonic strength properties, *Kovove Mater.*, *49*, 51–63, 2011.

Krasilnikov, N., W. Lojkowski, Z. Pakiela, and R. Valiev, Tensile strength and ductility of ultra-fine-grained nickel processed by severe plastic deformation, *Materials Science and Engineering: A*, *397*(1C2), 330 – 337, 2005.

Kulyasova, O., R. Islamgaliev, B. Mingler, and M. Zehetbauer, Microstructure and fatigue properties of the ultrafine-grained am60 magnesium alloy processed by equal-channel angular pressing, *Materials Science and Engineering A*, *503*, 176–180, 2009.

Kumar, K., S. Suresh, M. Chisholm, J. Horton, and P. Wang, Deformation of electrodeposited nanocrystalline nickel, *Acta Materialia*, *51*(2), 387 – 405, 2003.

Langdon, T. G., The principles of grain refinement in equal-channel angular pressing, *Materials Science and Engineering A*, *462*, 3–11, 2007.

Lee, Z., D. Witkin, V. Radmilovic, E. Lavernia, and S. Nutt, Bimodal microstructure and deformation of cryomilled bulk nanocrystalline al-7.5mg alloy, *Materials Science and Engineering A*, *410-411*, 462–467, 2005.

Lee, Z., V. Radmilovic, B. Ahn, E. J. Lavernia, and S. R. Nutt, Tensile deformation and fracture mechanism of bulk bimodal ultrafine-grained al-mg alloy, *Metallurgical and Materials Transactions A*, *41A*, 795–801, 2010.

Li, X., Y. Umakoshi, S. Wu, Z. Wang, I. Alexandrov, and R. Valiev, Temperature effects on the fatigue behavior of ultrafine-grained copper produced by equal channel angular pressing, *phys. stat. sol. (a)*, *201*(15), R119–R122, 2004.

Li, X.-W., Q.-W. Jiang, Y. Wu, Y. Wang, and Y. Umakoshi, Stress-amplitude-dependent deformation characteristics and microstructures of cyclically stressed ultrafine-grained copper, *Advanced Engineering Materials*, *10*(8), 720–726, 2008a.

Li, Y., Y. Zhang, N. Tao, and K. Lu, Effect of thermal annealing on mechanical properties of a nanostructured copper prepared by means of dynamic plastic deformation, *Scripta Materialia*, *59*, 475–478, 2008b.

Liu, F., and R. Kirchheim, Nano-scale grain growth inhibited by reducing grain boundary energy through solute segregation, *Journal of Crystal Growth*, *264*, 385–391, 2004.

Liu, F., G. Yang, H. Wang, Z. Chen, and Y. Zhou, Nano-scale grain growth kinetics, *Thermochimica Acta*, *443*, 212–216, 2006.

Liu, K., and F. Muecklich, Thermal stability of nano-rual produced by mechanical alloying, *Acta Mater.*, *49*, 395–403, 2001.

Lowe, T. C., and R. Z. Valiev, The use of severe plastic deformation techniques in grain refinement, *JOM*, *56*, 64–68, 2004.

Lu, K., Grain growth processes in nanocrystalline materials studied by differential scanning calorimetry, *Scripta Metallurgica et Materialia*, *23*(9), 2047–2052, 1991.

Lu, K., L. Lu, and S. Suresh, Strengthening materials by engineering coherent internal boundaries at the nanoscale, *Science*, *324*, 349–352, 2009.

Lu, L., Y. Shen, X. Chen, L. Qian, and K. Lu, Ultrahigh strength and high electrical conductivity in copper, *Science*, *304*, 422–426, 2004.

Lu, L., R. Schwaiger, Z. Shan, M. Dao, K. Lu, and S. Suresh, Nano-sized twins induce high rate sensitivity of flow stress in pure copper, *Acta Materialia*, *53*, 2169–2179, 2005.

Lukas, P., L. Kunz, and M. Svoboda, Effect of low temperature on fatigue life and cyclic stress-strain response of ultrafine-grained copper, *Metallurgical and Materials Transactions A*, *38A*, 1910–1915, 2007.

Malow, T., and C. Koch, Grain growth in nanocrystalline iron prepared by mechanical attrition, *Acta Mater.*, *45*(5), 2177–2186, 1997.

Marx, M., W. Schaef, and H. Vehoff, Interaction of short cracks with the local microstructure, *Procedia Engineering*, *2*, 163–171, 2010.

Meyers, M., A. Mishra, and D. Benson, Mechanical properties of nanocrystalline materials, *Progress in Materials Science*, *51*(4), 427 – 556, 2006.

Michels, A., C. Krill, E. Ehrhardt, R. Birringer, and D. Wu, Modelling the influence of grain size dependent solute drag on the kinetics of grain growth in nanocrystalline materials, *Acta Mater.*, *47*(7), 2143–2152, 1999.

Moelle, C., and H. Fecht, Thermal stability of nanocrystalline iron prepared by mechanical attrition, *NanoStructured Materials*, *6*, 421–424, 1995.

Moser, B., T. Hanlon, K. Kumar, and S. Suresh, Cyclic strain hardening of nanocrystalline nickel, *Scripta Materialia*, *54*(6), 1151 – 1155, 2006.

Mughrabi, H., and H. W. Hoeppel, Cyclic deformation and fatigue properties of ultrafine grain size materials: current status and some criteria for improvement of the fatigue resistance, *MRS Proceedings*, *634*, B2.1.1–B2.1.12, 2000.

Mughrabi, H., and H. W. Hoeppel, Cyclic deformation and fatigue properties of very fine-grained metals and alloys, *International Journal of Fatigue*, *32*(9), 1413 – 1427, 2010.

Mughrabi, H., H. Hoeppel, and M. Kautz, Fatigue and microstructure of ultrafine-grained metals produced by severe plastic deformation, *Scripta Materialia*, *52*, 807–812, 2004.

Murata, Y., I. Nakaya, and M. Morinaga, Assessment of strain energy by measuring dislocation density in copper and aluminium prepared by ecap and arb, *Materials Transactions*, *49*(1), 20–23, 2008.

Natter, H., and R. Hempelmann, Nanocrystalline copper by pulsed electrodepostion: The effects of organic additives, bath temperatures and ph, *J. Phys. Chem.*, *100*, 19,525–19,532, 1996.

Natter, H., and R. Hempelmann, Nanocrystalline metals prepared by electrodeposition, *Z. Phys. Chem.*, *222*, 319–354, 2008.

Natter, H., M. Schmelzer, and R. Hempelmann, Nanocrystalline nickel and nickel-copper alloys: synthesis, characterization, and thermal stability, *Journal of Materials Research*, *13*(5), 1186–1197, 1998.

Neishi, K., Z. Horita, and T. G. Langdon, Grain refinement of pure nickel using equal-channel angular pressing, *Materials Science and Engineering A*, *325*, 54–58, 2002.

Nelson, S., L. Ladani, T. Topping, and E. Lavernia, Fatigue and monotonic loading crack nucleation and propagation in bimodal grain size aluminum alloy, *Acta Materialia*, *59*, 3550–3570, 2011.

Noll, A., In-situ untersuchung der kornwachstumsmechanismen von elektrodeponiertem, nanokristallinem nickel im rasterelektronenmikroskop, Master's thesis, Universitaet des Saarlandes, 2006.

Ovid'ko, I., Deformation and diffusion modes in nanocrystalline materials, *International Materials Reviews*, *50*(2), 65–82, 2005.

Ovid'ko, I., Review on the fracture toughness in nanocrystalline materials, *J Mater Sci*, *42*, 1694–1708, 2007.

Ovid'ko, I., and T. Langdon, Enhanced ductility of nanocrystalline and ultrafine-grained metals, *Rev. Adv. Mater. Sci.*, *30*, 103–111, 2012.

Padilla-II, H., and B. Boyce, A review of fatigue behavior in nanocrystalline metals, *Experimental Mechanics*, *50*, 5–23, 2010.

Pao, P., H. Jones, S. Cheng, and C. Feng, Fatigue crack propagation in ultrafine grained alcmg alloy, *International Journal of Fatigue*, *27*(10C12), 1164 – 1169, 2005.

Pao, P., R. Holtz, H. Jones, and C. Feng, Effect of environment on fatigue crack growth in ultrafine grain al-mg, *International Journal of Fatigue*, *31*, 1678–1683, 2009.

Park, K.-T., Y.-S. Kim, J. G. Lee, and D. H. Shin, Thermal stability and mechanical properties of ultrafine grained low carbon steel, *Materials Science and Engineering A*, *293*, 165–172, 2000.

Patra, S., S. M. Hasan, N. Narasaiah, and D. Chakrabarti, Effect of bimodal distribution in ferrite grain sizes on the tensile properties of low-carbon steels, *Materials Science and Engineering A*, *538*, 145–155, 2012.

Petch, N., The cleavage strength of polycrystals, *J. Iron Steel Inst.*, *174*, 25, 1953.

Philippi, B., Gezielte variation der mikrostruktur bei der gepulsten elektrodeposition von nanokristallinem und ultrafeinkoernigem nickel, Master's thesis, Saarland University, 2011.

Prasad, M., S. Suwas, and A. Chokshi, Microstructural evolution and mechanical characteristics in nanocrystalline nickel with a bimodal grain-size distribution, *Materials Science and Engineering A*, *503*, 86–91, 2009.

Ramtani, S., G. Dirras, and H. Bui, A bimodal bulk ultra-fine-grained nickel: Experimental and micromechanical investigations, *Mechanics of Materials*, *42*(5), 522 – 536, 2010.

Randle, V., and D. Horton, Grain growth phenomena in nickel, *Scripta Metallurgica et Materialia*, *31*(7), 891–895, 1994.

Reihanian, M., R. Ebrahimi, N. Tsuji, and M. Moshksar, Analysis of the mechanical properties and deformation behavior of nanostructured commercially pure al processed by equal channel angular pressing (ecap), *Materials Science and Engineering A*, *473*, 189–194, 2008.

Riontino, G., C. Antonione, L. Battezzati, F. Marino, and M. Tabasso, Kinetics of abnormal grain growth in pure iron, *Journal of Materials Science*, *14*, 86–90, 1979.

Rofagha, R., R. Langer, A. El-Sherik, U. Erb, G. Palumbo, and K. Aust, The corrosion behaviour of nanocrystalline nickel, *Scripta Metallurgica et Materialia*, *25*(12), 2867 – 2872, 1991.

Rollett, A., A. Brahme, and C. Roberts, An overview of accomplishments and challenges in recrystallization and grain growth, *Materials Science Forum*, *558-559*, 33–42, 2007.

Sanders, P., J. Eastman, and J. Weertman, Elastic and tensile behavior of nanocrystalline copper and plalladium, *Acta Materialia*, *45*(10), 4019–4025, 1997a.

Sanders, P., C. Youngdahl, and J. Weertman, The strength of nanocrystalline metals with and without flaws, *Materials Science and Engineering A*, *234-236*, 77–82, 1997b.

Sangid, M. D., G. J. Pataky, H. Sehitoglu, R. G. Rateick, T. Niendorf, and H. J. Maier, Superior fatigue crack resistance, irreversibility, and fatigue crack growth - microstructure relationship of nanocrystalline alloys, *Acta Materialia*, *59*, 7340–7355, 2011.

Schaef, W., Ueber die wechselwirkung kurzer ermuedungsrisse mit korngrenzen - systematische experimente mit focussed ion beam microscope und mikrostruktureller tomographie, Ph.D. thesis, Universitaet des Saarlandes, 2010.

Schaef, W., and M. Marx, A numerical description of short fatigue cracks interacting with grain boundaries, *Acta Materialia*, *60*, 2425–2436, 2012.

Schaef, W., M. Marx, H. Vehoff, A. Heckl, and P. Randelzhofer, A 3-d view on the mechanisms of short fatigue cracks interacting with grain boundaries, *Acta Materialia*, *59*, 1849–1861, 2011.

Shen, Y., L. Lu, M. Dao, and S. Suresh, Strain rate sensitivity of cu with nanoscale twins, *Scripta Materialia*, *55*, 319–322, 2006.

Singh, A., L. Tang, M. Dao, L. Lu, and S. Suresh, Fracture toughness and fatigue crack growth characteristics of nanotwinned copper, *Acta Materialia*, *59*(6), 2437 – 2446, doi:10.1016/j.actamat.2010.12.043, 2011.

Skrotzki, W., L. Toth, B. Kloeden, H.-G. Brokmeier, and R. Arruffat-Massion, Texture after ecap of a cube-oriented ni single crystal, *Acta Materialia*, *56*, 3439–3449, 2008.

Srinivasarao, B., K. Oh-ishi, T. Ohkubo, T. Mukai, and K. Hono, Synthesis of high-strength bimodally grained iron by mechanical alloying and spark plasma sintering, *Scripta Materialia*, *58*, 759–762, 2008.

Suresh, S., *Fatigue of Materials, 2nd edition*, Cambridge University Press, 1998.

Swygenhoven, H. V., P. Derlet, and A. Froeseth, Stacking fault energies and slip in nanocrystalline metals, *Nature Materials*, *3*, 399–403, 2004.

Tellkamp, V., A. Melmed, and E. Lavernia, Mechanical behavior and microstructure of a thermally stable bulk nanostructured al alloy, *Metallurgical and Materials Transactions A*, *32A*, 2335–2343, 2001.

Thompson, C., H. Frost, and F. Spaepen, The relative rates of secondary and normal grain growth, *Acta Metallurgica*, *35*(4), 887–890, 1987.

Tsuji, N., Y. Ito, Y. Saito, and Y. Minamino, Strength and ductility of ultrafine grained aluminum and iron prodeced by arb and annealing, *Scripta Materialia*, *47*, 893–899, 2002.

Tsuji, N., Y. Saito, S.-H. Lee, and Y. Minamino, Arb (accumulative roll-bonding) and other new techniques to produce bulk ultrafine grained materials, *Advacned Engigeering Materials*, *5*, 338–344, 2003.

Valiev, R., Materials science: Nanomaterial advantage, *Nature*, *419*, 887–889, 2002.

Valiev, R., R. Mulyukov, and V. Ovchinnikov, Direction of a grain-boundary phase in submicrometre-grained iron, *Philosophical Magazine Letters*, *62*(4), 253–256, 1990.

Valiev, R., N. Krasilnikov, and N. Tsenev, Plastic deformation of alloys with submicron-grained structure, *Materials Science and Engineering A*, *137*, 35–40, 1991.

Valiev, R., R. Islamgaliev, and I. Alexandrov, Bulk nanostructured materials from severe plastic deformation, *Progress in Materials Science*, *45*(2), 103 – 189, 2000.

Valiev, R. Z., and T. G. Langdon, Principles of equal-channel angular pressing as a processing tool for grain refinement, *Progress in Materials Science*, *51*(7), 881 – 981, doi:10.1016/j.pmatsci.2006.02.003, 2006.

Vasudevan, A., and K. Sadananda, Classification of environmentally assisted fatigue crack growth behavior, *International Journal of Fatigue*, *31*, 1696–1708, 2009.

Vehoff, H., B. Yang, A. Barnoush, H. Natter, and R. Hempelmann, Mechanical properties of nanomaterials examined with a ni-afm, *Progress in Physical Chemistry*, *2*, 275–301, doi:10.1524/9783486598674.275, 2008.

Vinogradov, A., and S. Hashimoto, Multiscale phenomena in fatigue of ultra-fine grain materials - an overview, *Materials Transactions*, *42*(1), 74–84, 2001.

Vinogradov, A., and S. Hashimoto, Fatigue of severely deformed metals, *Advanced Engineering Materials*, *5*(5), 351–358, 2003.

Vinogradov, A., V. Stolyarov, S. Hashimoto, and R. Valiev, Cyclic behavior of ultrafine-grain titanium produced by sever plastic deformation, *Materials Science and Engineering A*, *318*, 163–173, 2001.

Vinogradov, A., V. Patlan, S. Hashimoto, and K. Kitagawa, Acoustic emission during cyclic deformation of ultrafine-grain copper processed by severe plastic deformation, *Philosophical Magazine A*, *82*(2), 317–335, 2002.

Vinogradov, A., S. Hashimoto, and V. Kopylov, Enhanced strength and fatigue life of ultra-fine grain fe-36ni invar alloy, *Materials Science and Engineering A*, *355*, 277–285, 2003a.

Vinogradov, A., A. Washikita, K. Kitagawa, and V. Kopylov, Fatigue life of fine-grain al-mg-sc alloys produced by equal-channel angular pressing, *Materials Science and Engineering A*, *349*, 318–326, 2003b.

Wang, Q., C. Bathias, N. Kawagoishi, and Q. Chen, Effect of inclusions on subsurface crack initiation and gigacycle fatigue strength, *International Journal of Fatigue*, *24*, 1269–1274, 2002a.

Wang, Q., C. Xu, M. Zheng, J. Zhu, and Z. Du, Fatigue crack initiation life prediction of ultra-fine grain chromium-bronze prepared by equal-channel angular pressing, *Materials Science and Engineering A*, *496*, 434–438, 2008a.

Wang, T., F. Zhang, M. Zhang, and B. Lv, A novel process to obtain ultrafine-grained low carbon steel with bimodal grain size distribution for potentially improving ductility, *Materials Science and Engineering A*, *485*, 456–460, 2008b.

Wang, Y., and E. Ma, Temperature and strain rate effects on the strength and ductility of nanostructured copper, *Applied Physics Letters*, *83*(15), 3165–3167, 2003.

Wang, Y., and E. Ma, Three strategies to achieve uniform tensile deformation in a nanostructured metal, *Acta Materialia*, *52*, 1699–1709, 2004a.

Wang, Y., and E. Ma, Strain hardening, strain rate sensitivity, and ductility of nanostructured metals, *Materials Science and Engineering A*, *375-377*, 46–52, 2004b.

Wang, Y., M. Chen, F. Zhou, and E. Ma, High tensile ductility in a nanostructured metal, *Nature*, *419*, 912–915, 2002b.

Wang, Y., S. Cheng, Q. Wei, E. Ma, T. Nieh, and A. Hamza, Effects of annealing and impurities on tensile properties of electrodeposited nanocrystalline ni, *Scripta Materialia*, *51*(11), 1023 – 1028, 2004.

Weissmueller, J., W. Krauss, T. Haubold, R. Birringer, and H. Gleiter, Atomic structure and thermal stability of nanostructured y-fe alloys, *NanoStructured Materials*, *1*(6), 439–447, 1992.

Witkin, D., and E. Lavernia, Synthesis and mechanical behavior of nanostructured materials via cryomilling, *Progress in Materials Science*, *51*, 1–60, 2006.

Witney, A., P. Sanders, J. Weertman, and J. Eastman, Fatigue of nanocrystalline copper, *Scripta Metallurgica et Materialia*, *33*(12), 2025–2030, 1995.

Wong, M., W. Kao, J. Lui, C. Chang, and P. Kao, Cyclic deformation of ultrafine-grained aluminum, *Acta Materialia*, *55*, 715–725, 2007.

Wu, S., Z. Wang, C. Jiang, G. Li, I. Alexandrov, and R. Valiev, The formation of psb-like shear bands in cyclic deformed ultrafine grained copper processed by ecap, *Scripta Materialia*, *48*, 1605–1609, 2003.

Wu, S., Z. Wang, C. Jiang, G. Li, I. Alexandrov, and R. Valiev, Shear bands in cyclically deformed ultrafine grained copper processed by ecap, *Materials Science and Engineering A*, *387-389*, 560–564, 2004.

Xie, J., X. Wu, and Y. Hong, Shear bands at the fatigue crack tip of nanocrystalline nickel, *Scripta Materialia*, *57*(1), 5 – 8, 2007.

Xie, J., X. Wu, and Y. Hong, Study on fatigue crack nucleation of electrodeposited nanocrystalline nickel, *Advanced Materials Research*, *33-37*, 925–930, 2008.

Xu, C., Q. Wang, M. Zheng, J. Li, M. Huang, Q. Jia, jiewu Zhu, L. Kunz, and M. Buksa, Fatigue behavior and damage characteristic of ultra-fine grain low-purity copper processed by equal-channel angular pressing (ecap), *Materials Science and Engineering A*, *475*, 249–256, 2008.

Yamakov, V., D. Wolf, S. Phillpot, A. Mukherjee, and H. Gleiter, Deformation-mechanism map for nanocrystalline metals by molecular-dynamics simulation, *Nature Materials*, *3*, 43–47, 2004.

Yang, B., Grain size effects on the mechanical behavior of polycrystalline nickel from micro to nanoscale, Ph.D. thesis, Saarland University, 2006.

Yang, B., and H. Vehoff, Grain size effects on the mechanical properties of nanonickel examined by nanoindentation, *Materials Science and Engineering A*, *400-401*, 467–470, 2005.

Youngdahl, C., J. Weertman, R. Hugo, and H. Kung, Deformation behavior in nanocrystalline copper, *Scripta mater.*, *44*, 1475–1478, 2001.

Youssef, K. M., R. O. Scattergood, K. L. Murty, J. A. Horton, and C. C. Koch, Ultrahigh strength and high ductility of bulk nanocrystalline copper, *Applied Physics Letter*, *87*, 091,904–1 – 091,904–3, 2005.

Yu, Q., L. Qi, K. Chen, R. K. Mishra, J. Li, and A. M. Minor, The nanostructured origin of deformation twinning, *Nano Lett.*, *12*, 887–892, 2012.

Zhang, W., S. Li, and S. Nutt, Parametric analysis of tensile properties of bimodal al alloys by finite element method, *J. Mater. Sci. Technol.*, *25*(2), 281–288, 2009.

Zhang, X., H. Wang, R. Scattergood, J. Narayan, C. Koch, A.V.Sergueeva, and A. Mukherjee, Studies of deformation mechanisms in ultra-fine-grained and nanostructured zn, *Acta Materialia*, *50*, 4823–4830, 2002.

Zhang, X., A. Misra, H. Wang, T. Shen, M. Nastasi, T. Mitchell, J. Hirth, R. Hoagland, and J. Embury, Enhanced hardening in cu/330 stainless steel multilayers by nanoscale twinning, *Acta Materialia*, *52*, 995–1002, 2004.

Zhao, M.-C., F. Yin, T. Hanamura, K. Nagai, and A. Atrens, Relationship between yield strength and grain size for a bimodal structural ultrafine-grained ferrite/cementite steel, *Scripta Materialia*, *57*, 857–860, 2007.

Zhao, Y., X. Liao, Z. Jin, R. Valiev, and Y. Zhu, Microstructures and mechanical properties of ultrafine grained 7075 al alloy processed by ecap and their evolutions during annealing, *Acta Materialia*, *52*, 4589–4599, 2004.

Zhao, Y., Y. Zhu, X. Liao, Z. Horita, and T. Langdon, Tailoring stacking fault energy for high ductility and high strength in ultrafine grain cu and its alloy, *Applied Physics Letters*, *89*, 121,906–1 – 3, 2006a.

Zhao, Y., Q. Zhan, T. Topping, Y. Li, W. Liu, and E. Lavernia, Improving ductility in ultrafine grained nickel with porosity and segregation wia deformation, *Materials Science and Engineering A*, *527*, 1744–1750, 2010a.

Zhao, Y., Y. Zhu, and E. J. Lavernia, Strategies for improving tensile ductility of bulk nanostructured materials, *Advanced Engineering Materials*, *12*(8), 769–778, 2010b.

Zhao, Y., T. Topping, Y. Li, and E. J. Lavernia, Strength and ductility of bi-modal cu, *Advanced Engineering Materials*, *13*(9), 865–871, 2011.

Zhao, Y., et al., High tensile ductility and strength in bulk nanostructured nickel, *Advanced Materials*, *20*, 3028–3033, 2008.

Zhao, Y.-H., et al., Simultaneously increasing the ductility and strength of ultra-fine-grained pure copper, *Advanced Materials*, *18*, 2949–2953, 2006b.

Zhilyaev, A., M. Baro, T. Langdon, and T. McNelley, An examination of microtexture and microstructure in ultrafine-grained nickel, *Rev. Adv. Mater. Sci.*, *7*, 41–49, 2004.

Zhilyaev, A., B.-K. Kim, J. Szpunar, M. Baro, and T.G.Langdon, The microstructural characteristics of ultrafine-grained nickel, *Materials Science and Engineering: A*, *391*(1C2), 377 – 389, doi:10.1016/j.msea.2004.09.030, 2005.

Zhu, L., and J. Lu, Modelling the plastic deformation of nanostructured metals with bimodal grain size distribution, *International Journal of Plasticity*, *30-31*, 166–184, 2012.

Zhu, L., A. Chen, and J. Lu, Achieving high strength and high ductility in nanostructured metals: Experiment and modelling, *Theoretical & Applied Mechanics Letters*, *2*, 021,001–9, 2012.

Zhu, Y., J. Huang, J. Gubicza, T. Ungar, Y. Wang, E. Ma, and R. Valiev, Nanostructures in ti processed by severe plastic deformation, *J. Mater. Res.*, *18*(8), 1908–1917, 2003.

Zhu, Y. T., and X. Liao, Nanostructured metals: Retaining ductility, *Nature Materials*, *3*, 351–352, 2004.